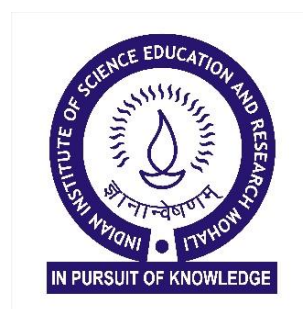


STRUCTURAL AND FUNCTIONAL STUDIES OF AN ALL- PROTEIN PROKARYOTIC NANO BIOREACTOR

NAIMAT KALIM BARI

*A thesis submitted for the partial fulfillment of the
degree of Doctor of Philosophy*



Institute of Nano Science and Technology,
Habitat Centre, Sector-64, Phase-10, Mohali, 160062, Punjab, India.

Indian Institute of Science Education and Research Mohali
Knowledge city, Sector 81, SAS Nagar, Manauli PO, Mohali, 140306, Punjab, India.

July, 2020

Dedicated to
Beloved Teacher's
&
Mentors

Declaration

The work presented in this thesis has been carried out by me under the guidance of Dr. Sharmistha Sinha at the Institute of Nano Science and Technology, Mohali. This work has not been submitted in part or in full for a degree, a diploma, or a fellowship to any other university or institute. Whenever contributions of others are involved, every effort is made to indicate this clearly, with due acknowledgment of collaborative research and discussions. This thesis is a bonafide record of original work done by me and all sources listed.

Naimat Kalim Bari

In my capacity as the supervisor of the candidate's thesis work, I certify that the above statements made by the candidate are true to the best of my knowledge.

Dr. Sharmistha Sinha

Acknowledgments

*And my success in my task can only come from
Allah,
In Him I trust and unto Him I turn”*

[Al-Quran]

*First of all, I bow in reverence to **ALLAH, The AL ALEEM. The Almighty, the Most Beneficent and the Merciful**, creator of the universe for providing enough patience, courage, and zeal that enabled me to accomplish my Ph.D. thesis work.*

The work presented in this thesis would not have been possible without the support and guidance that I received from many people. Towards the submission of this work, I would take this opportunity to extend my sincere gratitude and appreciation to all those who made this Ph.D. thesis possible.

*Foremost, I wholeheartedly thank my supervisor, **Dr. Sharmistha Sinha**, Senior Scientist, Institute of Nano Science and Technology, Mohali, Punjab, India. A lady with a passion for science with a “never say die” attitude. Her excellent academic and research knowledge, sincere and honest interest in my work, helped me to get a clear picture of the research envisaged for this thesis work. Discussion with her helped me to overcome the hurdles which came in my work and helped me to imbibe the passion of the undying quest for knowledge. Her passion, enthusiasm, and close monitoring of my work helped me to be on my toe. Her close supervision to build a scientific temperament during my stay at INST, as a Ph.D. student is beyond words. I feel lucky for being her first Ph.D. student because immense knowledge which I received from her during my stay is going to shape my future endeavors. Her guidance, tremendous support, motivation, helped me in all the time of research, and writing of this thesis. I could not have imagined having a better advisor and mentor for my Ph.D. I will be ever thankful to her, for the valuable teachings, out of league support and sustained encouragement.*

*I would also like to thank the members of my thesis committee: **Dr. Surajit Karmakar** and **Dr. P.S.Vijayakumar**, for their time, interest, insightful comments, and encouragement.*

*I would also like to thank my annual review committee members: **Dr. Sangita Roy, Dr. Asish Pal, Dr. Md Ehesan Ali, Dr. Prakash P. Neelakandan, Dr. Rahul K. Verma, and Dr. Deepa Ghosh**, for their time, insightful suggestions and encouragement.*

*I like to extend my sincere thanks and gratitude to **Dr. Sabyasachi Rakshit**, IISER Mohali, for allowing me to work in his Lab and to use the facilities. His cooperation, support, and motivation have always kept me going ahead.*

*I would also extend my gratitude to **Dr. Sharvan Sehwat and Dr. Rhitoban R. Choudhury**, IISER Mohali, for allowing me to use their lab facilities whenever needed.*

*My special thanks to INST, Founder Director, **Prof. A.K Ganguli**, and Officiating Director, **Prof. H.N. Ghosh**, and **Esteemed Faculty of INST** for the guidance and affectionate conversations during this course of time.*

*I am grateful to the **INST family** for providing me a healthy environment to work. Thanks to **Faraday Lab Committee** for providing us a vibrant lab atmosphere and making the facilities available for carrying out research. Thanks to the administrative staff, especially the purchasing department (**Rohit and Rajeev Sir**), for helping us to avail of all the logistics without delay. I would also extend my special regards to **Gurveen Ma'am, Shweta Ma'am, Suman Ma'am, Vibha Ma'am, and Mukesh Sir** for their support. I also extend my gratitude to the non-administrative staff who have always been for our help. Importantly, I extend my thanks to DST, Government of India, for providing me with fellowship during my Ph.D. tenure.*

*A special word of gratitude for our beloved **Datta sir**, a man of guidance, motivation, zeal, and passion. Be it in the lab or on the playing field, he was fantastic and always inspiring. Though he left us for his final journey, in the middle of our voyage depriving us of the irreplaceable love and care. May Allah rest his soul in peace, and he keeps guiding us in our journey ahead.*

*I am fortunate enough to have worked with wonderful people who joined our lab. I take this opportunity to extend my thanks to all my fellow lab-mates, **Ankush, Gaurav, Simer, Silky, Harpreet, and Tavishi**, who always motivated me that helped me to explore myself. I also extend my thanks to colleagues who joined our lab at different phases of my Ph.D.*

*and contributed significantly. Special Thanks to my Ph.D. colleague **Arka** and **Sandeep**; Post-doctoral fellows **Arun Sir**, **Prathna Ma'am**, **Shaswat Sir**, and **Sumit Sir** from whom I learned during their stay in our lab. My special Thanks to **Namrata**, **Kritika**, **Vaishali**, **Pranathi**, and **Deepika** for their contributions and help. I also take this opportunity to Thanks my lab members from Rakshit lab; **Gayathri**, **Jagadish**, **Anuj**, **Sai**, **Nisha**, **Sayan**, **Surbhi**, **Jess Bhaiya**, **Deb Da**, **Amin Sir**, **Malay Bhaiya**, **Kamran Sir**, **Varinder Bhaiya**, **Shweta S**, **Nilesh**, **Shweta M**, **Pritam**, **Anjana**, **Tanuja**, **Keshav**, **Bhati**, **Adarsh**, **Ankit**, **Sunanda**, **Satavisa**, **Lisha**, **Angel**, for their support and motivation. I have cherished their presence in the lab as it turned out to be a place for mutual exchange of ideas and stimulating discussions over the never-ending coffee breaks.*

***Friends** need a special mention because, without their support and encouragement, this small piece of work wouldn't have reached to its completion. My heartiest regards go to **Manpreet**, **Rafi**, **Dhanesh**, **Munish**, **Soumen**, **Anup**, **Sanjay**, **Ashmeet**, **Swati**, **Rashmi**, **Ritu**, **Rajender**, **Ankur**, and **Dimple**. I am also thankful to amazing people at INST who need to be acknowledged. The list is never-ending, but mentioning a few are **Neha**, **Ruchi**, **Renu**, **Harman**, **Anirban**, **Pulkit**, **Sandeep**, **Atul**, **Sunaina**, **Rohit**, **Harsimran**, **Pooja**, **Vijay**, **Saurav**, **Pranjali**, **Aashish**, **Ankush**, **Abhishek**, **Sudhakar**. Special regards for by brother's **Bilal Bhai**, **Hasan Bhai**, **Anas**, **Khalid**, **Arif**, **Selim**, **Mujeeb**, **Atikur**, **Nadim**, **Zubair**, **Raihan**, **Rejaul**, **Riyaz**, **Roman**, **Farhan**, **Kashif**, **Firdaus**, **Aquib**, **Nausad**, **Zaidi** for their unparalleled love, care and motivation.*

*I am indebted to my roommates, **Krishna**, and **Venu**, who have been helpful in numerous ways.*

*I also owe a deep sense of gratitude to my dear friend **Sobiya** and her family (**Uncle**, **Aunty**, **Yusra**, **Ausaf Bhai**, and **Dear Zobu**) for their support, encouragement, and love which can't be put in words.*

*I feel a deep sense of gratitude for my family, who formed part of my vision and taught me good things that matter in life. Their unfailing love and support have always been my strength. Their patience and sacrifice will remain my inspiration throughout my life. The teachings of **my father**, to be honest, truthful, and disciplined in one work has always been the guiding force. To have love and care for others, always ready to help as taught by **my mother**, has helped me to receive the same from others. Special thanks to my beloved*

brothers, **Rifat Bhai, Azmat, Danish, Tausif, Taseer, Fakid**, for their selfless love, motivation, constant support, and dedicated efforts, which contributed a lot to completion of my thesis. I am also very much grateful to all my family members, especially my maternal uncles and aunts (Mamu and Khala), who have taken care of my parents, which helped me to focus more on my work. I am thankful to my grandparents for providing me a beautiful family who has provided their constant support and encouragement. They selflessly encouraged me to explore new directions in life and seek my destiny. This journey would not have been possible if not for them, and I dedicate this milestone to them.

This work is never the work of an individual. It is more a combination of ideas, suggestions, and reviews, contributions, and efforts of many. I wish to express my appreciation to all those, with whom I have worked, interacted, and whose thoughts and insights have helped me in furthering my knowledge and understanding of the subject.

At last, I again bow in reverence to **ALLAH** and his most beloved **Prophet (PBUH)** for giving me this life, full of blessings and knowledge. I pray to **ALLAH**, "**The AR RASHEED**" to keep guiding and enriching me with knowledge so that I can dedicate my life to the cause of humanity.

Naimat Kalim Bari

ABBREVIATIONS

<i>MBTH</i>	<i>3-Methyl-2-benzothiazoline</i>
<i>AFM</i>	<i>Atomic Force Microscopy</i>
<i>BMCs/MCPs</i>	<i>Bacterial Microcompartments</i>
<i>BPER-II</i>	<i>Bacterial Protein Extraction Reagent</i>
β-CD	<i>Beta Cyclodextrin</i>
<i>CBC</i>	<i>Calvin Benson Cycle</i>
<i>CA</i>	<i>Carbonic anhydrase</i>
<i>CD</i>	<i>Circular dichroism</i>
<i>CLSM</i>	<i>Confocal Laser Scanning Microscopy</i>
<i>Crc</i>	<i>Curcumin</i>
<i>Cyt-C</i>	<i>Cytochrome C</i>
<i>DSF</i>	<i>Differential scanning fluorimetry</i>
<i>DMSO</i>	<i>Dimethyl sulphoxide</i>
<i>DDH</i>	<i>Diol dehydratase</i>
<i>Dox</i>	<i>Doxorubicin Hydrochloride</i>
<i>DLS</i>	<i>Dynamic Light scattering</i>
<i>Etu BMC</i>	<i>Ethanol Bacterial Microcompartment</i>
<i>Eut BMC</i>	<i>Ethanolamine Bacterial Microcompartment</i>
<i>FRET</i>	<i>Fluorescence resonance energy transfer</i>
<i>FS</i>	<i>Fluorescence spectroscopy</i>
<i>FTIR</i>	<i>Fourier Transform Infrared Resonance spectroscopy</i>
<i>Grp BMC</i>	<i>Glycyl radical-generating protein Bacterial Microcompartment</i>
<i>GRM2</i>	<i>Glycyl-radical enzyme-associated microcompartment</i>
<i>AuNP/AuNPs</i>	<i>Gold nanoparticles</i>
<i>IPTG</i>	<i>Isopropyl β-d-1-thiogalactopyranoside</i>
<i>ITC</i>	<i>Isothermal titration calorimetry</i>
<i>MCT</i>	<i>Micro Centrifuge Tubes</i>
<i>MGS</i>	<i>Microcompartment Genomic Signature</i>
<i>NHS</i>	<i>N-Hydroxy succinamide</i>
<i>NAD</i>	<i>Nicotinamide Adenine Dinucleotide</i>
<i>NR</i>	<i>Nile Red</i>
<i>PMSF</i>	<i>Phenylmethane sulfonyl fluoride</i>
<i>PBS</i>	<i>Phosphate Buffer Saline</i>

<i>PEG4000</i>	<i>Polyethylene glycol 4000</i>
<i>PAGE</i>	<i>Polyacrylamide Gel Electrophoresis</i>
<i>1,2-PD</i>	<i>Propane-1,2-diol</i>
<i>Pdu BMC</i>	<i>Propanediol bacterial microcompartment</i>
<i>PSs</i>	<i>Protein shells</i>
<i>R6G</i>	<i>Rhodamine 6G</i>
<i>RuBisCo</i>	<i>Ribulose-1,5-bisphosphate carboxylase/oxygenase</i>
<i>SEM</i>	<i>Scanning electron microscopy</i>
<i>SP/SPs</i>	<i>Shell protein/proteins</i>
<i>SDS</i>	<i>Sodium dodecyl sulphate</i>
<i>SO</i>	<i>Sypro orange</i>
<i>TSA</i>	<i>Thermal shift assay</i>
<i>TIRF-M</i>	<i>Total Internal Reflectance Fluorescence Microscopy</i>
<i>TEM</i>	<i>Transmission electron Microscopy</i>
<i>UV</i>	<i>Ultraviolet spectroscopy</i>
<i>VP</i>	<i>Vertex protein</i>
<i>Vit B₁₂</i>	<i>Vitamin B12 (Ado/Cyano cobalamin)</i>

ABSTRACT

Compartmentalization in the cellular organization is essential for the efficient working of cellular processes. It is a characteristic feature of eukaryotes but also observed in prokaryotes under specific metabolic conditions. In prokaryotes, they are involved in concentrating the substrate and enzymes locally, thus enhancing enzyme efficiency and turnover number, preventing cross-talk between spatially isolated processes and isolating the harmful intermediates. These prokaryotic organelles are referred to as bacterial microcompartments and are subcategorized as Carboxysomes and Metabolosomes. They are entirely protein bodies made by the assembly of 18000-20000 protein units of 10 to 20 different types. They have an enzymatic core with a signature enzyme wrapped within a peripheral shell protein boundary. These shell proteins are unique as they have evolved by horizontal gene transfer and comprises of bacterial microcompartment domain protein and bacterial microcompartment vertex protein. Mutational variations in the shell proteins followed by growth studies, along with their X-ray crystallization, have been performed for the better knowledge of these vast complex macromolecular assemblies. All these studies to date supported complexity because of shape complementarity and similar genetic origin. This makes it difficult to understand the functions *in vivo* for individual components. This thesis primarily concentrates on the understanding of the organizational assembly of one such MCP, i.e., 1,2-Propanediol bacterial microcompartment and also its components. Based on a simple spectroscopic method, the complexity, organizational assembly, and composition of Pdu BMC are dissected. Protein compartments are fabricated from these self-assembling shell proteins to understand the functional role of individual shell protein *in vitro*. These protein shells are investigated for their stability and their capability to transport substrates and co-factors across the conduit channels. The Pdu BMC is also explored as a novel substrate for the development of bio-nano hybrids where gold nanoparticles are fabricated in 3D on its scaffold with having inorganic catalysis, as well as the core enzyme, showed bio-organic catalysis.

SYNOPSIS

Living cells comprises of distinct sub-compartments to facilitate the regulation of various biological metabolic pathways. This phenomenon is known as compartmentalization and enhances the efficiency of the metabolic processes. The eukaryotic machinery preferentially depends on compartmentalization and has been well studied for its organization, structure, and function. Similar compartmentalization has been observed in prokaryotes, which do have similar functions like encompassing metabolic cycles and restricting their cross-talks but differ drastically in their composition and organization. These prokaryotic organelles because of the horizontal gene transfer have been observed in several bacterial species. Around 20 % of the sequenced bacterial genomes have the genes for the MCPs, suggesting the importance of compartmentalizing metabolic pathways in a cellular milieu as a competitive advantage towards growth and sustenance.

Bacterial microcompartments (MCPs), as these organelles are referred to as encloses within an all protein boundary a metabolic pathway for a specific carbon substrate with signature enzymes. These carbon substrates are found in nature, and their metabolism is essential for the natural cycling of matter and sustenance of bacteria. Their use provides an advantage to the metabolically capable organisms in a variety of unique environments. A recent literature search shows these polyhedral structures are found in 19 out of the 29 established bacterial phyla and are involved in the utilization of different carbon-containing compounds. These polyhedral structures are unique as they are made up of proteins only, and to date, no lipid components are reported. These compartments across different bacterial species are an assembly of 18000-20000 protein units of 10 to 20 different types. They carry out the metabolic reactions in few femtoliters and offer advantages such as concentrating the substrate and enzymes locally, thus enhancing enzyme efficiency and turnover number, preventing cross-talk between spatially isolated processes and isolating the harmful intermediates. To date, substantial work has been carried out to understand the genetic make of two main subcategories of MCPs, i.e., Carboxysomes and Metabolosomes. Mutational variations followed by growth studies, along with their X-ray crystallization, have been performed for the better knowledge of these large complex macromolecular structures. In the last half a decade, such compartments have received attention from bioengineering and biotechnological perspective and are being explored for various bio-nanotechnology applications.

This thesis primarily concentrates on the Understanding of the organizational assembly, Simplifying the complexity of such assembly for investigating the properties of its components and Exploring it's potential for being a novel substrate in the field of bio-nano hybrids. Thus this thesis 'USE' a BMC as its paradigm for achieving the goal. Using these types of organelles will have a significant contribution towards developing synthetic cellular systems and natural polymer-based biomaterials whose properties can be manipulated for distinct characteristics.

In *Chapter 1*, I started with the introduction on compartmentalization in eukaryotes and how this phenomenon has established its importance in prokaryotes also. A background sketch for the initial discovery and characterization of MCPs in bacteria along with a review on the various sub-types of these compartments and their functional diversity is done. The organizational pathway involved in the formation of these MCPs has also been highlighted. BMCs are all protein bodies and are made up of an outer protein coat with an enzymatic core. This outer protein coat is made up of specific Bacterial microcompartment domain proteins and bacterial microcompartment vertex proteins, which are called as shell proteins (SPs). A detailed inquiry on this unique category of domain proteins and their assembly as hexamer or trimer due to tandem repetition has also been included. How the assembly brings different features to these SPs such as concave and convex faces, a central pore, or other channels of conduits have also been discussed. A detailed sketch of 1,2-Propanediol microcompartment (Pdu BMC) has been made in the last part of the chapter. Composition of Pdu BMC in terms of shell proteins, the major enzymes bringing the catabolism of 1,2-propanediol (1,2 PD), are highlighted. The motivation for the thesis is also included where I emphasized how the structure and organization of Pdu BMC have only been studied based on genetic manipulation supported mainly by X-ray crystallography. The Pdu BMC have genetic makeup similar to other reported MCPs but vary in encapsulated metabolic pathways and thus must be different in their assembly and organization. Fast spectroscopic tools for characterizing the complex assembly of MCP and relatively flat SPs based on morphology were missing in the literature. Thus, I tried to dissect the complexity, organizational assembly, and composition of Pdu BMC in the solution phase based on spectroscopic observations. Along with MCP, the individual components, i.e., SPs and enzymes, are also characterized by the newly adopted tool, referred to as Differential scanning fluorimetry. To date, this technique has been used to understand the thermal stability of globular proteins only. Herein I report for using this method for the first time to

understand the complex multimeric protein assembly. To reduce the complexity and to understand the properties of the individual components, mainly SPs, I fabricated protein compartments similar in morphology to that of MCPs and have called them protein shells (PSs). At-last I also scrutinized the potential role of the Pdu BMC or its components, especially SPs, as a new platform for developing bio-hybrid systems.

The thesis involves various methods and different tools and techniques. **Chapter 2** summarizes all the methodologies used in the thesis with adequate details of all the instruments and techniques. All the new protocols developed for the thesis are detailed in this Chapter.

Chapter 3 provides insights into the morphological makeup of the Pdu BMC solution structure. It is for the first time where the structure of the intact MCP has been sketched based on the spectroscopic dissection, and to our satisfaction matches the predicted model. In MCPs, a biochemical pathway with all the enzyme machinery is encapsulated within an all protein coat. The SPs and the enzymes have distinct structural features. It is hypothesized that flat SPs align sideways to form extended sheets, and the globular enzymes fill up the central core of the organelle. Based on a high throughput technique, i.e., differential scanning fluorimetry, the organizational assembly along with structure-function correlation of the Pdu BMC are established. Our findings exhibit that these intact MCPs as a whole behave similarly to a globular protein with a rich hydrophobic core, which gets exposed upon thermal insult. The encapsulated enzymes, in line with the hydrophobic-collapse model of protein folding, have a strong hydrophobic core. The SPs, on the other hand, do not have a strong hydrophobic core rather a have significant exposed hydrophobic patches. This unique exposure of hydrophobic patches might be required for anchoring the enzymes leading to better packaging and stabilization of the micro-compartments. These observations indicate that the hydrophobic interactions between the shell and the enzymes are a critical factor in the genesis of these unique bacterial organelles and also provide insights for the development of novel encapsulated biomaterials.

Chapter 4 shows how mono-component shells can be developed *in vitro* from the components of the complex Pdu BMC. The complexity of Pdu BMC and the shape complementarity of SPs makes it challenging to study their properties *in vivo*. Thus, this study aims to understand the properties of the individual SPs *in vitro* away from the MCP setup. Protein compartments fabricated out of globular proteins that require additional

chemical crosslinking for stability are reported in the literature. Here I explore the fabrication of all-protein compartment using self-assembled SPs. These SPs have intrinsic interacting domains which are ionic, and spontaneously self-assemble into sheets when over-expressed. The formation of the protein shells (PSs) from the SPs are achieved without any external stimuli or crosslinker. The spontaneous self-assembly of the native protein sheets into PSs using the physical emulsification method helped to preserve the inherent functional properties of the protein. Assembly in PSs at the same time enhances their thermal stability compared to the free SPs. I further demonstrate that these compartments can encapsulate enzymes and, more interestingly, allow the free movement of small molecules through their intrinsic conduit channels. The porous nature of the shell housing active enzymes and allowing movement of substrate make them suitable as active bioreactors. Further, three different sheet proteins are used to fabricate the protein compartments, and properties such as stability, enzyme encapsulation, and permeability are compared to tender the tunability of the method, the SPs, and the PSs. Interestingly I find that all three protein shells show similar behavior concerning an encapsulated diol-dehydratase enzyme and Vit B12, which are native to the Pdu BMC system. Further, for the non-native enzyme CytC, small molecule R6G dye, doxorubicin, NR, and curcumin, they behave diversely. Insights from these observations will allow us to design and develop sheet protein-based synthetic active bioreactors requiring meticulous, compartmentalization for optimization of a specific process.

In **Chapter 5**, I present my investigation on exploring Pdu BMC as a platform for the development of a hybrid catalyst system. I expressed and purified the Pdu BMC from *Salmonella typhimurium* and fabricated an array of uniform-sized gold nanoparticles (AuNPs) (2.5 ± 0.5 nm) in 3D. The SP surface of the Pdu BMC provided an excellent scaffold for the fabrication, with the AuNPs spaced adjacently having an inter-particle distance of 5.75 ± 0.5 nm. The fabrication of AuNPs is assisted by the intrinsic nature of the amino acids to nucleate the precursor gold molecules, followed by their subsequent reduction. The fabrication is carried out in such a way that the macromolecular assembly of Pdu BMC is not disrupted. This fabrication resulted in the formation of AuNPs shell enclosing an active enzyme cluster. The catalytic role of AuNPs is demonstrated by the standard catalysis of p-nitrophenol to p-amino phenol on the AuNPs surface, whereas the enzyme core retained its diol-dehydratase activity. The spatial arrangement of AuNPs on the 3D scaffold resulted in plasmonic development, which helped in augmenting the

inorganic catalysis. At higher precursor concentration, pores involved in the conduit of substrates were blocked, and concentration-dependent reduction in the MCP enzymatic catalysis is compromised, whereas enhanced inorganic catalysis is observed. This report is perhaps the first of its kind, which directly demonstrates that ectopic blocking of the pore may lead to impaired microcompartment function with an active enzyme cluster inside. Previously, genetic engineering studies have shown that specific blocking of the PduA pore results in the compromised 1,2-PD uptake. The Pdu BMC-AuNPs hybrid catalysts inspired a new class of resources that can be used in a chemical reaction condition without perturbing the core biological (physiological) environment for enzymatic activity. This system provides a clue for fabricating uniformly ordered nanoparticles in 3D and the development of a new class of orthogonal hybrid catalytic material.

Chapter 6 summarizes the findings obtained by using Pdu BMC. I am successful in exploring the solution-phase structure of Pdu BMC using a spectroscopic probe. The fluorescent probe assay may be investigated for having a structure-function correlation of native complex macromolecular structure or even for protein conjugated macromolecular assemblies. I also showed for the first time the thermal unfolding profile of the Pdu BMC and BMC domain proteins, associating to its tertiary and quaternary structure. This understanding of the organizational assembly of Pdu BMC and its components will aid in developing quality control measures for the industrial application of this genre of proteins. This is the first time where the SPs of any MCP is used for fabricating protein compartments *in vitro*. The intrinsic self-assembly and substrate channeling features of the SPs helped in fabricating functional protein compartments. These PSs showing similar behavior towards channeling of the native components and different towards non-native extends a physiological relevance as it suggests the survival of *Salmonella* under stringent condition. Though still, this part needs rigorous *in vivo* genetic engineering studies to ensure whether similar behavior will be retained in the BMC or not. However, for the first time, our study shows that the three major Pdu SPs are not only structurally similar but also functionally concerning Pdu BMC native molecules *in vitro*.

At last, I have successfully fabricated a well-arrayed distribution of AuNPs on the Pdu BMC scaffold. The controlled fabrication of nanoparticles in 3D is capable of inorganic catalysis without disturbing the enzymatic core. The wrapping of AuNPs on the MCP surface blocks the conduits of substrate and cofactors, thus compromising the enzymatic catalysis. This is the first time where Pdu BMC has been used as a scaffold for

the generation of hybrid inorganic–organic system and thus initiated its use as a suitable biomaterial.

Appendix

The appendix of this thesis deals with another natural polymer expressed in bacteria: bacterial cellulose. Cellulose is one of the most abundant, inexpensive, and readily available carbohydrates. Globally plants are the significant contributors of cellulose, but keeping in view, the concern for global warming along with the purity of plant cellulose motivated us to look for an alternative sustainable source for cellulose. An alternative source is the bacteria, which also produces cellulose and is referred to as Bacterial Cellulose (BC). They are chemically equivalent to plant cellulose in terms of structure but are not contaminated with hemicellulose and lignin. BC has emerged as an essential industrial biomaterial in recent times, due to its purity and properties such as high porosity, water retention, and water absorption capacity, biocompatibility, biodegradability, and high surface area.

Appendix A;

In the first part of the Appendix, I have mainly worked to optimize BC yield in the Super Optimal Broth with catabolite repression (SOC) medium by using the strain *Gluconobacter xylinus*. Catabolite repression is a phenomenon where “Catabolism exceeds Anabolism” and involves inhibition of transcription factors responsible for enzymes that are involved in the quest of food. The limited yield in the conventional Hestrin Schramm (HS) media required other holistic media, and so we resorted to SOC media. This medium is used to revive *E. coli* cells after electroporation or chemoporation. Within 5 days of incubation in SOC medium, cellulose pellicles were observed as compared to HS media, where thin films can be seen (static culture). This is because of enhanced conversion of the carbon source to cellulose as SOC medium helped to maintain the pH close to 7.0 in static cultures, unlike in HS medium where the pH is acidic. The produced BC is characterized by X-ray Diffraction (XRD), Thermo Gravimetric Analysis (TGA), Brunauer-Emmett-Teller (BET) and Barrett-Joyner-Halenda (BJH), and Scanning Electron Microscopy (SEM) analyses. In SOC media, 50% of the carbon source gets converted to BC as compared to only 7% conversion in the case of traditional HS medium after 7 days of interaction. An increase in the hydration capacity of BC produced using SOC as compared to HS media is also observed.

Appendix B;

In the second part of the appendix, the BC produced in the lab is used to develop a metal-binding matrix. This metal-binding conjugate has been achieved by covalently linking physiological metal chelators known as metallothioneins (MT) to the chemically modified BC. This involves a two-step procedure, in the first step epoxy ring is introduced using the epoxy-amine chemistry followed by covalent conjugation with the amine groups of the proteins. 50% mass by mass of the metallothionein could be attached to bacterial cellulose. The altered morphology observed in SEM and high thermal stability for the conjugate as compared to pristine BC suggested binding of the MT to the epoxidized BC. A five-fold enhancement in the metal binding capacity of the matrix is also achieved as compared to native BC. No significant toxicity of the conjugate material is observed. This bacterial cellulose-metallothionein conjugate can be explored for health care applications where the management of metal toxicity is crucial. The epoxy-amine chemistry for covalent conjugation of protein can be applied for several other types of proteins to develop specific functional biocompatible and biodegradable cellulose matrices.

Table of Content

<i>Declaration</i>	<i>i</i>
<i>Acknowledgments</i>	<i>iii</i>
<i>Abbreviations</i>	<i>vii</i>
<i>Abstract</i>	<i>ix</i>
<i>Synopsis</i>	<i>xi</i>
<i>Table of Content</i>	<i>xix</i>
<i>List of Figures</i>	<i>xxiii</i>
<i>List of Tables</i>	<i>xxv</i>
1 Introduction	1
1.1 Compartmentalization: Isolation of relevant bioprocesses	1
1.1.1 Discovery and diversity of MCPs	1
1.1.2 Essential Features of the MCPs	4
1.1.3 Functional diversity of MCPs	4
1.1.3.1 Carboxysomes	6
1.1.3.2 Metabolosomes	7
1.1.3.2.1 Propanediol Bacterial Microcompartment (Pdu BMC).....	9
1.1.3.2.2 Ethanolamine Bacterial Microcompartment (Eut BMC).....	10
1.1.4 Assembly of MCP.....	11
1.1.4.1 Core First assembly Pathway	11
1.1.4.2 Concomitant Assembly Pathway	13
1.1.5 Structure of Bacterial Microcompartments.....	13
1.1.5.1 Bacterial microcompartment domain protein.....	14
1.1.5.2 Bacterial microcompartment vertex protein.....	16
1.2 Thesis motivation and perspective	18
2 Materials and Methods	21
2.1 Materials	21
2.2 Methods	25
2.2.1 Experimental study	25
2.2.1.1 Expression and Purification	25
2.2.1.1.1 Propanediol Bacterial Microcompartment.....	25
2.2.1.1.2 PduCDE and Pdu shell proteins (PduA/B/B'/N)	25
2.2.1.2 Fabricating protein shells (PSs)	26
2.2.1.2.1 Hollow PSs	26
2.2.1.2.2 Cargo loaded PSs.....	27
2.2.1.3 Enzyme assay	28

2.2.1.3.1	3-methyl-2-benzothiazoline hydrazine assay for Aldehyde.....	28
	detection: Diol-dehydratase activity assay	28
2.2.1.3.2	Pyrogallol oxidation assay.....	29
2.2.1.4	Dye labeling of shell and the enzyme proteins.....	29
2.2.1.5	Thermal Scanning Fluorimetry for the Pdu BMC, PduCDE, and SPs	29
2.2.1.6	Permeability study of small molecules in PSs.....	30
2.2.1.6.1	Rhodamine 6G.....	30
2.2.1.6.2	Vitamin B12	31
2.2.1.7	Encapsulation and release of small molecules from PSs.....	31
2.2.1.7.1	Doxorubicin (Dox)	31
2.2.1.7.2	Nile red.....	31
2.2.1.7.3	Curcumin.....	32
2.2.1.7.4	Gold nanoparticles.....	32
2.2.1.8	Studying the interaction of auric chloride with Pdu BMC	33
2.2.1.8.1	Biolayer interferometry	33
2.2.1.8.2	Isothermal titration calorimetry.....	34
2.2.1.9	Fabrication of Gold nanoparticles on Pdu BMC	34
2.2.1.10	Characterization techniques.....	35
2.2.1.10.1	Size distribution by Dynamic Light Scattering	35
2.2.1.10.2	Circular Dichroism	35
2.2.1.10.3	Fourier Transform Infrared spectroscopy.....	35
2.2.1.10.4	Atomic Force microscopy.....	36
2.2.1.10.5	Scanning Electron microscope	36
2.2.1.10.6	X-ray diffraction studies	36
2.2.1.10.7	Transmission electron microscopy	36
2.2.1.10.8	UV-visible spectroscopy.....	37
2.2.1.10.9	Steady-state fluorescence.....	37
2.2.1.10.10	Total Internal Reflection Fluorescence Microscopy.....	38
2.2.1.11	The catalytic activity of BMC-AuNP hybrid.....	39
2.2.2	Theoretical study	39
2.2.2.1	Docking studies of Sypro orange with proteins.....	39
3	<i>Understanding the assembly of Pdu BMC.....</i>	41
3.1	Introduction.....	41
3.2	Results and discussion	43
3.2.1	Thermal unfolding of Pdu BMC	43
3.2.2	Thermal unfolding of PduCDE	46

3.2.3	Unfolding signature of Pdu SPs.....	48
3.2.3.1	PduA and PduB: BMC domain protein.....	48
3.2.3.2	PduN: BMC vertex protein	51
3.2.4	SPs differ from globular protein in morphology.....	53
3.2.5	SPs provide thermal stability to encapsulated enzyme	55
3.2.6	Fate and structural stability of SPs in intact Pdu BMCs.....	55
3.3	Conclusions	58
4	<i>Simplifying Pdu BMC as protein shells</i>	61
4.1	Introduction	61
4.2	Results and discussion.....	64
4.2.1	Fabrication and characterization of <i>in vitro</i> protein compartments.....	64
4.2.2	Stability studies of the PSs.....	66
4.2.3	PSs behave as an active bioreactor	69
4.2.3.1	Encapsulation of the enzyme cargo.....	69
4.2.3.2	The activity of the enzyme cargo	71
4.2.4	Permeability of the PSs.....	73
4.2.5	PSs as broad range functional structures and as a cargo carrier	76
4.3	Conclusions	78
5	<i>Pdu BMC as template for bio-inorganic hybrid development.....</i>	81
5.1	Introduction	81
5.2	Results and discussion.....	82
5.2.1	Interaction of Au on the BMC surface and its templating	82
5.2.2	Characterizing the fabricated AuNPs.....	84
5.2.3	Stability of Hybrid catalyst	87
5.2.4	Characterizing the hybrid catalysis.....	88
5.2.5	Understanding the mechanism of AuNPs fabrication.....	91
5.3	Conclusion.....	93
6	<i>Summary and Conclusion</i>	95
	<i>Bibliography.....</i>	99
	<i>Appendix.....</i>	115

List of Figures

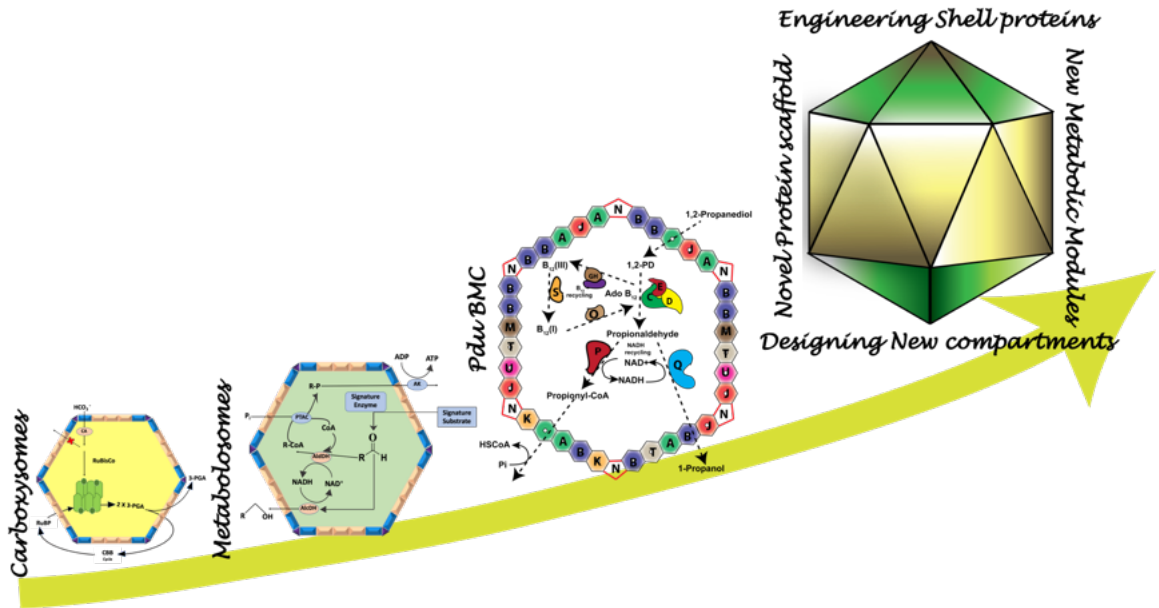
<i>Figure 1.1: Genomic signature of Bacterial Microcompartment.....</i>	<i>02</i>
<i>Figure 1.2: Essential features of Bacterial Microcompartment.....</i>	<i>03</i>
<i>Figure 1.3: Typical gene composition of Bacterial Microcompartment.....</i>	<i>06</i>
<i>Figure 1.4: A model for carboxysome.....</i>	<i>07</i>
<i>Figure 1.5: A model for metabolosomes.....</i>	<i>08</i>
<i>Figure 1.6: Gene composition of pdu gene locus encoding Pdu BMC.....</i>	<i>09</i>
<i>Figure 1.7: Gene composition of eut gene locus encoding Pdu BMC.....</i>	<i>10</i>
<i>Figure 1.8: Assembly mechanism in Bacterial Microcompartment.....</i>	<i>12</i>
<i>Figure 1.9: MCP domain Pfam00936 forming hexameric assembly.....</i>	<i>15</i>
<i>Figure 1.10: MCP domain Pfam00936 forming trimeric assembly.....</i>	<i>15</i>
<i>Figure 1.11: MCP domain Pfam03193 forming trimeric assembly.....</i>	<i>16</i>
<i>Figure 1.12: Assembly of a bacterial microcompartment.....</i>	<i>17</i>
<i>Figure 2.1: Scheme for protein shell fabrication.....</i>	<i>27</i>
<i>Figure 2.2: Scheme for fabricating cargo loaded protein shells.....</i>	<i>28</i>
<i>Figure 2.3: Scheme for carrying interaction study by bilayer interferometry.....</i>	<i>33</i>
<i>Figure 2.4: Scheme for fabricating gold nanoparticles on pdu BMC scaffold.....</i>	<i>34</i>
<i>Figure 2.5: Scheme to understand the mechanism of AuNPs templating.....</i>	<i>38</i>
<i>Figure 3.1: Scheme for Differential scanning fluorimetry study.....</i>	<i>42</i>
<i>Figure 3.2: Characterizing the Pdu BMC.....</i>	<i>44</i>
<i>Figure 3.3: Characterizing the enzyme PduCDE.....</i>	<i>47</i>
<i>Figure 3.4: Characterizing the shell proteins.....</i>	<i>50</i>
<i>Figure 3.5: Comparing the morphology and stability of Pdu BMC and PduCDE.....</i>	<i>54</i>
<i>Figure 3.6: Understanding the assembly of Pdu BMC</i>	<i>57</i>
<i>Figure 4.1: Self-assembling nature of the shell proteins (PduA/PduB/PduB').....</i>	<i>63</i>
<i>Figure 4.2: Characterizing protein shells.....</i>	<i>65</i>
<i>Figure 4.3: Assessing the stability of Shell proteins and protein shells.....</i>	<i>67</i>
<i>Figure 4.4: Encapsulating PduCDE inside the protein shells.....</i>	<i>70</i>
<i>Figure 4.5: Enzyme loaded protein shells as active bio-reactor.....</i>	<i>72</i>
<i>Figure 4.6: Permeability studies of the protein shells.....</i>	<i>75</i>
<i>Figure 4.7: Protein shells behave as a wide range of cargo carrier.....</i>	<i>77</i>
<i>Figure 5.1: Interaction of Au precursor to the Pdu BMC and formation of AuNPs....</i>	<i>83</i>
<i>Figure 5.2: Arrayed templating of AuNPs on the Pdu BMC scaffold.....</i>	<i>86</i>
<i>Figure 5.3: Stability of the Pdu BMC:AuNPs hybrid.....</i>	<i>88</i>
<i>Figure 5.4: Inorganic and bio-organic catalysis of the hybrid.....</i>	<i>89</i>
<i>Figure 5.5: Mechanism involved in templating of AuNPs on Pdu BMC scaffold.....</i>	<i>92</i>

List of Tables

<i>Table 1.1: Different types of MCPs and their functional role</i>	5
<i>Table 1.2: Different domain of proteins involved in the formation of MCP</i>	14
<i>Table 3.1: Temperature for initiation of unfolding, unfolding temperature, and aggregation temperature in Pdu BMC and PduCDE</i>	45
<i>Table 3.2: Diol-dehydratase activity for the Pdu BMC and PduCDE carried out by MBTH assay</i>	46
<i>Table 3.3: Solvent accessible surface area (SASA) for the Pdu BMC domain protein (PduA and PduB), vertex protein (PduN), and Pdu BMC signature enzyme. Diol dehydratase (PduCDE)</i> 52	
<i>Table 3.4: Transition temperature for various SPs as determined by Boltzmann Fit. Various peak positions corresponding to various transitions in broad DSF curve are determined by multiple peak fit in origin 8.6</i>	52
<i>Table 4.1: SPs of Pdu BMC and their percentage distribution</i>	62
<i>Table 4.2: The average size distribution of the PSs fabricated from three different SPs as observed by SEM</i>	66
<i>Table 4.3: % Distribution for the secondary structure component (α-helix and β-sheet) of major SPs of Pdu BMC and their derived PSs as determined by K2D3</i>	68
<i>Table 4.4: % Distribution for the secondary structure component (α-helix and β-sheet) of pre-melt PSs and post melt PSs determined by K2D3</i>	68
<i>Table 4.5: The thermal stability of PSs is higher as compared to individual SPs</i>	68
<i>Table 5.1: Dissociation constant(K_d) for the protein:$AuCl_3$ interactions determined by BLI (global fit)</i>	84
<i>Table 5.2: Zeta potential for the Pdu BMC and its shell proteins</i>	84
<i>Table 5.3: Specific enzyme activity for the diol dehydratase enzyme</i>	90

Chapter 1

Introduction



1 Introduction

1.1 Compartmentalization: Isolation of relevant bioprocesses

A cell is referred to as the fundamental unit of life and is packed with all the required components for effective orchestration of essential energy processes. It becomes vital for the cell to carry metabolic processes in confined spaces for better control, optimization and regulation. This creates the need for a subcellular organization, which in general, is referred to as compartmentalization(1–4). From a broader perspective, the cellular compartments facilitate the passage of substrate, bring localization of interconnected metabolic pathways, and also help in the integrative regulation of various cellular processes (5). It involves physical isolation and insulation of heterologous components involved in biological reactions from the cellular milieu, thereby controlling their spatial-temporal interactions (6). All these factors have a cumulative effect on the energy homeostasis of the cell (5). The phenomenon of compartmentalization is well established in eukaryotes, whereas prokaryotes are primarily represented as unstructured sacks of cytoplasm(7,8). Lately, in prokaryotes, compartment like structures have been identified and are referred to as Bacterial Microcompartments (MCPs/BMCs; For abbreviating microcompartment in general MCPs is used whereas for specific microcompartment BMC is used, For e.g. Pdu BMC, Eut BMC etc) (9–15). MCPs represent a bio-catalytic core within a semipermeable protein coat and are involved in a specific metabolic pathway in bacteria (14–17).

1.1.1 Discovery and diversity of MCPs

The first of the MCPs were detected more than seven decades ago in 1950 by transmission electron microscopy (TEM) in the cytoplasm of cyanobacteria *Phormidium uncinatum* (18,19). Initially they were considered to be inclusion bodies and also mistaken as viruses because of polyhedral appearance and their morphological resemblance to phage particles. Subsequent studies in *Thiobacillus* showed that these structures play an important role in CO₂ fixation by the Calvin cycle. For the first time in 1973, these polyhedral bodies were isolated and purified from the chemoautotrophic bacterium *Halothiobacillus neapolitanus*, by differential and sucrose step-gradient centrifugation (20,21). These all protein polyhedral bodies, aided carbon fixation by encapsulating the ribulose-1,5-bisphosphate

Introduction

carboxylase/oxygenase (RuBisCo) and carbonic anhydrase (CA) enzymes(20). Due to their involvement in CO₂ fixation, they were named carboxysomes. Subsequent studies of the carboxysomes and similar morphologies in bacteria, and their composition lead to the identification of nine such structures, which today are collectively known as MCPs. Interestingly in the present time, similar polyhedral structures are found in 19 out of the 29 established bacterial phyla (16) and are involved in the utilization of diverse carbon sources. These carbon compounds are present in nature in one form or other, and their metabolism is essential for the natural cycling of matter(14–16). Their use provides a growth advantage to the metabolically capable organisms in a variety of compromised environments.

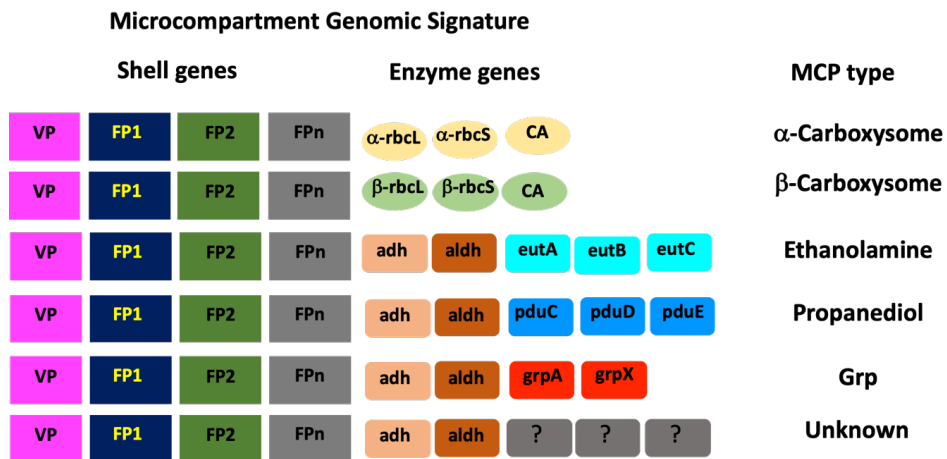


Figure 1.1: Microcompartment genomic signature showing a gene cluster where multiple shell genes are interspersed with structural genes encoding enzymes. All MCPs contain three or more shell face proteins (FP) and at least one copy of the vertex protein (VP). The presence of different signature enzymes functionally distinguishes these gene clusters as different types of MCPs. (Adopted from 10.4172/2329-9002.1000118)(22).

The isolation and purification of the polyhedral structures observed in carboxysome by density gradient ultracentrifugation showed that these structures are made up of entire protein and lack any lipid or genetic material unlike several other compartments observed in eukaryotes. Follow up studies have shown that these structures have an enzyme cluster inside a protein shell of 3 to 4 nm in thickness. The size of these compartments varies in the range of 100-150 nm. These prokaryotic MCPs differ from the mammalian organelles as they lack lipid membrane or genetic material. Although initially there were several propositions regarding the function of these structures (23), subsequent studies show that these are conditionally expressed

bio-reactors in bacteria for some specific functions. The GenBank (24) analysis of MCP gene clusters show that these shell gene homologs are present in 25 % of bacterial genomes suggesting their functional diversity(22).

A microcompartment genomic signature (MGS), represents a gene cluster where multiple shell genes are interspersed with structural genes encoding enzymes (*Figure 1.1*) (22,25). Presently this has become a nomenclature tool, because based on the type of the enzyme encoded within an MGS, MCPs are named accordingly.

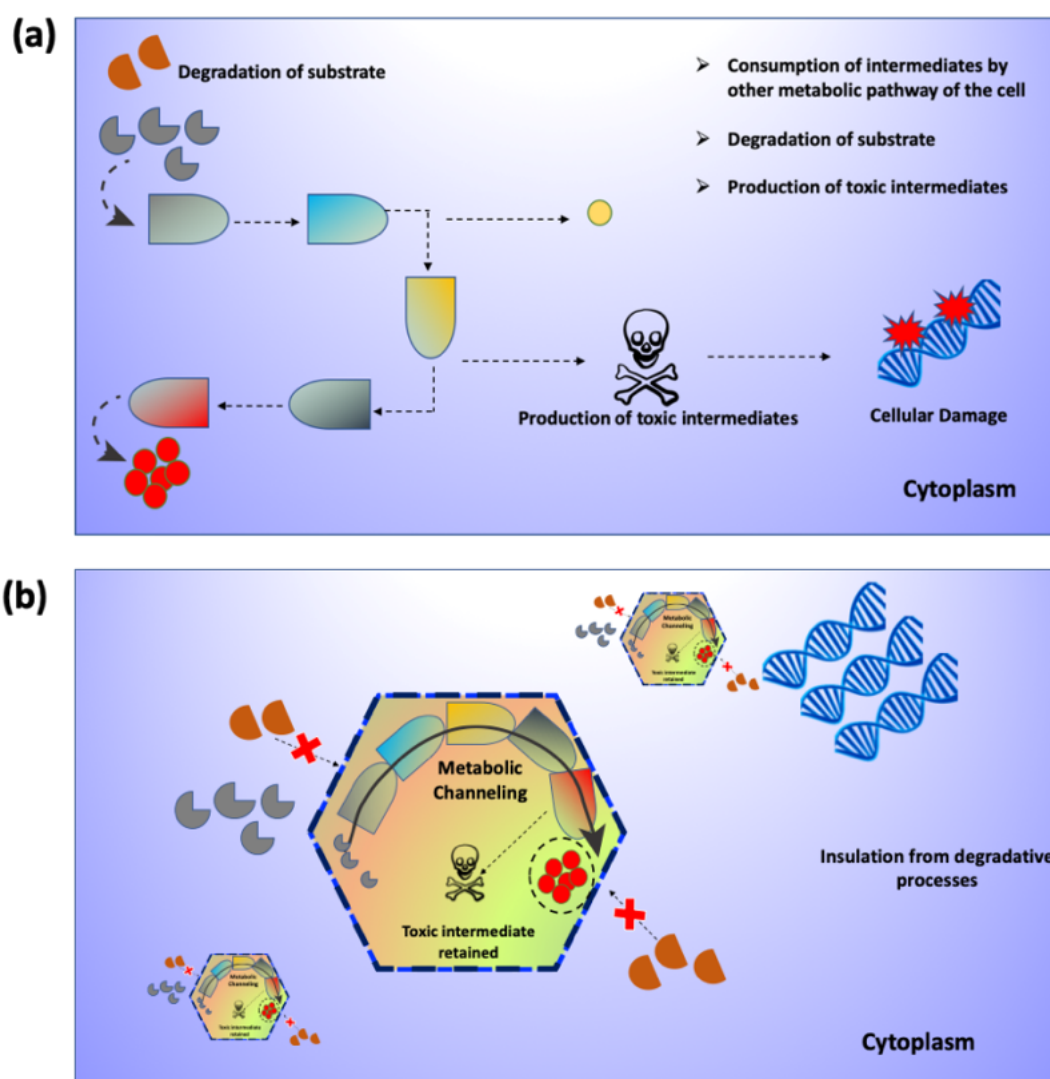


Figure 1.2: Metabolism of certain substrates generates volatile or toxic intermediates. In the absence of MCP, the volatile component escapes the cell bringing the loss of valuable carbon. On the other hand, toxic intermediates accumulate in the cytoplasm causing toxicity to the cell (a); When the metabolic cycle takes place in the MCP, the external shell of the MCP act as diffusion barrier and channel the volatile or toxic intermediate to the enzyme in the pathway thus preventing the carbon loss and also mitigating the toxicity (b). (Adopted from DOI: 10.1021/acsbio.5b00059(26))

1.1.2 Essential Features of the MCPs

MCPs offer the most unique mode of compartmentalization in the prokaryotes through conditional spatial organization of different metabolic processes (**Figure 1.2**). Till date, all the MCPs studied have similar polyhedral morphology in the size range of 100-150 nm, but differ in the metabolic machinery. In a typical MCP, there are close to 20,000 polypeptides of 10 to 20 different types (14,19,49,50, 51, 52). Interestingly, no lipid or genetic material have ever been found associated with MCPs (16,19,28,30,31).

Apart from the designated enzymatic reaction, the MCPs in general have some common function as listed below,

- **Concentration of metabolic machinery-** Compartmentalization increases the local concentration of the substrate to the enzymes in MCPs, thereby enhancing the turnover number. In fact due to the MCP genesis the essential components are concentrated in a few attoliters compared to the 10^{-15} L volume of a cell. This type of subcellular arrangement aids feeding and retention of optimized carbon source to the enzymes. Also in a multi-enzyme metabolic pathway, assembly of the related enzymes in a confined space leads to energy efficient substrate channelling.
- **Restricting the loss of volatile component-** MCP through their gated pores helps to minimize the diffusion of volatile intermediates. This prevents the loss of carbon source thereby maintaining the energy currency of the cell.
- **Mitigating the harmful effect of toxic intermediates-** Metabolic pathways generate toxic intermediates like aldehydes that restrict growth. MCPs either segregate themselves by preventing their escape or detoxify it by proper orchestration of the downstream metabolic pathways.
- **Minimizing competing reactions-** Compartmentalization within MCPs sequester enzymes and substrates so that they cannot engage in parallel or spurious reactions, thus enhancing enzyme activity and product yield.

1.1.3 Functional diversity of MCPs

Based on the variety of associated enzymes in the MGS, MCPs are involved in nine different metabolic processes. Broadly these MCPs are categorized into two subtypes, *carboxysomes* and *metabolosomes*. The carboxysomes, found mainly in

Table 1.1: Different types of MCPs and their functional role

S. No	Type of Micro-compartment	Species involved	Enzymes Present	Comments
1	Carboxysomes (16,20,21,32)	Cyanobacteria	Carbonic anhydrase; Rubisco	α -carboxysome β -carboxysome
2	Ethanolamine (Eut BMC) (16,33,34)	<i>Klebsiella</i> , <i>Mycobacterium</i> , <i>Pseudomonas</i> , <i>Achromobacter</i> , <i>Corynebacterium</i>	EutBC, EutD, EutE, EutG Catabolizes Ethanolamine as a sole source of carbon and nitrogen by a Vitamin B ₁₂ (Vit B ₁₂) dependent pathway	17 genes, 5 genes codes for SPs 12 genes code for enzymes
3	Ethanol (Etu BMC)(35,36)	<i>Clostridium kluyveri</i>	NAD-dependent ethanol dehydrogenase NAD(P)-dependent acetaldehyde dehydrogenase Involved in the fermentation of ethanol/acetate	Contain only two SPs
4	Propanediol (Pdu BMC) (14,15,37–44)	<i>Salmonella typhimurium</i>	PduCDE, PduGH, PduS, PduO, PduL, PduQ, PduP, PduW, Involved in Vit B ₁₂ dependent metabolism of 1,2-PD	Contain 8 SPs and 13 enzymes
5	Grp BMC (15,22,45,46)	<i>Desulfovibriosalexigenans</i> <i>Desulfovibriodesulfuricans</i>	Propanediol dehydratase, Propionaldehyde, Alcohol dehydrogenase, Phosphotransacylase Involved in Vitamin B ₁₂ in-dependent metabolism of 1,2-PD	Genes for hexameric/pseudo-hexameric BMC domain SPs and also a pentameric vertex protein (VP)
6	Amino alcohol (15,47,48)	<i>Mycobacterium smegmatis</i>	Class III aminotransferase Amino acid permease-associated protein aminoglycoside phosphotransferase	Involved in the metabolism of amino alcohols
7	Fuculose (49,50)	<i>Clostridium phytofermentans</i>	Involved in the metabolism of fucose and rhamnose	Genes for SPs are similar to that of 1,2 Pdu BMC
8	Choline (51–53)	<i>Proteobacteria</i> , <i>Firmicutes</i> , <i>Actinobacteria</i> , and <i>Fusobacteria</i>	Involved in choline degradation	Have 5 SP genes and enzymes for degradation of choline
9	GRM2 (54)	<i>Klebsiella pneumoniae</i>	CutC choline Lyase	

cyanobacteria and some chemoautotrophic bacteria. With low diversity, carboxysomes are the only MCPs that enclose an anabolic pathway and referred to as *anabolosomes*. MCPs that are involved in the metabolism of ethanol, fucose, rhamnose, amino alcohol, or other carbon substrates are referred to as *metabolosomes*. These metabolosomes are induced in the presence of the specific metabolite or substrate suggesting that these MCPs are under strict genetic control (37). **Figure 1.3** gives a schematic for a typical gene composition encoding a MCP. The gene composition shows the presence of a regulator gene apart from the envelope proteins and enzyme clusters (39,55). The different types of MCP based on the metabolic enzyme encoded within an MGS are listed in **Table 1.1**.

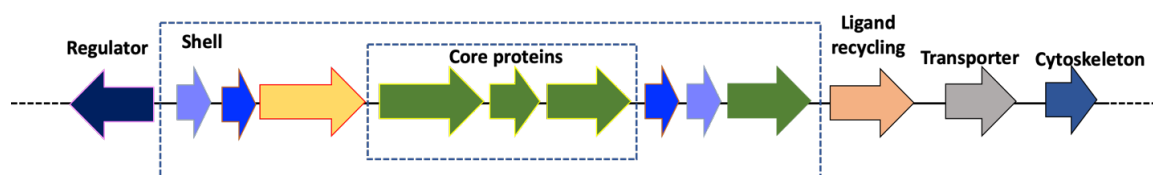


Figure 1.3: Schematic of a typical gene composition in a super locus encoding a BMC. In addition to genes encoding shell and core proteins, BMC super loci encode proteins for supporting and ancillary functions, such as transporters for the signature substrate.

1.1.3.1 Carboxysomes

The first microcompartments discovered in bacteria are the carboxysomes(20). These anabolic MCPs are involved in enhancing the autotrophic CO₂ fixation at low CO₂ levels by enhancing its local concentration(56–58). Low CO₂ concentrations, induce the formation of carboxysomes in cyanobacteria and chemoautotrophs and it is reported that mutant strains that cannot form fully functional carboxysomes needed a relatively higher CO₂ concentration for biogenesis (9,20,21). This underscores the importance of the carboxysomes in bacteria towards carbon concentration mechanism. RuBisCo is the central enzyme within the carboxysome boundary, which is involved in the fixation of atmospheric inorganic CO₂ through the Calvin Benson Cycle (CBC)(59). RuBisCo is a slow fixing enzyme as it fixes only 3 to 10 CO₂ molecule per second per molecule of the enzyme. It catalyses the carboxylation of Ribulose-1,5-biphosphate (RUBP) by facilitating the attack of CO₂ at the C2 carbon of RUBP and subsequent bond cleavage between C3 and C2 carbon, resulting in the formation of 2 molecules of glycerate-3-phosphate (enters into the Krebs Cycle). Being bifunctional in nature RuBisCo also

catalyses the fixation of O_2 . But carboxysomal shell differentially blocks oxygen from reaching the enzyme located inside thus enhancing its carboxylase activity (23,60,61). Another enzyme, CA, which has the role towards the conversion of the inorganic HCO_3^- to CO_2 is also associated with RuBisCo. Carboxysomes are of two types: α and β -carboxysomes. The α -carboxysomes (1A RuBisCo) are encoded by *cso* operon whereas β -carboxysomes (1B RuBisCo) by *ccm* operon. These two carboxysomes differ in the packing of the RuBisCo enzyme. In case of α -carboxysomes, interior appears to be less ordered or possesses one or more ordered layers bound to the inner surface of the shell whereas β -carboxysomes have significant internal structure with RuBisCo holoenzymes being scaffolded in three dimensions. Because of this packing differences, several lines of evidences indicate α -carboxysomes are more regular and smaller than the β -carboxysomes(19,61,62). The shape of carboxysomes, in general, is referred to as D6 polyhedra (23,63,64). Unlike viral capsids, the carboxysomes lack regular shape and icosahedral geometry. **Figure 1.4** shows a schematic of carboxysome composition and in the mechanism of their involvement in CO_2 fixation.

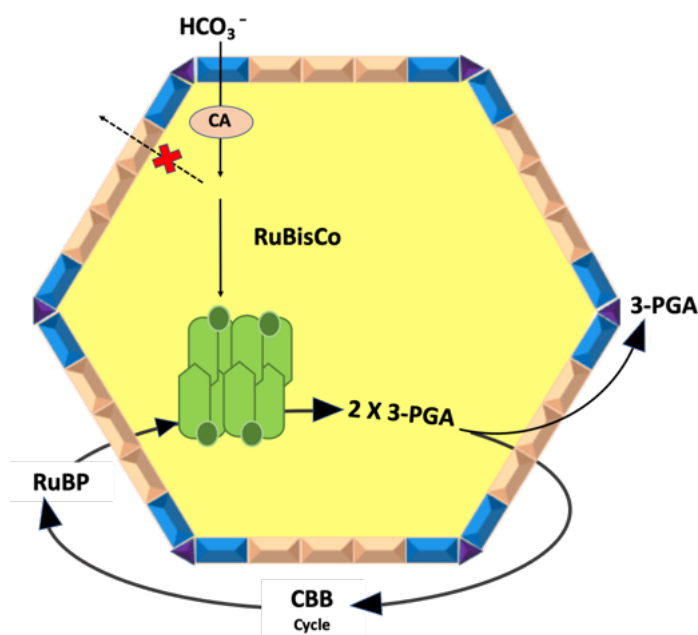


Figure 1.4: A carboxysome showing CA and RuBisCo encapsulated within a shell. CA is involved in the conversion of HCO_3^- to CO_2 , which is the substrate for RuBisCo. The shell protein inhibits the escape of CO_2 and thus increases its local concentration, and is fixed to useful carbon source by Calvin Benson Cycle.

1.1.3.2 Metabolosomes

Metabolosomes, are the MCPs involved in the metabolism of natural carbon sources like 1,2-PD, ethanolamine and ethanol etc. in bacteria. These carbon sources are

expected to be present in anaerobic environment as they are formed by the breakdown of common plant sugars such as rhamnose and fucose in anaerobic conditions. These sugars are present in plant cell walls, bacterial capsules, and the glycoconjugates of eukaryotic cells and so these metabolosomes are formed in microbes growing in these environment such as intestine or anaerobic soil conditions. Different substrates are involved with different metabolosomes that get metabolized by the encapsulated signature enzyme present in their catabolic pathway (**Figure 1.5**). What is common in all these metabolic pathways, is the presence of reactive and volatile aldehyde intermediate. Aldehydes are toxic to the cell and cause irreversible damage to the DNA. Certain aldehydes such as the acetaldehyde, an intermediate from Eut BMCs, are highly volatile and lipophilic. They tend to escape from the lipoidal cell membrane of bacteria resulting in carbon loss and damage to the cellular genetic material (26,28,65).

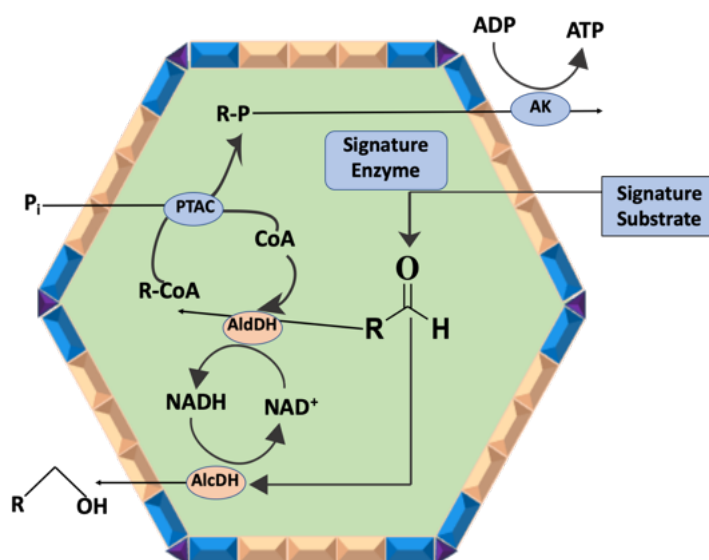


Figure 1.5: Metabolosomes share common biochemistry with the presence of a signature enzyme within the shell boundary with a diverse initial substrate. The metabolic pathway in the metabolosomes involves an aldehyde dehydrogenase (AldDH), an alcohol dehydrogenase (AlcDH), and a phosphotransacetylase (PTAC). The signature enzyme converts the substrate to the aldehyde, which is converted to the alcohol product by AlcDH. Separately AldDH uses CoA and NAD⁺ and gives R-CoA, which gets phosphorylated to R-P product. The phosphorylated product is dephosphorylated by AK to generate ATP. The shell prevents the escape of aldehyde, a toxic intermediate.

The shell of metabolosomes not only minimizes the diffusion of intermediates but also concentrates the substrate in the vicinity of the enzyme. A recent widely accepted theory related to metabolosomes is that their presence in certain class of pathogenic

bacteria under specific niche does provide a metabolic advantage to them (66). They have structure close to Johnson solid, as the polyhedral structure of metabolosomes is tiled by polygons of varying shape rather than one regular one. Presently two metabolosomes that are widely studied are the Pdu BMC and Eut BMC.

1.1.3.2.1 Propanediol Bacterial Microcompartment (Pdu BMC)

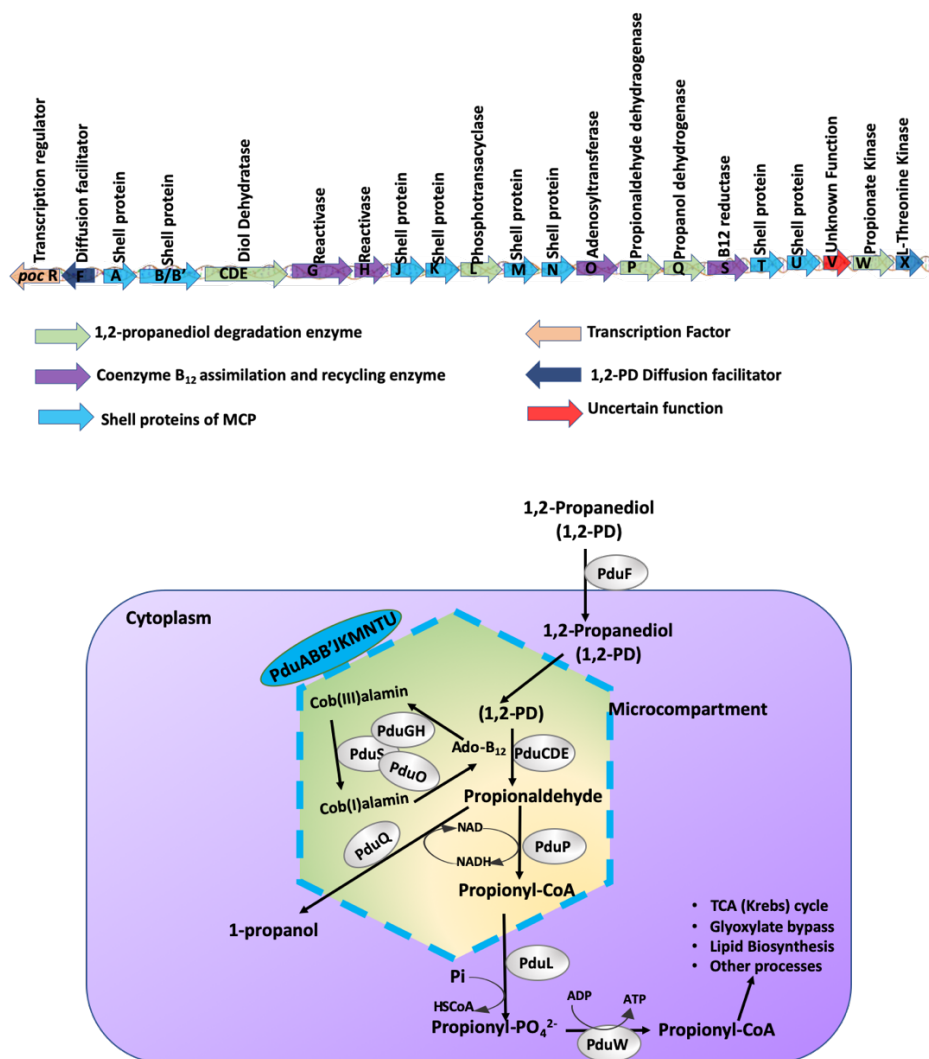


Figure 1.6: The *pdu* operon showing the genes encoding the regulator, shell proteins and enzymes. These genes are involved in propanediol degradation, including the one required for the formation of shell which encases the metabolic pathway.

For three decades, the only known MCP was the carboxysomes, involved in CO₂ fixation by enhancing the specificity and catalytic activity of RuBisCo enzyme. However, in 1994, Chen and co-workers carried out the genetic studies and sequence analysis of PduA protein in *pdu* operon (an operon involved in Vit B₁₂-dependent 1,2-PD degradation by *Salmonella*) through GenBank(24) and EMBL(67) database. They observed that this gene has 60 % sequence similarity to the proteins found in

photoautotrophic cyanobacteria (39). Subsequently, Bobik and Co-workers observed polyhedral structures similar to carboxysomes in *Salmonella* when grown only in the presence of 1,2-PD under aerobic or anaerobic conditions (42,44). These polyhedral bodies are involved in Vit B₁₂ dependent utilization of 1,2-PD (**Figure 1.6**). Analysis of the *pdu* gene cluster suggests frequent horizontal gene transfer of selected function and undergo operon reorganization (22,42). The gene cluster is found in many soil-dwelling and enteric bacteria and is highly conserved, (68–70). Recent studies also suggest that degradation of 1,2-PD plays a significant role in the enteric pathogenesis, and its restriction can be an essential drug target to overcome intestinal infection (71). A detailed discussion on Pdu BMC is provided in the latter part of this chapter.

1.1.3.2.2 Ethanolamine Bacterial Microcompartment (Eut BMC)

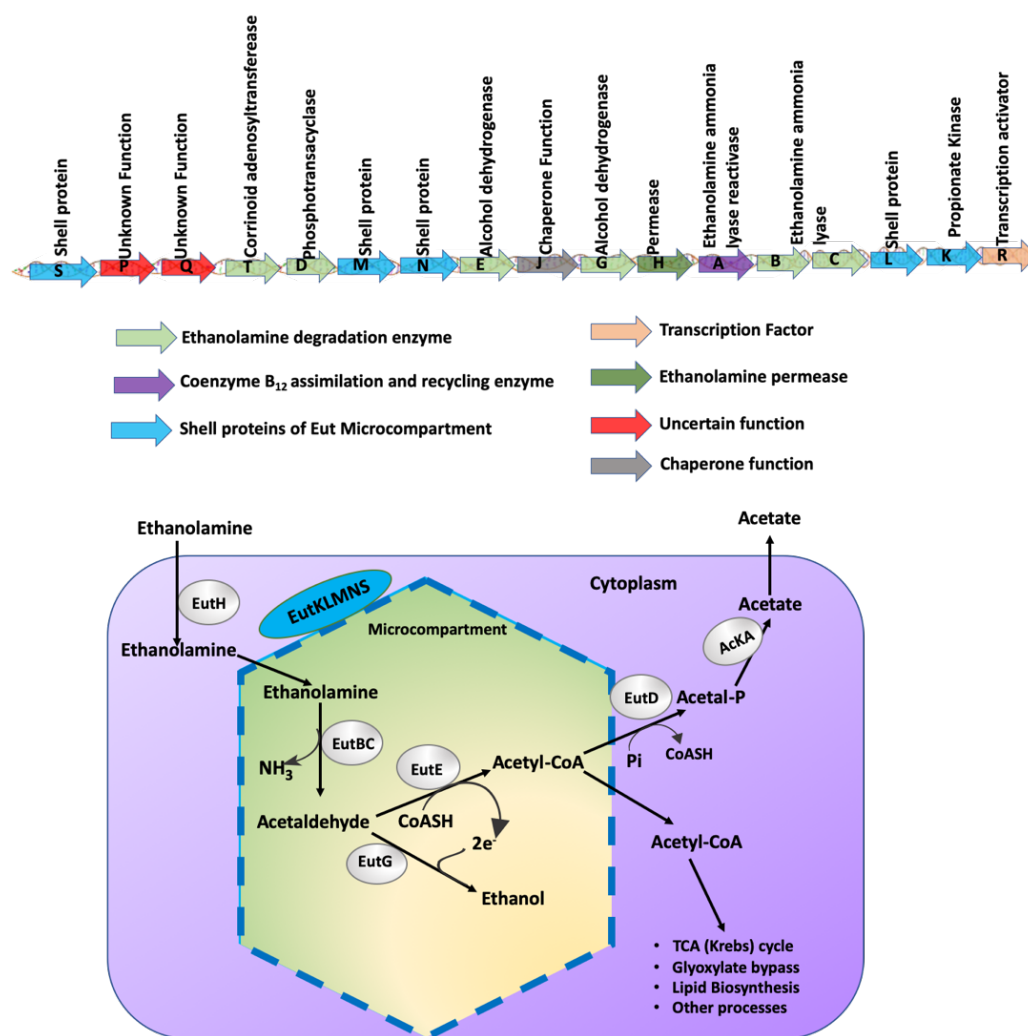


Figure 1.7: The *eut* operon having the genes cluster at a single locus. These genes are involved in ethanolamine degradation, including the one required for the formation of shell which encases the metabolic pathway.

Eut BMC is mainly found in enteric bacteria and involved in the metabolism of ethanolamine. Ethanol is a by-product of ethanolamine metabolism as shown in **Figure 1.7** and is mediated by a toxic intermediate i.e. acetaldehyde. The enzyme that brings this catalytic conversion is ethanolamine ammonia-lyase (EutBC) the signature enzyme of Eut BMC. Both the ethanolamine and 1,2-PD degradation occurs by a similar pathway (Figure 1.6 and 1.7) and the genes for Eut and 1,2-PD degradation are clustered together in *Salmonella* (72,73). Shively and co-workers showed that when *Salmonella* grows on ethanolamine, MCPs similar to those detected when grown in the presence 1,2-PD are observed (59). Eut BMC shell is composed of EutK, EutM, EutS, EutL, and EutN (27,72), and EutBC, EutE, EutG, and EutD make the core (28,72,74–77) (**Figure 1.7**). Studies have indicated that Eut BMC prevents the loss of volatile metabolite (acetaldehyde) through the cell membrane and, at the same time, protects the cell from the toxic effect of acetaldehyde. Some enterobacteria that cause food poisoning, including *Escherichia coli* and *Salmonella typhimurium*, uses this MCP for the degradation of ethanolamine and have the advantage to compete for the gut flora in survival thus increasing their virulence (34,71,78).

1.1.4 Assembly of MCP

The complexity, structural, and functional diversity of MCPs across carboxysomes and metabolosomes raises a general query. Do these architecturally similar but functionally distinct prokaryotic organelles assemble the same way? Though there are few studies which address the assembly of MCPs, two parallel theories have evolved. These theories have been primarily devised based on the study of carboxysomes assembly (38,61,79–82). The two theories are detailed below:

1.1.4.1 Core First assembly Pathway

Observed in β -carboxysomes, this pathway hypothesizes the initial assembly of the enzyme core followed by its encapsulation inside the shell. The encapsulation occurs with the aid of targeting peptides reported in several enzymes that interact with respective interacting peptides in the shell proteins. These interactions assist in the final outfitting of MCPs into the polyhedral geometry (**Figure 1.8-a**). Studies have shown that these targeting peptides remain in the N- or C-terminal of the protein and

Introduction

acquire a helical conformation upon interaction (79,83–86). This pathway studied in *Synechococcus* shows that initially, there is the formation of pro-carboxysome by the assembly of enzymes, RuBisCo and CA. This pro-carboxysome is then surrounded by a shell that pinches off excess cargo leading to the formation of matured carboxysome. The enzyme assembled core is active functionally and acts as the nucleus for the biogenesis of other similar structures (79,80).

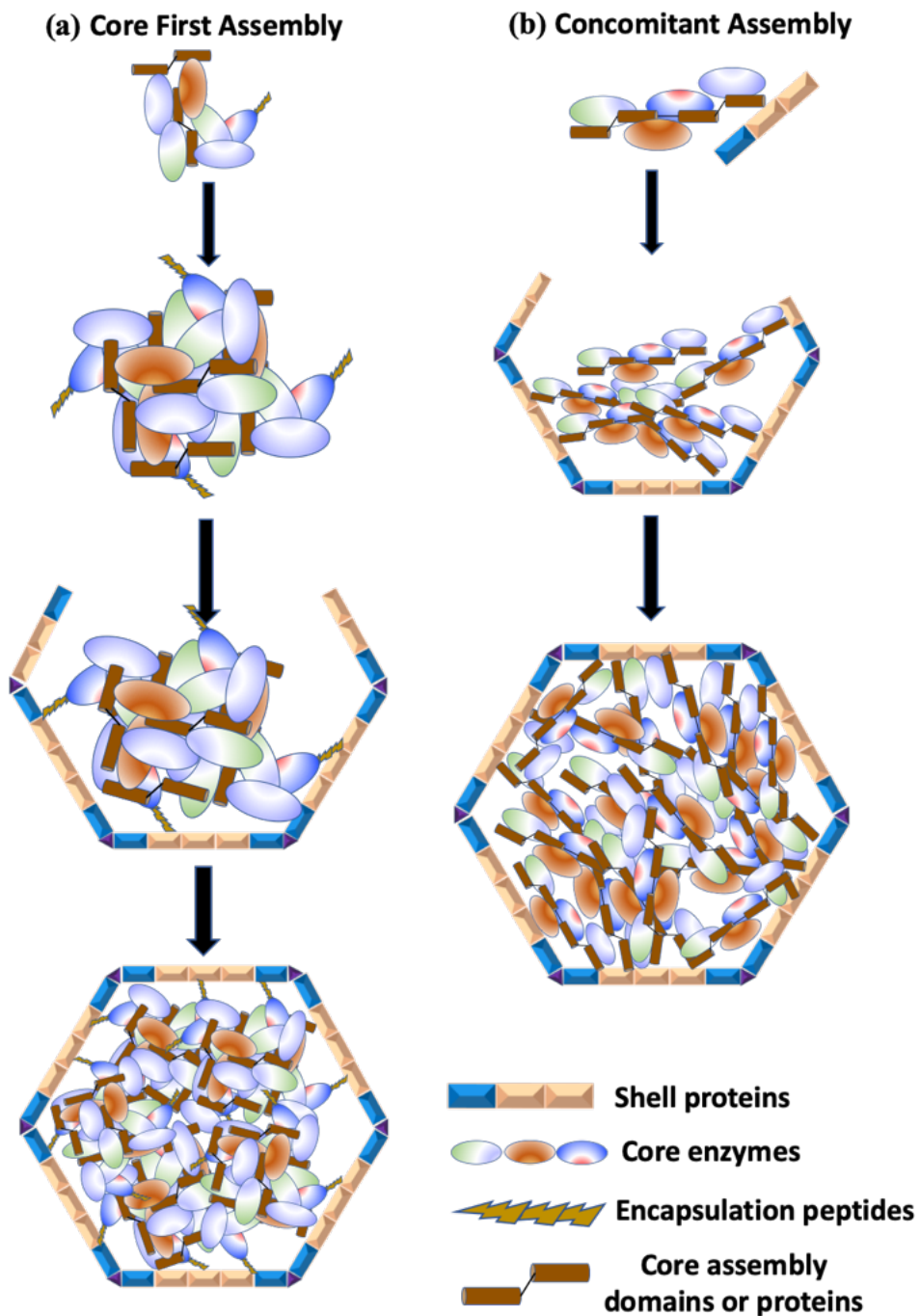


Figure 1.8: Assembly pathway in MCP mainly driven by two principles a) core first assembly b) concomitant assembly (Adopted from 10.1038/nrmicro.2018.10)(48)

1.1.4.2 Concomitant Assembly Pathway

In this pathway, the core and the enzyme co-assemble simultaneously leading to the formation of the polyhedral MCPs. This assembly pathway has been observed in α -carboxysomes of *Halothiobacillus*. In a series of experiments performed by cryo-electron tomography, the authors observe partially assembled shells attached to core proteins. These images suggest simultaneous assembly of shell and the enzyme. A schematic representation is shown in **Figure 1.8-b** (61).

Though the assembly of MCPs other than carboxysomes is not experimentally observed in other MCPs, but drawing a link between several lines of studies suggest the similarity between the metabolosomes and the β -carboxysomes. For example, in GRMs a subset of the enzymes contain domains with homology to their catalytically active encapsulated counterparts and is analogous to the small subunits like domain of the β -carboxysomes. Besides this, encapsulation peptides(83,86–88) are now an established feature of many different metabolosome enzymes such as CoA-dependent propionaldehyde dehydrogenase PduP(86) and the phosphotransacylase PduL(89) of the Pdu BMC and also in EutG and EutC in Eut BMC(90). All these findings bring homology between the metabolosomes and β -carboxysomes and so similarity in their assembly pathway. Even direct evidences such as presence of polar bodies containing enzymes are observed in the BMC-H protein deletion mutant of Pdu BMC. These polar bodies are probably pro-metabolosomes similar to pro-carboxysomes. It also suggests the basic principle of core first assembly pathway that aggregation of the core is not dependent on shell formation (38,44). A recent work by Lehmann et al., shows that a short N-terminal α -helix of the major SP PduB' is required for the BMC assembly as it is crucial for the interaction between core and shell (88).

1.1.5 Structure of Bacterial Microcompartments

The MCPs, as discussed, are made up of only proteins of more than 20000 units of 10 to 20 types in a typical example. MCP purification and their gene sequence analysis till date has revealed that the enzymatic and non-enzymatic component have equal contribution towards the total protein content (91). Over the years a growing body of literature suggest a similarity in the structure of the components of the outer

shell. Since 2005, when the first crystal structure of the carboxysome SP was solved, more than 40 SPs crystal structures are solved from both carboxysomes and

Table 1.2: Different domain of proteins involved in the formation of MCP

	BMC domain (Pfam00936)	BMV domain (Pfam03319)
Carboxysomes		
α-Carboxysomes	CsoS1A,B,C,D	CsoS4A,B
β-Carboxysomes	CcmK1,K2,K3,K4,O,P	CcmL
Propanediol	PduA,B,J,K,T,U	PduN
Ethanolamine	EutK,L,M,S	EutN
Ethanol	EtuA,B	CKL_0849

metabolosomes (92). Despite the phylogenetic distances found in the microorganism, the crystal structures of the SPs are highly conserved. These SPs belonged to either of the members of one of the two protein domains. These two domains are the BMC domain (Pfam Pf00936)(93), and the BMC vertex (BMV) domain (Pfam: Pf03319)(94). **Table 1.2** gives the list of various proteins belonging to either BMC domain or BMV domain.

1.1.5.1 Bacterial microcompartment domain protein

The BMC domain belongs to the conserved family of a small protein, typically 100 amino acids long. The domain is characterized by four β -strands, flanked by terminal α -helices (*Figure 1.9-a*). BMC domain associate in a six-fold rotational symmetry to form a cyclic flat hexamer (BMC-H) (*Figure 1.9-b*). These hexamers constitute the basic building blocks of the microcompartment envelope. The hexamers have a central pore which behaves as conduits for the substrates or the metabolites (*Figure 1.9-c*). The self-associated BMC domain giving rise to flat hexamer provides two faces to these shell proteins which differ in their amino acid distribution on the two surfaces and also in their shape and curvature. One of the faces has a bowl-like depression is referred to as concave, whereas the other face with a bulge is convex (*Figure 1.9-d*) (12,95). Although it is not clear as to which side (concave or convex) of the SPs faces the bacterial cytoplasm, a growing body of evidence suggest that the convex side is the one that faces the cytoplasm of the cell whereas the concave face is towards the lumen of the compartment. A single BMC

has more than one type of SPs, which differ in their sequence but not the general structure.

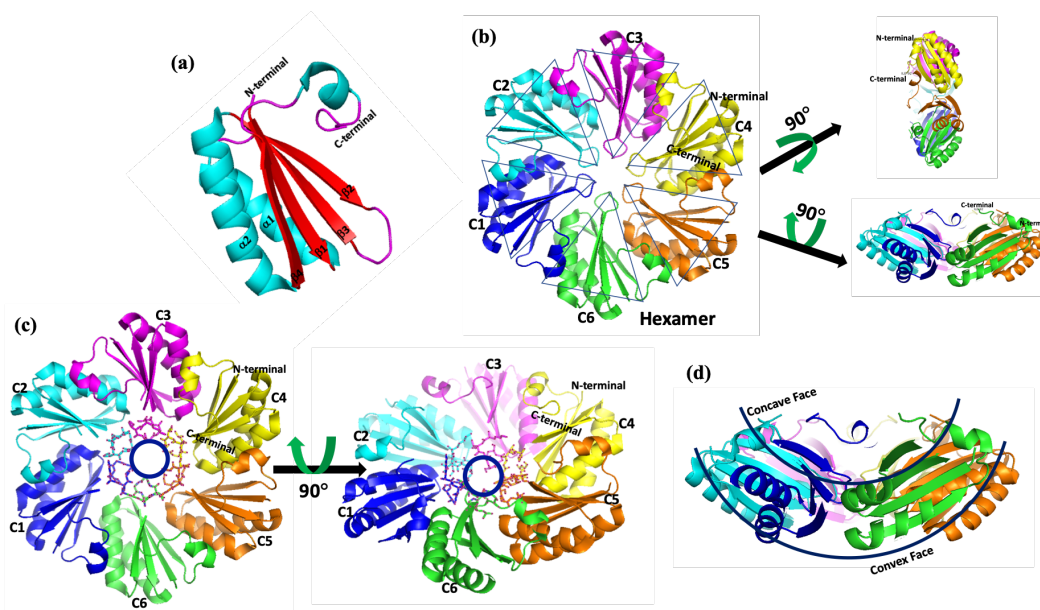


Figure 1.9: The BMC domain protein of family Pf00936 having four β -strands, flanked by α -helices (PDB-ID:3NGK) (a); six of the BMC domain arranges sidewise in a hexamer (BMC-H) as a disc with the N and C terminal lying on the same side (b); the hexamer at the six-fold axis of the symmetry has a pore which behaves as conduit and is highly selective for the substrates or the cofactors (c); the hexamer has a two-faced structure with one side having a bowl-like depression referred as concave face, and the other side is convex (d).

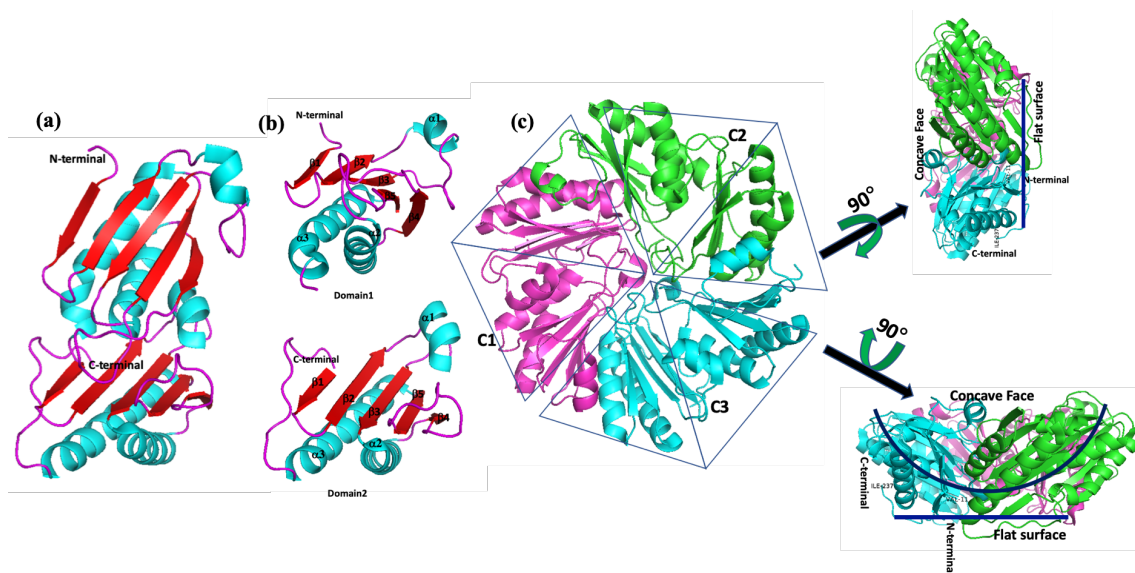


Figure 1.10: Tandem repeat of BMC domain of family Pfm00936 observed in SP of BMC have β -strands, flanked by α -helices on either side (PDB-ID:4FAY) (a and b); the BMC domain assembles as a trimer and referred to as BMC-T. They are relatively flat on the convex side with bowl-like depression on the concave side. The N terminal lies on the flat sides, whereas C-terminal lies at the edges (c).

Certain SPs have 2 BMC domain repeats. These tandem repeat of the BMC domain, referred to as BMC-T or pseudo-hexameric, form trimers (**Figure 1.10-a and b**). Due to the tandem repeat, they are identical in structure, and they also look like discs with hexagonal shape (**Figure 1.10-c**). These tandem repeats provide SPs with added flexibility by virtue of their additional loop regions. The central pores in these trimers also serve as conduits for transport. The crystal structure of EutB, EutL, and PduB are few examples of such trimers (33,35,40). Beside selective pore, these trimer units also have larger central pore (CcmP), thus allowing larger substrate across it (96). They also provide pore of a tendency to bind electron transporters, as observed in PduT (97). In BMC-T, a distinct crystal form has is reported, which suggests that MCP SPs, in particular, the trimer exist as protein bi-layer shell(98), or feeble chances of two-tier trimers, which is absent in hexameric assembly(99).

1.1.5.2 Bacterial microcompartment vertex protein

The BMC-H and BMC-T proteins can form extended 2D sheets. These sheets are closed into polyhedral structure by the pentameric BMV proteins (**Figure 1.11-a and b**) (94,100). The combination of hexamer and pentamer protein helps the BMC to attain a closed polyhedral structure as observed by the transmission electron microscope (TEM) imaging(37).

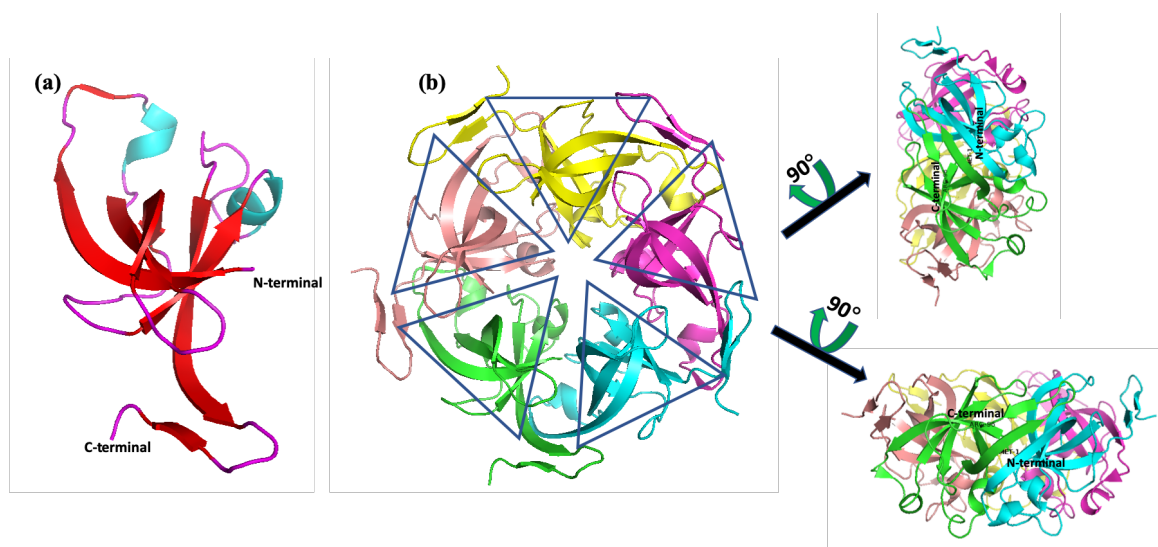


Figure 1,11: BMC vertex protein assembles as a pentamer and belongs to family Pfm03319 (PDB ID: 2QW7). Pentamer, too, has a relatively flat surface on the convex side, whereas the concave side in having depression with a pore for which the role is not known (a and b).

The polyhedral structure of BMC relies on BMC-H for the faces of the polyhedra while BMC-V for the vertices. The BMC-H and BMC-T further tessellate, forming mosaic sheets getting folded in a closed shell-like structure, and the vertices acquired by BMC-V protein (**Figure 1.12**) (101–103).

The variation in the assembly of BMC domain fold has resulted in the formation of more than 40 types of BMC SPs reported to date (48). The variation in the domain assembly also leads to different morphology observed in individually expressed protein. These SPs have different pore properties in terms of substrate conduits across them. Some of the pores also are reported to be redox centres indicating presence of electron transport reactions in these genre of organelles. These SPs also play a significant role in the encapsulation of enzyme cascade through encapsulating peptides. All these properties make the MCP and SPs a new system to understand and to explore for various applications, as discussed in this thesis.

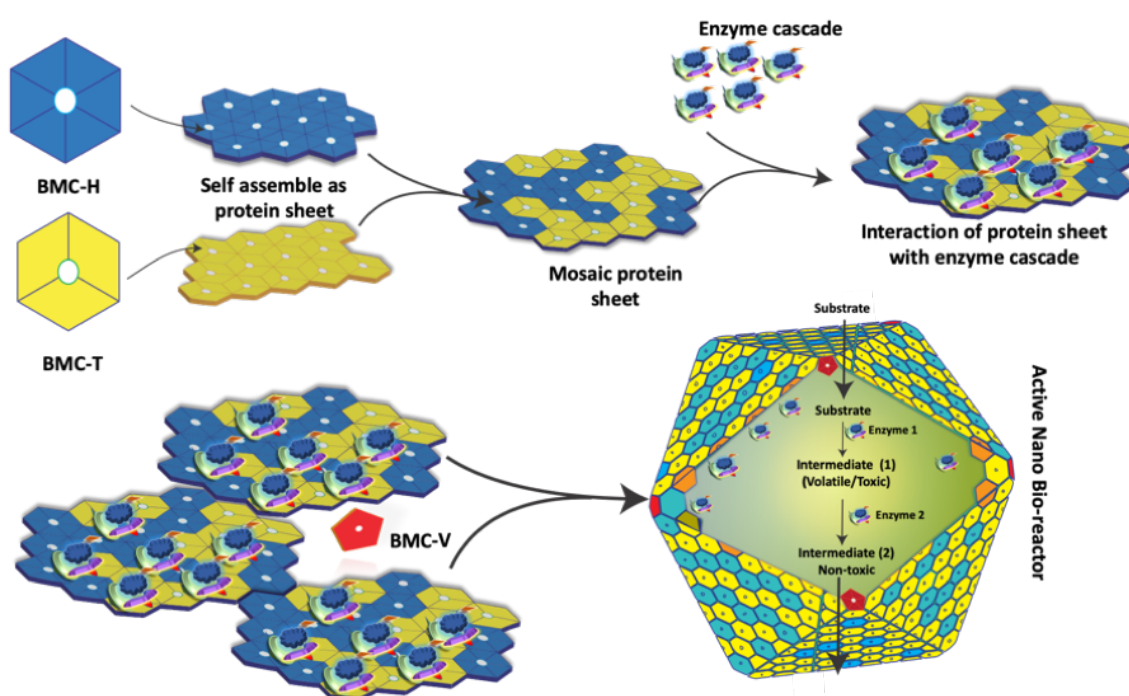


Figure 1.12: BMC-H and BMC-T assemble in 2D and form a mosaic sheet that interacts with the enzyme cascade. Latter with the help of BMC-V protein, the scaffold closes as a closed shell structure which carries out bio-catalysis within the periphery of the shell proteins.

1.2 Thesis motivation and perspective

Compartmentalization offers efficient way of performing functions *in vitro* or *in vivo*. Several of native compartments such as viral capsids(104,105), lumazine synthase capsids(106), or *in vitro* compartments fabricated from globular proteins(107), protein-polymer conjugates(108) have been explored for encapsulating cargo, delivery vehicle, synthetic nanoreactor and also protocell development(104,109–112). Nevertheless, the characteristic features of the SPs such as scaffolding enzymes, capacity to sequester toxic intermediates, to enhance the local concentration of substrate, channelizing the substrate, and the intermediate to minimize carbon loss makes them a perfect candidate to be explored for various metabolic engineering processes for the development of complex bioreactors *in vitro*. The investigation on the potential of MCPs for encapsulation of heterologous enzymes within the enclosed boundary of SPs is also under exploration (113–116). Studies have shown the incorporation of non-native genes in the MCPs operon with proper functioning. These studies put forward the potential of exploring these MCP for nanobiotechnological applications including bio-reactor development, development of catalytic hub or cargo carrier. The anticipated cargo can be small drug molecules, enzymes, metal nanoparticles, or even toxic constituents(117,118). Also the understanding of the selective permeability(119) across the pores at the molecular level will help to explore MCPs as molecular sieves. It will also help to modulate the selectivity of the pore to maintain the specific microenvironment within the closed periphery of MCPs. All these manipulations to explore MCPs needs an understanding of the assembly and also the composition.

This thesis, “USE” i.e., Understand, Simplify and Explore the Pdu BMC, observed in *Salmonella enterica* typhimurium as its paradigm. An understanding of the stability and assembly of Pdu BMC is outlined through studies discussed in this thesis. In the last decade, studies such as genetic deletion of individual shells from *pdu locus*, change of gene position of SPs, point mutations in SPs have provided information, which has given lead towards an understanding of the assembly of Pdu BMC(37,88,101,120). The mutational studies followed by growth assay, microscopic, and crystallographic characterization are meticulous. Also identifying the roles of potential amino acids by mutation in a megadalton structure with

structural and functional similarity becomes a challenge. The effect of external environments such as pH, temperature (103,121), or other stimuli also needs to be investigated to understand the stability of these supramolecular structures. On the other hand, the scientists are intensely designing and building different supramolecular assemblies(104,122) (BMC or assemblies made up of proteins) with new functions and diverse cargo, which also need to be characterized. This motivates us to look for any simple laboratory technique which can provide information on the assembly, stability, and morphological makeup of macromolecular structures. Also, a quick literature search provides no evidence for such a study that sought to bring a correlation in the structural stability and its function in MCPs like structure through Differential scanning fluorimetry (DSF)/Thermal Shift Assay (TSA). This is the first report where a macromolecular assembly and morphology are studied using DSF in *Chapter 3*, and the new observations related to the structural organization of Pdu BMC are discussed.

MCP is a macromolecular structure formed by the self-assembly of several protein molecules under strict genetic control. The SPs of the MCPs have intrinsic nature to self-assemble into a 2D sheet(102). Several reports have shown that the SPs attain different nanostructures when over-expressed(63). This intrinsic self-assembling property opens up a new paradigm of exploring these SPs for various applications including development of bioreactor in a suitable micro-environment, a cargo carrier that can be tuned to deliver the product at the desired location or an enzyme immobilization scaffold for single or cascade enzyme reactions. In *Chapter 4*, I explored the self-assembling properties of major SPs, i.e., PduA, PduB, and PduB' for fabricating protein compartments called Protein Shells (PSs). I simplified the heterogenous Pdu BMC as homogenous protein compartment and investigated the intrinsic properties of the MCPs such as substrate and co-factor channelling, active bioreactor and also as cargo carrier.

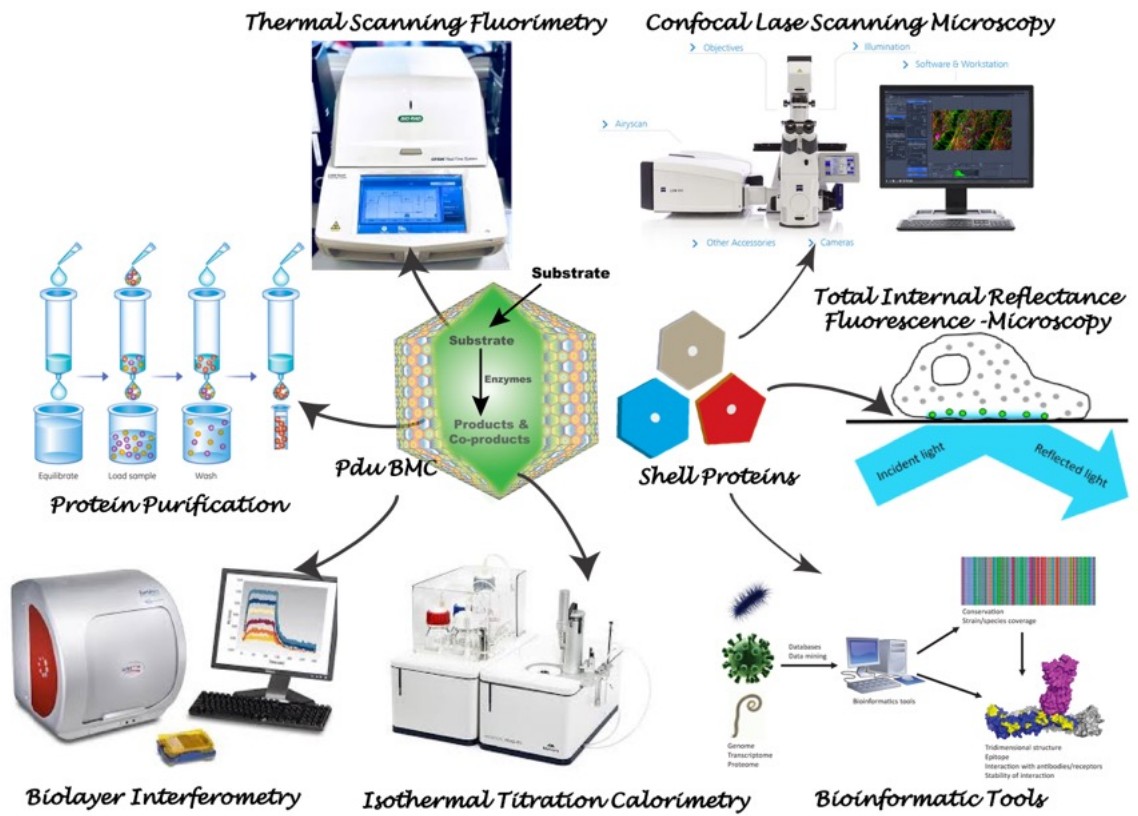
From the material perspective, the two-dimensional (2D) SP sheet may have diverse potential applications including fabrication of 2D self-standing sheets or scaffold for nanoparticle fabrication for application in optoelectronics or sensing. In *Chapter 5* of this thesis, the self-assembled protein scaffold of the SPs are used for nucleation and fabrication of gold nanoparticles(Though the fabrication of gold

Introduction

nanoparticles on the SPs is not shown in the thesis). Subsequently, the intact Pdu BMC is investigated as a scaffold for developing bio-hybrids. With bio-catalysis inside the shell covering and the fabricated gold nanoparticles on the Pdu BMC surface are evaluated for inorganic catalysis. With much interest in these MCPs, this approach for the development of bio-hybrid conjugate in native MCP will open the door for its exploitation as potential biogenic material in days to come. The thesis work indeed opens up a new paradigm for exploring these MCPs for a wide range of applications.

Chapter 2

Materials & Methods



2 Materials and Methods

In this section, I have detailed all the reagents and protocols used in this thesis. The entire work uses a combination of molecular biology, biochemical, biophysical, chemical, spectroscopic, and theoretical approaches. The following sections give the meticulous detail of the materials used and the methods employed. The same has been referred wherever essential in the later chapters.

2.1 Materials

Reagent and source	Source	Identifier
Experimental Models: Organisms/Strain		
<i>Salmonella enterica</i> serovar Typhimurium LT2	Gift from Dr. TA Bobik, Iowa State University	LT2
<i>E. coli</i> BL21(DE3)/pET41a-PduA	Gift from Dr. TA Bobik, Iowa State University	BE1721
<i>E. coli</i> BL21(DE3)/pET41a -PduB	Gift from Dr. TA Bobik, Iowa State University	BE1726
<i>E. coli</i> BL21(DE3)/pET41a -PduB'	Gift from Dr. TA Bobik, Iowa State University	BE1724
<i>E. coli</i> BL21(DE3)/pET41a-PduN	Sinha Laboratory Collection	SS98
<i>E. coli</i> BL21(DE3)/pET41a-PduCDE	Sinha Laboratory Collection	SS78
Chemicals and Reagents		
2-Ethylhexan-1-ol	Sigma Aldrich, India, India	Cat #W315109
3-methyl-2-benzothiazoline hydrazine	Sigma Aldrich, India	Cat # 129739
Acrylamide	Hi-Media, India, India	Cat # MB068
Ado-Cbl	Sigma Aldrich, India	Cat # C0884
Ammonium persulphate	Sigma Aldrich, India	Cat #A3678
Auric chloride	Sigma Aldrich, India	Cat # 520918
B-PER II	Thermo Fischer Scientific, India	Cat # 78260
Bis-acrylamide	Sigma Aldrich, India	Cat #M7256
Bradford reagent	Sigma Aldrich, India	Cat # B6916
Citric Acid	Merck, India	Cat # 1.93011.0521

Materials & Methods

Curcumin	Sigma Aldrich, India	Cat # C1386
Cyanocobalamin	Sigma Aldrich, India	Cat # V2876
DMSO	Sigma Aldrich, India	Cat # 276855
DNase	Sigma Aldrich, India	Cat #DN25
Doxorubicin.HCl	Cipla, India	Oncodox 10
EDTA disodium salt dihydrate	Hi-Media, India	Cat # MB011
Ethanol	Hayman, UK	Cat # F203640
Glycine	Hi-Media, India	Cat # MB013
HCl	Molychem, Mumbai, India	Cat #14860
HEPES	Hi-Media, India	Cat # MB016
Hydrogen peroxide	Merck, India	Cat # 1.93407.0521
Imidazole	Hi-Media, India	Cat # MB019
IPTG	Hi-Media, India	Cat #MB072
LB Agar	Hi-Media, India	Cat #M1151
Luria Broth	Hi-Media, India	Cat #M575
Lysozyme	Hi-Media, India	Cat #MB098
Magnesium chloride hexahydrate	Hi-Media, India	Cat #MB040
Magnesium sulphate	Hi-Media, India	Cat #MB171
NHS ester-Alexa 488	Tocris Bioscience, UK	Cat 6257
NHS ester-Cy3	Tocris Bioscience, UK	Cat # 5435
NHS ester-Cy5	Tocris Bioscience, UK	Cat # 5346
NHS ester-Texas red	Tocris Bioscience, UK	Cat # 5442
Ni-NTA resin	Qiagen, Thermo Fischer Scientific, India	Cat # 30230
Nickel sulphate hexahydrate	Sigma Aldrich, India	Cat # 72285
Nile red	Sigma Aldrich, India	Cat # N3013
4-Nitrophenol	Hi-Media, India	Cat # GRM1182
PEG4000	Hi-Media, India	Cat # RM400
PMSF	Sigma Aldrich, India	Cat #P7626
Potassium Chloride	Hi-Media, India	Cat # MB043
Potassium Hydroxide	Hi-Media, India	Cat #GRM1015
Potassium phosphate monobasic anhydrous	Hi-Media, India	Cat # MB050
Propane-1,2-diol	Sigma Aldrich, India	Cat # 134368
Rhodamine 6G	Sigma Aldrich, India	Cat # 252433
Sodium Azide	Merck, India	Cat # 1.94911.0121
Sodium Borohydride	Supelco, Sigma, India	Cat # 1.06371
Sodium Chloride	Hi-Media, India	Cat # MB023
Sodium Do-decyl sulphate	Hi-Media, India	Cat # GRM886
Sodium Hydroxide pellets	Hi-Media, India	Cat #MB095

Sodium phosphate dibasic anhydrous	Hi-Media, India	Cat # MB024
Sodium phosphate dibasic dihydrate	Hi-Media, India	Cat # MB126
Sodium phosphate monobasic anhydrous	Hi-Media, India	Cat # MB183
Succinic acid disodium salt	Sigma Aldrich, India	Cat #224731
Sypro Orange	Sigma Aldrich, India	Cat # S5692
TEMED	Sigma Aldrich, India	Cat #T9281
Tris Base	Hi-Media, India	Cat # MB029

Others

96-well, 0.2 mL thin-wall PCR plates	BIO-RAD, USA	Cat # HSS9601
Eppendorf®Uvette®	Eppendorf, Sigma Aldrich, India	Cat # Z618683
Amicon Ultra-0.5 Centrifugal Filter Unit 10 kDa MWCO	Millipore Sigma Aldrich, India	Cat # UFC5010BK
3kDa Cut off mini dialysis bag	Thermo Fischer Scientific, India	Cat # 68035
14 kDa dialysis bag	Sigma Aldrich, India	Cat # D9527
PD10-desalting columns	Ge-Health care Life Science, India	Cat # GE17-0851-01
APS sensor	Pall Life Science, USA	Cat # 18-5045
Precision Plus Protein Dual colour standards	BIO-RAD, USA	Cat # 1610374

Software's and Algorithms

Adobe Illustrator CS6	Adobe System, Inc. USA	https://www.adobe.com/products/illustrator/free-trial-download.html
AutoDock Vina 1.1.2	AutoDock Vina, USA	http://vina.scripps.edu
CFX Manager 3.1	BIO-RAD, USA	BIO-RAD, USA
Forte Bio	Octet CFR software, USA	https://www.fortebio.com/products/octet-systems-software
Jasco software	Spectra manager, Japan	Jasco, Japan
Nanoscope	Nanoscale world, Bruker, USA	http://nanoscaleworld.bruker-axs.com/nanoscaleworld/forums/t/812.aspx
Origin 8.6	Origin Lab, USA	https://www.originlab.com

Materials & Methods

PeakITC200	Malvern	Malvern, UK
PyMOL	PyMOL.org	https://pymol.org/2/
Swiss Model	University of Basel	https://swissmodel.expasy.org
VMD 1.9.3	VMD	https://www.ks.uiuc.edu/Research/vmd/

Instruments

Atomic Force Microscopy	Bruker Multimode 8 scanning probe	Bruker, USA
Bio-Rad Gel electrophoresis	BIO-RAD	BIO-RAD, USA,
Biolayer Interferometry	Octet QK, Forte Bio	Menlo Park, Pall Life Science, USA
CFX96 real time PCR	BIO-RAD	BIO-RAD, USA,
Circular Dichroism Spectroscopy	Jasco-J 1500	JASCO, Japan
Confocal Laser Scanning Microscope	LSM 880 Confocal microscope	Carl Zeiss AG, Germany
Dynamic light scattering	Nano-ZSP	Malvern, UK
Fourier Transform Infrared Spectroscopy	Cary Agilent 660 IR	Agilent technology
High speed centrifuge	Eppendorf	Hamburg, Germany
Incubator	Eppendorf	Hamburg, Germany
Isothermal Titration calorimetry	MicroCal-iTC ₂₀₀	Malvern Pananalytical
Microtiter Multimode plate reader	Biotek-Eon TM	Vermont, USA
Scanning Electron Microscopy	JSM-IT300	JEOL, Japan
Steady state fluorescence	FS5	Edinburgh Instruments
Table top centrifuge	Avanti JXN-26,	Beckman Coulter
TIRF-M	Iexplore Tif	Olympus
Transmission Electron Microscopy	JEM 2100	JEOL, Japan
UV	Cary 60 UV	Double Beam Agilent technology
X-ray Diffraction	Bruker ECO D8	Bruker, US

2.2 Methods

2.2.1 Experimental study

2.2.1.1 Expression and Purification

2.2.1.1.1 Propanediol Bacterial Microcompartment

Pdu BMC is purified according to a protocol developed(37,123). Briefly, *Salmonella enterica* serovar Typhimurium LT2(124) cultures are grown in 400 ml of non-carbon E growth medium (supplemented with 0.6 % Propane-1,2-diol (1,2-PD), 0.5 % Succinic acid and 1mM of MgSO₄). The culture is left overnight (for 12-16 h at 37 °C with shaking at 180 rpm) to grow till an OD₆₀₀ of 1-1.2 is attained. The cells are harvested by centrifugation using Avanti JXN-26 centrifuge (Beckman Coulter, 6000X g for 10 min) and is washed twice with 40 ml of Buffer A (50 mM Tris Base pH 8, 500 mM KCl, 25 mM NaCl, 12.5 mM MgCl₂, 1.5 % 1,2-PD; 8000X g for 5 min at 4 °C). The cells are then re-suspended in Buffer A containing 75% bacterial protein extraction reagent (BPER-II, Thermo Scientific™), DNase (2 mg, Sigma Aldrich, India), 0.4 mM phenylmethane sulfonyl fluoride (PMSF, Sigma Aldrich, India), and lysozyme (Hi-Media, India) at a final concentration of 1 mg/ml. The re-suspended cells are shaken at room temperature for 45 min using Innova 2000 at 45-50 rpm followed by incubation on ice for 5 min. The cell suspension is centrifuged (12,000 X g for 5 min, 4 °C), and the supernatant is collected and centrifuged (20000X g for 20 min, 4 °C). A thin glassy film is obtained containing Pdu BMCs along with associated debris. The film is re-suspended at 4 °C in a solution of Buffer A containing 60% of B-PER II and 0.4 mM PMSF followed by centrifugation at 20,000X g for 20 min at 4 °C. The thin film obtained is re-suspended in pre-chilled 0.5 ml of Buffer B (50 mM Tris Base pH 8, 50 mM KCl, 5 mM MgCl₂, 1 % 1,2-PD) and centrifuged (12,000 X g for 5 min at 4 °C). The supernatant is collected and stored at 4 °C. The purified Pdu BMC is analyzed using 12 % SDS-PAGE. Concentrations for the Pdu BMC is determined by Bradford reagent (Sigma Aldrich, India Aldrich) (125).

2.2.1.1.2 PduCDE and Pdu shell proteins (PduA/B/B'/N)

Propane-1,2-diol diol dehydratase complex (PduCDE) construct is cloned in the pET41a vector (Novagen, Merck), and the protein is expressed in *E. coli*

BL21CodonPlus (DE3)-cells (Stratagene) cultured in Luria Bertani broth (Hi-Media, India). For optimum expression, the cells are grown at 37 °C to an OD600 of 0.5 and then induced with 1 mM IPTG (Hi-Media, India) at 37 °C for 4 h. After induction, cells are lysed by sonication in column buffer (50 mM Tris-base, 200 mM NaCl, 5 mM imidazole, pH 7.5, all from Hi-Media, India) and centrifuged at 4 °C for 30 min at 10000X g. The supernatant is loaded onto Ni-NTA agarose (Qiagen, Thermo Fischer Scientific, India, after equilibrating the Ni-NTA with column buffer). The column is washed with wash buffer (50 mM Tris-base, 200 mM NaCl, 50 mM imidazole, pH 7.5, all from Hi-Media, India), and then protein is eluted in 1 ml elution buffer (50 mM Tris-base, 200 mM NaCl, 200 mM imidazole, pH 7.5). The elutions are checked for protein concentration using Bradford reagent (Sigma Aldrich, India) (125). The protein fractions are pooled and dialyzed in the sodium-phosphate buffer (10 mM, pH 7.5) with three buffer changes. SPs of 1,2-Pdu BMC are expressed and purified using the reported protocol. The clones for SPs, i.e., PduA and PduB and PduB' are a gift from Prof. Thomas A. Bobik, Iowa State University, USA. Whereas PduN is cloned in SS Lab, INST, Mohali. PduN, is cloned between NdeI and XhoI sites in the pET41a vector (Novagen, Merck). The SPs are expressed similar to that of PduCDE, except that OD600 of 0.5 is induced with 0.5 mM IPTG (Hi-Media, India) at 28 °C for 10-12 h. The dialyzed proteins are tested for purity by SDS-PAGE and Bradford reagent(125) is used to check the concentration.

2.2.1.2 Fabricating protein shells (PSs)

2.2.1.2.1 Hollow PSs

The SPs mediated PSs are fabricated at the water-oil interface as per the method for the fabrication of proteinosomes with modifications(108,110,112,126). The purified proteins are used in the concentration range of 0.25 to 1 mg/ml, of which 60 µl is taken in 1.5 ml microcentrifuge tubes (MCT) and added with 1 ml of oil (2-ethyl-1-hexanol from Sigma Aldrich, India) (water: oil ratio 0.06). The MCTs are gently shaken for 60 sec, which leads to the formation of the water in oil emulsion. The PSs formed in the bulk oil phase slowly settled down at the oil-water interface. After careful removal of upper oil (oil also wicked off along the surface of the MCTs) the PSs formed are transferred to 60 % ethanol to remove any associated oil. The PSs are then dialyzed (24 h with change after every 8 h) in Mili-Q to remove associated

ethanol. Post dialysis, the PSs are stored at 4 °C for further characterization. The scheme for the fabrication of PSs is provided in *Figure 2.1*.

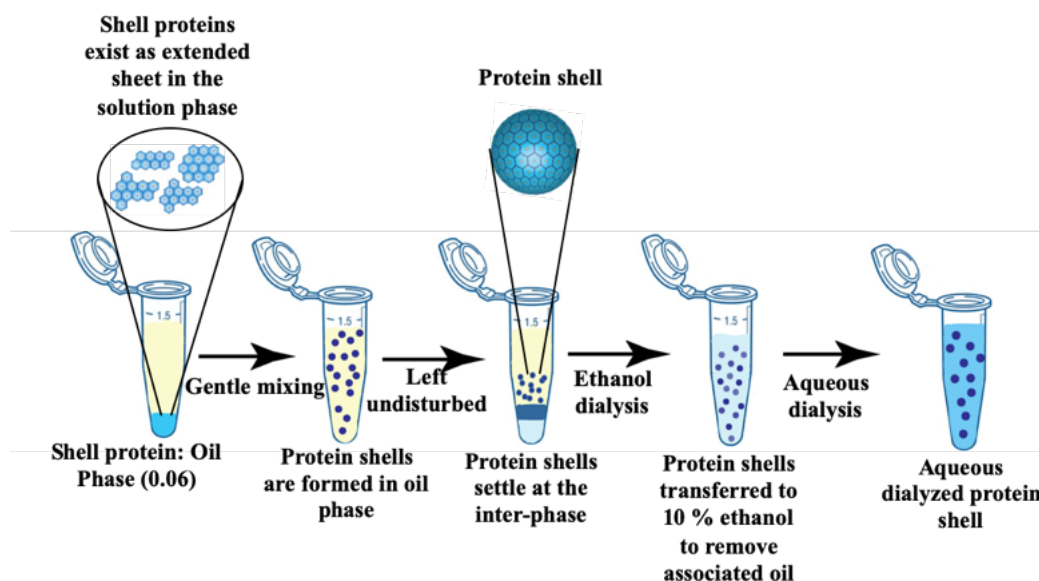


Figure 2.1: SPs of the Pdu BMC are explored for the fabrication of PSs. The SPs have the intrinsic nature to self-assemble as 2D sheet in the aqueous phase. The SPs in the aqueous phase is mixed with the oil through gentle shaking. The PSs separated at the interface are transferred to ethanol (10 %) and subsequently dialyzed in water. Ethanolic transfer and aqueous dialysis remove the associated oil and ethanol, respectively. The final dialyzed PSs can be stored at 4 °C or can be lyophilized.

2.2.1.2.2 Cargo loaded PSs

For fabricating enzyme/small molecules encapsulated PSs, the required encapsulant (enzymes, small molecules, etc.) is added to the SPs in the aqueous phase. Molecules with very low hydrophilicity are encapsulated in the PSs (techniques such as solid dispersion preparation, complexation in hydrophilic molecules are carried out). The physical mixture is incubated for the interaction of the two, followed by PSs fabrication as per the above-discussed method. For enzyme encapsulated PSs, to protect the encapsulated enzyme from the denaturing effect of ethanol, after removal of the oil phase, only minimal ethanol (10 % ethanol) is used for removal of associated oil. Subsequently they are dialyzed in water for removal of associated ethanol. Enzyme activity for the non-dialyzed enzyme encapsulated PSs (without being transferred to ethanol phase and aqueous dialysis) are also carried out. The scheme for the fabrication of encapsulated PSs from the SPs is provided in *Figure 2.2*.

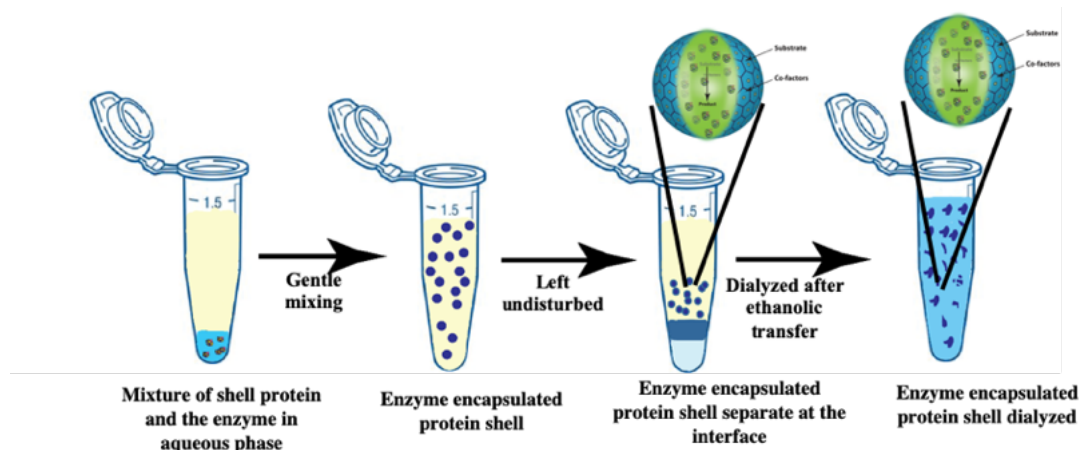


Figure 2.2: Scheme for the fabrication of cargo loaded PSs. The component to be encapsulated is incubated along with the SPs in the aqueous phase, and then PSs are fabricated. The encapsulated PSs settle at the water: oil interphase similar to hollow PSs and are transferred to ethanol (10%) for removal of associated oil and subsequently dialyzed in the aqueous medium.

Note: Typically, 10 μ l of PduCDE solution (2 mg/ml, 10mM PBS buffer pH 7.4) and 50 μ l of PduA/B/BB (1 mg/ml) was mixed and enzyme encapsulated PSs were fabricated at the water-oil interface.

2.2.1.3 Enzyme assay

2.2.1.3.1 3-methyl-2-benzothiazoline hydrazine assay for Aldehyde

detection: Diol-dehydratase activity assay

The diol dehydratase activity of Pdu BMC and PduCDE is estimated by the 3-methyl-2-benzothiazoline hydrazine (MBTH) method (127,128). 5 μ g of Pdu BMC or 2.5 μ g of PduCDE is added to 900 μ l of the assay buffer (0.2 M 1,2-PD, 0.05 M KCl, 0.035 M potassium phosphate buffer (pH 8.0)) at 37 $^{\circ}$ C. The reaction is induced by adding 50 μ l of adenosylcobalamin (Ado Cbl) (15 μ M) and quenched after 10 min by adding 1 ml of potassium citrate buffer (pH 3.6). 0.5 ml of 0.1 % MBTH is added, and the reaction mixture is incubated at 37 $^{\circ}$ C for 15 min. After 15 min, 1 ml of double-distilled water is added, and absorbance of the product formed is taken at 305 nm using a UV spectrophotometer. We define specific activity as μ mol of product formed by one milligram of the enzyme in one min. In the case of enzyme encapsulated PSs, a control experiment is carried out where PduCDE without SPs is subjected to similar conditions (conditions in which PSs are fabricated), and the diol-dehydratase activity is measured. The activity (for enzyme encapsulated PSs or free enzymes) is measured in triplicate, and the results are presented as Mean \pm SD.

2.2.1.3.2 Pyrogallol oxidation assay

For Cyt-C encapsulation, the required amount of enzyme is added (10 mg/ml; enzyme protein concentration in the reaction mixture is $50 \mu\text{g mL}^{-1}$) to 50 μl of PduA/B/B' (1.0 mg/ml), and PSs are fabricated as per the method discussed in 2.2.1.2.1 (Figure 2.2). The Cyt-C encapsulated PSs are transferred in a quartz cell and added with 5 μL of pyrogallol (3 M stock in water, the substrate for Cyt-C), and final volume is made up to 1 ml by Mili-Q. Finally, the required amount of H_2O_2 (8.82 M stock) is added to initiate the reaction. The absorbance is monitored instantaneously after the addition of H_2O_2 . The progress of the reaction is monitored at 420 nm by the formation of purpurogallin, the oxidized product of pyrogallol, for the initial 5-30 min ($\epsilon_{420 \text{ nm}}$ is $2640 \text{ M}^{-1}\text{cm}^{-1}$ in water) (129).

2.2.1.4 Dye labeling of shell and the enzyme proteins

NHS (N-Hydroxy Succinimide) esters of dyes Alexa 488, Cy3, Cy5, and Texas red are used to label the SPs and the enzyme. Free amine groups on the protein surface react with the NHS ester-activated dye at physiologic conditions (pH 7.2 to 9) to yield stable amide bonds. The dye is added to the protein in a ratio of 2:1 (dye:protein; μM) and incubated overnight at 4 °C with gentle mixing. After overnight incubation, the mixture is passed through a PD10 desalting column (GE Healthcare life sciences, India) containing Sephadex G-25 resin. The tagged protein is eluted in phosphate buffer (pH 7.5). A UV spectrophotometer checked the elutions for the labeling of the different proteins. The dye-labeled SPs are used as starting material for fabricating the PSs, and observed under a Confocal laser scanning microscope (CLSM) (LSM 880 Confocal microscope (Carl Zeiss AG, Germany). For fabricating enzyme encapsulated PSs, the dye-labeled enzyme (PduCDE/CytC) is added to the dye-labeled SPs in the aqueous phase, and the PSs are fabricated as per the method and observed under the confocal microscope.

2.2.1.5 Thermal Scanning Fluorimetry for the Pdu BMC, PduCDE, and SPs

For carrying out the DSF experiments, a working stock of Sypro orange SO (200X) is prepared in the final dialyzed buffer from a DMSO stock of 5000X. The working stock is mixed with the varying concentration of protein samples in order to get a different final concentration of SO in the mixture (5X/10X/20X). The mixture is incubated and then loaded onto 96-well, 0.2 mL thin-wall PCR plates (BIO-RAD, USA) sealed with optical-quality sealing tape (BIO-RAD, USA). Thermal

denaturation is performed using a CFX96 real time-PCR instrument (BIO-RAD, USA) where the temperature is increased from 20 to 95 °C at 1°C/cycle with an equilibration time of 60 sec at each temperature. The change in SO fluorescence is monitored over time ($\lambda_{\text{ex}} = 450\text{--}490$ nm, $\lambda_{\text{em}} = 610\text{--}650$ nm) with the help of the CFX96 Touch System, which includes one channel with an LED-filter photodiode combination designated for single-color fluorescence resonance energy transfer (FRET). The fluorescence intensity (I) obtained upon thermal denaturation is fitted to a Boltzmann function (130) according to the Eq. 1 where A_L is the lower and A_U the upper limit of the fluorescence intensity, T_m is the temperature at the midpoint of the transition (transition temperature), and dT is the slope of the transition.

$$I(T) = \frac{A_L - A_U}{1 + e^{\frac{T - T_m}{dT}}} \quad \text{Eq. 1}$$

The thermal denaturation curve is fitted to multiple peak fit after base-line subtraction. Each of the peaks are assigned to transitions by carrying out the best fit, and the peak position is referred to as transition temperatures.

2.2.1.6 Permeability study of small molecules in PSs

2.2.1.6.1 Rhodamine 6G

The permeability of the fabricated PSs is studied by carrying out the uptake and release of a water-soluble dye, i.e., Rhodamine 6G (R6G). The dialyzed PSs are taken in small dialysis tubing and placed in a beaker containing the dye solution (20 μM). At regular time intervals, the PSs are removed and put on an activated glass coverslip. The PSs are imaged using an inverted fluorescence microscope at 40X objective. Fluorescence images are collected by radiating the sample with a 532 nm laser with an exposure time of 100 ms with 30 % laser power. At each time point, fluorescence is collected from various regions covering more than hundreds of PSs. The images having PSs are analyzed using Olympus cell-sens software. After background correction, images are segmented to detect the particles having fluorescence (More than 100 PSs). Then the average fluorescence intensity per unit area of each particle is calculated. Histogram is plotted for all the averaged intensity of all PSs at each time point. Each histogram is fitted using Gaussian distribution, and the peak intensity value is calculated. The mean peak fluorescence intensity for uptake and

release are plotted against time and best fitted using a single exponential decay model as per Eq. 2 to calculate the rate constants.

$$y = y_0 + Ae^{-\frac{x}{t}} \quad \text{Eq. 2}$$

2.2.1.6.2 Vitamin B12

For studying the interaction along with uptake of VitB₁₂ (Cyanocobalamin) by the PSs dialysis bag method is adopted. The dialyzed PSs are taken in dialysis tubing (Thermo Fischer Scientific, Cut-off 3kDa, volume 500 ml) and is placed in a beaker containing Vit B₁₂ (20 μM). At each time interval (0, 1/2/4/6/12 h), the SPs/ PSs are checked for of VitB₁₂ absorption using a UV spectrophotometer. The absorbance is plotted against time, and using single exponential decay, the rate of VitB₁₂ uptake inside the PSs is determined.

2.2.1.7 Encapsulation and release of small molecules from PSs

2.2.1.7.1 Doxorubicin (Dox)

Doxorubicin at a concentration of 0.16 mg/ml is mixed with the SPs (1mg/ml) and incubated overnight. The mixture is used for the fabrication of Dox loaded PSs by the method discussed in section 2.1.2.2. The PSs formed at the junction are transferred to ethanol and dispersed in water. The dispersed samples are checked for drug loading. The release study is then carried out by dialysis bag method (Small dialysis bags from Thermo Fischer Scientific, Cut-off 3kDa, volume 500 μl). At regular time intervals (0, 1/2/4/6/12 h), the PSs are removed from the dialysis bag and checked by a UV spectrophotometer. As a control, only aqueous drug solution is mixed with the oil phase, mixed, followed by separation of two phases. The oil layer is removed, and an aqueous drug solution is transferred to the dialysis bag to check the release of the free drug molecule. The release rate is determined by fitting the curve in single exponential decay (Eq. 2).

2.2.1.7.2 Nile red

The pre-incubated mixture of SPs and NR-β-CD is used for fabrication of Nile Red (NR) (10 μM) encapsulated PSs (pre-incubated mixture is used to check the interaction of the dye with SPs) as per method discussed above. The PSs formed at the juncture of oil-water are separated and transferred to ethanol. The PSs are

subsequently dispersed in water, and the release study is carried out by the dialysis bag method (Small dialysis bags from Thermo Fischer Scientific, Cut-off 3kDa, volume 500 μ l). At regular time intervals, the PSs are removed from the dialysis bag and checked for fluorescence intensity (Excitation – 550 nm; Emission 600 to 750 nm) using a fluorescence spectrophotometer. The release rate is determined by fitting the release curve in single exponential decay (Eq. 2). (Note: NR is a hydrophobic dye. Initially, the NR is mixed with SPs, but encapsulation is not achieved. Then the dye hydrophilicity is increased by entrapping it in beta-cyclodextrin (β -CD) hydrophobic core (For 10 μ M of NR 0.3 mM of β -CD is used).

2.2.1.7.3 Curcumin

The curcumin (Cur) loaded PSs are fabricated from the physical mixture of Cur-PEG complex and SPs as per the method discussed above. The PSs formed at the oil-water junction are transferred to the ethanolic phase before being dispersed in water. The aqueous dispersion is transferred to a dialysis bag (Thermo Fischer Scientific, Cut-off 3kDa, volume 500 μ l) to study the release of Cur from the PSs. At regular time intervals, the PSs are removed from the bag and checked for fluorescence intensity (Excitation – 480 nm; Emission 500 to 750 nm) using a fluorescence spectrophotometer. The release rate is determined by fitting the release curve in single exponential decay. (Note: Cur has low aqueous solubility, thus, Cur solid dispersion is prepared to enhance its solubility. Cur is mixed with PEG4000 at a ratio of 1:8 (2 mg of Cur and 16 mg of PEG 4000) and heated at 75 $^{\circ}$ C for 1 h. A homogeneous solution is obtained, which is cooled to get a solid mass. The prepared solid dispersion is weighed, triturated, and dissolved in water such that final cur concentration is 100 μ M in the physical mixture with the SP. The physical mixture is checked for cur interaction with the SPs.)

2.2.1.7.4 Gold nanoparticles

Gold nanoparticles (AuNPs) encapsulated PSs are fabricated from the physical mixture of AuNPs (18-20 nm (volume %)) and SPs as per the method discussed above. The PSs formed at the oil-water junction are transferred to the ethanolic phase before being dispersed in water. Both physical mixture and AuNPs encapsulated PSs are used to carry out the reduction of p-nitrophenol to p-aminophenol (in the presence of NABH_4), which is measured by UV spectrophotometer.

2.2.1.8 Studying the interaction of auric chloride with Pdu BMC

The interaction of Pdu BMC with AuCl_3 is studied by methods such as measuring the AuCl_3 peak in the matrix using UV-Vis spectroscopy or the decrease in tryptophan fluorescence. An optical method such as Biolayer interferometry (BLI) and thermodynamic method such as Isothermal titration calorimetry (ITC) is also investigated for studying the interaction.

2.2.1.8.1 Biolayer interferometry

Interaction experiments are carried out by Biolayer interferometry (BLI) on a FortéBio (Menlo Park, CA) Octet QK biosensor using aminopropyl silane (APS) sensors. It is a label-free method extensively used for the analysis and characterization of protein interactions, quantitation of proteins, affinity for macromolecules and kinetics of interactions. Initially, before loading the proteins the sensors are hydrated for 10 min. On the hydrated sensors after a short baseline (60 sec) proteins (Pdu BMC @ 0.1 mg/ml, whereas SPs at 50-200 $\mu\text{g/ml}$) are loaded through hydrophobic interactions (till saturation is achieved) followed by baseline in water to remove non-specific bound protein.

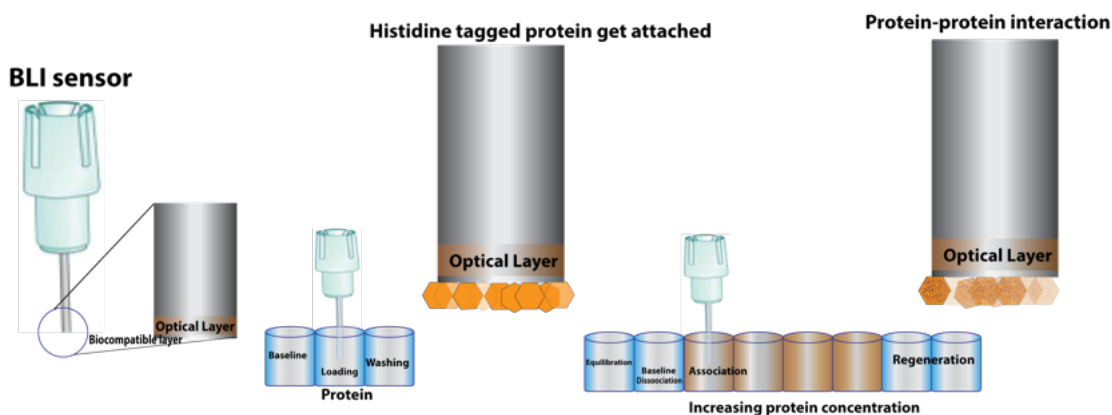


Figure 2.3: Scheme for studying the interaction of Pdu BMC with the Auric chloride through BLI. Initially, Pdu BMC is immobilized on APS sensor through hydrophobic interaction and then is made to interact with different auric chloride concentration

After a stable baseline (60 sec), the sensor is moved to well containing AuCl_3 for association (300 sec) and immediately moved to well where an initial baseline before the association is carried out for dissociation (300 sec). This step of a stable baseline followed by association and dissociation is carried out for minimal 4 AuCl_3 concentration (5 to 250 μM). After each step, the complete conjugate is removed by

carrying out a regeneration step. The curves obtained are corrected for control (interaction of bare sensor with AuCl_3) sensors and are fitted to determine the dissociation constant. The scheme for the same is provided in **Figure 2.3**.

2.2.1.8.2 Isothermal titration calorimetry

Interaction experiments in the solution phase between the Pdu BMC or SPs with AuCl_3 is carried by Isothermal Titration calorimetry (ITC) using MicroCal-iTC₂₀₀ instrument (Malvern Panalytical). It is used mainly for studying the interaction of small molecules with large macromolecules. AuCl_3 in water is used at 30 μM and is titrated with Pdu BMC (0.1 mg/ml) or shell proteins (5-10 μM) at different injection volume (for Pdu BMC, 39 injections @ 1 μl /injection with an interval of 150 sec between two injection; whereas for Pdu shell proteins 19 injections @ 2 μl /injection with an interval of 150 sec between two injection). Titration carried out with SPs is fitted into a one-site binding model using PeakITC software.

2.2.1.9 Fabrication of Gold nanoparticles on Pdu BMC

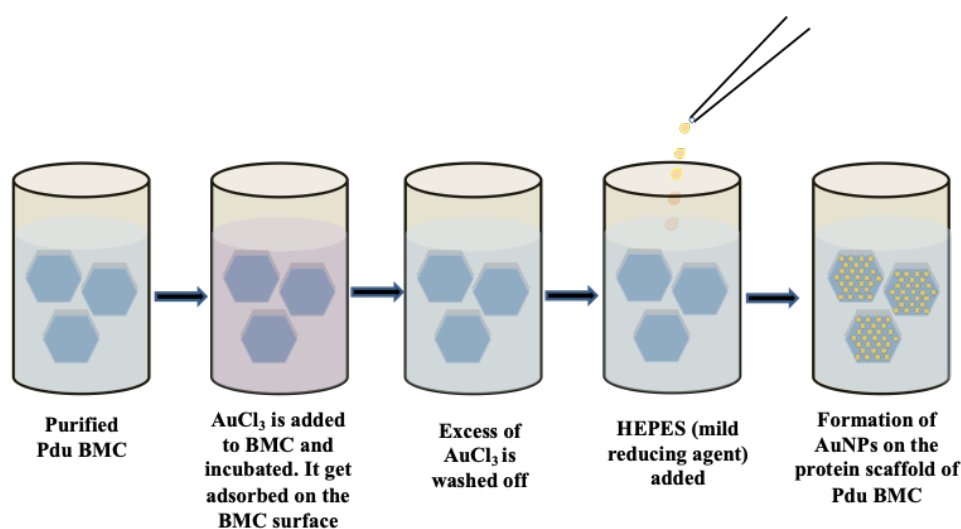


Figure 2.4: Scheme for the reduction of AuCl_3 on the Pdu BMC scaffold. Initially, AuCl_3 is adsorbed on the BMC surface, and then the reduction is carried out in the presence of HEPES.

Pdu BMC (concentration ranging of 0.1 to 1 mg/ml) is incubated with AuCl_3 solution (5 μM to 500 μM), as shown in **Figure 2.4**. The excess of AuCl_3 is removed by centrifugation (20,000 X g), and the matrix at the bottom of MCT is checked for BMC- AuCl_3 interaction by measuring the AuCl_3 peak intensity and also tryptophan

fluorescence of Pdu BMC. The matrix is added with equimolar HEPES (ranging from 5 μM to 500 μM) for fastening the reduction of AuCl_3 to AuNP. The reduction (from Au(III) to Au(0)) is checked on a multimode plate reader at a fixed wavelength of 540 nm with a step time of 10 sec. End spectra are also taken for the conjugate from 250 to 900 nm using a UV-Vis spectrophotometer.

2.2.1.10 Characterization techniques

2.2.1.10.1 Size distribution by Dynamic Light Scattering

The hydrodynamic diameter of the sample is determined using the Nano-ZSP (Malvern) instrument (5 mW HeNe laser $\lambda = 632$ nm, at a backscattering angle of 173°). 100 μl of the samples (Pdu BMC, SPs, Pdu BMC-AuNP hybrid) are taken in disposable cuvettes (Eppendorf® UVette®, Optical path length- 10 mm). All the samples are measured in triplicate.

For showing the full distribution in the SPs and PSs, all of the population is plotted where 'x' axis represents the hydrodynamic diameter and y-axis the intensity percent.

2.2.1.10.2 Circular Dichroism

Secondary structure and conformational stability of the protein samples (in the concentration range of 5-20 μM , Pdu BMC @ 0.1-0.5 mg/ml) are recorded with the Circular Dichroism (CD) spectrophotometer (Jasco J-1500). A quartz cell with a path length of 0.1 cm is used in a nitrogen atmosphere for measurement in the far-UV range (200-250 nm). An accumulation of three scans is carried out (scanning speed of 200 nm/min) for each sample. For determining the thermal stability of the proteins, peltier based CD measurement is carried out. Samples are scanned from 25 to 100 $^\circ\text{C}$ (temperature wavelength scan) at a rate of 2.5 $^\circ\text{C}/\text{min}$ and at the interval of 5 $^\circ\text{C}$ in the far-UV range (200-250 nm). The α/β content for the same is determined using K2D3 software(131).

2.2.1.10.3 Fourier Transform Infrared spectroscopy

The secondary structure of Pdu BMC and hybrid are determined by Fourier Transform Infrared (FTIR) spectroscopy after depositing it as thin on the ATR cell (diamond ATR crystal) in Cary Agilent 660 IR spectrophotometer. Spectrum is collected in a range of 400–4000 cm^{-1} wavenumbers. Each sample is an average of

20 scans at 4 cm⁻¹ resolutions. The spectra are analyzed for secondary structure components.

2.2.1.10.4 Atomic Force microscopy

The morphology of the SP and PSs is carried out using Bruker multimode 8 scanning probe microscopes. In brief, 20 μl of the sample is placed on silicon wafers, allowed to settle down for 5 min and then washed with Mili-Q (to wash off any associated salts and debris). The samples are then dried and purged with nitrogen. The scanning is carried out using tapping mode in the air with a gold-coated cantilever. The images obtained by Atomic Force Microscopy (AFM) are processed using Nanoscope software (Bruker) to determine the morphology and height profile.

2.2.1.10.5 Scanning Electron microscope

The shape and the morphology of the PSs are observed using a scanning electron microscope (SEM) (JEOL, JSM-IT300, USA) at 10-15 kV with a probe current of 30-40 μA. The PSs after dialysis are dropped cast on silicon wafer followed by drying at room temperature. The air-dried samples are gold-sputtered for 60 s at 30 μA current and scanned at different magnification. The size for the PSs is presented as Mean ± Standard error of the mean.

2.2.1.10.6 X-ray diffraction studies

The X-ray diffraction (XRD) pattern for the bio-inorganic hybrid is recorded using a Bruker ECO D8 advance with Cu K α radiation wavelength of 0.1542 nm at a voltage of 40 kV and a current of 25 mA. The data is collected from 10 to 80 two theta (2 θ) with an increment of 0.02. For carrying out the XRD, the Pdu BMC-hybrid is fabricated in the MCT as described above and is drop-casted as thin films on specially designed glass sample holders. *In situ* fabrication of NPs on the BMC surface is carried out on sample holder, and XRD pattern is collected. XRD for only Pdu BMC is also collected.

2.2.1.10.7 Transmission electron microscopy

Transmission electron microscopic (TEM) images of purified BMC and BMC-AuNP are obtained with a JEM 2100 TEM (JEOL, USA) operated at 120 kV or 200 kV. The sample for Pdu BMC (1-2 mg/ml) is added on formvar or carbon-coated grids (300/ 200 mesh size). The Pdu BMC are stained with uranyl nitrate (0.2-0.5 %

w/v, freshly prepared and filtered) followed by Mili-Q (pH 7.3-7.5). For TEM of Pdu BMC-AuNP hybrid, the samples are prepared either *in situ* on grids or in tubes followed by transferring to the grids. For the *in situ* preparation, 10 μ L of Pdu BMC (at 0.1 mg/ml) is added to the surface of the grid and allowed to settle. The excess buffer is wicked off, followed by adding 10 μ L of AuCl₃ (31.5 μ M). It is allowed to interact with Pdu BMC for 3-5 min. Excess AuCl₃ is wicked off, followed by the addition of 10 μ L of HEPES (31.5 μ M, pH 7.4). Post incubation excess of HEPES is removed, and the grids are washed twice with Mili-Q, followed by drying.

2.2.1.10.8 UV-visible spectroscopy

UV-visible spectra of the dye-labeled SPs for fabrication of PSs, product formation in MBTH assay at 305 nm, pyrogallol to purpurogallin formation at 402 nm, tryptophan absorption at 280 nm in AuCl₃ and BMC interaction or Pdu BMC-AuCl₃ hybrid at 540 nm are recorded on an UV-Vis spectrophotometer (Double beam Agilent technology, Cary 60 UV-Vis) at respected wavelength or in a particular UV range. Quartz cell with a path length of 1 cm is used in UV-Vis with bandwidth 1 nm.

Kinetics of AuCl₃ reduction on Pdu BMC or SPs surface is studied on a microtiter multimode plate reader (Biotek – Eon™) at 540 nm in transparent flat 96 well plates.

2.2.1.10.9 Steady-state fluorescence

Steady-state fluorescence spectrophotometer from Edinburgh spectrophotometer (FS5, Module SC-5, Module SC-25 (liquid sample module for temperature-dependent study) Standard cuvette holder from Edinburgh Instruments, UK) is used to study the initial binding of SO to the BMC proteins, tryptophan fluorescence studying the stability of Pdu BMC or PduCDE, FRET study enzyme encapsulated PSs, release study of various fluorescent small molecules, interaction of AuCl₃ with Pdu BMC and to study the mechanism involved in the formation of AuNPs on the Pdu BMC surface.

For the SO binding experiment, protein samples are mixed with increasing SO concentration (1X to 5X). The SO-protein mixtures are excited at 490 nm, and emission spectra are recorded between 500 to 750 nm at the bandwidth of 3 nm each. Three scans are collected, and the spectra shown are the sum of three scans. For studying the stability of Pdu BMC and PduCDE as a function of temperature, the

sample is ramped from 20 to 100 °C using peltier. The change in the tryptophan fluorescence emission (from 300 to 500 nm) is collected after excitation at 290. FRET between Cy3 and Cy5 tagged SPs and enzyme is checked after exciting for Cy3 and collecting the emission for Cy5. Release study for small molecules such as Cur, NR, and Dox is collected by measuring the emission after exciting at the appropriate wavelength.

The interaction of AuCl₃ is studied by assessing the tryptophan fluorescence (excitation at 290 nm and emission from 300 to 500 nm) using a fluorescence spectrofluorometer. The mechanism involved in the formation of AuNPs on the Pdu BMC surface is also studied by steady-state fluorescence. The Pdu BMC: Au hybrid is excited at 365 nm, and the emission is collected from 600 to 700 nm with excitation and emission bandwidth of 5 nm each (concentration for MCP, AuCl₃, and HEPES are similar to that of UV experiments). The emission spectra are collected at a one-minute interval till saturation. After saturation excess, AuCl₃ or HEPES is added, and the emission is collected under similar conditions.

2.2.1.10.10 Total Internal Reflection Fluorescence Microscopy

The mechanism involved in the fabrication of AuNP on the Pdu BMC surface is studied by Total Internal Reflection Fluorescence microscopy (TIRF-M). It potential

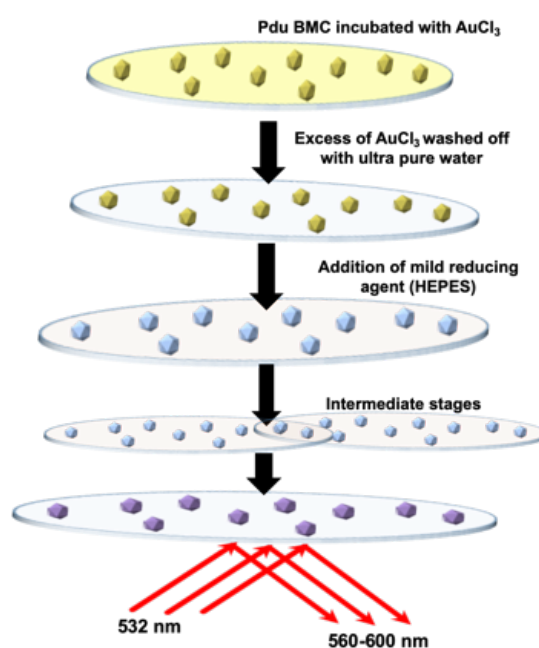


Figure 2.5: Studying the formation of fluorescent gold nanoparticles on the Pdu BMC surface by TIRF-M

benefits in any application requiring imaging of minute structures or single molecules in specimens having large numbers of fluorophores located outside of the optical plane of interest, such as molecules in solution in Brownian motion, vesicles undergoing endocytosis or exocytosis, or single protein trafficking in cells. For the TIRF-M experiment, 0.1 mg/ml of the Pdu BMC is incubated on ultra-clean glass coverslips. The excess of Pdu BMC is removed by gentle washing with Milli-Q. Then AuCl_3 is added and allowed to interact with the BMC surface, followed by HEPES addition. Immediately the sample is excited with 532 nm laser (Cy3), and emission is collected from 550 to 630 nm. Imaging is performed using the IX83 P2ZF inverted microscope (Olympus) combined with the IX3 TIR MITICO TIRF illuminator. Fluorescence is collected using an oil-immersion objective (60X, NA 1.45, Olympus) split into two channels by a dichroic beam splitter and recorded by electron-multiplying charge-coupled device (EMCCD) camera (Q-Imaging Roller Thunder). The filters used are Quad-band LF405/488/532/635-A-000 Bright Line Full Multi-Band Laser Filter set. Cy3 (532 nm) and the laser is used at 50% power. The samples are exposed for a duration of 1 s, and the interval between two exposures is 5s. The scheme for the experiment is shown in **Figure 2.5**. Image acquisition and processing are performed using CellSens Dimension (Olympus) software.

2.2.1.11 The catalytic activity of BMC-AuNP hybrid

The reduction of p-nitrophenol to p-aminophenol is monitored by UV-Vis spectroscopy. For the experiments, 100 μL of 0.360 mmol L^{-1} p-Nitrophenol is diluted with 380 μL of Milli-Q and mixed with 20 μL of 25 mmol L^{-1} sodium borohydride in a quartz cuvette before directly adding the BMC-AuNPs. UV-Vis spectra following the catalytic reaction of p-nitrophenol are subsequently taken with 1 min intervals for 30 min(132).

2.2.2 Theoretical study

2.2.2.1 Docking studies of Sypro orange with proteins

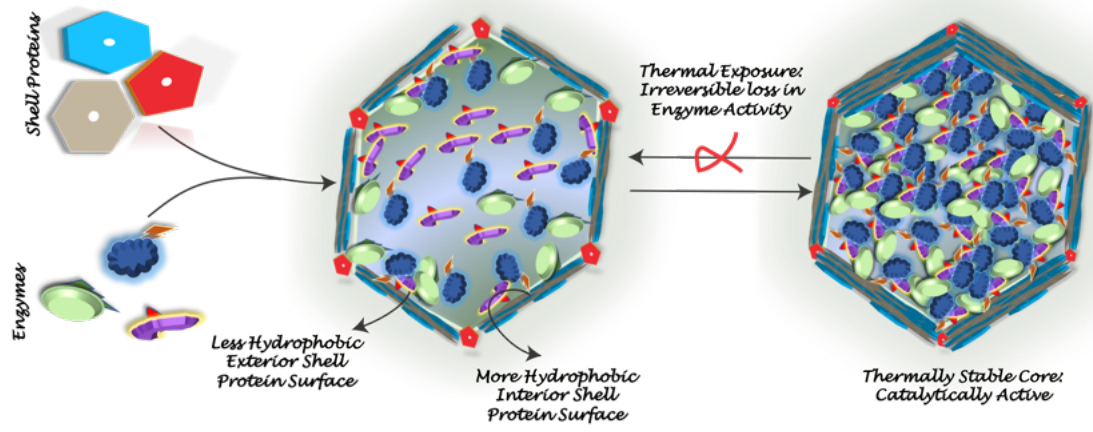
Protein structures are taken from Brookhaven Protein Data Bank(133) (PDB ID: Pdu A-3NGK; Diol dehydratase-1IWB). Hydrogen atoms are added to the protein and Kollmann charges (Kollamn charges are template values for each amino acid

Materials & Methods

that are derived from the corresponding electrostatic potential using quantum mechanics. If no charges are added, all the electrostatic interactions between protein and ligand are absent, and the Van der Waals interactions will become dominant) are added. Auto dock tools are used to prepare the macromolecule and ligand. Lamarckian genetic algorithm(134) implemented by an adaptive local method search is utilized by auto dock vina(135) to produce different ligand conformations. A grid box of size 20*20*20 Å is prepared for the docking. For hexameric PduA (PDB ID: 3NGK)(41,136) unit and diol dehydratase (PDB ID: 1IWB)(137), docking is performed separately by creating multiple cubic boxes covering the entire protein surface. Docking is performed multiple times (more than 50). We kept the number of ligand modes to 20 at a time and an exhaustiveness value of 50. Although there is no standard way to set the value of exhaustiveness, which is by default eight but increasing this value increases the sampling, which in turn raises the accuracy of the auto dock vina program. Analysis of the potential binding site and mapping of surface hydrophobicity has been performed using pymol and VMD (135,138–140).

Chapter 3

*Understanding the assembly of
Pdu BMC*



3 Understanding the assembly of Pdu BMC

3.1 Introduction

In general, MCPs have been an attractive target for functional studies because of their assembly and diverse metabolic interactions. Various factors responsible for these characteristic features are intactness, size scale of BMC, geometry, structural complementarity of various proteins, inter-play of forces (ionic, hydrophobic) across different proteins etc. All these factors bring complexity, and thus a challenge to realize BMC *in vitro*. Various biophysical methods such as X-ray crystallography, TEM, AFM and biochemical assays are adopted to study the structure-function correlation of these complex supramolecular assemblies, however, they involve time and cost intensive protocols (40,141–143). Most of these studies have attempted to characterize the structures of the component proteins individually (40,101,120,141,142,144,145). Information from several crystal structures combined with the morphological features of the MCP seen in microscopic images led to the proposition of the global MCP structure (16,27). There are, however, no direct understanding that relates to the forces that keeps all the components together in the MCP. Such an understanding will help development of smart bioreactors with novel function.

This chapter highlights the factors that bring all the components of the Pdu BMC together to make a functional assembly. Pdu BMC is a complex protein assembly that involves 22 different proteins. *pduABB'CDEGHJKLMNQPSTUVWX*, is the *pdu operon* having 22 genes and is involved in the expression and regulation of this proteinaceous organelle. The morphological assembly of Pdu BMC is sensitive to genetic manipulations, with compromised structures and activity. For example, it has been observed that a point mutation in the *pduA* gene, *pduA*[K26A] forms poorly assembled Pdu BMC whereas deletion of *pdu shell* gene results in unorganized assembly (deletion of *pduJ* gene generates elongated MCP; deletion of PduB/B' results absence of MCP assembly, etc.) (37,43,101,143,146). All these genetic studies including, deletions and mutations, focus on the role of the individual shell proteins in MCP structure and function. Here I attempted to analyze the overall solution phase structure of the Pdu BMC using an ensemble assay in solution. The

assay involves a spectroscopic method where a fluorescent dye that binds to the hydrophobic surfaces on proteins is used to probe the Pdu BMCs under different conditions, and so have an understanding of its solution phase structure. The probe used here is Sypro orange that has high fluorescence in the non-polar environment, and its fluorescence gets quenched in polar one. As protein unfolds, the hydrophobic surfaces get exposed, and the fluorescent probe gets partitioned from the polar environment to these non-polar surfaces, resulting in the fluorescence (**Figure 3.1**)(147). Since 2007, this method has been used for understanding the stability of globular proteins, protein unfolding, protein-protein interaction, protein-drug interaction, etc. based on hydrophobic assessment (148–151). Recently Kant and co-workers used this method to study the growth and morphological changes of macromolecular viral protein assembly (152). The initial and final Sypro orange fluorescence depends respectively on the extent of exposed hydrophobic residues in the folded protein and the exposure of the hydrophobic core upon unfolding. Depending on these values of relative Sypro orange fluorescence, a qualitative sketch of the Pdu BMC is developed. This chapter describes those different observations that led to the development of the sketch and its comparison with the existing knowledge in the literature.

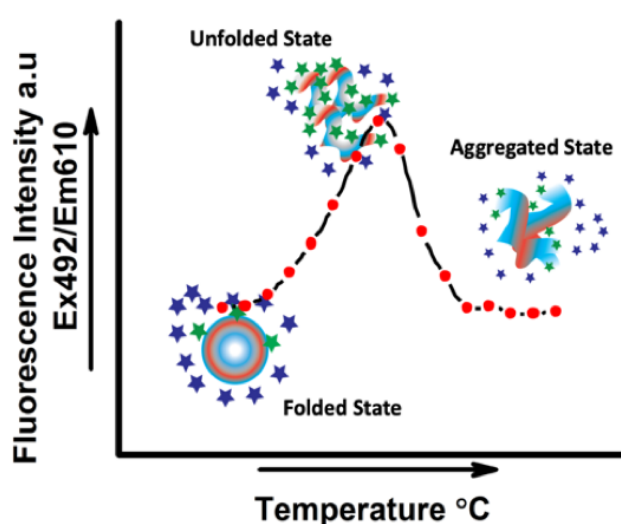


Figure 3.1: Scheme for studying the morphology of a protein through TSA using a probe, which is minimal fluorescent in the polar environment and fluoresces when moves to the non-polar environment. With an increase in temperature, the protein unfolds, exposing the hydrophobic regions to which the dye binds and fluoresces. Further increase in temperature leads to the aggregation of the protein molecule expelling the dye molecule, and the fluorescence gets quenched (Blue star symbolizes free SO, whereas Green stars symbolize hydrophobic bound SO).

The study also brings correlating correlation between the Pdu BMC structure and its catalytic role as function of temperature. The signature curve for the SPs (PduA[Hexamer]; PduB[Trimer]; PduN[Pentamer]) are obtained which provides their morphological makeup, corroborating well with the available crystal structures of SPs. The differences between the two categories of proteins, i.e., SPs and the enzyme, based on the integrity of the hydrophobic core are also obtained. The study shows that the encapsulation of the enzymes by the MCP shell enhances their thermal performances. This spectroscopic assay which scans the hydrophobicity of proteins can be an efficient technique to highlight the assembly of such macromolecular structure.

3.2 Results and discussion

3.2.1 Thermal unfolding of Pdu BMC

The Pdu BMC is purified to mono-dispersity (Size = 110 ± 3 nm; PDI < 0.1 by DLS). The structural integrity and component analysis is assessed by TEM and SDS-PAGE (*Figure 3.2-a, 3.2-b, 3.2-c*). The CD spectra of the Pdu BMC mainly consist of α -helix with peaks at 208 and 222 nm (*Figure 3.2-d*). This indicates that the component proteins are mainly α -helical as observed in crystal structures also. SDS-PAGE (*Figure 3.2-c*) for the same show the presence of major proteins from both categories, i.e., SPs and the enzyme(37,38,44). The thermal shift assay of the Pdu BMCs are carried out in the presence of SO. SO is a dye, which has higher fluorescence when present in the non-polar environment(153–155). *Figure 3.2-e* shows a weak fluorescence for SO in aqueous solution (orange curve), however, when mixed with Pdu BMC at a ratio of 1:5 (protein:dye), a 20-fold increase in fluorescence along with a blue shift in λ_{\max} (from 640 nm to 590 nm) is observed. This suggests the partitioning of the dye from the polar to the non-polar environment, indicating presence of hydrophobic patches on the surface of the BMC. Next, the thermal unfolding of Pdu BMC in the presence of SO is carried out from 15 to 95 °C. The signature curve for Pdu BMC is broad comprising of several transitions that corresponds to various protein components. This curve (*Figure 3.2-f*) initially shows a decrease in fluorescence with an increase in temperature from 15 to 40 °C, followed by a sharp rise, which continues till 55 °C. With the further increase in temperature,

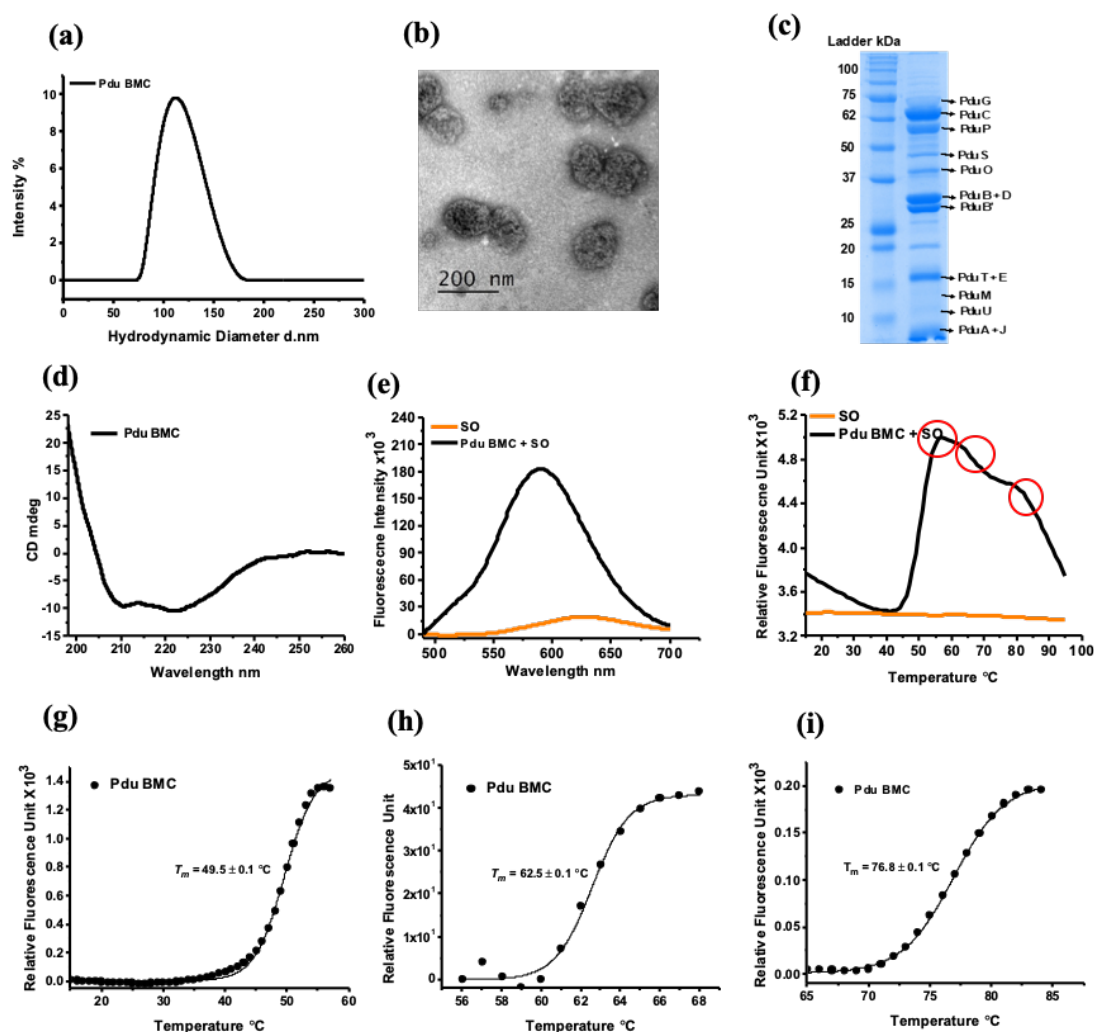


Figure 3.2: DLS of the purified Pdu BMC showing a size distribution of 110 ± 3 nm with $PDI < 0.1$ (a); TEM image for the Pdu BMC showing intact polyhedral structures (b); 12 % SDS-PAGE for Pdu BMC shows all the proteins as discussed in the pdu operon (c); CD spectra for Pdu BMC mainly contains α -helix (d); Enhanced steady-state fluorescence of Pdu BMC and SO mixture as compared to SO aqueous solution (e); Thermal unfolding of Pdu BMC by DSF shows a signature curve. More than one transition (regions with increased fluorescence, red circled) are observed, which represents the protein heterogeneity of Pdu BMC (f); The DSF curve for Pdu BMC is baseline corrected, and transition temperatures are determined after fitting it to Boltzmann equation. These transitions correspond to initial destabilization of intact BMC followed by unfolding of its component, i.e., enzyme cascade and shell proteins (g, h, and i) and finally their aggregation.

there is a gradual decrease in fluorescence, which continues till 95 °C. At around ~50, ~60 and ~80 °C slight enhancement in the SO fluorescence is observed. These regions are indicated by red circles in **Figure 3.2-f**. The curves for each of the transition are fitted as per the Eq. 1 (Boltzmann Fit) post baseline correction (**Figure 3.2-g,h,i**). From each of the fit, three indicative temperatures are determined: the onset of transition temperature (T_o), transition temperature (T_m), and aggregation temperature

(T_{agg}) (**Table 3.1**). T_o is the temperature at which the protein begins to unfold; T_m is the temperature where 50 % of the protein is unfolded. The T_m of a protein is related to its thermodynamic equilibrium between the folded and the unfolded state. T_{agg} is the temperature where aggregation begins to dominate over unfolding and denaturation, as indicated by a monotonous decrease in the SO fluorescence (hydrophobic patches get buried because of aggregation).

Table 3.1: Temperature for initiation of unfolding, unfolding temperature, and aggregation temperature in Pdu BMC and PduCDE

	T_{m1} (°C)	T_{m2} (°C)	T_{m3} (°C)	$T_{m@PduCDE}$ (°C)
T_o	40 °C	60 °C	71 °C	34 °C
T_m	49.7 ± 0.1	62.5 ± 0.1	76.8 ± 0.1	42.8 ± 0.3
T_{agg}	54 ± 2	66 ± 2	82 ± 2	50 ± 1

The first melting of the Pdu BMC, T_{m1} , is observed at 49.7 ± 0.1 °C (**Figure 3.2-g**). Interestingly, the catalytic activity of the Pdu BMC is significantly compromised beyond after this temperature (**Table 3.2**). It shows that the transition at this temperature results in the structural destabilization of the catalytic complex, which underscores the importance of this temperature in the structure-activity balance of the Pdu BMC(83,84,87). The structural destabilization is a result of the compromised interactions between the SPs and the enzyme clusters. For bare PduCDE, loss in enzyme activity is observed above 45 °C (**Table 3.2**) as compared to 55 °C in Pdu BMC. It shows the importance of the shell in rendering higher thermal stability to the encapsulated enzyme. This is probably because of the packaging and interaction of enzyme to that the SPs on the lumen side of the BMCs. Besides T_{m1} (49.7 ± 0.1 °C), two transitions in Pdu BMC at T_{m2} (62.5 ± 0.1 °C) (**Figure 3.2-h**) and T_{m3} (76.9 ± 0.1 °C) (**Figure 3.2-i**) are observed. These transitions correspond to the unfolding of Pdu BMC SPs, which is discussed in the later part of the chapter. It is important to note that the T_m value depends on the assembly of the protein, and thus, it is possible to obtain overlapping unfolding transitions in case of a multi-protein complex, which

are often difficult to analyze. Further each transition is associated with an aggregation that may overlap with the following transitions. This apparently leads to less exposure in the hydrophobic surfaces. Whether it is because of reduced exposure of hydrophobicity or because of the nature of the SPs present in Pdu BMC is not clear at this stage and can be understood better when individual SPs are studied.

Table 3.2: Diol-dehydratase activity for the Pdu BMC and PduCDE carried out by MBTH assay

S. No	Temperature (°C)	Pdu BMC Diol-dehydratase activity mol mg ⁻¹ min ⁻¹	PduCDE Diol-dehydratase activity mol mg ⁻¹ min ⁻¹
1	25	24.8 ± 0.3	23.1 ± 2.4
2	37	27.5 ± 1.3	24.1 ± 2.6
3	45	26.9 ± 1.0	12.9 ± 1.6
4	50	25.9 ± 1.5	1.5 ± 0.1
5	55	15.7 ± 0.3	ND

3.2.2 Thermal unfolding of PduCDE

Next, the thermal shift assay of the enzyme PduCDE is carried out. It is the main enzyme of the Pdu BMC and is involved in the oxidation of propane-1,2-diol to propionaldehyde. This trimer dimer complex (*Figure 3.3-a*) is mainly α -helical as observed by CD (*Figure 3.3-b*). Similar to our observations in the case of Pdu BMC, the interaction of PduCDE with SO also caused an enhanced fluorescence associated with a blue shift (*Figure 3.3-c*) indicating the presence of exposed hydrophobic patches on the protein surface (Observed in the crystal structure of the related diol-dehydratase (PDB ID: 1IWB) shown in inset of *Figure 3.3-c*). From the crystal structure, the exposed hydrophobic surface area is estimated at around ~24 % (*Table 3.3*). The DSF curve obtained for PduCDE (*Figure 3.3-d*) is similar to another globular protein (Lysozyme, *Figure 3.3-e*) and is narrow and sharp (broadens post initialization of aggregation because of simultaneous unfolding and aggregation

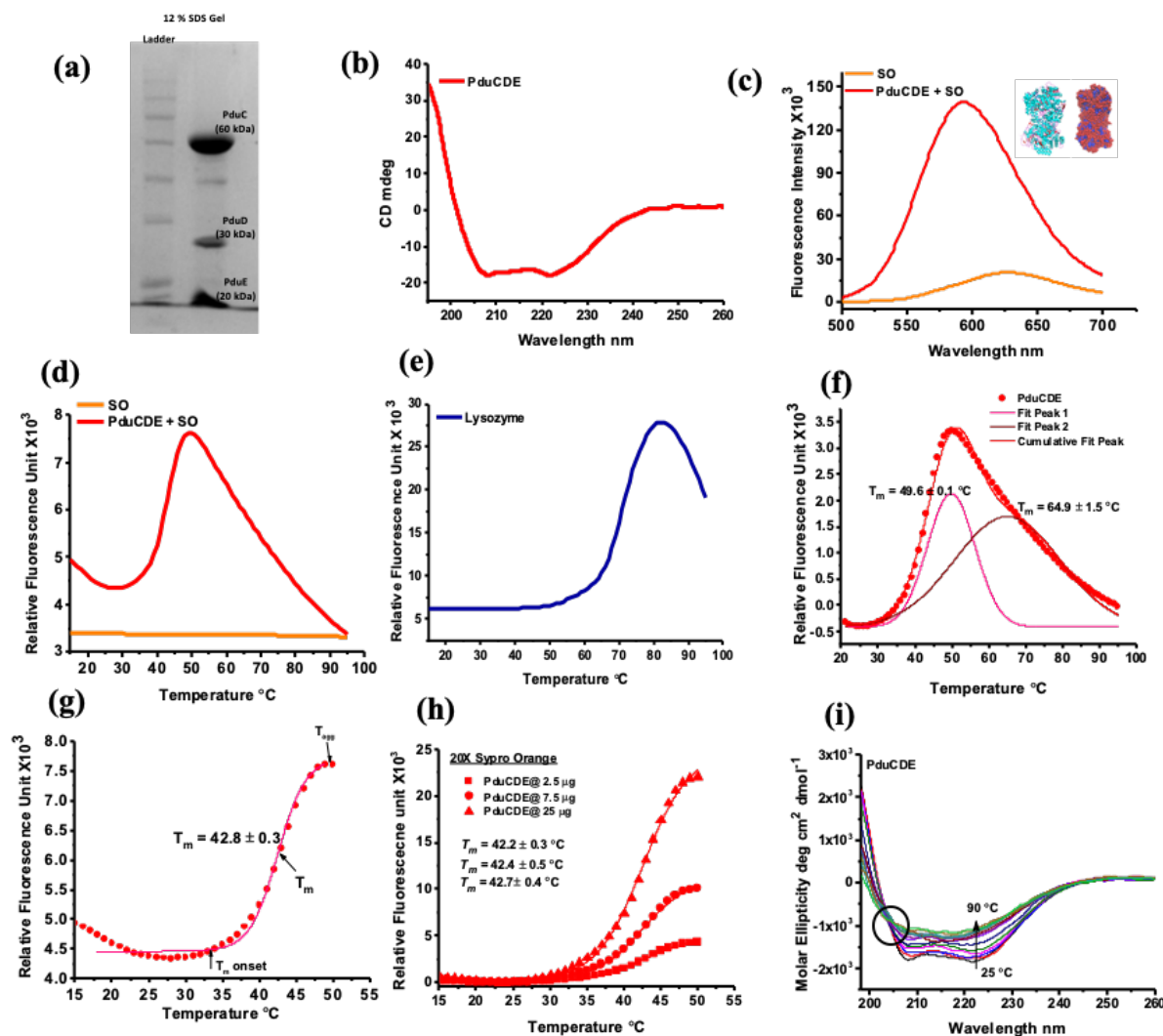


Figure 3.3: SDS PAGE for PduCDE showing the bands for PduC, PduD and PduE at 50, 30 and 20 kDa band positions (a); CD spectra for Pdu CDE having the signature alpha-helical structure with characteristic peaks at 208 and 222 nm (b); Binding of SO to the hydrophobic surface of the PduCDE results in enhanced SO fluorescence. The inset shows the crystal structure for the globular protein Pdu CDE (PDB ID- 1IWB), along with the distribution of hydrophobic and hydrophilic residues (Blue- Hydrophobic; Red-Hydrophilic) (c); DSF for PduCDE shows a very sharp signature curve (red curve) suggesting a homogeneous composition. It also shows that all the sub-units unfolds together (d); The thermal unfolding of lysozyme carried out by DSF (e); Multiple peak fit of PduCDE shows unfolding of native protein followed by unfolding of aggregates (f); Boltzmann Fit for the single transitions observed in PduCDE showing T_m around 42.8 ± 0.3 °C (g); DSF curve for PduCDE at three different concentration after baseline correction shows no shift in transition temperature. The dimer-trimer complex does not show any co-operative unfolding; instead, a single unfolding curve is observed, suggesting no self-assembly (h); Peltier based circular dichroism for PduCDE shows the change in the conformation of the protein as a function of temperature. The change in conformation shows one iso-dichroic point, which suggests that the unfolding is a two-state process with no intermediate (i).

observed by curve fitting, **Figure 3.3-f**), which supports the homogeneous assembly. The DSF curve also confirms that despite being a trimer-dimer complex, all the subunits of PduCDE unfold together. When the PduCDE DSF curve is fitted to Eq. 1 (**Figure 3.3-g**), the T_o , T_m and T_{agg} are observed at 33 ± 1 °C, 42.8 ± 0.3 °C and 50 ± 0.5 °C respectively. As shown in **Table 3.2**, the diol-dehydratase activity of the free enzyme is compromised above 45 °C. This observation is of importance because, in Pdu BMC, the diol-dehydratase activity is observed until 55 °C; thus, a 10 °C higher thermal stability as compared to the bare enzyme. It shows the importance of the Pdu BMC shell and the role of confined crowding towards rendering thermal stability to the encapsulated enzyme. A comparison of the DSF curve of the intact Pdu BMC and PduCDE also suggests that the T_{m1} observed in the Pdu BMC curve mainly corresponds to the destabilization and denaturation of the encapsulated enzyme. A concentration-dependent DSF study is also carried out to check if the stability is affected by the cooperativity of the oligomeric nature of PduCDE.

A ten-fold increase in the concentration does not shift the T_m from 42.8 ± 0.5 °C (**Figure 3.3-h**), nor does a four-fold increase in the SO concentration alters it. Thermal denaturation of the PduCDE probed by circular dichroism show an isodichroic point (black circle, **Figure 3.3-i**) suggesting that the thermal unfolding of the enzyme is indeed a two-state process without any intermediate. The T_m calculated by this method is 47.8 ± 1.1 °C, which is higher than the T_m observed in DSF. The main reason for this anomaly is that the two methods probe different aspect: while CD probes the secondary structure, the signal from DSF probes the disposition of the amino acids. The main aim for conducting the CD studies is to show the two-state nature of the unfolding process.

3.2.3 Unfolding signature of Pdu SPs

3.2.3.1 PduA and PduB: BMC domain protein

The SPs are the essential component of the Pdu BMC. They belong to the BMC domain protein family (Pfam00936)(93,156). These BMC domain proteins are flat, as observed in their crystal structures (hexamer and trimer, from various origins). In this study, two SPs are taken: hexamer (PduA) and trimer (PduB). The PduA and PduB SPs, when overexpressed (**Figure 3.4-a**) and purified, exhibit sheet in TEM

and show majorly α -helical structure in CD (**Figure 3.4-b**). Similar to Pdu BMC and PduCDE upon addition of SO to the SPs (PduA; (**Figure 3.4-d.i**) and PduB; (**Figure 3.4-e.**)) enhancement in the SO fluorescence is observed. An estimate of the exposed hydrophobic surface area for the proteins show around 25-30% of exposure (**Table 3.3**). Hence for all the proteins, the initial fluorescence should be similar. However, 4-5 times enhancement in SO fluorescence is observed for SPs compared to enzyme PduCDE or the intact Pdu BMC. The extended sheet of the SPs in the solution phase favors higher hydrophobic patches resulting in enhanced SO fluorescence. Generation of the electrostatic potential map by Pymol for the enzyme PduCDE and SP PduA shows that the SP has more hydrophobic patches as compared to the enzyme. This is because of the extended 2-dimensional sheets formed by PduA in contrast to the globular form of PduCDE (102,103,136). Next, the thermal scan of the SPs is carried out where the PduA (**Figure 3.4-d.ii**) and PduB (**Figure 3.4-e.ii**) are heated from 15 °C to 95 °C. Similar to the decrease in SO fluorescence for other proteins, SPs also show an initial decrease. It has been attributed to the quenching of the SO fluorescence due to solvent fluctuations. Following this decrease, there is a monotonous increase in the SO fluorescence, but this increase is relatively small compared to the increase in the enzyme PduCDE or the intact Pdu BMC. As the SO fluorescence correlates to the presence of hydrophobic surfaces, it can be inferred from the DSF curve of SPs that the hydrophobicity exposure for it is comparatively less as compared to the globular proteins or the Pdu BMC. It suggests that the hydrophobic core for the folded SPs is much weaker compared to the folded globular enzyme, which corroborates well with the available crystal structure of the SPs across different BMC.

These unique DSF curves for SPs post-baseline subtraction are observed with broad peaks (PduA and Pdu B) with multiple transitions (PduB)(151,157). The broad peak in the case of PduA (**Figure 3.4-d.iii**) is best fitted to two deconvoluted peaks (56.6 ± 3.6 °C and 69.6 ± 2.2 °C) whereas to four deconvoluted peaks in PduB (**Figure 3.4-e.iii**) (41.4 ± 0.8 °C; 53.6 ± 0.4 °C; 66.7 ± 1.5 °C; 76.1 ± 1.7 °C). For PduA, the peak at 56.6 ± 3.6 °C corresponds to an exposure of the buried hydrophobic core (major contribution), whereas the peak at 69.6 ± 2.2 °C is assigned to disassembly of formed aggregates. In the case of PduB, four different peaks are observed, the first one at 41.4 ± 0.8 °C, which has a minimal contribution and is due

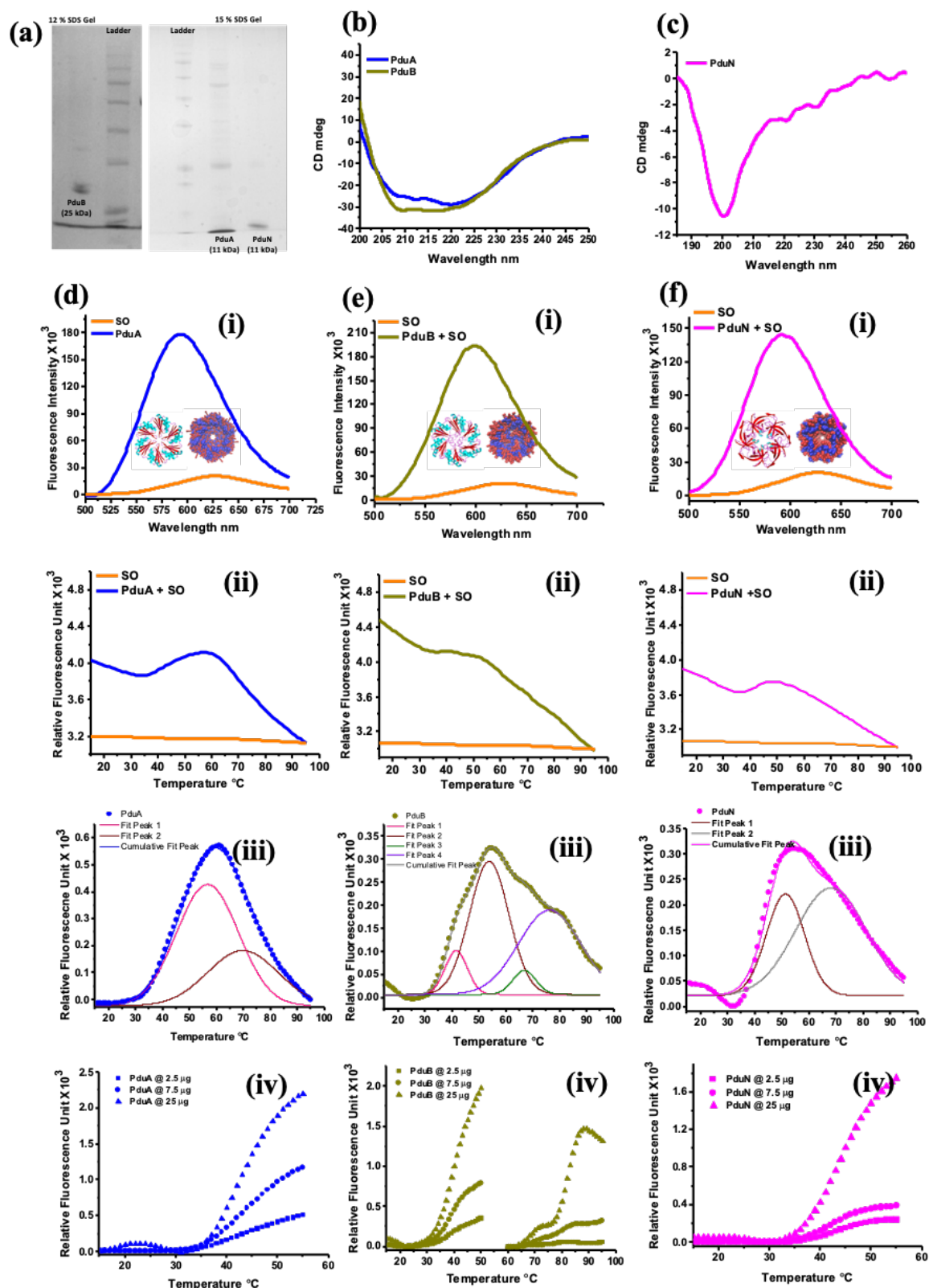


Figure 3.4: SDS PAGE for three different shell proteins of Pdu BMC which differ structurally (PduA (Hexamer) PduB(Trimer) and PduN (Pentamer) (a); CD spectra for the BMC domain protein (PduA and PduB) (b) and BMC vertex protein (PduN) (c). PduA and PduB are rich in α -helix, whereas PduN is mainly random coil; Binding of the dye to the hydrophobic surface of the folded and assembled sheet protein results in enhanced

fluorescence for SO as observed by steady-state fluorescence. It shows that in the solution phase, the shell proteins have hydrophobic regions (inset). Crystal structure for the proteins along with the distribution of hydrophobic and hydrophilic residues (Blue-Hydrophobic; Red- Hydrophilic) (Hexamer-PduA, (PDB ID- 3NGK) (inset of d-i), Trimer-PduB, (Modelled from PDB ID- 4FAY (inset of e-i), and Pentamer-PduN (Modelled from PDB ID-2RCF (inset of f-i)) DSF curve for different shell proteins present in the Pdu BMC shows that with increase in temperature there is decrease in the fluorescence probably because of the disassembly of the extended sheet (PduA, d-ii) (PduB, e-ii) and PduN, f-ii). DSF curve for PduA, PduB, and PduN are baseline corrected and fitted to multiple peak fit (PduA, d.iii) (PduB, e-iii) (PduN, f-ii). The peak positions are reported in Table 3.4; the DSF curve for PduA (d-iv), PduB (e-iv), and PduN (f-iv) at three different concentrations are baseline corrected, and transition temperatures are determined from the Boltzmann fit as per Eq. 1 and reported in Table 3.4.

to the higher-order assemblies. The major peak is derived at 53.6 ± 0.4 °C and 76.1 ± 1.7 °C, which can be due to exposure of the buried hydrophobic core. A small peak at 66.7 ± 1.5 °C is similar to the second peak of PduA (69.6 ± 2.2 °C) and also PduCDE and is assigned to the unfolding of formed aggregates. The peak at 76.1 ± 1.7 °C in Pdu B is due to higher-order assemblies or unfolding of formed aggregates. When the DSF curve is best fitted using Eq. 1 after baseline subtraction, the T_m for PduA (**Figure 3.4-d.iv**) is observed at 44.2 ± 0.2 °C, whereas for PduB (**Figure 3.4-e.iv**) three different T_m corresponding to 39.9 ± 0.2 °C, 67.1 ± 0.5 °C and 79.9 ± 0.2 °C are observed.

3.2.3.2 PduN: BMC vertex protein

Another important structural element of a BMC is the vertex protein that finally outfits the polyhedral structure. In the Pdu BMC, the vertex protein is PduN, which is a pentamer(94). The pentamer form of the protein at the vertex fits well in the folded hexamer/trimer conjugated extended mosaic sheet, thus lowering the rigidity and providing junctions of flexibility. The CD spectra for the PduN (**Figure 3.4-c**) in solution does not show any proper secondary structure, which is unlikely for any BMC domain protein. It can, however, be well correlated with the role it has to play. For maintaining a proper strain-free polyhedral structure, the vertex must be flexible and can only be achieved by conformationally flexible proteins. So PduN having conformational flexibility fits well with the BMC vertex protein. Report for the vertex protein EutN from Eut BMC, having a hexamer geometry is present in literature, which suggests the dynamic nature of vertex protein, i.e., switching from pentamer

Understanding the assembly of Pdu BMC

to hexamer and vice versa. Similar to other SPs, PduN also has exposed hydrophobicity, as demonstrated by enhanced SO fluorescence upon interaction (**Figure 3.4-f.i**). The thermal scan for PduN (**Figure 3.4-f.ii**) from 15 to 95 °C upon deconvolution provides two peaks (51.2 ± 0.5 °C, 67.9 ± 2.6 °C) (**Figure 3.4-f.iii**) and when fitted to Eq. 1, the observed $T_m = 42.5 \pm 0.1$ °C (**Figure 3.4-f.iv**) is recorded.

Table 3.3: Solvent accessible surface area (SASA) for the Pdu BMC domain protein (PduA and PduB), vertex protein (PduN), and Pdu BMC signature enzyme. Diol dehydratase (PduCDE)

	Hydrophobic SASA (Å ²)	Hydrophilic SASA (Å ²)	Total SASA (Å ²)
PduCDE	13074	39424	52498
PduA (Hexamer)	5709	15411	21110
PduB (Trimer)	5784	18071	23855
PduN (Pentamer)	5548	17824	23372

Table 3.4: Transition temperature for various SPs as determined by Boltzmann Fit. Various peak positions corresponding to various transitions in broad DSF curve are determined by multiple peak fit in origin 8.6

	PduA	PduB	PduN
T_m	44.2 ± 0.2 °C	39.9 ± 0.2 °C 67.1 ± 0.5 °C 79.9 ± 0.2 °C	42.5 ± 0.1 °C
Peak Fit	56.6 ± 3.6 °C 69.6 ± 2.2 °C	41.4 ± 0.8 °C 53.6 ± 0.4 °C 66.7 ± 1.5 °C 76.1 ± 1.7 °C	51.2 ± 0.5 °C 67.9 ± 2.6 °C

Interestingly, the transitions observed in SPs are also observed in the deconvoluted curves of the Pdu BMC, indicating that the SPs retain their structure in the Pdu BMC. The broad and multiple transitions in the SPs (PduA, PduB, and PduN) are indicative

of the different protein assemblies present and the aggregation events during unfolding. Earlier reports and light scattering experiments indicate very high polydispersity and suggest that these SPs exist in the dynamic oligomeric state. Like globular proteins, the SPs (PduA and PduN) did not show a change in the T_m with a ten-fold increase in the concentration. However, due to a higher propensity of self-assembly in PduB, SP results in increased T_m (77.9 ± 0.6 °C to 81.2 ± 0.1 °C) with a ten-fold increase in the concentration.

3.2.4 SPs differ from globular protein in morphology

An interesting finding of this assay is morphological difference between the SPs and the enzymes(11,14). First, the SPs have a very high initial fluorescence as compared to PduCDE because of the exposed hydrophobic surface (**Figure 3.5-a**). Second, in the case of PduCDE, a more significant enhancement in the SO fluorescence upon thermal denaturation is observed as compared to the Pdu BMC or individual SPs. In the case of Pdu BMC, a relatively higher increase in fluorescence during the first transition as compared to second and third transition suggest that the first transition is related to the destabilization of the compact hydrophobic core which is significantly contributed by the packing of the enzyme protein (as reported by BMC models). The transition for PduCDE is due to the hydrophobic collapse model required for a stable protein.

Though transition in Pdu BMC and PduCDE represent the exposed hydrophobicity but in case of Pdu BMC it arises because of unpacking of the enzyme cascade whereas for PduCDE it is due to protein unfolding. Thus hydrophobicity in the two cases arises through a different mechanism and are serving different purposes. Because of the assembly of the enzyme cascade inside the closed shell of Pdu BMC, a hydrophobic core is formed (**Figure 3.5-b**) and so it behaves like a globular protein. The hydrophobic burial in the case of SPs is less in comparison to Pdu BMC (**Figure 3.5-c**) because the latter comprises of the enzyme -cluster whose destabilization exposes hydrophobic surfaces. For SPs, the hydrophobic exposure on destabilization is small as they are flat (observed in crystal structures) in nature. This is further validated by increasing the SO concentration during an unfolding event where a four-fold increase of SO from 5X to 20X lead to two-fold enhancement in the fluorescence intensity for the enzyme PduCDE (**Figure 3.5-d**), however, in case

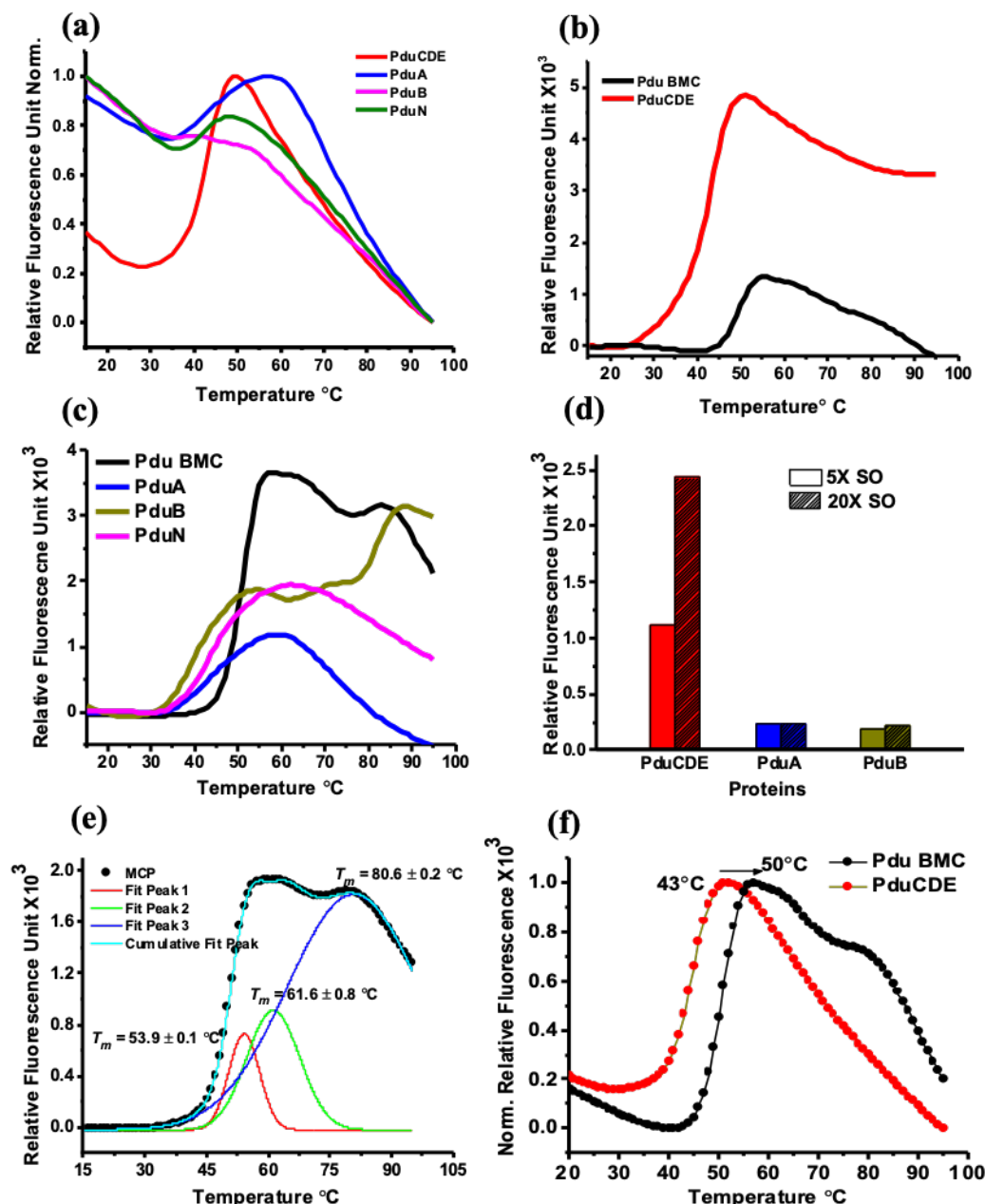


Figure 3.5: Normalized initial fluorescence (at 15 °C) for the proteins shows that shell proteins have relatively higher hydrophobic patches. The higher hydrophobicity is because of the flat SPs sheet with exposed surface (a); Buried hydrophobicity for Pdu BMC and PduCDE measured by relative change in the fluorescence intensity of SO as a function of temperature (b); Buried hydrophobicity for Pdu BMC as compared to shell proteins shows the efficient packing of the globular proteins inside the relatively flat sheet nature of shell proteins (c); Relative change in fluorescence intensity is higher for PduCDE as compared to shell proteins with increase in dye concentration from 5X to 20 X which suggest the rich hydrophobicity of PduCDE and relatively flat sheet nature of shell proteins(d); Best peak fit for Pdu BMC DSF curve in Origin 8.6 shows three different transition temperature at (53.9 ± 0.1 °C; 61.6 ± 0.8 °C; 80.6 ± 0.2 °C) (e); Over-layed DSF curve for Pdu BMC and PduCDE showing a shift in the temperature where hydrophobicity of the two is exposed (from 43 °C to 50 °C) suggesting that the shell proteins do provide stability to the encapsulated components (f).

of the SPs the signal is saturated. This suggests that the hydrophobic core for the SPs is small as compared to that of the enzyme PduCDE. The high initial fluorescence and minimal buried hydrophobicity observed in the case of SPs establish the morphology of the SPs as an extended flat sheet tending to self-assemble. The high hydrophobic burial in the case of PduCDE categorizes it as a globular protein.

3.2.5 SPs provide thermal stability to encapsulated enzyme

Analyzing the DSF curve suggests that the Pdu BMC destabilizes around 55 °C (*Figure 3.5-e*), resulting in loss of activity, as discussed earlier. The bare diol-dehydratase enzyme loses its activity around 43 °C. The higher stability of the BMC encapsulated enzyme is due to the robust nature of the SPs (*Figure 3.5-f*). The major destabilization peak for bare SPs (PduA- 56.6 ± 3.6 °C, PduB- 53.6 ± 0.4 °C, and PduN- 51.2 ± 0.5 °C) are observed in between 50-60 °C, the temperature around which Pdu BMC activity get compromised. It suggests that the loss in activity is due to the destabilization of BMC domain protein, which provides stability to the encapsulated enzyme. The flat sheet SP is also suitable for scaffolding and can thermally insulate the enzyme on its surface, which makes these SPs a novel biomaterials for varied applications.

3.2.6 Fate and structural stability of SPs in intact Pdu BMCs

The DSF findings on the intact Pdu BMC and its components are summarized to provide an insight into its intact assembled structure. SPs show a completely different signature curve compared to globular proteins. This kind of DSF signature is perhaps one of the earliest reports in the literature for this genre of BMC domain proteins. The high initial fluorescence of SPs immediately after interaction with SO indicates that there are exposed hydrophobic patches on the surface of the SPs (*Figure 3.6-a*). Interestingly, the percentage of exposed hydrophobic residues in both PduA and diol dehydratase enzyme are the same. However, the disposition of the exposed surfaces in both the proteins is such that in the case of the SPs, enhanced SO binding is observed compared to the enzyme. This kind of surface disposition has interesting physiological consequences. The exposed hydrophobic surface in diol dehydratase is probably involved in the interaction of enzyme units with the shell surface in the luminal side of the compartment for better packing. To have further insights, SO is

docked on to the SP PduA (PDB ID: 3NGK)(158,159)(Crystal structure is known for PduA and literature is available for the interaction of PduCDE with shell protein PduA)(160). In the docking studies, it is observed that per hexamer, there are 13 binding sites. Six SO bind to the concave side; one binds to the pore region whereas remaining bind at the edges. Interestingly, there are no SO docked on the convex side of the PduA protein. It indicates a greater extent of hydrophobic patches on the concave side of PduA compared to the convex side (**Figure 3.6-b**). As we see higher SO fluorescence in the protein alone compared to the intact Pdu BMC, our results indicate that the concave side faces towards the lumen of the Pdu BMC. If this is the case, then the concave side should be interacting with the enzyme cluster. Next, the PduCDE protein is docked on to the hexameric PduA using the ClusPro online server (158). It was observed that the enzyme docks onto the concave face of PduA (**Figure 3.6-c.i and ii**), which further suggests that concave side must be on the luminal side of the intact MCP.

The question arises if the SPs have exposed hydrophobic patches, what happens when the microcompartment is formed? In the native microcompartment structure, we see initial low SO fluorescence compared to the SPs alone, indicating that the presence of hydrophobic patches on the cytoplasmic side. With increase in concentration from 0.05 mg/ml to 0.8 mg/ml, there is a linear increase in the initial SO fluorescence indicating equal hydrophobic contribution from each of the Pdu BMC (**Figure 3.6-d.i and ii**). Earlier it has been observed that with destabilization of Pdu BMC there is increase in exposed hydrophobicity which suggest that during the genesis of microcompartment more of the hydrophobic surface of SPs faces the lumen side. To have an experimental verification, we heated the microcompartments to different temperatures ranging from 25°C to 90°C followed by cooling them to 15 °C. Post cooling, the thermal scan assay in the presence of SO (**Figure 3.6-e.i**) is carried out. It can be seen that the samples which are preheated below 50 °C, show an unfolding profile similar to that of untreated samples. However, post 50 °C, preheating results in very high initial SO fluorescence. These results indicate that the thermal insult of the Pdu BMC is not reversible once the luminal side of the microcompartment is exposed. The exposure of the luminal side is associated with high SO fluorescence (**Figure 3.6-e.ii**) as a non-linear curve is observed indicating that the hydrophobic

region of the SPs get buried during microcompartment formation with less of the hydrophobic surface towards the cytoplasmic side.

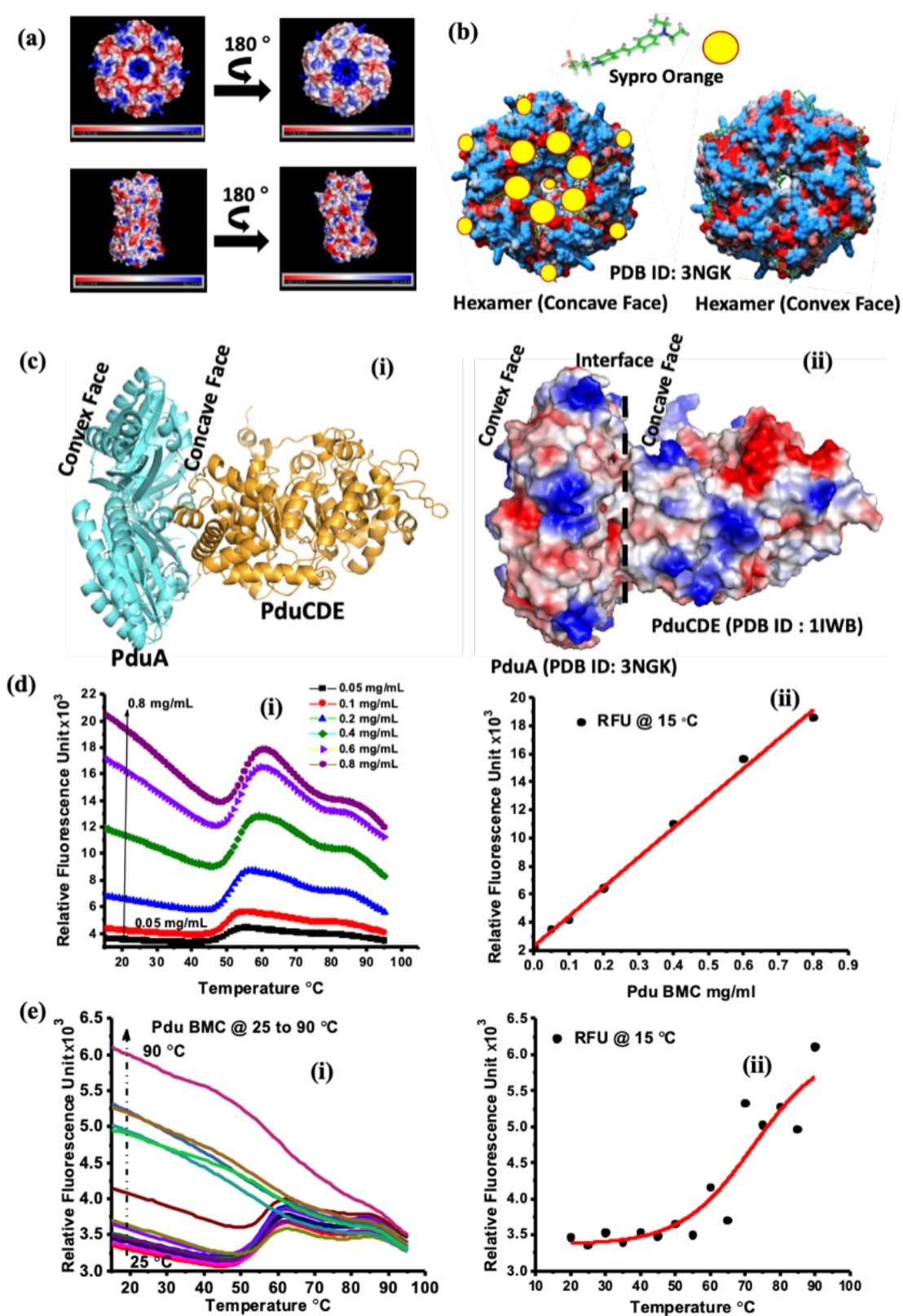


Figure 3.6: Electrostatic potential map of the shell protein PduA (PDB ID – 3NGK) and enzyme PduCDE (PDB ID – 1IWB) and generated by the Pymol software (a); (c); Docking

of hexameric unit of PduA and PduCDE with SO. Protein has been color-coded according to the hydrophobicity index. Blue is hydrophilic, and red is most hydrophobic with a transition colour of grey. In surface representation and SO represented as the ball and stick model with coloring the heteroatoms. Docking of hexameric PduA reveals around 13 potential SO binding sites, whereas PduCDE reveals around 12 potential SO binding sites. As the SPs further self-assemble as a sheet, thus creating a more SO binding site. Shown in the figure, both concave and convex surface SO binding sites. SO also binds at the junction of two monomeric units in the hexameric conformation (b); Docking studies of a hexamer of PduA and PduCDE using the ClusPro server. The images are generated using the Pymol software (c); Pdu BMC in its intact form behave as globular protein with exposed hydrophobicity on its shell surface which interacts at higher concentration resulting in the formation of pockets where SO binds and fluoresces (i). As the contribution from each of the compartment is equal there is a linear correlation (ii) (d); Thermal insults affect the stability of the BMC, and the buried hydrophobicity gets exposed. This shows that the though involved in the assembly of the intact compartment, but the individuality of the shell proteins is not lost with its genesis. With increase in temperature the enzyme cascade destabilizes and the shell proteins facing the luminal side having higher hydrophobicity is accessed by the SO resulting in enhanced fluorescence (i) which is having a non-linear correlation (ii) (e).

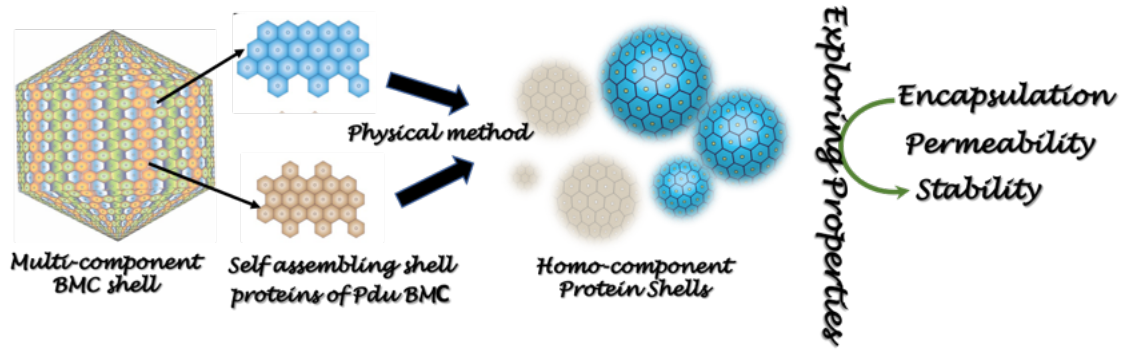
3.3 Conclusions

Inside a cell, there are several associations of macromolecules that work towards a particular metabolic goal. A proper balance of intra and intermolecular interactions is very crucial towards the proper functioning of these associations. Pdu BMC is one such complex multigene encoded prokaryotic organelle. The entire architecture of the BMCs are formed of two different genres of proteins: the enzymes residing in the central core and the exterior SPs that act as a semipermeable barrier to the essential metabolism of the BMCs. The solved crystal structures indicate the globular and flat nature of the enzymes and SPs, respectively. However, the factors that contribute to the stability of these proteins in the BMCs are not well understood. This work highlights the role of DSF for understanding the structure or functional alteration of BMC involving tertiary or quaternary structures. It is observed that the secondary structures in Pdu BMC are disrupted at higher temperatures. However, the activity of the enzyme is lost post disruption of the tertiary structure, indicating the importance of balanced interactions at the tertiary structure level to maintain the structure-activity relationships in these metabolosomes. For the first time, using a spectroscopic probe we have explored the solution-phase structure of any microcompartment. The thermal unfolding profile of the BMC domain proteins, are observed which differ from the enzyme proteins because of the morphological differences between them. These observations will also aid in developing quality control measures for the industrial application of this genre of proteins. The scaffolding nature of SPs, and their

capability to thermally shield the enzyme on its surface, makes them a novel material to be genetically engineered to produce a smart self-assembled natural polymer. Insights from this work will aid in the genetic and biochemical engineering of thermostable efficient enzymatic biomaterials can also be applied for assemblies created out of protein-polymer conjugates.

Chapter 4

Simplifying Pdu BMC as protein shells



4 Simplifying Pdu BMC as protein shells

4.1 Introduction

The previous chapter is focussed on understanding the forces that aid the assembly of Pdu BMC. The result suggests that the SPs have hydrophobic surface disposed towards the lumen of the MCP while, the more hydrophilic surface, face towards the cytoplasm. It is observed that the MCPs as a whole behave like a globular protein with a rich hydrophobic core contributed by the encapsulated enzymes. The surface facing the cytoplasm has more hydrophilic residues. The studies also show that the encapsulation imparts greater thermal stability to the enzymes beyond physiological range. The crystal structure of the SPs shows the hexamer or trimer units interacting along the edges to form 2D sheets (102,103,136). Further, the presence of channels promotes the movement of substrate, co-factors, and products in and out of the MCPs (37,43,119,161). Attempts to understand the functional role of individual SPs (**Table 4.1** gives an account of various SPs of Pdu BMC and its functional role) either through gene deletion or through point mutations had been made. For example, a $\Delta pduA$ mutant forms porous enlarged MCPs, whereas in $\Delta pduAB$ or $\Delta pduB'$ mutant no MCPs are formed. Both the PduA and PduB proteins are known to form faces of the MCP. The deletion of the PduJ protein ($\Delta pduj$) which is known to form the edge of the MCPs results in highly elongated structures. When the vertex protein, PduN is deleted, ($\Delta pduN$) MCPs with variety of morphology (elongated, enlarged, aggregated, rounded) are observed. The deletion of the PduM gene leads to the formation of unstable MCPs (37). The location of the gene also influences the interactions among the BMC proteins and is critical for the higher-order structure and assembly and also dictates their function in the BMC as demonstrated for *pduA* and *pduJ* genes in the operon (120). The mutation of individual amino acids also had a profound physiological consequence. For example, in PduA, the residues K26, N29, and R79 are found crucial for the stability of the Pdu BMC. PduA[K26A] variant did not yield any MCP suggesting its role in stabilizing the protein sheet forming the shell of the Pdu BMC(101). Point mutations in N terminal of PduB' leads to MCP shell depleted of core enzymes suggesting the role of SPs towards interaction and packing of the enzymes. Point mutation not only

alters the morphological of Pdu BMC but also its physiology such as transport of substrates, factors, and co-factors. E.g., a point mutation in central pore region of PduA SPs i.e., PduA[S40L] and PduA[S40GSG] results in reduced movement of the substrate, 1,2-PD because of an energy barrier for its diffusion (119) across pore. The altered growth is also observed in PduA[K37A] and PduA[K55A] because of the altered permeability of 1,2-PD. However, large substrates are capable of moving through these mutant MCPs, suggesting either other conduit channels or having specialized SPs with pores that can open or close under the specific trigger. In Eut BMC, the SPs EutL and EutM are similar in structure but differ in their pore properties under specific stimulus such as exposure to zinc ions promote opening of EutL pore (162). However, in none of these genetic engineering studies it is observed that a morphologically complete/incomplete MCP is functionally inactive. This indicates that whenever a native or mutant MCP is formed *in vivo*, the structure adapts itself in such a way that it is functional. This means the existing structural components adjust themselves in a way to allow the passage of the essential substrates and cofactors to maintain minimal MCP activity. This makes very challenging to study the properties of the individual SPs *in vivo*. Hence, it becomes important to devise a protocol *in vitro* that studies the properties of the SPs. This is the main focus of the present chapter.

Table 4.1: SPs of Pdu BMC and their percentage distribution

	% protein content Pdu BMC	% protein among SPs	Role
PduA	7.5	15.6	Face protein
PduB	12.8	26.6	Face protein
PduB'	12.1	25.1	Face protein
PduJ	11	22.8	Edge Protein
PduK	1.6	3.3	Edge Protein
PduT	1.6	3.3	Transporter protein
PduU	1.5	3.1	Transporter protein
PduN	ND	ND	Vertex protein
PduM	ND	ND	ND

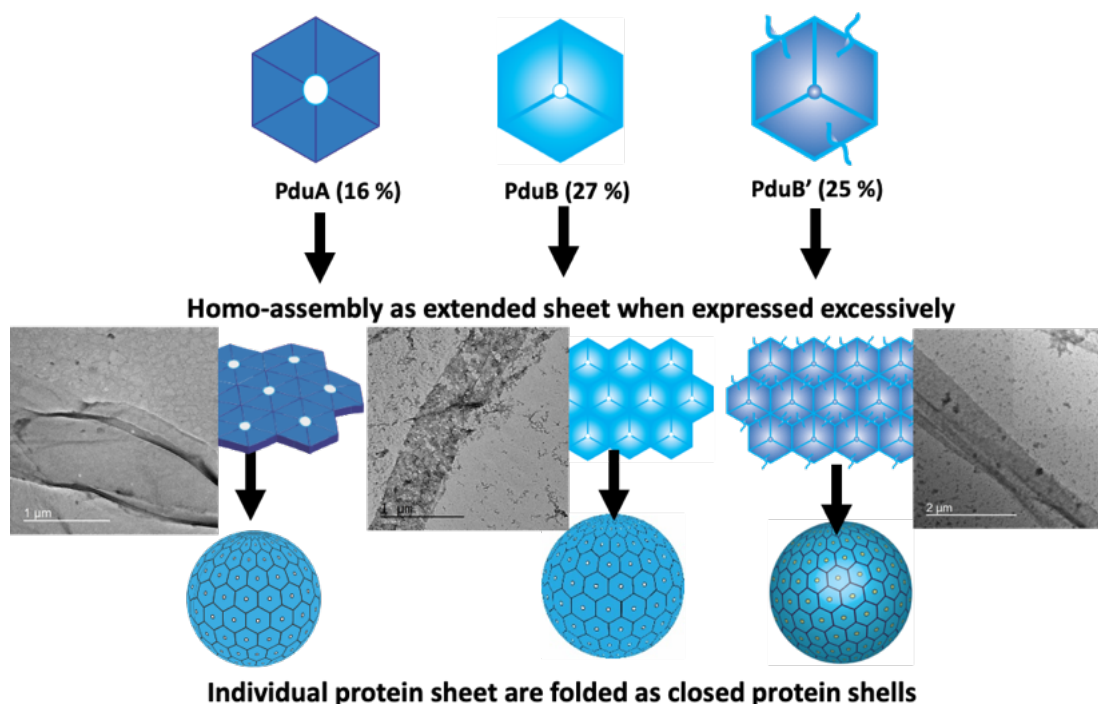


Figure 4.1: The hexamer or the trimer units of SPs (*PduA/PduB/PduB'*) interact along the edges through ionic interaction and form an extended 2D sheet as observed in TEM images and also modelled. Using Pickering emulsification, these 2D sheets are folded to fabricate PSs.

It is well established in reports that the SPs form extended sheets when expressed in bacterial overexpression systems. In this chapter, I have attempted to fold these sheets in closed shell like structures with the hypothesis that these closed shells would behave like a microcompartment with a single component. These single component simplistic model of the MCP are next tested for the exploration of the properties related to stability, diffusion and encapsulation. The protein compartments are fabricated based on principle of Pickering emulsification and are referred as Protein shells (PSs). Chemical treatment or harsh fabrication step is avoided to retain native conformation of the SPs in these PSs. These PSs proved to be suitable *in vitro* model for studying SP features. The conduit channels present in the SPs provide an added advantage for exploiting these PSs as active cargo carriers and bioreactors. Once fabricated, these protein compartments, besides being explored for studying their inherent properties, may also be explored for various applications as discussed. This chapter, through experiments such as native and non-native enzyme encapsulation and permeability of small molecules across SPs conduit, provides lead towards the development of active bioreactors, which needs precise compartmentalization.

4.2 Results and discussion

4.2.1 Fabrication and characterization of *in vitro* protein compartments

Pdu BMC SPs (PduA/B/B') under *in vitro* expression form 2D sheet as observed by AFM (**Figure 4.2-a**). With slight changes in pickering emulsification method which had been instrumental for fabricating proteinosomes, the PS formation by three different sheet forming proteins is carried out as per the scheme provided in **Figure 2.1**. The individual SPs in the aqueous phase are mixed with the oil phase (2-ethyl-hexan-1-ol) by gentle mixing for 1 min and allowed to stand for 45 min at room temperature. The oil and aqueous phase separate with a distinct layer of protein structure at their interface. The oil phase is removed and the protein layer at the interface is carefully collected and transferred to ethanol (dialyzed) to remove any associated residual oil followed by aqueous dialysis to remove ethanol. The PSs are fabricated at varying SPs concentration (0.25 to 1 mg/ml) and also changing water:oil ratio (0.02 to 0.08). It is observed that with varying SP concentration, the yield of PSs changes, whereas the water:oil ratio is optimized at 0.06 as a higher ratio leads to unambiguous separation of two phases. SPs concentrations beyond 1 mg/ml are not explored as they tend to form various nanostructures beyond this concentration. The optimized water:oil ratio (0.06) had also been observed by others while fabricating protein compartments with BSA. Initially the fabricated PSs are characterized by DLS, and the intensity % is plotted against the hydrodynamic diameter (**Figure 4.2-b**). When SPs distribution is assessed by DLS and compared to PSs, it is observed that for SPs two (PduA, 100-200 nm and 400-700 nm) or more than two (PduB, 10-50, 100- 200 and 400-700 nm) distribution is observed whereas in case of PSs only one size distribution (1-2 μm) is observed. The broad size distribution in SPs is due to their self-assembling nature in the solution phase, which, when fabricated assembles to form PSs in micron range as observed above.

Next, to observe the morphology of the PSs, imaging techniques such as Fluorescence Microscopy (FM), SEM and AFM are employed. For observing under FM, Texas Red NHS ester tagged SPs are used for the fabrication of PSs. Under FM, the PSs are observed as spherical bodies (**Figure 4.2-c**); in contrast, the SPs can be seen as non-spherical extended assemblies. The SEM images, as shown in **Figure**

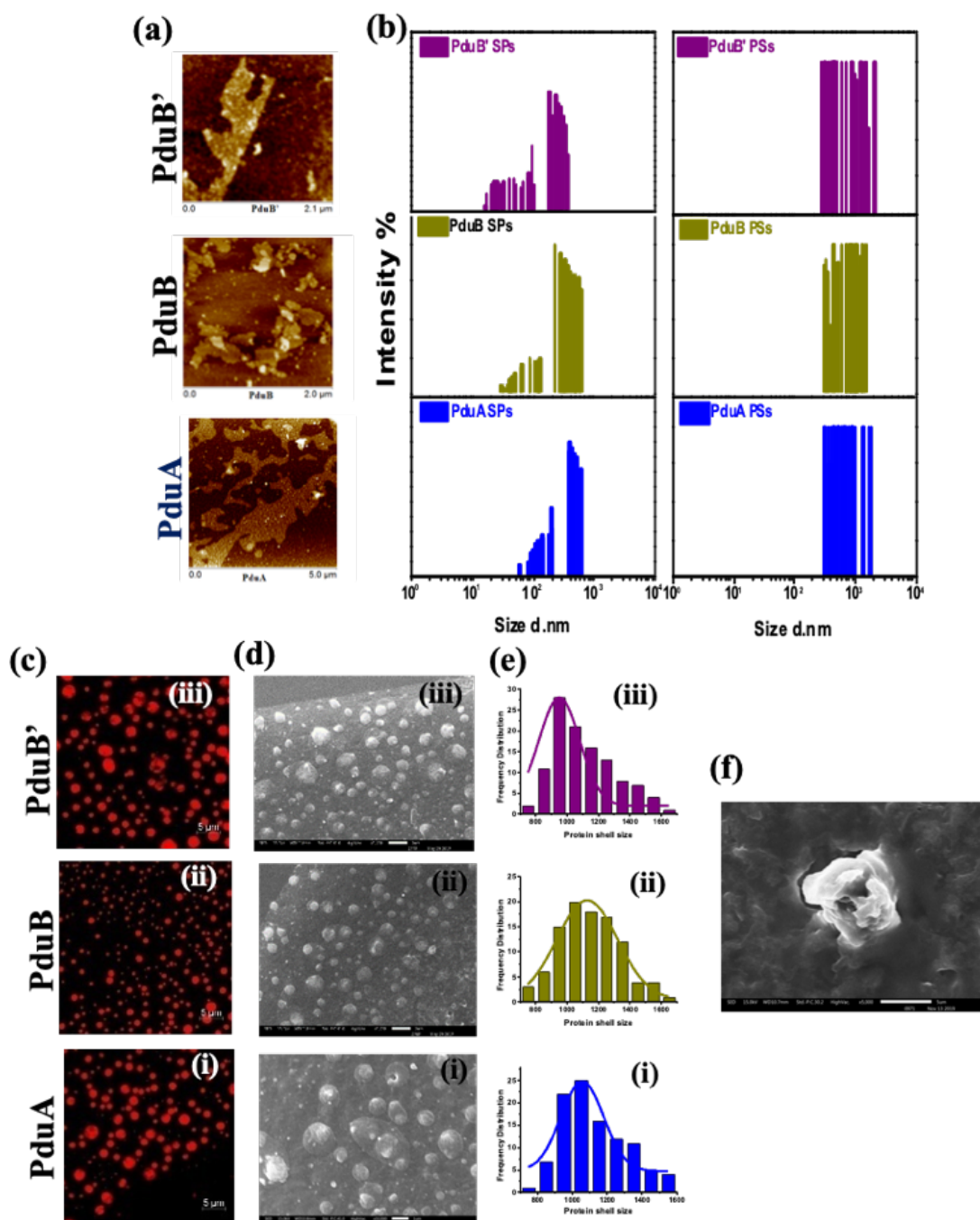


Figure 4.2 : Self-assembly of adjacent hexamer/trimeric units of the Pdu BMC SPs(PduA/B/B') as a 2D sheet (a); The SPs are dynamic in nature and self-assemble as an extended sheet in solution phase which can be well observed in DLS with a broad size distribution. PSs fabricated from the SPs mainly contains higher size distribution with missing smaller size fraction suggesting their assembly during fabrication (b); CLSM images of the PSs fabricated from Texas Red NHS ester tagged SPs as polydisperse spherical bodies (observed in red channel) (c); Spherical PSs for the SPs of PduA (i), PduB and PduB'(iii) observed in SEM (d); The average size distribution for the PSs as assessed by SEM are around 1000-1500 nm (e); SEM image for the PS fabricated from the K26A protein, mutated form of PduA (f).

4.2-d, are spherical as compared to the extended protein sheet of SPs, suggesting that fabrication brings assembly and folding of sheets as spherical bodies. From the SEM images, the overall distribution and average size of the different PSs are estimated and are shown in **Figure 4.2-e** and reported in **Table 4.2** (100 PSs from the 5 different frames of SEM micrographs of three different set of samples are measured for determining the average size distribution). The method for fabrication of PSs avoided any chemical crosslinker and is expected to be mainly driven by the self-assembling property of the SPs. To justify this, a mutated variety of PduA, PduA[K26A] that does not form extended sheet, is checked for fabricating PSs. As expected this mutant does not form shell like structures (**Figure 4.2-f**).

Table 4.2: The average size distribution of the PSs fabricated from three different SPs as observed by SEM

Shell Protein	Size of protein shells (Mean \pm SE) nm
PduA	1086 \pm 184
PduB	1127 \pm 195
PduB'	950 \pm 130

4.2.2 Stability studies of the PSs

Post-fabrication, the secondary structure estimation of the PSs is carried out through CD and compared with the native SPs. The secondary structure components viz. α -helix and β -sheet are similar in both PS and SPs indicating that the *in vitro* fabrication process does not denature the SPs (**Figure 4.3-a.i to iii**) (**Table 4.3 and 4.4**). By monitoring the change in the ellipticity with an increase in temperature using CD, the thermal stability of the SPs and PSs are compared. For all the SPs and their respective PSs, a gradual decrease in ellipticity is observed with increasing temperature, except for PduB' PS. The temperature versus molar ellipticity (at 222 nm) plot is fitted to a Boltzmann fit (Equation 1). All the PSs show a higher T_m compared to the respective SPs (**Figure 4.3-b to e; Table 4.5**). A shift of +8 °C and +17 °C in the T_m of the PduA and PduB PSs is observed as compared to the T_m of their respective SPs. For PduB' SP as there is no decrease in ellipticity with temperature, the T_m could not be

determined (Figure 4.3-b to e). The higher stability of PduB' PSs can be due to the presence of extra 37 amino acid at the N terminal (but this need to be investigated).

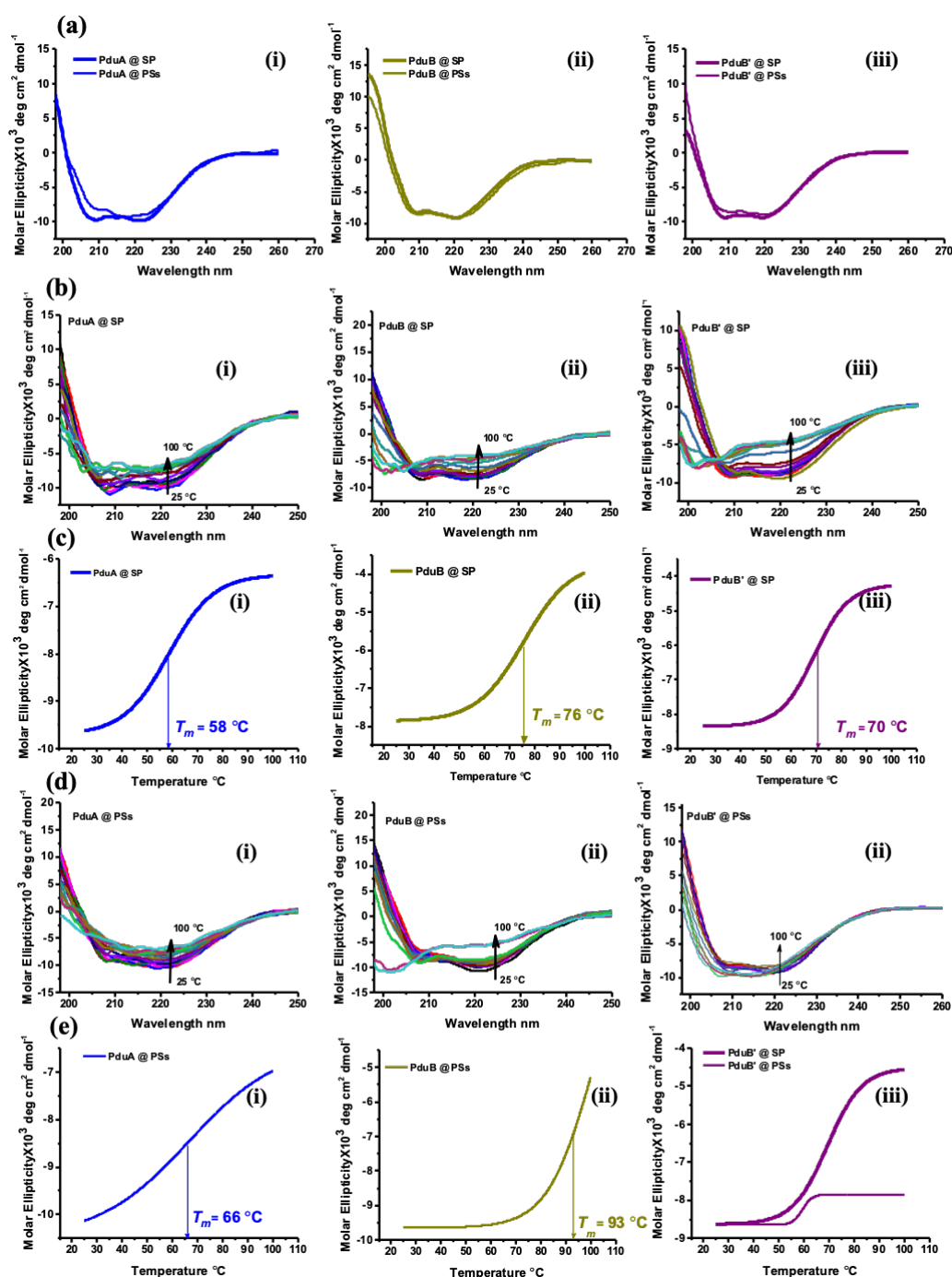


Figure 4.3: CD for the fabricated PSs does not show any change in their secondary structure as the two spectra overlay. No change in the characteristic α -peak at 222 or 208 nm is observed after PSs formation. When estimated by K2D3 for the secondary structure content, the SPs and the PSs have the similar α -helical content. (a); Temperature-dependent CD for the SPs (b) and the PSs (c) shows the conformational stability of the proteins. Secondary structure conformation is not lost during the fabrication of PSs from SPs. The PSs formed due to self-assembly of SPs further add on to the thermal stability of the protein compartments.

Table 4.3: % Distribution for the secondary structure component (α -helix and β -sheet) of major SPs of Pdu BMC and their derived PSs as determined by K2D3.

	PduA		PduB		PduB'	
	SP	PSs	SP	PSs	SP	PSs
α -Helix	93.2	93.1	86.2	86.12	83.9	83.9
β -sheet	0.11	0.11	0.74	0.71	1	1.04

Table 4.4: % Distribution for the secondary structure component (α -helix and β -sheet) of pre-melt PSs and post melt PSs determined by K2D3.

	PduA		PduB		PduB'	
	Pre melt PSs	Post Melt PSs	Pre melt PSs	Post Melt PSs	Pre melt PSs	Post Melt PSs
α -Helix	93.2	93.1	86.12	86.1	83.9	83.2
β -sheet	0.11	0.11	0.71	0.65	1.04	0.85

Table 4.5: The thermal stability of PSs is higher as compared to individual SPs

Proteins	SP T_m	PS T_m	ΔT
PduA	58 \pm 1 $^{\circ}$ C	66 \pm 2 $^{\circ}$ C	8 $^{\circ}$ C
PduB	76 \pm 2 $^{\circ}$ C	93 \pm 3 $^{\circ}$ C	17 $^{\circ}$ C
PduB'	70 \pm 1 $^{\circ}$ C	ND	ND

Besides thermal stability, conformational reversibility is also observed in the SPs, which are used for the fabrication of PSs. The higher stability and conformational stability imply that the PSs fabrication have no damaging effect on the SP's native secondary structure. The higher stability of the PSs derived from SPs also suggests

the role of assembly and scaffolding behaviour in imparting stability(122,163–165). The structural stability observed in all the PSs, assures the conservation of the intrinsic properties such as enzyme immobilization, encapsulation, channelling of the substrate, cofactors, and products, etc. of the SPs in the *in vitro* PSs.

4.2.3 PSs behave as an active bioreactor

4.2.3.1 Encapsulation of the enzyme cargo

The objective of this work aims to fabricate single protein component closed shells that would behave like a microcompartment. Thus after fabrication of hollow PSs from the SPs of Pdu BMC *in vitro*, to warranty that these single protein component PSs behave as broad range microcompartment both native (PduCDE) and non-native enzyme (CytC) are encapsulated and are checked for their enzyme activity. Before proceeding for encapsulation, the physical mixture (PM) of dye labelled SPs {PduA/B/B' are labelled with Texas red (red channel)} and the enzyme PduCDE {labelled with Alexa488 (green channel)} are observed under CLSM for interaction and co-localization. **Figure 4.4-a** shows PduCDE distributed all along the SPs surface indicating interaction of the duo. The PM for the same is made to fabricate enzyme encapsulated PS as per scheme provided in **Figure 2.2**. Post fabrication the enzyme encapsulation within the PSs is confirmed by confocal microscopy and FRET studies. The CLSM images in **Figure 4.4-b** shows that the SPs (red channel) makes a rigid boundary around the enzyme (green channel). The inherent scaffolding nature of the Pdu BMC SPs can be observed in these *in vitro* enzyme encapsulated PSs, as dye tagged SPs are making the external periphery. The edges seem to be more rigid as compared to the core, which is fluidic. The stable SPs plays a significant role in imparting closed environment to the enzyme encapsulated in the PSs. For the FRET studies, the SPs and enzymes are labelled with Cy3 and Cy5 dyes using NHS ester chemistry. The FRET profile for the physical mixture of the SPs with the enzyme PduCDE shown in **Figure 4.4-c**. A weak emission at around 660 nm is observed for Cy5 in the physical mixture. In the enzyme encapsulated PSs four times higher emission for Cy5 is observed when excited for Cy3 indicating a

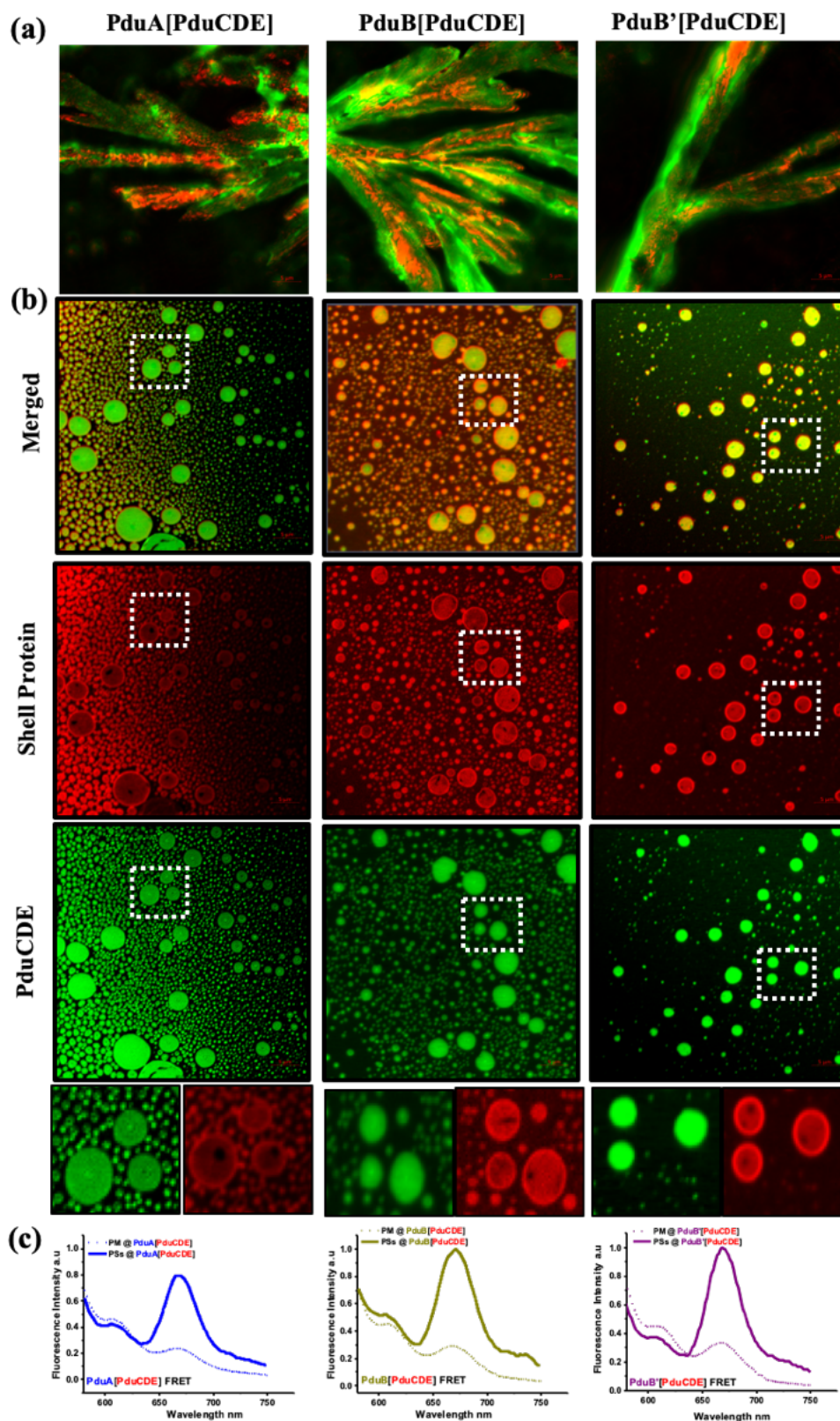


Figure 4.4: A physical mixture of dye-labeled PduCDE (Alexa 488) and SPs(PduA/B/B') (Texas Red) shown as fluorescent images proves the interaction of the enzyme with the SPs. As these SPs tend to self-assemble, they can be seen as an extended sheet in the microscopic images (a); CLSM images for the enzyme encapsulated PSs. SPs are labeled with Texas red NHS ester (Excitation laser 594, red channel), whereas the enzyme is labeled with Alexa 488 NHS ester (Excitation laser 594, green channel) observed in red

and green channel. The merged channel shows the co-localization of the two. In b, the lowermost panel shows a small section zoomed in where a rigid shell boundary can be observed (b); Co-localization of enzyme and the SPs in the PS is confirmed by FRET study. For FRET-based co-localization, shell protein is tagged with Cy3 NHS ester, whereas enzyme is tagged with Cy5 NHS ester. Upon excitation of SP at 550 nm because of the co-localization of enzymes within the periphery, we observed an emission for the cy5 labeled enzyme at 670 nm. For the PM, the FRET signal obtained (dotted lines) is less as compared to the encapsulated system (c); Scale bar in all the images is 5 μm .

stronger FRET in PSs compared to the PM. It reinforces that fabrication and encapsulation in a closed compartment bring better packing of cargo.

Following the studies with the native enzyme, a non-native enzyme (Cyt-C) is encapsulated inside the PSs. **Figure 4.5-a** shows co-localization and encapsulation of Cyt-C within the PSs by confocal microscopy. The enzyme encapsulation within PSs *in vitro* suggests that the encapsulation is more of a stochastic process and is not driven by any specific protein-protein interaction. It also shows that characteristic feature of these unique category of SPs to act as scaffold for enzyme immobilization and encapsulation. In general high thermal stability of the SPs (as observed in earlier section) along with their scaffolding nature makes them an important category of biomaterial for encapsulating thermolabile encapsulant.

4.2.3.2 The activity of the enzyme cargo

CLSM and FRET studies show that the enzymes are encapsulated within the PSs. Next, the activity of the encapsulated enzyme is carried out using standard enzyme assay. Initially, the enzyme activity of the PduCDE is checked in the PM by using the MBTH assay (**Figure 4.5-b**). Both the PM and the pure enzyme show similar activity. It is important to note here that the fabrication methodology does not alter the conformation of the enzyme as seen in CD spectra of the pure enzyme in buffer and in oil phase (**Figure 4.5-c**). We also checked the enzyme activity of the enzyme PduCDE in the oil phase by the MBTH assay where propionaldehyde formed is measured as a function of time (enzyme assay is performed as per the method discussed in chapter 2). It is observed that the catalytic activity of PduCDE in native form or when mixed with oil phase (**Figure 4.5-d**) (the enzyme protein makes a thin film at the oil-water junction which is separated and evaluated for enzyme activity) saturate at 20 min. A decrease in absorbance at 305 nm corresponding to product formation is observed for PduCDE in the oil phase, that can be due to loss of enzyme during fabrication. The catalytic performance of the encapsulated enzyme is

measured and is compared to the free enzyme under different conditions (*Figure 4.5-e*).

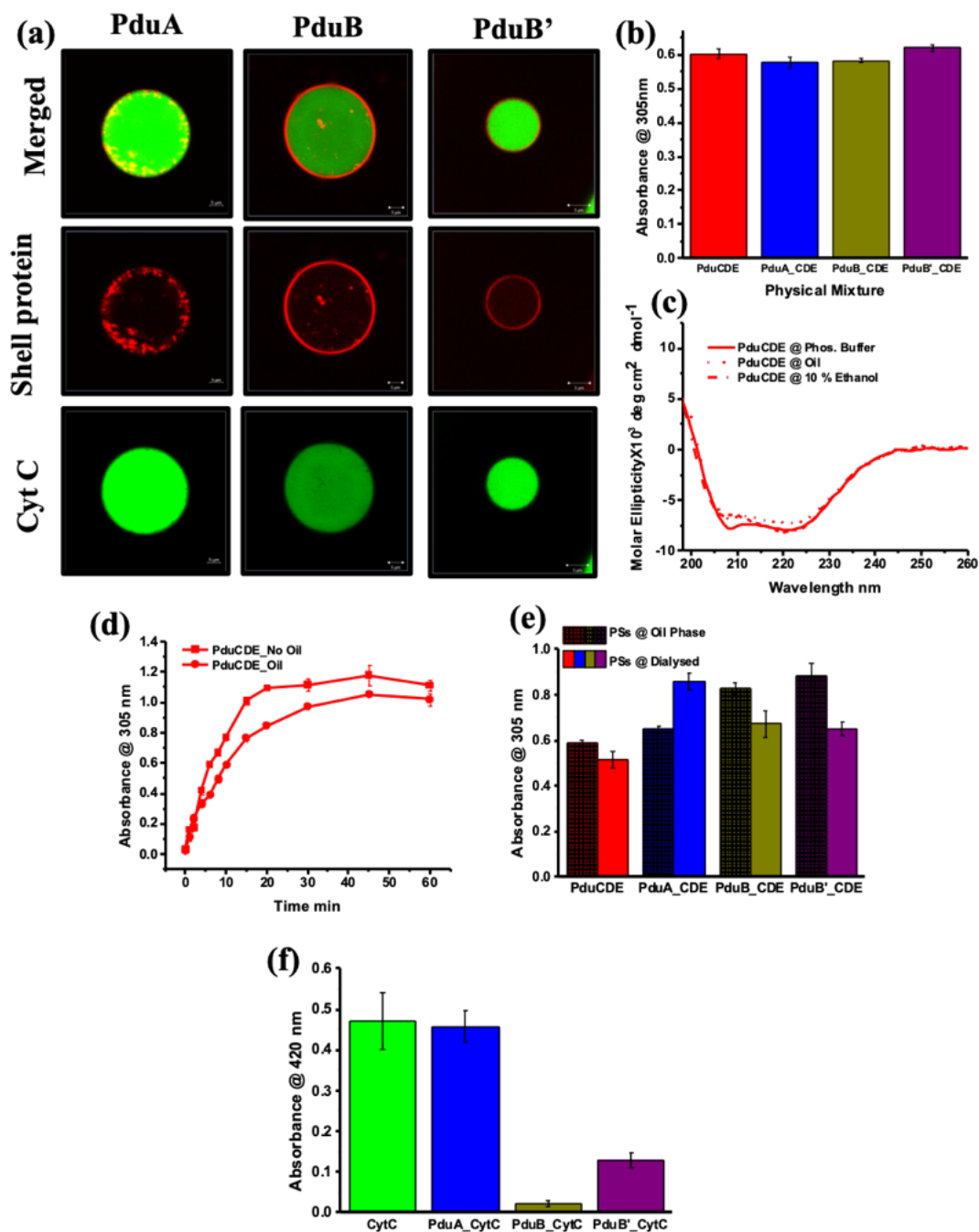


Figure 4.5: CLSM images for the non-native enzyme (CytC; labeled with Alexa 488 NHS ester) encapsulated PSs (a); MBTH assay of the enzyme PduCDE present in the PM with SPs PduA/B/B' (b); CD spectra for the PduCDE in phosphate buffer, oil and 10 % ethanol shows no change in the conformation (c); The MBTH assay for the PduCDE in oil phase is similar to the native one (d); PSs behave as active bioreactor and convert the 1,2-PD to propionaldehyde which is estimated by MBTH assay (e). Conversion of pyrogallol to phloroglucinol carried out by CytC is measured at 420 nm in the enzyme encapsulated PSs of PduA/B/B' (f). Scale bar for the confocal images is 5 μ m.

The catalysis performed by the encapsulated enzyme it is better than that of the bare enzyme emphasizing the importance of compartmentalization towards enhancing the catalytic efficiency of enzymes. These results also indicate that the substrate (1,2-PD), and co-factor, i.e., Vit B₁₂ can transfer freely across the PS barrier. A higher or similar activity of the encapsulated enzyme in PSs (PduA[PduCDE]; PduB[PduCDE]; PduB'[PduCDE] is observed. PSs provide a suitable environment to the encapsulated enzymes as higher product formation is observed.

The CytC encapsulated in the PSs is also assessed for its activity by a standard assay as discussed in chapter 2. The formation of phloroglucinol from pyrogallol is measured in the presence of H₂O₂ at 420 nm. A higher phloroglucinol formation is observed in the case of PduA[CytC] as compared to PduB[CytC] and PduB'[CytC] PSs (**Figure 4.5-f**). It is probably because of the higher permeability of pyrogallol to the PduA PSs as compared to PduB and PduB' SPs. The higher permeability can be because of the structural complementarity of pyrogallol to propanediol (having 3 and 2 hydroxyl groups, respectively). Affinity of hydroxyl for the PduA central pore might be facilitating higher transport resulting in the higher conversion rate to phloroglucinol from pyrogallol for the PduA[CytC] PSs ($12.7 \pm 0.1 * 10^6$ M/min) as compared to PduB[CytC] ($4.3 \pm 0.8 * 10^6$ M/min) and PduB'[CytC] ($2.1 \pm 0.1 * 10^6$ M/min) PSs. The similar catalytic activity for PduA[CytC] PSs ($12.7 \pm 0.1 * 10^6$ M/min) as compared to the native CytC ($10.9 \pm 0.2 * 10^6$ M/min) suggest that SPs do not impede the activity of non-native enzyme also. The SPs are capable of encapsulating both native and non-native enzymes, but once encapsulated, the selectivity of the conduit towards substrate governs the catalytic activity of the encapsulant. It also suggests that the though SPs have similar geometrical structures or the tendency to self-assemble, but they differ among themselves at the molecular level interactions with the substrates, factors, and cofactors.

4.2.4 Permeability of the PSs

The PSs are behaving as an active bioreactor, and that is possible only if they allow the movement of both substrate and co-factors. In this regard, permeability of PSs is assessed across the known conduit channels for a native cofactor, i.e., Vit B₁₂. It is important cofactor for the activity of the diol-dehydratase enzyme. Based on the dialysis method, saturation in the uptake of VitB₁₂ is observed for the PSs whereas

the uptake rate is prolonged ($13.1 \pm 6 \text{ h}^{-1}$ for PduA, $25.1 \pm 14 \text{ h}^{-1}$ for PduB, $11.9 \pm 4 \text{ h}^{-1}$ for the PduB') (**Figure 4.6-a**) for the SPs in their native form. The PSs in all the cases show a similar uptake rate of $2.4 \pm 0.2 \text{ h}^{-1}$ for PduA, $2.2 \pm 0.1 \text{ h}^{-1}$ for PduB, and $2.9 \pm 0.6 \text{ h}^{-1}$ for PduB' (**Figure 4.6-b**). A 6-10 times faster uptake in the PSs as compared to SPs suggests the role of compartmentalization of the SPs in channelizing the cofactor and thus supporting better catalytic efficiency observed in the encapsulated system as compared to free enzymes. Interestingly no major difference in the uptake across PduA, PduB or PduB' PSs is observed, and this can be the reason earlier researchers in the field of BMC had observed that even a mutant MCP with compromised morphology are functionally active. It is because the mutated structure adapts to get a functional form *in vivo* so that it allows the passage of the essential substrates and cofactors to maintain minimal MCP activity.

For establishing that PSs are permeable to both native and non-native molecules, a small hydrophilic dye R6G (non-native) uptake and release is monitored and quantified with the help of total internal reflection fluorescence (TIRF) microscopy. The uptake and release of R6G is quantified by measuring the fluorescence intensity of the same as a function of time. For PduA and PduB PSs, the uptake is monophasic, whereas for PduB' a biphasic uptake is observed. An absence of lag phase in all the PSs suggested immediate uptake, probably because of the hydrophilic core. The extent of R6G incorporation is minimum in the case of PduB PSs, while apparently similar incorporation is observed for both PduA and PduB' PSs. However, meticulous observation of the curves suggests that the extent of initial incorporation in both PduB and PduB' is the same with almost similar time constant (t) ($t = 0.97 \pm 0.1 \text{ h}^{-1}$ for PduB) and ($t = 0.42 \pm 0.1 \text{ h}^{-1}$ for PduB'). After this initial phase, there is a second uptake for PduB' with a rate similar to PduA ($t = 2.7 \pm 0.2 \text{ h}^{-1}$), leading to enhanced incorporation of R6G dye in PduB' PSs (**Figure 4.6-c**). This apparent higher uptake in PduB' PSs can be due to the interaction of the N-terminal extension of PduB' with R6G, but it needs further investigation in near future.

When the release rate is assessed, all the PSs behaved differently. The PduB' ($t = 0.73 \pm 0.1 \text{ h}^{-1}$) PSs show the fastest release followed by PduA ($t = 2.5 \pm 0.4 \text{ h}^{-1}$), while PduB ($t = 4.9 \pm 1.2 \text{ h}^{-1}$) shows the maximum retention of the dye. It suggests that in the case of PduB shells, the dye interacts with the shell, thereby slowing the

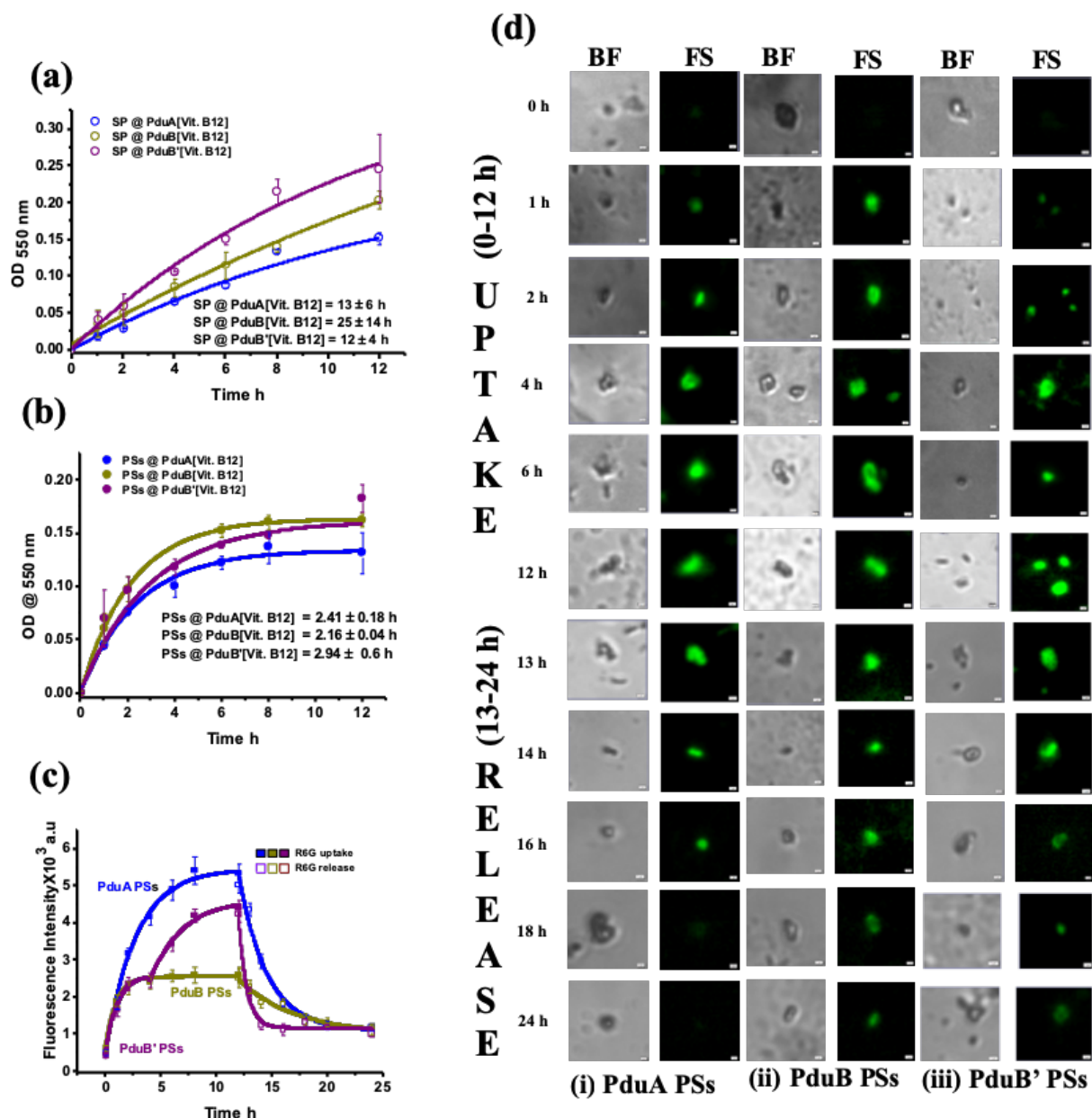


Figure 4.6: Vit B12 interaction and uptake to the SPs and the PSs of Pdu BMC studied by the dialysis method. A non-saturating interaction with VitB12 is observed with the SPs (a); A saturating interaction with VitB12 is observed with PSs where an equilibrium state follows an initial uptake (Open square box – for SPs; Filled square box- PSs) (b); The uptake and release of R6G in and out of the PSs are plotted as fluorescence intensity of encapsulated R6G concerning time for PduA (blue line), PduB (dark yellow line) and PduB' protein shell (violet line) Solid squares depicts the uptake of R6G whereas lined square is its release from the PSs. The data presented here is a mean of more than 100 PSs at each time point and is Mean \pm Standard error of the mean (c); Uptake and release of R6G inside the aqueous dialyzed PSs. Uptake is studied for 12 h (0-12 h), followed by its release for the next 12 h (13 -24 h). At each time point, images are captured for the PSs of PduA (i), PduB (ii), and PduB' (iii) with TIRF microscopy after excitation with 540 nm laser (d).

release. At this point, it further needs molecular level understanding to have an insight into differential uptake and release.

These differences in the permeability quantified by uptake and release rates suggest that although these SPs bear resemblance in their geometry or originate from the same BMC domain proteins, they differ markedly among themselves. Besides this, it also shows that these PSs are functional and dynamic, and the intrinsic features are not compromised or lost *in vitro*.

4.2.5 PSs as broad range functional structures and as a cargo carrier

The protein compartments reported to date had been used for various applications, such as active reactors, synthetic cellularity, protocell development, etc. which shows the functional diversity of such macromolecular assemblies. Like others, these PSs are also explored as a vehicle for small molecules, which include hydrophobic, hydrophilic, and also inorganic nanoparticles (NPs). Dox is selected as a hydrophilic molecule, which is a commonly used anticancer drug. In the Dox loaded PSs, a quenching in the doxorubicin fluorescence is observed, which confirms its interaction with SPs. Around 40% of dox loading is obtained through encapsulation and interaction with SPs (**Figure 4.7-a.i**). When release study of encapsulated dox is carried out by the dialysis method, the free drug shows fastest release with more than 60 % of the encapsulated drug is released with a rate of $1.36 \pm 0.29 \text{ h}^{-1}$ whereas in the PSs slower release is observed ($5.8 \pm 1.2 \text{ h}^{-1}$ @ PduA PSs; $3.1 \pm 0.6 \text{ h}^{-1}$ @ PduB PSs; $3.1 \pm 0.5 \text{ h}^{-1}$ @ PduB' PSs (**Figure 4.7-a.ii**). Next, a hydrophobic molecule (Nile Red, NR) is encapsulated inside the PSs. Owing to its low hydrophilicity, NR is first made hydrophilic by encapsulating inside the β -cyclodextrin (β -CD). A blue shift is observed in the emission maxima (NR emission) of the NR- β -CD loaded PSs as compared to free NR- β -CD, thus showing interaction of the two (**Figure 4.7-b.i**). The NR- β -CD loaded PSs, is further used for carrying out the release study. Different release rate is observed for the three PSs, $2.88 \pm 0.3 \text{ h}^{-1}$ @ PduA PSs; $1.52 \pm 0.5 \text{ h}^{-1}$ @ PduB PSs; $1.73 \pm 0.2 \text{ h}^{-1}$ @ PduB' PSs (**Figure 4.7-b.ii**).

Another hydrophobic molecule, Curcumin is loaded in the PSs by developing its solid dispersion in PEG4000 (Curcumin has low aqueous solubility and thus is made

hydrophilic by developing its solid dispersion). Blue shift in the emission maxima of curcumin is observed in the PSs loaded with Curcumin-solid dispersion (*Figure 4.7-*

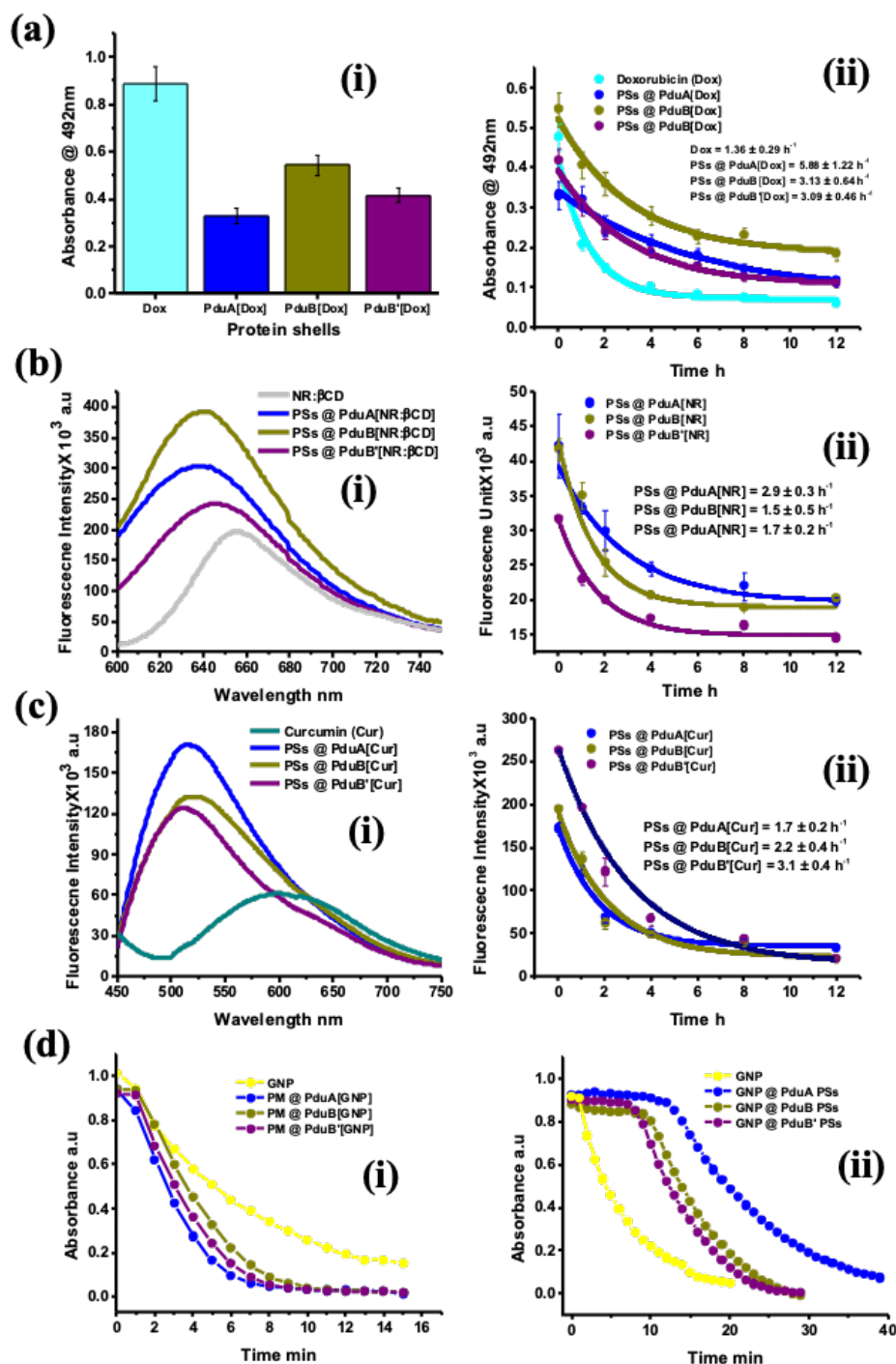


Figure 4.7: Loading of Doxorubicin in the PSs of PduA/B/B' SPs. (a.i). Doxorubicin release from the PSs as a function of time. For the free drug, the release is the fastest as there is no SPs whereas different release rates observed in Dox encapsulated in PSs indicate its interaction within the PSs (a.ii); Interaction of SPs with NR encapsulated in cyclodextrin as shown for the SPs[NR:βCD] which are used for fabrication of PSs (b.i) These PSs[NR:βCD] are employed for studying the release of NR through dialysis method (b.ii); Interaction of SPs with Curcumin as shown for the SPs[Cur] which are used for

fabrication of PSs (c.i) These PSs[Cur] are employed for studying the release of curcumin through dialysis method (c.ii); Conversion of p-nitrophenol to p-aminophenol by the GNP in the PM and in the PSs.

c.i). The curcumin loaded PSs are subsequently checked for release studies by dialysis method. The release rates observed are $1.74 \pm 0.1 \text{ h}^{-1}$ @ PduA PSs; $2.2 \pm 0.4 \text{ h}^{-1}$ @ PduB PSs and $3.14 \pm 0.4 \text{ h}^{-1}$ @ PduB' PSs (**Figure 4.7-c.ii**).

Finally, inorganic AuNPs of 18-20 nm in size are encapsulated in the PSs, and their catalytic role is assessed. Compared to PM (**Figure 4.7-d.i**), the encapsulated AuNPs shows a higher lag time before the start of inorganic catalysis. This is probably due to the restricted movement of the substrate or cofactor, *p*-aminophenol or sodium borohydride respectively across the SPs conduits in the PSs (**Figure 4.7-d.ii**). The loading of wide range of molecules inside the PSs and their release or their functional activity inside the PSs suggest the functional diversity of these protein compartments and they can be exploited as wide range functional cargo carrier. In summary, these small molecule encapsulation and release seems to be a strategic tool towards differentiating between the different types of the SPs observed across the different BMC. Further meticulous studies of these PSs could help to optimize the various *in vitro* metabolic process, which needs compartmentalization.

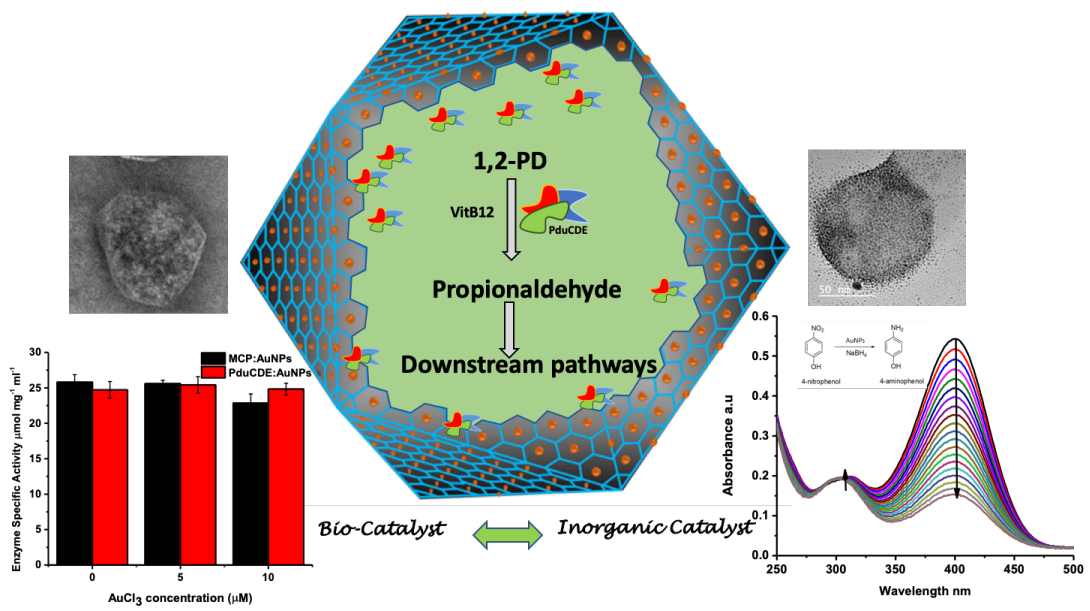
4.3 Conclusions

PSs are fabricated from the self-assembled 2D sheets of the SPs of Pdu BMC. The intrinsic self-assembling nature of these SPs is exploited, and thus no external stimuli or crosslinkers are employed for the fabrication of PSs. The pickering emulsion based fabrication strategy helped to retain the secondary structure of the SPs in the PSs. The macromolecular assembly of the SPs in the PSs also imparted thermal stability. These PSs are also explored for encapsulating both native and non-native enzyme, thus generating a active bioreactor *in vitro*. The substrate channelling in the active bioreactor is also explored through the movement of Vit B₁₂ (a native cofactor for Pdu BMC). It is observed that the diol-dehydratase activity is higher for the encapsulated enzymes as compared to the free enzyme. This is because of the encapsulation and crowding effect in PSs as compared to the free one. This justifies the importance of compartmentalization in the optimization of biochemical pathways. Though the differences between the SPs properties are not observed when

the native components are explored. Differences in encapsulation, channelling of substrate and co-factors can only be observed when the SPs are interacted with some non-native components such as CytC, R6G, and Doxorubicin. This extends a physiological relevance as it reinforces *Salmonella* survival under the stringent condition of 1,2-PD metabolism within Pdu BMC. Although the behaviour of the individual SPs under *in vitro* condition is examined here, but whether the same will be retained *in vivo* or not is not clear at this stage. Such a realization certainly needs rigorous *in vivo* genetic engineering studies. However, for the first time, this work showed that the three major Pdu BMC SPs are not only similar structurally but also functionally concerning Pdu BMC native molecules *in vitro*.

Chapter 5

Pdu BMC as template for Bio-inorganic hybrid development



5 Pdu BMC as template for bio-inorganic hybrid development

5.1 Introduction

This chapter explores the potential of MCPs for the development of a hybrid catalyst combining a natural and a synthetic component. Pdu BMC, one of the most explored MCP, represents a natural bio-nano reactor involved in optimizing the metabolism of 1,2-PD. The unique feature of this prokaryotic organelle is the spatial organization and assembly of SPs and enzymes. The SP coat encloses the enzyme cascade and provides stability, as discussed in Chapter 3. In nature, there are enough examples where the protein interacts with metals, form hybrids that have excellent functional properties(166–170). The in-organic components introduce novel properties including catalysis, sensing, targeting and so on (168,171–175). The SPs represent a natural scaffold that can be manipulated at the molecular level to achieve a specific assembly. The nanoscopic structural features of the protein and their manipulation at the molecular scale make protein a suitable scaffold (176–181). The proteins or peptide-based structures represent three-dimensional crystalline materials, in which amino acids provide a defined environment with open functional groups such as amines, alcohols, or thiols. Motivated by nature and SPs *in vitro* assembly as a 2D sheet along with their stability, encouraged us to explore the scaffold for developing bio-inorganic hybrid materials (63,102,136). The potential of metals to interact with amino acid and getting reduced largely depends on the reduction potential of the metals, i.e., the tendency to gain electrons(174,182–185). Gold a noble metal is less reactive due to a filled 5d valence shell which results in higher ionization potential bulk gold with poor catalytic properties. On the other-hand, AuNPs have demonstrated substantial catalytic activity due to the alteration of the electron structure resulting from Au-Au bond contraction in Au-NPs (186,187). Charged amino acids in proteins are known to mediate interaction, reduction, and fabrication of the gold precursors to AuNPs.

In this chapter, I used this property of the proteins to fabricate AuNPs on the surface of Pdu BMC. This study has two main focuses. The first one is the development of a hybrid catalyst. The next focus is to demonstrate global substrate channelling through the pores on the MCP surface.

5.2 Results and discussion

5.2.1 Interaction of Au on the BMC surface and its templating

To test if the Pdu BMC interacts with gold precursor I studied their interactions using ITC and BLI. Pdu BMCs are purified and tested for their composition, morphology and structure using SDS-PAGE, DLS, and TEM as described in Chapter 3 (*Figure 3.1-a to d*). The interaction studies carried out using BLI and ITC are shown in *Figure 5.1-a and 5.1-b*. It is observed that with increasing concentration of AuCl₃, an enhanced association is achieved by interferometry. The global dissociation-constant (K_d) for the interaction of AuCl₃ with BMCs is $16 \pm 0.2 \times 10^{-6}$. Similar dissociation constants are observed in BLI as shown in *Table 5.1* when interaction of AuCl₃ with the SPs (PduA and PduB) is carried out. In the ITC isotherms for the binding of the AuCl₃ with the Pdu BMC a saturation is observed. This data is only qualitative as lack of information on the exact molecular weight of Pdu BMCs did not allow the calculation of the thermodynamics parameters for interactions. The Pdu BMC and the SPs have negative zeta potential (*Table 5.2*), which helped in the interaction of gold precursor (Au³⁺) to the shell coat in intact Pdu BMC or the SPs. These interactions are further verified by absorption and fluorescence spectroscopy. A pool-down assay is conducted, where AuCl₃ is allowed to interact with the Pdu BMC for 10 min. Next, the entire mass is centrifuged to separate the un-associated AuCl₃ with the AuCl₃ interacting with Pdu BMC. The supernatant of the centrifuged solution show a decreased absorption compared to the absorption of the AuCl₃ pre-incubation with the Pdu BMCs (*Figure 5.1-c*). The interaction is further checked by studying the tryptophan-fluorescence at 323 nm upon addition of AuCl₃ to the Pdu BMC (*Figure 5.1-d*). The interaction of gold precursor to the Pdu BMC and the SPs indicates the presence of charged amino acids on the surface of Pdu BMC that can capture the Au precursor (*Figure 5.1-e*).

The above interaction studies of AuCl₃ with Pdu BMC and SPs show moderate binding to the shell surface. The gold precursor is then reduced to AuNPs by the charged amino acids on the surface of the Pdu BMC. In order to quicken the reduction, the equimolar concentration of HEPES is used after the interaction of Au³⁺ to the shell surface. Post reduction on the Pdu BMC surface an absorbance peak is observed at 540 nm, which is typical to that of AuNPs (*Figure 5.1-f*). The kinetics

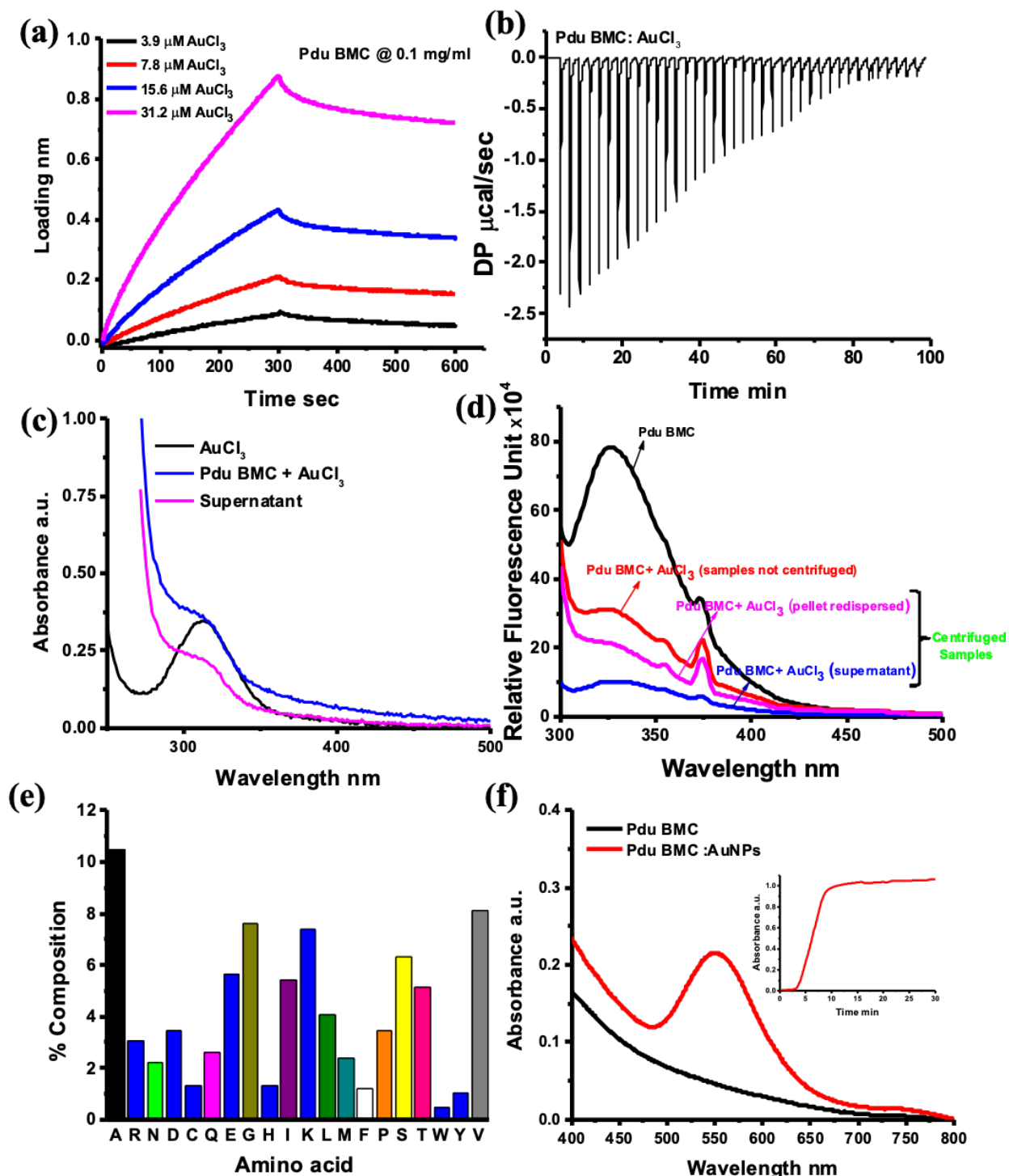


Figure 5.1: Interaction of increasing auric chloride concentration with Pdu BMC by BLI (a); Interaction auric chloride with Pdu BMC by ITC showed complete saturation (b); UV spectra are showing the interaction of auric chloride with the Pdu BMC. Supernatant shows decreased auric chloride concentration due to protein-assisted pull-down (c); Tryptophan fluorescence quenching of the Pdu BMC in the presence of AuCl_3 (d); Amino acid composition of the shell proteins (PduA, PduB, PduJ, PduK, PduN, PduK, PduU, PduV) of Pdu-BMC shell (e); In situ formation of AuNPs on BMC scaffold as observed from the characteristic peak of AuNPs with UV spectroscopy; Kinetics of AuNPs formation on the Pdu BMC surface (Inset) (f).

for AuNPs formation, i.e. reduction of Au^{3+} to Au^0 on the BMC surface is measured by monitoring the development of the absorption peak at 540 nm. This peak saturates after 10 min indicating the completion of the reduction process (inset of **Figure 5.1-f**). My experiments so far suggest that the gold precursor instantaneously interacts with the Pdu BMC surface, get scaffolded and then is slowly reduced by the charged amino acids present on the surface or fast reduction is carried out in the presence of external reducing agent (HEPES), and better signals are obtained. For fabricating a stable Pdu BMC-AuNP hybrid, Pdu BMC and AuCl_3 are titrated against each other in the concentration range of 0.1–0.5 mg/mL and from 2.5–250 μM for Pdu BMC and AuCl_3 , respectively. It is observed that Pdu BMC concentration beyond 0.1 mg/ml leads to aggregate formation. Though AuCl_3 is used till 250 μM , the acidic nature of the AuCl_3 solution (pH 3-4) lead to compromised enzyme activity and hence low concentration in the range of 5–50 μM are used.

Table 5.1: Dissociation constant (K_d) for the protein: AuCl_3 interactions determined by BLI (global fit)

S.No	Protein	K_d (10^{-6} M)
1	Pdu BMC	16 ± 0.2
2	PduA	7.8 ± 1.8
3	PduB	4.3 ± 2.2
4	PduB'	3.2 ± 1.3

Table 5.2: Zeta potential for the Pdu BMC and its shell proteins

S.No	Protein	Zeta potential (mV)
1	Pdu BMC	-9 ± 2
2	PduA	-19 ± 3
3	PduB	-24 ± 4
4	PduB'	-29 ± 3

5.2.2 Characterizing the fabricated AuNPs

After the initial proof for the formation of the AuNPs on the BMC surface by spectroscopic studies a series of characterization studies are carried out. In the X-ray diffraction pattern, AuNPs fabricated on the Pdu BMC show peaks at 2θ values of

38.1, 44.3, 64.5, and 77.7, which are indexed to (1 1 1), (2 0 0), (2 2 0), (3 1 1) which are reflections of face-centred cubic structure of metallic gold (*Figure 5.2-a*). The highest intensity is for the 111 plane (closed plane) at 2θ value of 38.1, which indicates a catalytic role for the AuNPs as discussed in the latter part. After this we analysed the TEM micrographs of the bare Pdu BMCs with the Pdu BMCs having AuNPs fabricated on them. The bare Pdu BMCs show polyhedral protein bodies in the size range of 100-150 nm with the negative staining (0.5 % uranyl acetate). In the Pdu BMC fabricated with AuNP the entire BMC surface is decorated with spherical NPs in the size range 2-3 nm. These images are obtained without any staining. The images indicate that the NPs are majorly present within the periphery of the MCPs. At certain places, however, it is observed that there are some peeling off of a section of the SPs with the NPs along the boundary of the MCPs (*Figure 5.2-b*). This is because of the drying effect during the TEM sample preparation.

Next we studied the electron micrograph images of the Pdu BMC fabricated with AuNPs to analyse the size and the morphology of the fabricated NPs. An estimation by the Image J software show that these NPs have a size of 2.5 ± 0.5 nm. The average distance between two adjacent NPs is 5.7 ± 0.5 nm. (*Figure 5.2-c*). This is an interesting observation because the centres of the two adjacent hexamer/trimer units of the BMC domain protein in their crystal structure are 5.0–6.5 nm apart. As the SPs act as a scaffold on which AuNPs get fabricated, the particles are arrayed at an interval of 5 to 6.5 nm. The development of the regular AuNPs array on the Pdu BMC surface is a unique observation. Since this is observed by TEM next set of experiments are aimed to understand if this arraying is due to a drying effect of the NPs on the TEM grid or due to precision scaffolding by the SPs on the BMC. In the absorbance spectra, a peak at 750 nm is observed which corresponds to a plasmonic development due to patterned arraying (*Figure 5.2-d*) on the self-assembled SPs surface which reinforces the meticulous scaffolding by the SPs (*Figure 5.2-e*). In another control experiment, non-assembling globular protein BSA is used for fabrication of AuNPs. In this case neither there is any array development in TEM images nor there is any plasmonics development in absorbance. Further no uniform size distribution of the fabricated NPs are observed with BSA. These studies combined indicate the uniqueness of the SPs on the BMC surface towards the development of new class of hybrid material (*Figure 5.2-f*).

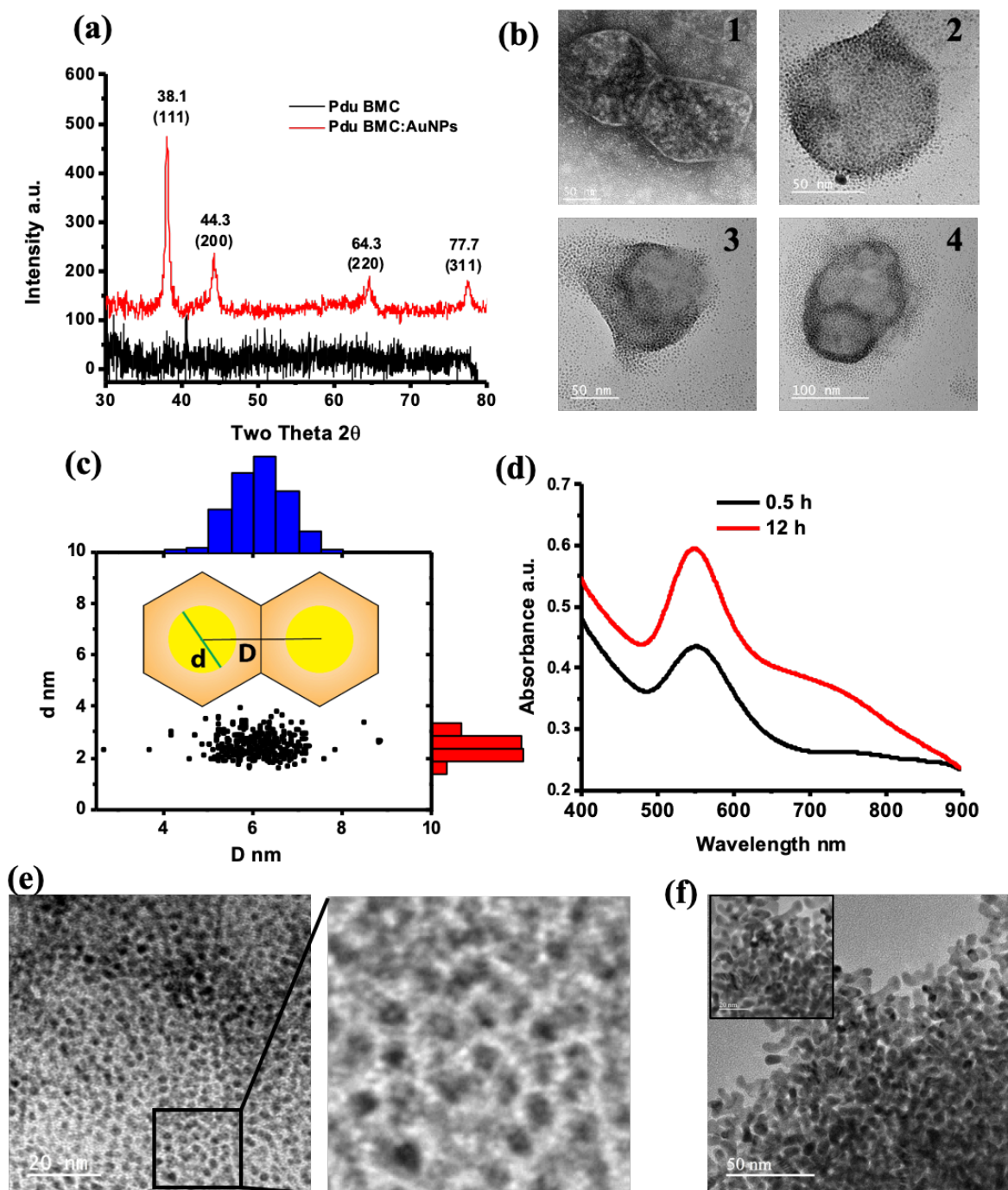


Figure 5.2: X-ray diffraction for in situ Pdu BMC: AuNPs (a); TEM micrograph for the negatively stained Pdu BMC(1), AuNPs on the scaffold of Pdu BMC shell proteins (2,3,4) (b); Size distribution of the AuNPs on the BMC scaffold (red bars), distribution of the distance between the adjacent NPs on the BMC scaffold (blue bars)(c); Absorption spectra of AuNPs observed on the scaffold of BMC after 0.5 h, and 12 h showed development of spatial interaction between NPs resulting in plasmonics around 750 nm. This development of plasmonics is a result of fabrication of nanoparticles in 3D on the mat like structure of the shell proteins which makes the external shell of the BMC (d); Pdu BMC SPs scaffold act as template because of arrayed hexameric or trimeric unit (e); BSA lacks self-assembly thus no arrayed templating (f).

5.2.3 Stability of Hybrid catalyst

The conformation stability of the native Pdu BMC and Pdu BMC-AuNPs hybrid are examined with CD and FTIR spectroscopy. It is observed that the conformation of Pdu BMC remained intact and is retained post the formation of AuNPs on its surface. The characteristic CD signals corresponding to α -helix at 222 and 208 nm in native Pdu BMC is not disturbed and is observed in the hybrid CD spectra (**Figure 5.3-a**). In the FTIR spectra, the amide-I vibrations are smoother for the hybrid than that of native Pdu BMC, suggesting the interaction of the Pdu BMC shell surface with gold precursor and its reduction on the BMC scaffold. Also when individual SPs are fabricated with AuNPs, their conformation remains unaltered, as observed by CD and FTIR. A slight contraction in the size of BMC:AuNPs (90 ± 10 nm) compared with the size of the BMC (110 ± 30 nm) alone, however is observed (**Figure 5.3-b**). The decrease in size is observed only at higher concentrations (50–100 μ M) of the gold precursor is used. At lower concentrations (5–10 μ M), no significant size variations in size are observed. When Pdu BMC is absent as scaffold two size distributions 30 ± 4 nm and 160 ± 25 nm are observed whereas, in the presence of the BMC as a scaffold, only one size distribution is observed (90 ± 10 nm). The unimodal size distribution in the presence of BMC and the precise size of the AuNPs obtained in the electron micrograph, as discussed earlier, suggests that the BMC shell precisely confines the size of the NPs to less than 3 nm on the Pdu BMC surface. The structural stability of the Pdu BMC at lower auric chloride concentration is further confirmed by carrying out the thermal unfolding studies by DSF and steady-state fluorescence. The fabrication of AuNPs on the BMC surface does show quenching of fluorescence, but no shift in the transition temperature, suggesting the presence of intact Pdu BMC-Au conjugate in solution phase (**Figure 5.3-c**). When stability of hybrid conjugate and native Pdu BMC is compared by DSF studies, no shift in transition temperature is observed as the the signature curve observed for both are same. These studies indicate no disruption in the intact polyhedral structure of Pdu BMC upon NPs fabrication. However, the presence of AuNP on the shell surface does bring change in transition curve correlating to the SPs (as studied in chapter 3) present in the DSF curve of Pdu BMC-Au hybrid (smoothing of curve at around 60 °C) (**Figure 5.3-d**).

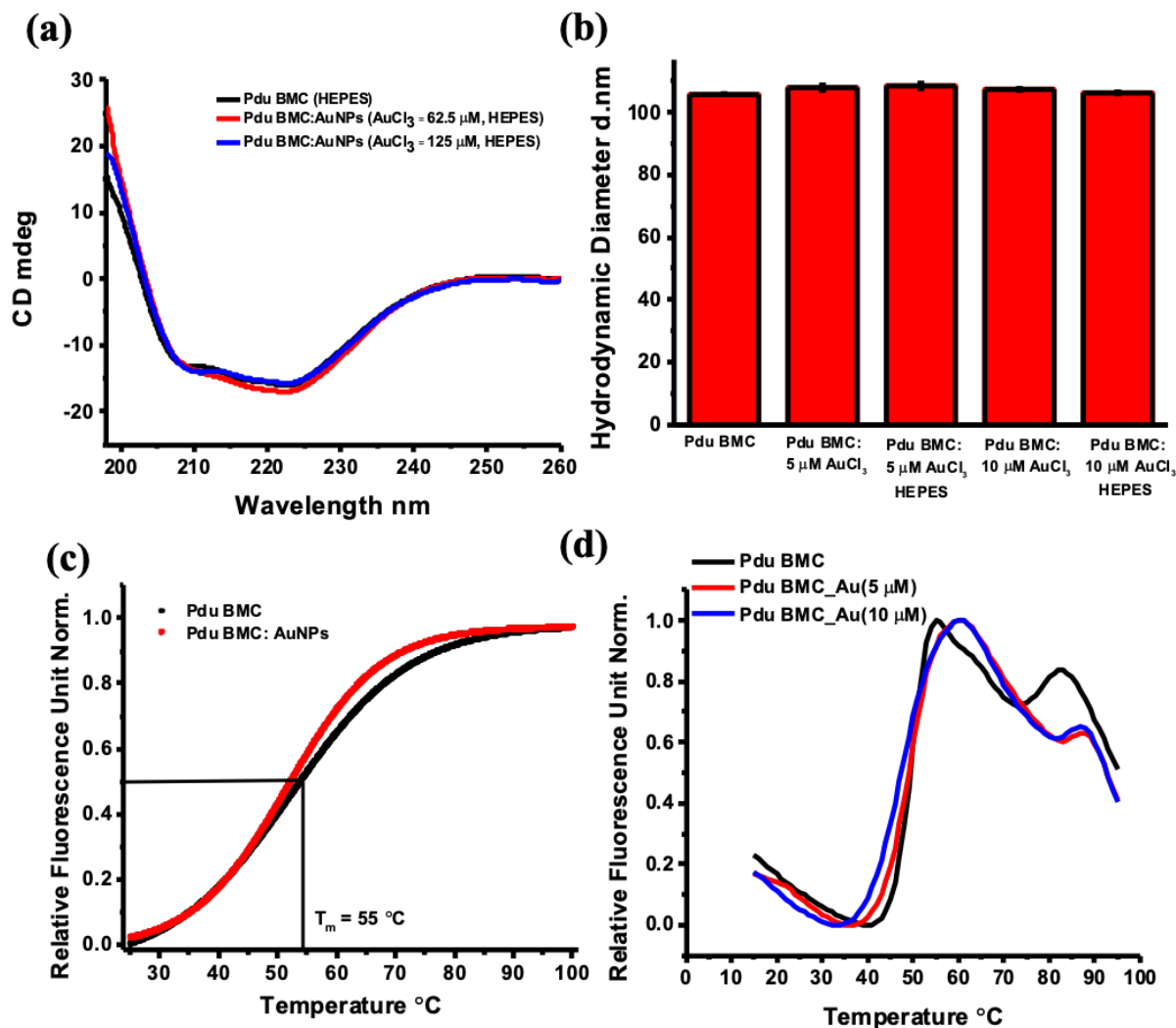


Figure 5.3: CD spectra for Pdu BMC as compared to hybrid Pdu BMC: AuNPs showed no effect on the conformation of the Pdu BMC (a); Size distribution for the Pdu BMC, Pdu BMC: AuNPs conjugates. At low concentration of AuCl₃ there is no effect on the size on Pdu BMC (b); Steady-state fluorescence based determination of the thermal stability of the hybrid in comparison to native Pdu BMC (tryptophan fluorescence) (c); Thermal Shift Assay for Pdu BMC and Pdu BMC: AuNPs hybrid. The conjugate material does not show any downward shift in melting temperature, which suggests that the macromolecular assembly is not disturbed with the nanoparticle fabrication in 3D under optimal condition(d).

5.2.4 Characterizing the hybrid catalysis

Next, the catalytic role of the hybrid conjugate is tested where both inorganic catalysis on the Pdu BMC scaffold and organic catalysis of the encapsulated enzyme is carried out. AuNPs are known to show heterogeneous catalysis because of their particle size and change in the electronic distribution. The BMC-AuNPs hybrid show efficient inorganic catalysis for the model reaction i.e., reduction of *p*-nitrophenol to *p*-aminophenol in the presence of NaBH₄ (*Figure 5.4-a*). The spatial disposition of

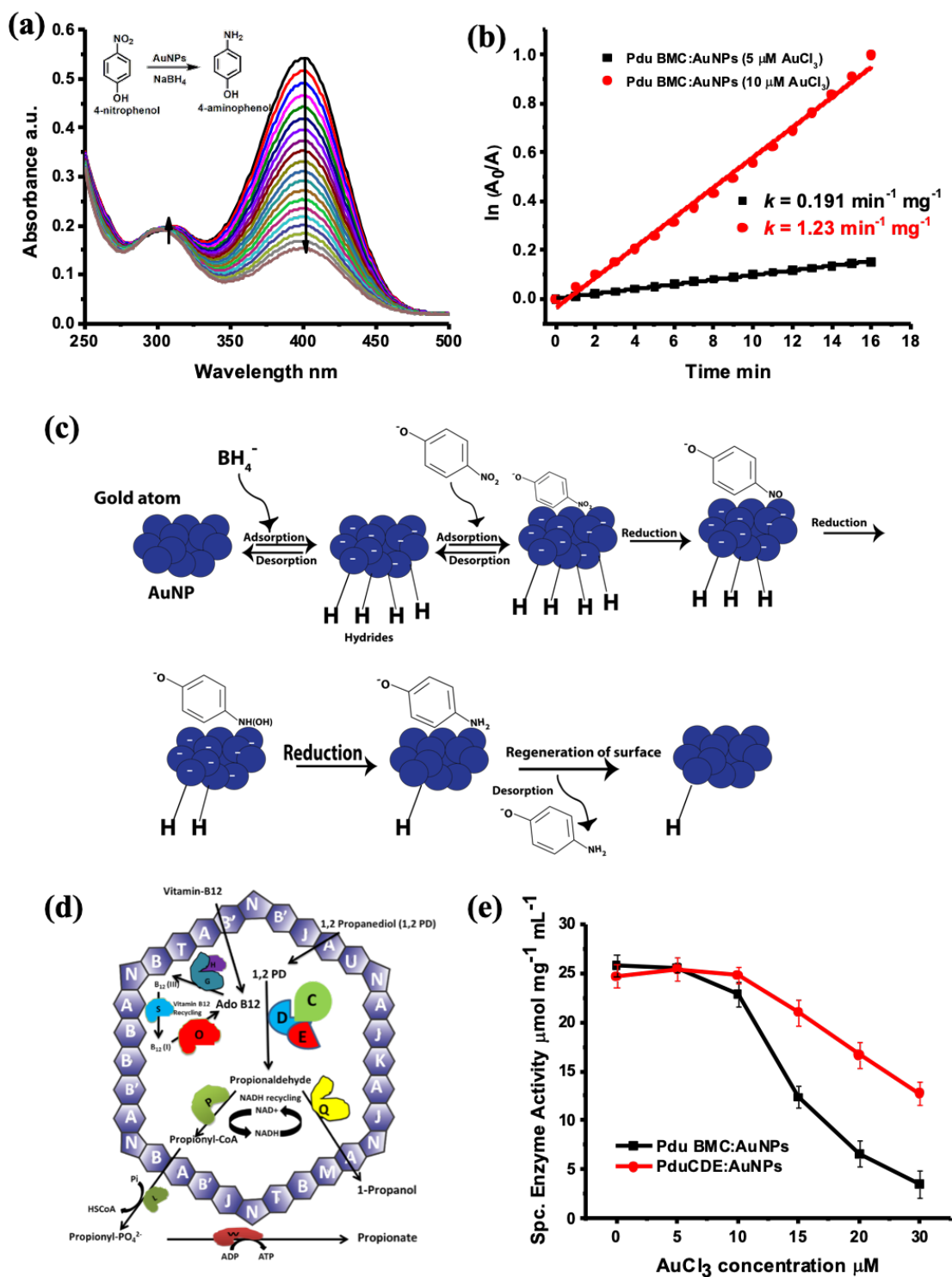


Figure 5.4: The catalytic activity of Pdu BMC:AuNPs conjugate showing the conversion *p*-nitrophenol to *p*-amino phenol (a); Increased catalytic activity of 10 μM HAuCl₄ fabricated nanoparticles in comparison to 5 μM HAuCl₄ (b); NaBH₄ act as a donor for hydride ions on the fabricated gold nanoparticles. AuNPs provides the surface to carry out the reduction (c); Pdu BMC model showing the channelling of 1,2-PD and Vit B₁₂ across the conduits for the organic catalysis (d); Enzyme catalysis for Pdu BMC:AuNPs and PduCDE:AuNPs

Table 5.3: Specific enzyme activity for the diol dehydratase enzyme

AuCl₃ concentration	Specific enzyme activity of Pdu BMC ($\mu\text{mol mg}^{-1} \text{ml}^{-1}$)	Specific enzyme activity of PduCDE ($\mu\text{mol mg}^{-1} \text{ml}^{-1}$)
0	25.8 \pm 1.06	24.7 \pm 1.17
5	25.6 \pm 0.49	25.4 \pm 1.17
10	22.8 \pm 1.29	24.9 \pm 0.83
15	12.6 \pm 1.11	21.0 \pm 1.31
20	6.6 \pm 1.34	16.8 \pm 1.31
30	3.5 \pm 1.38	12.7 \pm 1.13

the AuNPs in 3D on the BMC surface showed an increase in inorganic catalysis with increasing the AuCl₃ concentration from 5 to 30 μM . With doubling of AuCl₃ concentration from 5 to 10 μM , a 5–6-fold enhancement in the catalytic activity is observed (**Figure 5.4-b**). This corresponds to a large surface area of a typical icosahedral BMC ($3.04 \times 10^4 \text{ nm}^2$) being provided for NPs fabrication (**Figure 5.4-c**) (although the Pdu-BMC do not have the regular icosahedral structure, an approximation of the size is made taking the TEM images in consideration). The enhanced inorganic catalysis is also contributed due to the spatial arrangement of NPs in 3D on the Pdu BMC surface, resulting in plasmonics development. Although an increase in inorganic catalysis due to AuNP fabrication is observed by increasing the precursor concentration beyond 10 μM , organic catalysis by the encapsulated PduCDE enzyme inside the Pdu BMC is compromised (**Figure 5.4-d**). Though the diol dehydratase activity of the encapsulated enzyme is compromised beyond 10 μM , the activity is not compromised to that extent for the free enzyme as observed (Red curve, **Figure 5.4-e**). This has exciting implications because the compromise in the enzyme catalysis above 10 μM of AuCl₃ in the Pdu BMC can be due to two reasons: either the BMC catalytic components are getting deformed upon Au-NPs fabrication or AuNPs on the surface are blocking the transport of substrates and cofactors inside the lumen of the BMC. To confirm the above hypothesis, the specific activity of the bare enzyme PduCDE is evaluated as per MBTH assay, in the presence and absence of AuNPs (PduCDE:AuNPs hybrid are fabricated *in vitro* as per the method discussed). The diol dehydratase activity for the free or the encapsulated PduCDE enzyme (**Figure 5.4-e**) is not compromised till 10 μM AuCl₃. But beyond this

concentration, there is a gradual decrease in activity of the encapsulated enzymes. The decrease in enzyme activity of the Pdu BMC-AuNPs is, however, more pronounced compared to the PduCDE-AuNPs. This observation, along with the conformational studies, supported our other speculation that the AuNPs block the passage of substrates and cofactors from the surface of the BMC to the central lumen. The role of the pores in the SPs as conduits for substrate and cofactor is known in the literature. As the AuNPs are formed on the surface of the BMC and considering their size (2.5–3 nm), they likely block the conducting pores of the shell proteins, thus retarding the BMC activity (**Table 5.3**). Previously, genetic engineering studies have shown that specific blocking of the PduA pore results in the compromised uptake of 1,2-PD uptake, which has also been shown theoretically through molecular dynamics simulations by Park and co-workers.

5.2.5 Understanding the mechanism of AuNPs fabrication

As discussed earlier that the charged amino acids on the Pdu BMC surface assisted the interaction of gold precursor followed by reduction. The BMC-AuNPs hybrid conjugate exhibited a sharp, stable fluorescence that peaks at 660 nm at a wide range of excitation in solution by steady-state fluorescence and total internal reflection fluorescence microscopy (TIRF-M). As per the TIRF-M images (**Figure 5.5-a**), the fluorescence evolves 5–6 min after the addition of AuCl₃ to the BMC. After this, there is a continuous increase in fluorescence intensity, which saturates after 15 min (**Figure 5.5-b**), because of interaction with charged amino acids and its reduction from Au³⁺ to Au⁰. Control experiments performed with AuCl₃ and HEPES showed no visible fluorescence in TIRF-M (Pdu BMC is not used as template) (**Figure 5.5-c**). No detectable signals are observed in TIRF-M for Pdu BMC alone in the absence of AuCl₃ (**Figure 5.5-d**). These observations lead us to conclude that that fluorescent clusters are formed on the Pdu BMC surface. The fluorescence of the gold nanoclusters disappears upon the addition of an excess amount of the gold precursor or external reducing agent (**Figure 5.5-e and f**), suggesting the formation of nonfluorescent AuNPs. Typically, AuNPs with size <3 nm are reported to be fluorescent, whereas size ≥3 nm are nonfluorescent(188). The formation of nonfluorescent particles in the absence of BMC as template suggests that the BMCs scaffold the AuNPs and confine their size below 3 nm. This precise size distribution

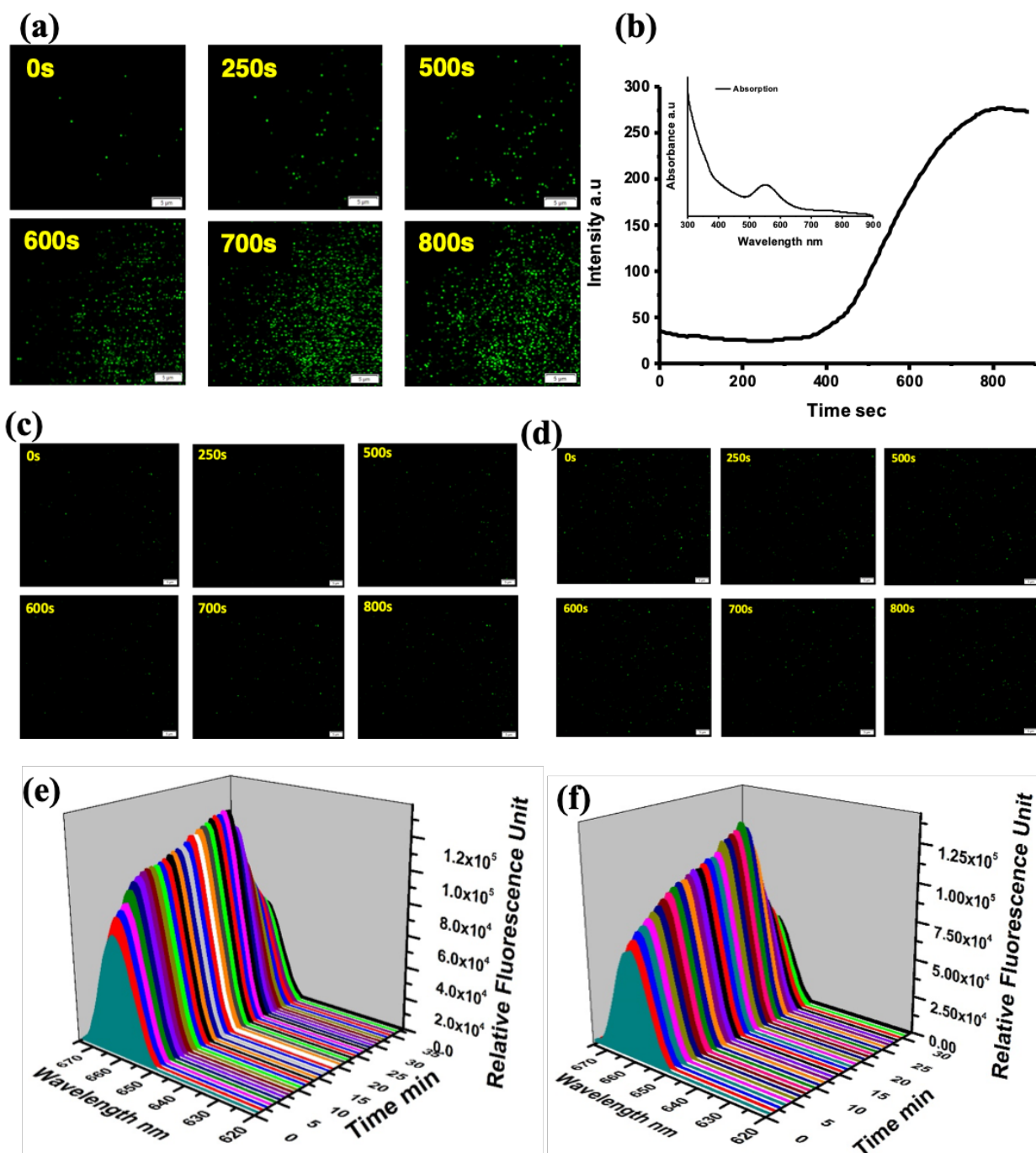


Figure 5.5: Microscopic images for the formation of AuNPs on the Pdu BMC scaffold observed by TIRF-M at a different time point (a); Time-dependent increase in the fluorescence due to the formation of fluorescent AuNPs. Excitation scan of Pdu BMC-AuNPs (Inset) (b); Only Pdu BMC (c) or absence of Pdu BMC as scaffold (Auric chloride + HEPES) shows no fluorescence as captured by TIRF-M (d); Formation of AuNPs on Pdu BMC studied with steady-state fluorescence and showing the transition from fluorescent AuNPs to non-fluorescent in excess of precursor (e) and reducing agent (f).

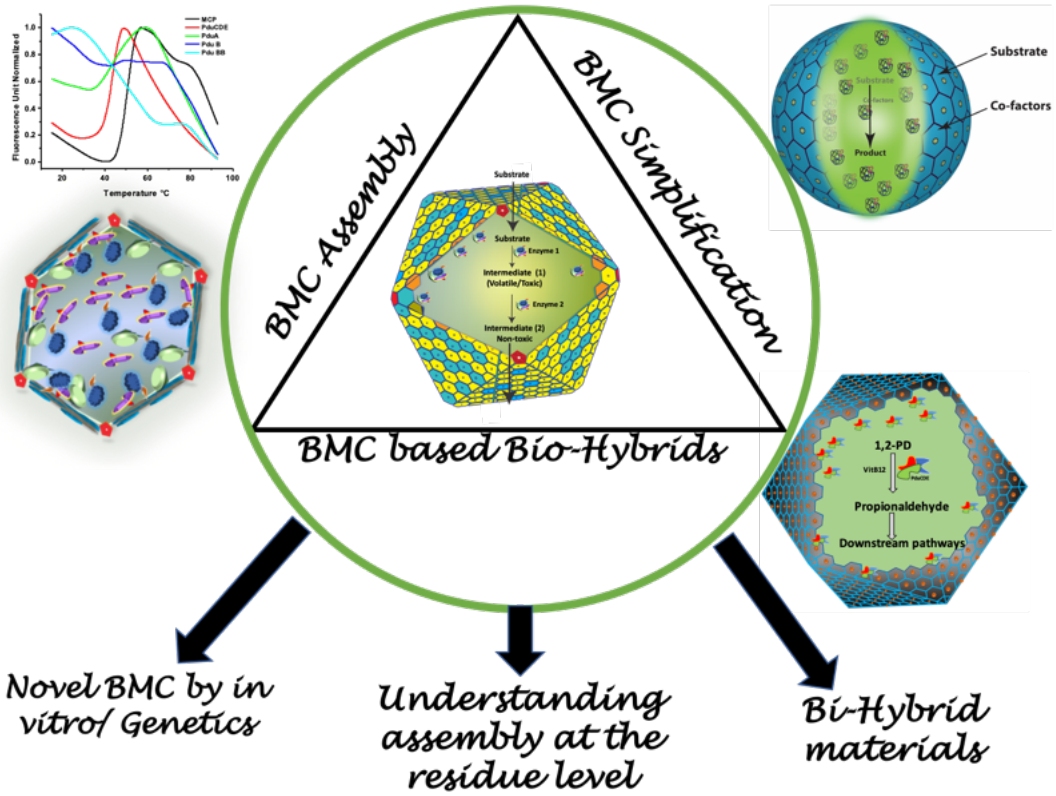
can be obtained by a careful manipulation of the scaffold (BMC) and the precursor (AuCl_3). In general we conclude that in the course of fabrication of AuNPs on the 3D scaffold there is the formation of gold clusters initially followed by AuNPs.

5.3 Conclusion

The robust shell surface of Pdu BMC made up of self-assembled hexameric and trimeric protein units act as a scaffold and helped in the fabrication of AuNPs in 3D. The fabrication is assisted by the charged amino acids, which assist the nucleation of the precursor molecules, followed by its reduction. The surface scaffolded AuNPs demonstrated standard catalysis, while the internal enzyme cluster of the BMC demonstrated organic catalysis. Under ambient conditions for *in vitro* inorganic reaction, the SPs sturdily maintain the barrier between the luminal enzyme and the surface fabricated inorganic catalysts and preserve the functionality of the encapsulated enzyme. Though Pdu BMC has been explored for various biotechnological applications as synthetic bioreactors, this is the first report where any prokaryotic bacterial organelle has been explored as a template for the development of the bio-inorganic hybrid. The Pdu BMC-AuNPs hybrid inspire a pristine class of resources that can be used in a chemical reaction condition without perturbing the core biological (physiological) environment for enzymatic activity. This system provides insight for fabricating uniformly ordered nanoparticles in 3D towards the development of orthogonal hybrid catalytic material. This study also opens the door to explore these self-assembling SPs in the field of material science for wide range of applications.

Chapter 6

Summary & Conclusion



6 Summary and Conclusion

This thesis is an attempt to understand the structure-function relationship of Pdu BMC and exploring its component as new class of biomaterial. In this chapter, I have summarized the main findings of this thesis. The unique way by which these MCPs manage specific metabolism in bacteria combined with the special morphological features of the SPs motivated me to have a meticulous understanding of the interactions that outfit these structures and also to look for the means to explore them for other biotechnological uses. I hope to the reader, this thesis work opens up a new paradigm for exploring these MCPs for a wide range of applications. The MCPs and their SPs can be an excellent scaffold for integrating different fields of science at the interface of nanotechnology.

In *Chapter 1*, I have provided a background on the basic understanding of the MCP in general and Pdu BMC in particular. The characteristic features of the components of the MCP, i.e., SP and the enzyme cascade, are discussed. The motivation and perspective for the thesis are also highlighted based on earlier studies. This thesis “USE” i.e., Understand, Simplify, and Explore the Pdu BMC, observed in *Salmonella enterica typhimurium*.

In *Chapter 2*, I have discussed the various techniques used in this study. I have used an integrated methodology using molecular biology, spectroscopy, microscopy, and computational approaches for carrying out the thesis work.

Chapter 3, mainly focusses on understanding the packing of the Pdu BMC. Using a spectroscopic technique, and the concept of differential scanning fluorimetry, I explored how the SPs and enzymes behave individually and in the assembled MCP. The findings of this chapter exhibit that these intact BMCs as a whole behave similar to a globular protein having a rich hydrophobic core, which is exposed upon thermal insult. The encapsulated enzymes being globular in nature had a strong hydrophobic core, which is in line with the hydrophobic-collapse model of protein folding. For the first time, the thermal unfolding profile of the BMC domain proteins is investigated, and it is observed that unlike globular protein, they lack a strong buried hydrophobic core and significant portion of hydrophobic patches are exposed. These unique exposed hydrophobic patches might be required for anchoring the enzymes inside the compartment resulting in better packaging of the microcompartments. It is observed that the secondary structures are disrupted at higher temperatures. However, the

activity of the enzymes is lost post disruption of the tertiary structure, indicating the importance of balanced interactions at the tertiary structure level to maintain the structure-activity relationships in these metabolosomes.

Chapter 4 attempts to understand the properties of individual SPs *in vitro*. Mono-component protein compartments are fabricated from individual SP sheets using a self-assembling approach at the interface of oil and water. The mild fabrication technique adopted here does not involve any crosslinker, and the resultant protein compartments demonstrate higher stability compared to the SP sheets without any loss of the conformation of the component proteins. These protein compartments are capable of encapsulating macromolecular enzymes and permit the free exchange of small molecules and substrates through their intrinsic conduits channels making these PSs suitable as active bioreactors *in vitro*. It is observed that the three major Pdu SPs (Pdu A/B/B') have functional similarity when it comes to native functions such as substrate channelling for VitB₁₂ and DDH enzyme activity. However, in the presence of non-native molecules, the PSs show varied responses indicating that they can be explored for different applications *in vitro*. The present study suggests that for having a molecular-level understanding of the properties of the SPs rigorous *in vivo*, genetic engineering studies are needed.

In Chapter 5, I explored the Pdu BMC as a scaffold for the fabrication of inorganic nanoparticles. Though Pdu BMC has been explored for applications in synthetic bioreactors, their surface has yet not been explored for any ectopic function. This is the first report where a prokaryotic organelle is explored as a template for the development of the bio-inorganic hybrid system. The development of this bio-inorganic hybrid system, helped to achieve a protein scaffolded AuNPs shell enclosing an active enzyme cluster. The protein templated AuNPs demonstrated standard inorganic catalysis, without any activity loss for the internal enzyme cluster. The SPs owing to its sturdy and robust nature, maintained a barrier between the luminal enzyme and surface fabricated inorganic catalysts. This system provides insight for fabricating uniform size AuNPs in 3D for the development of orthogonal hybrid catalytic material. The Pdu BMC-AuNPs hybrid catalysts inspire a pristine class of resources that can be used in a chemical reaction condition without perturbing the core biological (physiological) environment for enzymatic activity.

The work presented in this thesis opens up a new paradigm of research by bringing the assimilation of molecular biology, biochemistry, nanotechnology, and

material science. DSF based understanding of the thermal stability *will aid in* developing quality control measures for the industrial application of this genre of proteins. It can also be applied for an understanding of the assemblies created out of protein-polymer conjugates and also various genetically engineered protein compartments *in vitro*. Coupled to microscopy, physiological growth assays, and structural techniques like NMR and crystallography, DSF can be explored to understand the assembly and stability at the residue level of such complex macromolecular assembly. Fabrication of PSs provides insight into the development of the protein compartment from such self-assembling proteins without any chemical modification. These PSs also motivate to engineer stable protein compartments through genetic modulation for various biochemical applications and other critical biosynthetic pathways *in vitro*. At last, development of the Pdu BMC-AuNPs hybrid opens up a new class of bacterial biomaterials that can be integrated with inorganic nanoparticles for the development of hybrid functional materials. This system provides insight for fabricating uniformly ordered nanoparticles in 3D with angstrom level precision. The ease of encapsulation in the PSs *ex vivo* and fabrication strategy on these self-assembled protein templates, which are robust and sturdy, pave the way for the generation of a pristine class of hybrid inorganic-organic materials. In general this thesis highlights the potential of BMC for application in field of bio-engineering (to produce natural self-assembled polymer), biomaterial science (designing efficient thermostable natural polymer) and hybrid functional materials

Bibliography

Bibliography

1. Fox SW. A theory of macromolecular and cellular origins. *Nature*. 1965;205(4969):328–40.
2. Diekmann Y, Pereira-Leal JB. Evolution of intracellular compartmentalization. *Biochem J*. 2013;449(2):319–31.
3. Kojima T, Takayama S. Membraneless compartmentalization facilitates enzymatic cascade reactions and reduces substrate inhibition. *ACS Appl Mater Interfaces*. 2018;10(38):32782–91.
4. Martin W. Evolutionary origins of metabolic compartmentalization in eukaryotes. *Philos Trans R Soc B Biol Sci*. 2010;365(1541):847–55.
5. Hanke GT, Busch KB, Deckers-Hebestreit G, Mulkidjanian AY, Biology C. Dynamics of bioenergetic microcompartments. *Biol Chem*. 2013 Feb;394(2):163–88.
6. Chen AH, Silver PA. Designing biological compartmentalization. *Trends Cell Biol*. 2012 Dec;22(12):662–70.
7. Tu BP, Kudlicki A, Rowicka M, McKnight SL. Logic of the yeast metabolic cycle: temporal compartmentalization of cellular processes. *Science (80-)*. 2005;310(5751):1152–8.
8. Vellai T, Vida G. The origin of eukaryotes: the difference between prokaryotic and eukaryotic cells. *Proc R Soc London Ser B Biol Sci*. 1999;266(1428):1571–7.
9. Cannon GC, Bradburne CE, Aldrich HC, Baker SH, Heinhorst S, Shively JM. Microcompartments in prokaryotes: carboxysomes and related polyhedra. *Appl Environ Microbiol*. 2001;67(12):5351–61.
10. Kerfeld CA, Heinhorst S, Cannon GC. Bacterial Microcompartments. *Annu Rev Microbiol*. 2010;64(1):391–408.
11. Tanaka S, Kerfeld CA, Sawaya MR, Cai F, Heinhorst S, Cannon GC, et al. Atomic-level models of the bacterial carboxysome shell. *Science (80-)*. 2008;319(5866):1083–6.
12. Yeates TO, Thompson MC, Bobik TA. The protein shells of bacterial microcompartment organelles. Vol. 21, *Current Opinion in Structural Biology*. 2011. p. 223–31.
13. Bobik TA, Lehman BP, Yeates TO. Bacterial microcompartments: widespread

-
- prokaryotic organelles for isolation and optimization of metabolic pathways. *Mol Microbiol.* 2015;98(2):193–207.
14. Bari NK, Kumar G, Sinha S. The wrappers of the 1,2-propanediol utilization bacterial microcompartments. *Adv Exp Med Biol.* 2018;1112:333–44.
 15. Chowdhury C, Sinha S, Chun S, Yeates TO, Bobik TA. Diverse Bacterial Microcompartment Organelles. *Microbiol Mol Biol Rev.* 2014;78(3):438–68.
 16. Kerfeld CA, Aussignargues C, Zarzycki J, Cai F, Sutter M. Bacterial microcompartments. *Nat Rev Microbiol.* 2018;16(5):277–90.
 17. Schoonen L, van Hest JCM. Compartmentalization approaches in soft matter science: from nanoreactor development to organelle mimics. *Adv Mater.* 2016;28(6):1109–28.
 18. G Drews WN. Beiträge zur Cytologie der Blaualgen. II. Zentroplasma und granulare Einschlüsse von *Phormidium uncinatum*. *Arch Mikrobiol.* 162nd ed. 1956;24.
 19. Yeates TO, Kerfeld CA, Heinhorst S, Cannon GC, Shively JM. Protein-based organelles in bacteria: carboxysomes and related microcompartments. *Nat Rev Microbiol.* 2008;6(9):681.
 20. Shively JM, Ball F, Brown DH, Saunders RE. Functional organelles in prokaryotes: polyhedral inclusions (carboxysomes) of *Thiobacillus neapolitanus*. *Science* (80-). 1973;182(4112):584–6.
 21. Shively JM, Ball FL, Kline BW. Electron microscopy of the carboxysomes (polyhedral bodies) of *Thiobacillus neapolitanus*. *J Bacteriol.* 1973;116(3):1405–11.
 22. Abdul-Rahman F, Petit E, Blanchard JL. The Distribution of Polyhedral Bacterial Microcompartments Suggests Frequent Horizontal Transfer and Operon Reassembly. *J Phylogen Evol Biol.* 2013;1:4.
 23. Cannon GC, Bradburne CE, Aldrich HC, Baker SH, Heinhorst S, Shively JM. MINIREVIEW Microcompartments in Prokaryotes : Carboxysomes and Related Polyhedra. *Appl Environ Microbiol.* 2001;67(12):5351–61.
 24. GenBank [Internet]. [cited 2020 Mar 3]. Available from: <https://www.ncbi.nlm.nih.gov/pmc/articles/PMC2808980/>
 25. Ravcheev DA, Moussu L, Smajic S, Thiele I. Comparative genomic analysis reveals novel microcompartment-associated metabolic pathways in the human gut microbiome. *Front Genet.* 2019;10(7):636.
 26. Chessher A, Breitling R, Takano E. Bacterial Microcompartments: Biomaterials for Synthetic Biology-Based Compartmentalization Strategies. *ACS Biomater Sci Eng.*

-
- 2015;1(6):345–51.
27. Tanaka S, Sawaya MR, Yeates TO. Structure and mechanisms of a protein-based organelle in *Escherichia coli*. *Science* (80-). 2010;327(5961):81–4.
 28. Chowdhury C, Sinha S, Chun S, Yeates TO, Bobik TA. Diverse bacterial microcompartment organelles. *Microbiol Mol Biol Rev*. 2014;78(3):438–68.
 29. Yeates TO, Jorda J, Bobik TA. The shells of BMC-type microcompartment organelles in bacteria. *J Mol Microbiol Biotechnol*. 2013;23(4–5):290–9.
 30. Havemann GD, Bobik T a. Protein Content of Polyhedral Organelles Involved in Coenzyme B₁₂-Dependent Degradation of 1,2-Propanediol in *Salmonella enterica* Serovar Typhimurium LT2. *Society*. 2003;185(17):5086–95.
 31. Sutter M, Greber B, Aussignargues C, Kerfeld CA. Assembly principles and structure of a 6.5-MDa bacterial microcompartment shell. 2017;356(6344):1293–7.
 32. Kerfeld CA, Heinhorst S, Cannon GC. Bacterial Microcompartments. *Annu Rev Microbiol*. 2010 Oct 13;64(1):391–408.
 33. Sagermann M, Ohtaki A, Nikolakakis K. Crystal structure of the EutL shell protein of the ethanolamine ammonia lyase microcompartment. *Proc Natl Acad Sci U S A*. 2009;106(22):8883–7.
 34. Garsin DA. Ethanolamine utilization in bacterial pathogens: Roles and regulation. *Nat Rev Microbiol*. 2010;8(4):290–5.
 35. Heldt D, Frank S, Seyedarabi A, Ladikis D, Parsons JB, Warren MJ, et al. Structure of a trimeric bacterial microcompartment shell protein, EutB, associated with ethanol utilization in *Clostridium kluyveri*. *Biochem J*. 2009 Oct 15;423(2):199–207.
 36. Yeates TO, Thompson MC, Bobik TA. The protein shells of bacterial microcompartment organelles. *Curr Opin Struct Biol*. 2011;21(2):223–31.
 37. Sinha S, Cheng S, Fan C, Bobik TA. The PduM protein is a structural component of the microcompartments involved in coenzyme B₁₂-dependent 1,2-propanediol degradation by *Salmonella enterica*. *J Bacteriol*. 2012;194(8):1912–8.
 38. Cheng S, Sinha S, Fan C, Liu Y, Bobik TA. Genetic analysis of the protein shell of the microcompartments involved in coenzyme B₁₂-dependent 1,2-propanediol degradation by *Salmonella*. *J Bacteriol*. 2011;193(6):1385–92.
 39. Chen P, Andersson DI, Roth JR. The control region of the pdu/cob regulon in *Salmonella typhimurium*. *J Bacteriol*. 1994;176(17):5474–82.
 40. Pang A, Liang M, Prentice MB, Pickersgill RW. Substrate channels revealed in the

-
- trimeric *Lactobacillus reuteri* bacterial microcompartment shell protein PduB. *Acta Crystallogr Sect D Biol Crystallogr*. 2012;68(12):1642–52.
41. Crowley CS, Cascio D, Sawaya MR, Kopstein JS, Bobik TA, Yeates TO. Structural insights into the mechanisms of transport across the *Salmonella enterica* Pdu microcompartment shell. *J Biol Chem*. 2010;285(48):37838-37846.
 42. Bobik TA, Havemann GD, Busch RJ, Williams DS, Aldrich HC. The Propanediol Utilization (pdu) Operon of *Salmonella enterica* Serovar Typhimurium LT2 Includes Genes Necessary for Formation of Polyhedral Organelles Involved in Coenzyme B 12-Dependent 1,2-Propanediol Degradation †. *J Bacteriol*. 1999;181(19):5967–75.
 43. Lehman BP, Chowdhury C, Bobik TA. The N Terminus of the PduB Protein Binds the Protein Shell of the Pdu Microcompartment to Its Enzymatic Core. *J Bacteriol*. 2017;199(8):e00785-16.
 44. Havemann GD, Sampson EM, Bobik TA. PduA is a shell protein of polyhedral organelles involved in coenzyme B12-dependent degradation of 1,2-propanediol in *Salmonella enterica* serovar typhimurium LT2. *J Bacteriol*. 2002;184(5):1253–61.
 45. Wheatley NM, Gidaniyan SD, Liu Y, Cascio D, Yeates TO. Bacterial microcompartment shells of diverse functional types possess pentameric vertex proteins. *Protein Sci*. 2013;22(5):660–5.
 46. Thompson MC, Wheatley NM, Jorda J, Sawaya MR, Gidaniyan SD, Ahmed H, et al. Identification of a unique Fe-S cluster binding site in a glycyl-radical type microcompartment shell protein. *J Mol Biol*. 2014;426(19):3287–304.
 47. Urano N, Kataoka M, Ishige T, Kita S, Sakamoto K, Shimizu S. Genetic analysis around aminoalcohol dehydrogenase gene of *Rhodococcus erythropolis* MAK154: a putative GntR transcription factor in transcriptional regulation. *Appl Microbiol Biotechnol*. 2011;89(3):739–46.
 48. Kerfeld CA, Aussignargues C, Zarzycki J, Cai F, Sutter M. Bacterial microcompartments. *Nat Publ Gr*. 2018;16(5):277–90.
 49. Petit E, LaTouf WG, Coppi M V, Warnick TA, Currie D, Romashko I, et al. Involvement of a bacterial microcompartment in the metabolism of fucose and rhamnose by *Clostridium phytofermentans*. *PLoS One*. 2013;8(1):e54337.
 50. Erbilgin O, McDonald KL, Kerfeld CA. Characterization of a planctomycetal organelle: a novel bacterial microcompartment for the aerobic degradation of plant saccharides. *Appl Environ Microbiol*. 2014;80(7):2193–205.
 51. Jameson E, Fu T, Brown IR, Paszkiewicz K, Purdy KJ, Frank S, et al. Anaerobic

-
- choline metabolism in microcompartments promotes growth and swarming of *P. roteus mirabilis*. *Environ Microbiol.* 2016;18(9):2886–98.
52. Craciun S, Balskus EP. Microbial conversion of choline to trimethylamine requires a glyceryl radical enzyme. *Proc Natl Acad Sci.* 2012;109(52):21307–12.
 53. Herring TI, Harris TN, Chowdhury C, Mohanty SK, Bobik TA. A bacterial microcompartment is used for choline fermentation by *Escherichia coli* 536. *J Bacteriol.* 2018;200(10):e00764-17.
 54. Kalnins G, Cesle EE, Jansons J, Liepins J, Filimonenko A, Tars K. Encapsulation mechanisms and structural studies of GRM2 bacterial microcompartment particles. *Nat Commun.* 2020;11(1):1–13.
 55. Chen P, Ailion M, Bobik T, Stormo G, Roth J. Five promoters integrate control of the cob/pdu regulon in *Salmonella typhimurium*. *J Bacteriol.* 1995;177(19):5401–10.
 56. Dou Z, Heinhorst S, Williams EB, Murin CD, Shively JM, Cannon GC. CO₂ fixation kinetics of *Halothiobacillus neapolitanus* mutant carboxysomes lacking carbonic anhydrase suggest the shell acts as a diffusional barrier for CO₂. *J Biol Chem.* 2008/02/09. 2008;283(16):10377–84.
 57. Faulkner M, Rodriguez-Ramos J, Dykes GF, Owen S V, Casella S, Simpson DM, et al. Direct characterization of the native structure and mechanics of cyanobacterial carboxysomes. *Nanoscale.* 2017;9(30):10662–73.
 58. Tsai Y, Sawaya MR, Cannon GC, Cai F, Williams EB, Heinhorst S, et al. Structural analysis of CsoS1A and the protein shell of the *Halothiobacillus neapolitanus* carboxysome. *PLoS Biol.* 2007;5(6):e144.
 59. Shively JM, Bradburne CE, Aldrich HC, Bobik TA, Mehlman JL, Jin S, et al. Sequence homologs of the carboxysomal polypeptide CsoS1 of the thiobacilli are present in cyanobacteria and enteric bacteria that form carboxysomes - polyhedral bodies. *Can J Bot.* 1998;76(6):906–16.
 60. Rae BD, Long BM, Badger MR, Price GD. Functions , Compositions , and Evolution of the Two Types of Carboxysomes : Polyhedral Microcompartments That Facilitate CO₂ Fixation in Cyanobacteria and Some Proteobacteria. *Microbiol Mol Biol Rev.* 2013;77(3):357–79.
 61. Iancu C V., Morris DM, Dou Z, Heinhorst S, Cannon GC, Jensen GJ. Organization, Structure, and Assembly of α -Carboxysomes Determined by Electron Cryotomography of Intact Cells. *J Mol Biol.* 2010;396(1):105–17.

-
62. Rae BD, Long BM, Badger MR, Price GD. Functions, compositions, and evolution of the two types of carboxysomes: polyhedral microcompartments that facilitate CO₂ fixation in cyanobacteria and some proteobacteria. *Microbiol Mol Biol Rev.* 2013;77(3):357–79.
 63. Uddin I, Frank S, Warren MJ, Pickersgill RW. A Generic Self-Assembly Process in Microcompartments and Synthetic Protein Nanotubes. *Small.* 2018;14(19):1704020.
 64. Yeates TO, Crowley CS, Tanaka S. Bacterial Microcompartment Organelles: Protein Shell Structure and Evolution. *Annu Rev Biophys.* 2010;39(1):185–205.
 65. Kerfeld CA. A bioarchitectonic approach to the modular engineering of metabolism. *Philos Trans R Soc B Biol Sci.* 2017;372(1730):20160387.
 66. Jakobson CM, Tullman-Ercek D. Dumpster Diving in the Gut: Bacterial Microcompartments as Part of a Host-Associated Lifestyle. *PLOS Pathog.* 2016;12(5):e1005558.
 67. EMBL Nucleotide Sequence Database | Nucleic Acids Research | Oxford Academic [Internet]. Available from: <https://academic.oup.com/nar/article/28/1/19/2384388>
 68. Jorda J, Lopez D, Wheatley NM, Yeates TO. Using comparative genomics to uncover new kinds of protein-based metabolic organelles in bacteria. *Protein Sci.* 2013;22(2):179–95.
 69. Bobik TA. Polyhedral organelles compartmenting bacterial metabolic processes. *Appl Microbiol Biotechnol.* 2006;70(5):517–25.
 70. Cheng S, Liu Y, Crowley CS, Yeates TO, Bobik TA. Bacterial microcompartments: Their properties and paradoxes. *BioEssays.* 2008;30(11–12):1084–95.
 71. Thiennimitr P, Winter SE, Winter MG, Xavier MN, Tolstikov V, Huseby DL, et al. Intestinal inflammation allows *Salmonella* to use ethanolamine to compete with the microbiota. *Proc Natl Acad Sci U S A.* 2011;108(42):17480–5.
 72. Kofoed E, Rappleye C, Stojiljkovic I, Roth J. The 17-gene ethanolamine (eut) operon of *Salmonella typhimurium* encodes five homologues of carboxysome shell proteins. *J Bacteriol.* 1999;181(17):5317–29.
 73. Stojiljkovic I, Baumler AJ, Heffron F. Ethanolamine utilization in *Salmonella typhimurium*: Nucleotide sequence, protein expression, and mutational analysis of the *cchA cchB eutE eutJ eutG eutH* gene cluster. *J Bacteriol.* 1995;177(5):1357–66.
 74. Mori K, Bando R, Hieda N, Toraya T. Identification of a reactivating factor for adenosylcobalamin-dependent ethanolamine ammonia lyase. *J Bacteriol.*

-
- 2004;186(20):6845–54.
75. Buan NR, Escalante-Semerena JC. Purification and initial biochemical characterization of ATP:Cob(I)alamin adenosyltransferase (EutT) enzyme of *Salmonella enterica*. *J Biol Chem*. 2006;281(25):16971–7.
 76. Sheppard DE, Penrod JT, Bobik T, Kofoed E, Roth JR. Evidence that a B12-adenosyl transferase is encoded within the ethanolamine operon of *Salmonella enterica*. *J Bacteriol*. 2004;186(22):7635–44.
 77. Buan NR, Suh SJ, Escalante-Semerena JC. The *eutT* gene of *Salmonella enterica* encodes an oxygen-labile, metal-containing ATP: Corrinoid adenosyltransferase enzyme. *J Bacteriol*. 2004;186(17):5708–14.
 78. Penrod JT, Roth JR. Conserving a volatile metabolite: A role for carboxysome-like organelles in *Salmonella enterica*. *J Bacteriol*. 2006;188(8):2865–74.
 79. Cameron JC, Wilson SC, Bernstein SL, Kerfeld CA. Biogenesis of a bacterial organelle: The carboxysome assembly pathway. *Cell*. 2013;155(5):1131.
 80. Chen AH, Robinson-Mosher A, Savage DF, Silver PA, Polka JK. The Bacterial Carbon-Fixing Organelle Is Formed by Shell Envelopment of Preassembled Cargo. *PLoS One*. 2013;8(9):e76127.
 81. Bonacci W, Teng PK, Afonso B, Niederholtmeyer H, Grob P, Silver PA, et al. Modularity of a carbon-fixing protein organelle. *Proc Natl Acad Sci U S A*. 2012;109(2):478–83.
 82. Parsons JB, Dinesh SD, Deery E, Leech HK, Brindley AA, Heldt D, et al. Biochemical and structural insights into bacterial organelle form and biogenesis. *J Biol Chem*. 2008;283(21):14366–75.
 83. Fan C, Cheng S, Sinha S, Bobik TA. Interactions between the termini of lumen enzymes and shell proteins mediate enzyme encapsulation into bacterial microcompartments. 2012;109(37):14995–5000.
 84. Fan C, Bobik TA. The n-terminal region of the medium subunit (pdud) packages adenosylcobalamin-dependent diol dehydratase (pducde) into the pdu microcompartment. *J Bacteriol*. 2011;193(20):5623–8.
 85. Aussignargues C, Pandelia ME, Sutter M, Plegaria JS, Zarzycki J, Turmo A, et al. Structure and Function of a Bacterial Microcompartment Shell Protein Engineered to Bind a [4Fe-4S] Cluster. *J Am Chem Soc*. 2016 Apr 27;138(16):5262–70.
 86. Fan C, Cheng S, Sinha S, Bobik TA, Roth JR. Interactions between the termini of lumen enzymes and shell proteins mediate enzyme encapsulation into bacterial

-
- microcompartments. *Proc Natl Acad Sci.* 2012;109(37):14995-15000.
87. Fan C, Cheng S, Liu Y, Escobar CM, Crowley CS, Jefferson RE. Short N-terminal sequences package proteins into bacterial microcompartments. 2010;107(16):7509–14.
88. Lehman BP, Chowdhury C, Bobik TA. The N terminus of the PduB protein binds the protein shell of the Pdu microcompartment to its enzymatic core. *J Bacteriol.* 2017;199(8):e00785-16.
89. Erbilgin O, Sutter M, Kerfeld CA. The Structural Basis of Coenzyme A Recycling in a Bacterial Organelle. Petsko GA, editor. *PLOS Biol.* 2016;14(3):e1002399.
90. Choudhary S, Quin MB, Sanders MA, Johnson ET, Schmidt-Dannert C. Engineered protein nano-compartments for targeted enzyme localization. *PLoS One.* 2012;7(3):e33342.
91. Havemann GD, Bobik TA. Protein content of polyhedral organelles involved in coenzyme B₁₂-dependent degradation of 1,2-propanediol in *Salmonella enterica* serovar Typhimurium LT2. *J Bacteriol.* 2003;185(17):5086–95.
92. Kerfeld CA, Aussignargues C, Zarzycki J, Cai F, Sutter M. Bacterial microcompartments. *Nat Rev Microbiol.* 2018;16(5):277–90.
93. Pfam: Family: BMC (PF00936) [Internet]. Available from: <https://pfam.xfam.org/family/PF00936>
94. Pfam: Family: EutN_CcmL (PF03319) [Internet]. Available from: <https://pfam.xfam.org/family/PF03319>
95. Tanaka S, Sawaya MR, Phillips M, Yeates TO. Insights from multiple structures of the shell proteins from the β -carboxysome. *Protein Sci.* 2008;18(1):108–20.
96. Cai F, Sutter M, Cameron JC, Stanley DN, Kinney JN, Kerfeld CA. The structure of CcmP, a tandem bacterial microcompartment domain protein from the β -carboxysome, forms a subcompartment within a microcompartment. *J Biol Chem.* 2013;288(22):16055–63.
97. Pang A, Warren MJ, Pickersgill RW. Structure of PduT, a trimeric bacterial microcompartment protein with a 4Fe-4S cluster-binding site. *Acta Crystallogr Sect D Biol Crystallogr.* 2011;67(2):91–6.
98. Samborska B, Kimber MS. A dodecameric CcmK2 structure suggests β -carboxysomal shell facets have a double-layered organization. *Structure.* 2012;20(8):1353–62.
99. Klein MG, Zwart P, Bagby SC, Cai F, Chisholm SW, Heinhorst S, et al.

-
- Identification and Structural Analysis of a Novel Carboxysome Shell Protein with Implications for Metabolite Transport. *J Mol Biol.* 2009;392(2):319–33.
100. Cai F, Menon BB, Cannon GC, Curry KJ, Shively JM, Heinhorst S. The pentameric vertex proteins are necessary for the icosahedral carboxysome shell to function as a CO₂ leakage barrier. *PLoS One.* 2009;4(10):e7521.
 101. Sinha S, Cheng S, Sung YW, McNamara DE, Sawaya MR, Yeates TO, et al. Alanine scanning mutagenesis identifies an asparagine-arginine-lysine triad essential to assembly of the shell of the Pdu microcompartment. *J Mol Biol.* 2014;426(12):2328–45.
 102. Sutter M, Faulkner M, Aussignargues C, Paasch BC, Barrett S, Kerfeld CA, et al. Visualization of bacterial microcompartment facet assembly using high-speed atomic force microscopy. *Nano Lett.* 2015;16(3):1590–5.
 103. Faulkner M, Zhao L-S, Barrett S, Liu L-N. Self-Assembly Stability and Variability of Bacterial Microcompartment Shell Proteins in Response to the Environmental Change. *Nanoscale Res Lett.* 2019;14(1):54.
 104. Luo Q, Hou C, Bai Y, Wang R, Liu J. Protein Assembly: Versatile Approaches to Construct Highly Ordered Nanostructures. *Chem Rev.* 2016;116(22):13571–632.
 105. Matsuura K. Synthetic approaches to construct viral capsid-like spherical nanomaterials. *Chem Commun.* 2018;54(65):8944–59.
 106. Azuma Y, Edwardson TGW, Hilvert D. Tailoring lumazine synthase assemblies for bionanotechnology. *Chem Soc Rev.* 2018;47(10):3543–57.
 107. Shimanovich U, Efimov I, Mason TO, Flagmeier P, Buell AK, Gedanken A, et al. Protein microgels from amyloid fibril networks. *ACS Nano.* 2015;9(1):43–51.
 108. Huang X, Li M, Green DC, Williams DS, Patil AJ, Mann S. Interfacial assembly of protein-polymer nano-conjugates into stimulus-responsive biomimetic protocells. *Nat Commun.* 2013;4(1):2239.
 109. Zhao L, Li Y, Wang T, Qiao S, Li X, Wang R, et al. Photocontrolled protein assembly for constructing programmed two-dimensional nanomaterials. *J Mater Chem B.* 2017;6(1):75–83.
 110. Huang X, Patil AJ, Li M, Mann S. Design and construction of higher-order structure and function in proteinosome-based protocells. *J Am Chem Soc.* 2014;136(25):9225–34.
 111. Booth R, Qiao Y, Li M, Mann S. Spatial positioning and chemical coupling in coacervate-in-proteinosome protocells. *Angew Chemie Int Ed.* 2019;131(27):9218–

-
- 22.
112. Li M, Huang X, Tang TYD, Mann S. Synthetic cellularity based on non-lipid microcompartments and protocell models. *Curr Opin Chem Biol.* 2014;22:1–11.
 113. Lawrence AD, Frank S, Newnham S, Lee MJ, Brown IR, Xue W-F, et al. Solution structure of a bacterial microcompartment targeting peptide and its application in the construction of an ethanol bioreactor. *ACS Synth Biol.* 2014;3(7):454–65.
 114. Frank S, Lawrence AD, Prentice MB, Warren MJ. Bacterial microcompartments moving into a synthetic biological world. *J Biotechnol.* 2013;163(2):273–9.
 115. Juodeikis R, Lee MJ, Mayer M, Mantell J, Brown IR, Verkade P, et al. Effect of metabolosome encapsulation peptides on enzyme activity, coaggregation, incorporation, and bacterial microcompartment formation. *Microbiologyopen.* 2020;e1010.
 116. Mayer MJ, Juodeikis R, Brown IR, Frank S, Palmer DJ, Deery E, et al. Effect of bioengineering on size, shape, composition and rigidity of bacterial microcompartments. *Sci Rep.* 2016;6:36899.
 117. Bari NK, Kumar G, Hazra JP, Kaur S, Sinha S. Functional Protein Shells Fabricated from the Self-Assembling Protein Sheets of Prokaryotic Organelles. *J Mater Chem B.* 2019;8:523–33.
 118. Lee EJ, Lee NK, Kim I-S. Bioengineered protein-based nanocage for drug delivery. *Adv Drug Deliv Rev.* 2016;106:157–71.
 119. Chowdhury C, Chun S, Pang A, Sawaya MR, Sinha S, Yeates TO, et al. Selective molecular transport through the protein shell of a bacterial microcompartment organelle. *Proc Natl Acad Sci.* 2015;12(10):2990–5.
 120. Chowdhury C, Chun S, Sawaya MR, Yeates TO, Bobik TA. The function of the PduJ microcompartment shell protein is determined by the genomic position of its encoding gene. *Mol Microbiol.* 2016;101(5):770–83.
 121. Kim EY, Slininger MF, Tullman-Ercek D. The effects of time, temperature, and pH on the stability of PDU bacterial microcompartments. *Protein Sci.* 2014;23(10):1434–41.
 122. Pieters BJGE, van Eldijk MB, Nolte RJM, Mecinović J. Natural supramolecular protein assemblies. *Chem Soc Rev.* 2016;45(1):24–39.
 123. Bari NK, Kumar G, Bhatt A, Hazra JP, Garg A, Ali ME, et al. Nanoparticle Fabrication on Bacterial Microcompartment Surface for the Development of Hybrid Enzyme-Inorganic Catalyst. *ACS Catal.* 2018;8(9):7742–8.

-
124. Liu Y, Leal NA, Sampson EM, Johnson CL V, Havemann GD, Bobik TA. PduL is an evolutionarily distinct phosphotransacylase involved in B12-dependent 1, 2-propanediol degradation by *Salmonella enterica* serovar Typhimurium LT2. *J Bacteriol.* 2007;189(5):1589–96.
 125. Bradford MM. A rapid and sensitive method for the quantitation of microgram quantities of protein utilizing the principle of protein-dye binding. *Anal Biochem.* 1976;72(1–2):248–54.
 126. Wang L, Wen P, Liu X, Zhou Y, Li M, Huang Y, et al. Single-step fabrication of multi-compartmentalized biphasic proteinosomes. *Chem Commun.* 2017;53(61):8537–40.
 127. Cheng S, Sinha S, Fan C, Liu Y, Bobik TA. Genetic analysis of the protein shell of the microcompartments involved in coenzyme B12-dependent 1, 2-propanediol degradation by *Salmonella*. *J Bacteriol.* 2011;193(6):1385–92.
 128. Toraya T, Honda S, Fukui S. Fermentation of 1,2-propanediol with 1,2-ethanediol by some genera of Enterobacteriaceae, involving coenzyme B12-dependent diol dehydratase. *J Bacteriol.* 1979;139(1):39–47.
 129. Kapil N, Singh A, Das D. Cross- β Amyloid Nanohybrids Loaded With Cytochrome C Exhibit Superactivity in Organic Solvents. *Angew Chemie.* 2015;127(22):6592–5.
 130. Wright TA, Stewart JM, Page RC, Konkolewicz D. Extraction of Thermodynamic Parameters of Protein Unfolding Using Parallelized Differential Scanning Fluorimetry. *J Phys Chem Lett.* 2017;8(3):553–8.
 131. Louis-Jeune C, Andrade-Navarro MA, Perez-Iratxeta C. Prediction of protein secondary structure from circular dichroism using theoretically derived spectra. *Proteins Struct Funct Bioinforma.* 2012;80(2):374–81.
 132. Bolisetty S, Mezzenga R. Amyloid–carbon hybrid membranes for universal water purification. *Nat Nanotechnol.* 2016;11(4):365–71.
 133. Bernstein FC, Koetzle TF, Williams GJB, Meyer EF, Brice MD, Rodgers JR, et al. The protein data bank: A computer-based archival file for macromolecular structures. *J Mol Biol.* 1977;112(3):535–42.
 134. Morris GM, Goodsell DS, Halliday RS, Huey R, Hart WE, Belew RK, et al. Automated Docking Using a Lamarckian Genetic Algorithm and an Empirical Binding Free Energy Function. *J Comput Chem.* 1998;19(14):1639–62.
 135. Bikadi Z, Hazai E. Application of the PM6 semi-empirical method to modeling

-
- proteins enhances docking accuracy of AutoDock. *J Cheminform.* 2009;1(1):15.
136. Sinha S, Cheng S, Sung YW, McNamara DE, Sawaya MR, Yeates TO, et al. Alanine scanning mutagenesis identifies an asparagine–arginine–lysine triad essential to assembly of the shell of the Pdu microcompartment. *J Mol Biol.* 2014;426(12):2328–45.
137. Shibata N, Masuda J, Morimoto Y, Yasuoka N, Toraya T. Substrate-induced conformational change of a coenzyme B12-dependent enzyme: crystal structure of the substrate-free form of diol dehydratase. *Biochemistry.* 2002;41(42):12607–17.
138. DeLano WL. Pymol: An open-source molecular graphics tool. *CCP4 Newsl protein Crystallogr.* 2002;40(1):82–92.
139. Humphrey W, Dalke A, Schulten K. VMD: visual molecular dynamics. *J Mol Graph.* 1996;14(1):33–8.
140. Pettersen EF, Goddard TD, Huang CC, Couch GS, Greenblatt DM, Meng EC, et al. UCSF Chimera - A visualization system for exploratory research and analysis. *J Comput Chem.* 2004;25(13):1605–12.
141. Pang A, Warren MJ, Pickersgill RW. Structure of PduT, a trimeric bacterial microcompartment protein with a 4Fe–4S cluster-binding site. *Acta Crystallogr Sect D Biol Crystallogr.* 2011;67(2):91–6.
142. Crowley CS, Cascio D, Sawaya MR, Kopstein JS, Bobik TA, Yeates TO. Structural insight into the mechanisms of transport across the *Salmonella enterica* Pdu microcompartment shell. *J Biol Chem.* 2010;285(48):37838–46.
143. Chowdhury C, Chun S, Pang A, Sawaya MR, Sinha S, Yeates TO, et al. Selective molecular transport through the protein shell of a bacterial microcompartment organelle. *Proc Natl Acad Sci U S A.* 2015;112(10):2990–5.
144. Crowley CS, Sawaya MR, Bobik TA, Yeates TO. Structure of the PduU shell protein from the Pdu microcompartment of *Salmonella*. *Structure.* 2008;16(9):1324–32.
145. Sutter M, Faulkner M, Aussignargues C, Paasch BC, Barrett S, Kerfeld CA, et al. Visualization of Bacterial Microcompartment Facet Assembly Using High-Speed Atomic Force Microscopy. *Nano Lett.* 2015;16(3):1590–5.
146. Chowdhury C, Chun S, Sawaya MR, Yeates TO, Bobik TA. The function of the PduJ microcompartment shell protein is determined by the genomic position of its encoding gene. *Mol Microbiol.* 2016;101(5):770–83.
147. Johnson RJ, Savas CJ, Kartje Z, Hoops GC. Rapid and adaptable measurement of protein thermal stability by differential scanning fluorimetry: updating a common

-
- biochemical laboratory experiment. *J Chem Educ.* 2014;91(7):1077–80.
148. Jiang B, Jain A, Lu Y, Hoag SW. Probing Thermal Stability of Proteins with Temperature Scanning Viscometer. *Mol Pharm.* 2019;16(8):3687–93.
149. Rodrigues J V, Prosinecki V, Marrucho I, Rebelo LPN, Gomes CM. Protein stability in an ionic liquid milieu: on the use of differential scanning fluorimetry. *Phys Chem Chem Phys.* 2011;13(30):13614–6.
150. Hellman LM, Yin L, Wang Y, Blevins SJ, Riley TP, Belden OS, et al. Differential scanning fluorimetry based assessments of the thermal and kinetic stability of peptide–MHC complexes. *J Immunol Methods.* 2016;432:95–101.
151. Menzen T, Friess W. High-throughput melting-temperature analysis of a monoclonal antibody by differential scanning fluorimetry in the presence of surfactants. *J Pharm Sci.* 2013;102(2):415–28.
152. Kant R, Llauro A, Rayaprolu V, Qazi S, de Pablo PJ, Douglas T, et al. Changes in the stability and biomechanics of P22 bacteriophage capsid during maturation. *Biochim Biophys Acta (BBA)-General Subj.* 2018;1862(6):1492–504.
153. Niesen FH, Berglund H, Vedadi M. The use of differential scanning fluorimetry to detect ligand interactions that promote protein stability. *Nat Protoc.* 2007;2(9):2212.
154. Wan KF, Wang S, Brown CJ, Yu VC, Entzeroth M, Lane DP, et al. Differential scanning fluorimetry as secondary screening platform for small molecule inhibitors of Bcl-XL. *Cell Cycle.* 2009;8(23):3943–52.
155. Miyazaki Y, Koma T, Adachi A, Nomaguchi M. Novel In Vitro Screening System Based on Differential Scanning Fluorimetry to Search for Small Molecules against the Disassembly or Assembly of HIV-1 Capsid Protein. *Front Microbiol.* 2017;8:1413.
156. Kerfeld CA, Sawaya MR, Tanaka S, Nguyen C V, Phillips M, Beeby M, et al. Protein structures forming the shell of primitive bacterial organelles. *Science (80-).* 2005;309(5736):936–8.
157. Matulis D, Kranz JK, Salemme FR, Todd MJ. Thermodynamic stability of carbonic anhydrase: measurements of binding affinity and stoichiometry using ThermoFluor. *Biochemistry.* 2005;44(13):5258–66.
158. Kozakov D, Hall DR, Xia B, Porter KA, Padhorny D, Yueh C, et al. The ClusPro web server for protein–protein docking. *Nat Protoc.* 2017;12(2):255.
159. Kroeger T, Frieg B, Zhang T, Hansen FK, Marmann A, Proksch P, et al. EDTA aggregates induce SYPRO orange-based fluorescence in thermal shift assay. *PLoS*

-
- One. 2017;12(5):e0177024.
160. Jorda J, Liu Y, Bobik TA, Yeates TO. Exploring bacterial organelle interactomes: a model of the protein-protein interaction network in the Pdu microcompartment. *PLoS Comput Biol.* 2015;11(2):e1004067.
161. Park J, Chun S, Bobik TA, Houk KN, Yeates TO. Molecular Dynamics Simulations of Selective Metabolite Transport across the Propanediol Bacterial Microcompartment Shell. *J Phys Chem B.* 2017;121(34):8149–54.
162. Takenoya M, Nikolakakis K, Sagermann M. Crystallographic insights into the pore structures and mechanisms of the EutL and EutM shell proteins of the ethanolamine-utilizing microcompartment of *Escherichia coli*. *J Bacteriol.* 2010;192(22):6056–63.
163. Bai W, Sargent CJ, Choi J-M, Pappu R V, Zhang F. Covalently-assembled single-chain protein nanostructures with ultra-high stability. *Nat Commun.* 2019;10(1):1–10.
164. Kuan SL, Bergamini FRG, Weil T. Functional protein nanostructures: a chemical toolbox. *Chem Soc Rev.* 2018;47(24):9069–105.
165. Li S, Roy P, Travesset A, Zandi R. Why large icosahedral viruses need scaffolding proteins. *Proc Natl Acad Sci.* 2018;115(43):10971–6.
166. Györvary E, Schroedter A, Talapin D V, Weller H, Pum D, Sleytr UB. Formation of nanoparticle arrays on S-layer protein lattices. *J Nanosci Nanotechnol.* 2004;4(1–1):115–20.
167. Qiu L, McCaffrey R, Zhang W. Synthesis of Metallic Nanoparticles Using Closed-Shell Structures as Templates. *Chem Asian J.* 2018;13(4):362–72.
168. Krajina BA, Proctor AC, Schoen AP, Spakowitz AJ, Heilshorn SC. Biotemplated synthesis of inorganic materials: An emerging paradigm for nanomaterial synthesis inspired by nature. *Prog Mater Sci.* 2018;91:1–23.
169. Ghosh D, Lee Y, Thomas S, Kohli AG, Yun DS, Belcher AM, et al. M13-templated magnetic nanoparticles for targeted in vivo imaging of prostate cancer. *Nat Nanotechnol.* 2012;7(10):677–82.
170. Wang W, Anderson CF, Wang Z, Wu W, Cui H, Liu C-J. Peptide-templated noble metal catalysts: syntheses and applications. *Chem Sci.* 2017;8(5):3310–24.
171. Neltner B, Peddie B, Xu A, Doenlen W, Durand K, Yun DS, et al. Production of hydrogen using nanocrystalline protein-templated catalysts on M13 phage. *ACS Nano.* 2010;4(6):3227–35.
172. Oh D, Qi J, Han B, Zhang G, Carney TJ, Ohmura J, et al. M13 virus-directed

-
- synthesis of nanostructured metal oxides for lithium-oxygen batteries. *Nano Lett.* 2014;14(8):4837–45.
173. Oh D, Dang X, Yi H, Allen MA, Xu K, Lee YJ, et al. Graphene sheets stabilized on genetically engineered M13 viral templates as conducting frameworks for hybrid energy-storage materials. *Small.* 2012;8(7):1006–11.
174. Dujardin E, Peet C, Stubbs G, Culver JN, Mann S. Organization of metallic nanoparticles using tobacco mosaic virus templates. *Nano Lett.* 2003;3(3):413–7.
175. Beck T, Tetter S, Künzle M, Hilvert D. Construction of Matryoshka-Type Structures from Supercharged Protein Nanocages. *Angew Chemie Int Ed.* 2015;54(3):937–40.
176. McMillan RA, Paavola CD, Howard J, Chan SL, Zaluzec NJ, Trent JD. Ordered nanoparticle arrays formed on engineered chaperonin protein templates. *Nat Mater.* 2002;1(4):247–52.
177. McMillan RA, Howard J, Zaluzec NJ, Kagawa HK, Mogul R, Li Y-F, et al. A self-assembling protein template for constrained synthesis and patterning of nanoparticle arrays. *J Am Chem Soc.* 2005;127(9):2800–1.
178. Yang W, Guo W, Chang J, Zhang B. Protein/peptide-templated biomimetic synthesis of inorganic nanoparticles for biomedical applications. *J Mater Chem B.* 2017;5(3):401–17.
179. Lee J, Bhak G, Lee J, Park W, Lee M, Lee D, et al. Free-Standing Gold-Nanoparticle Monolayer Film Fabricated by Protein Self-Assembly of α -Synuclein. *Angew Chemie Int Ed.* 2015;54(15):4571–6.
180. Böker A, Lin Y, Chiapperini K, Horowitz R, Thompson M, Carreon V, et al. Hierarchical nanoparticle assemblies formed by decorating breath figures. *Nat Mater.* 2004;3(5):302–6.
181. Dannhauser PN, Platen M, Böning H, Schaap IAT. Durable protein lattices of clathrin that can be functionalized with nanoparticles and active biomolecules. *Nat Nanotechnol.* 2015;10(11):954–7.
182. Lystvet SM, Volden S, Singh G, Rundgren IM, Wen H, Halskau Ø, et al. Anticancer activity from gold-alpha-lactalbumin nanoconstructs? *J Phys Chem C.* 2013;117(5):2230–8.
183. Slocik JM, Naik RR, Stone MO, Wright DW. Viral templates for gold nanoparticle synthesis. *J Mater Chem.* 2005;15(7):749–53.
184. Lee Y, Kim J, Yun DS, Nam YS, Shao-Horn Y, Belcher AM. Virus-templated Au and Au-Pt core-shell nanowires and their electrocatalytic activities for fuel cell

-
- applications. *Energy Environ Sci.* 2012;5(8):8328–34.
185. Chen PY, Dang X, Klug MT, Courchesne NMD, Qi J, Hyder MN, et al. M13 virus-enabled synthesis of titanium dioxide nanowires for tunable mesoporous semiconducting networks. *Chem Mater.* 2015;27(5):1531–40.
186. Villa A, Dimitratos N, Chan-Thaw CE, Hammond C, Prati L, Hutchings GJ. Glycerol oxidation using gold-containing catalysts. *Acc Chem Res.* 2015;48(5):1403–12.
187. Corma A, Garcia H. Supported gold nanoparticles as catalysts for organic reactions. *Chem Soc Rev.* 2008;37(9):2096–126.
188. Yarramala DS, Baksi A, Pradeep T, Rao CP. Green synthesis of protein protected fluorescent gold nanoclusters (AuNCs): Reducing the size of the AuNCs by partially occupying the Ca²⁺ site by La³⁺ in apo- α -lactalbumin and the utility of AuNCs in sensing Hg²⁺. *ACS Sustain Chem Eng.* 2017;5(7):6064-6069.

Appendix



Enhanced bacterial cellulose production from *Gluconobacter xylinus* using super optimal broth

Prathna T. Chandrasekaran · Naimat Kalim Bari · Sharmistha Sinha

Received: 15 February 2017 / Accepted: 15 July 2017 / Published online: 22 July 2017
© Springer Science+Business Media B.V. 2017

Abstract The bacterial cellulose (BC) produced by *Gluconobacter xylinus* due to its versatile properties, is used in healthcare and industrial applications. However, its use is restricted owing to the limited yield from the existing culture protocols. In the current study, BC production is studied in the presence of Super Optimal Broth with catabolite repression (SOC) medium which is used to revive *Escherichia coli* cells after electroporation or chemoporation. In SOC medium, *Gluconobacter xylinus* produces cellulose pellicles within 5 days of incubation with an enhanced conversion of the carbon source to cellulose compared to traditional Hestrin–Schramm (HS) medium. SOC medium also maintains the pH close to 7.0 in static cultures unlike in HS medium where the pH is acidic. The physico-chemical and morphological characteristics of the BC produced in SOC are determined using powder X-ray diffraction (pXRD), thermo gravimetric analysis (TGA), Brunauer–Emmett–Teller (BET) and Barrett–Joyner–Halenda (BJH), and scanning electron microscopy (SEM) analyses. Our results indicate that

SOC enhance the yield of bacterial cellulose and allows conversion of 50% of the carbon source to bacterial cellulose, compared to only 7% conversion in the case of traditional HS medium after 7 days of interaction. We also observe an increase in hydration capacity of BC produced using SOC as compared to HS media.

Keywords *Gluconobacter xylinus* · Bacterial cellulose (BC) · Super optimal broth · Static cultures · Brunauer–Emmett–Teller (BET) · Barrett–Joyner–Halenda (BJH)

Introduction

Bacterial cellulose is an important biomaterial with diverse industrial applications owing to its versatile properties including high biocompatibility, biodegradability, high surface area, high flexibility, transparency and mechanical strength, high porosity, water retention and water absorption capacity. It has demonstrated remarkable applications in health care, sensor substrate development, food, textiles, composite membranes, electronic paper, acoustic diaphragms, to name a few (Shah et al. 2005; Klemm et al. 2006; Hong and Qiu 2008; Kurosumi et al. 2009; Zeng et al. 2011). Among the various species, *Gluconobacter xylinus* is one of the most commonly studied bacteria for producing commercial quantities of cellulose for various applications (Nguyen et al. 2008). One of the common and traditional media used for the optimized

Electronic supplementary material The online version of this article (doi:10.1007/s10570-017-1419-2) contains supplementary material, which is available to authorized users.

P. T. Chandrasekaran · N. K. Bari · S. Sinha (✉)
Institute of Nano Science and Technology (An
Autonomous Institute Supported by Department of
Science and Technology, Govt. of India), Habitat Center,
Sector 64, SAS Nagar, Mohali, Punjab, India
e-mail: sinhas@inst.ac.in

production of cellulose from bacteria is Hestrin and Schramm medium (Lin et al. 2013; Hestrin and Schramm 1954; Ruka et al. 2012). However, low yield and prolonged fermentation conditions are major drawbacks limiting its scale up and use in the industrial scale for cellulose production (Esa et al. 2014; Lin et al. 2014). Hence, it is imperative to devise strategies to enhance the yield of cellulose with a shorter fermentation time thereby enabling its commercialization. To this end researchers in the field have explored the use of media containing high glucose content such as fruit juices, maple syrup, various agricultural and industrial waste products such as molasses, thin stillage from rice wine distilleries, waste water from candied jujube processing industries with the aim to enhance cellulose production (Kurosumi et al. 2009; Zeng et al. 2011; Wu and Liu 2012; Li et al. 2015; Tyagi and Suresh 2016). However, the use of non-defined media leads to the generation of unknown by-products such as water soluble oligosaccharides and unknown metabolic intermediates which eventually lead to low bacterial cellulose yield and inconsistent quality (Khan et al. 2008; Ul-Islam et al. 2013; Tyagi and Suresh 2016). Few strains of *Gluconobacter* contain the enzyme invertase to metabolize sucrose (Embuscado et al. 1994) and few studies have indicated that certain strains of *Gluconobacter* produce levan and other polysaccharides from HS medium containing sucrose and this interferes with cellulose yield (Bae and Shoda 2004). Another major drawback in using agro industrial waste and other biomaterials as substrates for cellulose production is the difficulty in standardizing the process as the percent composition of the substrate may vary from time to time and place to place.

In the current study, the use of a modified medium, namely Super Optimal Broth with catabolite repression (SOC) for the production of cellulose from *Gluconobacter xylinus* has been reported. The modified medium is commonly used for revival of *Escherichia coli* post plasmid transformation (Hanahan 1983; Fierro et al. 2004; Maeda et al. 2004; Sun et al. 2009). Catabolite repression is a regulatory mechanism by which an organism preferentially uses carbon sources that are more readily accessible thereby limiting the expression of functions for use of secondary carbon sources and activities of corresponding enzymes. This mechanism ensures rapid growth of the organism (Gorke and Stulke 2008).

Apart from enhanced amount of glucose, SOC media is enriched with sodium, potassium and magnesium metal ions. The major objective of the present study is to determine the effect of SOC medium in influencing the cellulose production and if super optimal broth for catabolite repression could be used to enhance cellulose production in *Gluconobacter xylinus* which is also a gram negative bacteria like *E. coli*.

To the best of our knowledge, there are no available reports on the use of the SOC medium for cellulose production in *Gluconobacter xylinus*. Since studies have indicated the influence of medium composition and cultivation conditions in enhancing cellulose production (Shezad et al. 2010; Mohite and Patil 2014), the influence of various process variables like incubation time, surface area, presence of additives on cellulose production is investigated in detail in the SOC medium and compared with HS medium.

Materials and methods

Bacterial strain

Gluconobacter xylinus is obtained from the Microbial Type Culture Collection, India (MTCC 7795/ATCC 11142). The strain is cultured on Luria–Bertani medium and glycerol stocks are preserved at -80°C . Working cultures are routinely prepared for the studies from the stock.

Methods

Media

The medium used in this study is modified SOC medium at pH 5.5 (Super Optimal Broth with Catabolite Repression) (Lessard 2013) hereafter denoted as SOC_{5.5}. The medium is constituted by adding 2 g Luria–Bertani Broth, 0.36 g glucose, 0.05 g sodium chloride, 0.018 g potassium chloride, 0.095 g magnesium chloride, 0.25 g magnesium sulphate per 100 ml of medium. The pH of the medium is adjusted to 5.5 using 0.1 g of citric acid. Hestrin–Schramm medium which has previously been reported to be an optimal medium for the cultivation of *Gluconobacter xylinus* is used as a control (Hestrin and Schramm 1954).

Synthesis and purification of bacterial cellulose

10% (v/v) of 12 h overnight cultures of *Gluconobacter xylinus* are inoculated into fresh medium and incubated at 30 °C under static conditions. To enhance the reproducibility of the results, the factorial design of experiments is employed in the study wherein one factor at a time is varied keeping the others constant.

In one variation of the synthesis process, the culture is incubated for different time points (for 3, 5 and 7 days) keeping the other factors like incubation conditions (static), ionic concentration, medium volume and surface area constant.

The effect of sub-culturing is also studied by replacing the spent medium with fresh medium and culture after 2 days of inoculation and further incubated for additional 5 days. The influence of ionic concentrations is also determined by carrying out cellulose synthesis in the presence of increased concentration of ions in SOC_{5.5} (0.1 g sodium chloride, 0.036 g potassium chloride, 0.19 g magnesium chloride, 0.50 g magnesium sulphate).

In another variation of the synthesis process, the culture is incubated under agitated conditions keeping the other factors like ionic concentration, medium volume, incubation time and surface area constant. The flasks are maintained at 30 °C with agitation at 150 rpm.

The effect of surface area to volume ratio of the medium on cellulose production is also studied by incubating the culture in different culture vessels (petri plates and beakers) while maintaining the other parameters such as medium volume, incubation time, incubation conditions (static/agitated) and ionic composition constant.

After incubation, the pellicles produced are harvested and washed with distilled water followed by boiling at 60 °C with 0.1% NaOH for 1 h to remove the cell debris and medium components (Mohite and Patil 2014). This process of washing is repeated until the pH of the water is neutral. The resulting bacterial cellulose is freeze-dried using a lyophilizer (BenchTop Pro with Omnitronics, VirTis SP Scientific, Pennsylvania) and stored at room temperature till further use.

Determination of dry weight and yield of bacterial cellulose

Dry weight of bacterial cellulose is calculated in terms of weight of cellulose obtained per liter of

medium used as described in Mohammadkazemi et al. (2015).

$$\text{Dry weight} = \frac{\text{weight of cellulose (g)}}{\text{volume of media (l)}} \quad (1)$$

% yield is calculated from the dry weight of cellulose according to a protocol developed in Erbas Kiziltas et al. (2015).

$$\text{Yield} = \frac{\text{dry weight of cellulose (g)}}{\text{weight of carbon source (g)}} \times 100 \quad (2)$$

Hydration studies on bacterial cellulose

Hydration capacity

The hydration capacity of bacterial cellulose is calculated as described in Lin et al. (2013), Oliveira Barud et al. (2015), Bakre and Jaiyeoba (2009), and Mohamad et al. (2014). Briefly, weighed quantities of freeze dried bacterial cellulose are added to distilled water followed by vortexing of the resulting solution. The solution is then allowed to stand for 3–5 min followed by centrifugation at 10,000 rpm for 10 min. The supernatant is discarded and the pellet is subjected to drying at 37 °C and weighed at different time points to determine the hydration capacity, swelling ratio, moisture content as per the equations below.

$$\text{Hydration capacity} = \frac{\text{Weight of hydrated sample (g)}}{\text{dry weight (g)}} \quad (3)$$

$$\text{Swelling ratio (\%)} = \frac{H_s - H_d}{H_d} \times 100 \quad (4)$$

$$\text{Moisture content ratio (\%)} = \frac{H_s - H_d}{H_s} \times 100 \quad (5)$$

where H_s and H_d are the weights of swollen and dry weights of bacterial cellulose respectively.

Physico-chemical characterization

Scanning electron microscopy (SEM)

The morphology and the surface topography of the freeze dried bacterial cellulose samples under freeze-dried condition and air dried conditions are determined using Scanning Electron Microscope (JEOL

JSM-IT300, USA) at 15 kV with a probe current of 40 μA with different magnification in various areas. The freeze dried samples are obtained as mentioned in the purification protocol above. The freeze dried samples are mounted on carbon tapes followed by gold sputtering for 60 s. For the air dried samples (0.4 wt%), bacterial cellulose is suspended in Mili-Q water and left at room temperature for 2 h. The resultant sample is drop-casted on silicon wafers and then subjected to air drying at 37 °C for 12 h. The samples are then stored at room temperature till imaging. Prior to imaging the samples are gold sputtered for 60 s.

Brunauer–Emmett–Teller (BET) and Barrett–Joyner–Halenda (BJH) surface area analysis

The pore size and surface area of the lyophilized bacterial cellulose are determined with a Nova Quantachrome, BET surface area analyzer. To remove moisture from the samples, the samples were placed in sample cells, which were then heated up to 75 °C for 5 h and cooled down to room temperature before the BET and BJH analysis. The pore size and surface area are determined with N_2 adsorption at -196.15 °C. The pore volume and average pore size (pore size distribution) is calculated based on summing through the pore size distribution which is subjected to BJH model. This method is based on the assumption that the initial relative pressure is close to unity and all pores are filled with liquid. The following equation is employed to calculate the pore dimensions.

$$V_{pn} = \left(\frac{r_{pn}}{r_{kn+\Delta t_n/2}} \right)^2 \left(\Delta V_n - \Delta t_n \sum_{j=1}^{n-1} A c_j \right) \quad (6)$$

where r_{pn} : pore radius; V_{pn} : pore volume; r_{kn} : inner capillary radius; Δt : thickness of adsorbed layer of nitrogen; $A c$: area exposed by the pore from which the physically adsorbed gas is desorbed.

Powder X ray diffraction (pXRD)

pXRD patterns of cellulose were obtained using a diffractometer (D8 Advance Eco, Bruker, Germany) using nickel filtered Cu $K\alpha$ radiation ($\lambda = 1.54060$ Å) with a scanning range between $2\theta = 10^\circ$ – 50° at room temperature. The freeze dried samples were placed on a clean glass slide for analysis. The

crystallinity index (CrI) was determined using the following equation:

$$CrI = \frac{I_{110} - I_{am}}{I_{110}} \times 100 \quad (7)$$

where I_{110} is the maximum intensity of diffraction of the (110) lattice peak and I_{am} is the minimum intensity of the amorphous material between 2θ of 18° – 19° (Segal et al. 1959; French and Santiago Cintrón 2013; French 2014).

Fourier transform infra-red (FT-IR) spectroscopy

FT-IR analysis is performed to determine the chemical structure of BC. The samples were oven dried at 105 °C for 4–5 h, mixed with KBr in a ratio of 1:200 (w/w) and pressed under vacuum to form pellets. The FT-IR spectra were examined in the mid IR range (4000 – 500 cm^{-1}) using a FT-IR spectrophotometer (Cary 600 series, FTIR Spectrophotometer, Agilent Technologies).

Thermogravimetric analysis (TGA)

TGA analysis is performed to determine the thermal stability of the material. TGA measurements were carried out using a Simultaneous Thermal Analyzer (STA 8000, Perkin Elmer, USA). 10 mg of the samples were used for the analysis and were scanned over a temperature range of 50 – 800 °C at a heating rate of 10 °C/min with N_2 gas flow rate of 20 ml/min. The analysis was performed under inert N_2 atmosphere to avoid sample oxidation (Amin et al. 2014; Mohite and Patil 2014).

Results and discussion

In this article we report biosynthesis of bacterial cellulose in super optimal growth medium with catabolite repression. SOC is used to regenerate *E. coli* cells after introduction of foreign genetic material by electroporation or chemoporation. Using a combination of microbiological, biochemical and biophysical techniques, we attempted to determine if SOC medium is an efficient growth medium for *Gluconobacter xylinus* which leads to an increased production of bacterial cellulose in a shorter time compared to traditional HS medium. It has been previously

reported that process parameters like time, temperature, pH as well as the media compositions play crucial roles in the form and structure of bacterial cellulose (Ruka et al. 2012). As it has already been reported that the optimal pH for cellulose production in *Gluconobacter* is 5.5, we have modified the initial pH of SOC medium (hereafter mentioned as SOC_{5.5} in the manuscript) to the same. We observe that in SOC_{5.5} medium, the growth of *Gluconobacter xylinus* progresses with a very small lag phase of 8 h compared to 24 h in the traditional HS medium in static cultures (Fig. 1a). Also, at the end of 168 h or 7 days, the OD₆₀₀ for SOC_{5.5} is ~2 times more compared to the HS medium suggesting a much faster metabolism or growth rate in SOC_{5.5} compared to HS medium. In shaking cultures also similar trend is observed (Supplementary Fig. S1a). This is interesting considering the amount of glucose in the SOC_{5.5} medium which is nearly one-fifth compared to that used in HS medium. We also monitored the change in pH of the medium during the course of cellulose production in both static and shaking cultures in both media (Fig. 1b and Supplementary Fig. S1b). In static cultures, for both SOC_{5.5} and HS media, the pH immediately after the commencement of the interaction is 5.5. In the case of SOC_{5.5}, immediately after the lag phase there is a monotonous increase in the pH value which stabilizes around ~7.0. Conversely in the case of HS medium, after an initial increase in the pH till 24 h, there is a drop in the pH value with time. This suggests that in the case of HS medium there is an accumulation of acidic metabolites (viz. gluconic acid) as is observed in the case of bacterial cellulose production (Yang et al. 2014; Huang et al. 2015a, b; Park et al. 2015). Previous studies have also reported the inhibition of bacterial cellulose production due to the accumulation of gluconic acid in HS medium (Kuo et al. 2016). In SOC_{5.5} medium the acidic metabolites are produced in minimal quantities and they are utilized immediately to be reflected in the pH change of the medium; simultaneously, the presence of metal ions in the media might lead to the increase in the pH from 5.5–7.0. Likewise, in the shaking cultures, the growth rates are higher in SOC_{5.5} compared to HS cultures (Supplementary Fig. S1a). Interestingly, in the case of shaking cultures, the pH monotonously rises in both the cases and stabilizes ~8 for HS medium and ~8.5 for SOC_{5.5} medium. Decrease in gluconic acid production in shaking cultures could be due to

decrease in cell concentration possibly due to the instability of the bacteria, resulting in *Cel*⁻ mutants thereby interfering with the metabolism of glucose utilization to gluconic acid (Huang et al. 2015a, b; Park et al. 2015; Yang et al. 2016).

The next part of the study is designed to determine the effect of incubation time on bacterial cellulose production. We observe that the formation of cellulose film at the aqueous-air interface is dependent on the bacteria aging time in both HS and SOC_{5.5} media. For HS medium, at the end of 3 days a thin cellulose film is observed which increases in thickness on further incubation till 5 days. A consistently thicker pellicle is observed in SOC_{5.5} medium under similar conditions. At the end of 5 days, the % yield of cellulose using HS medium is 6.7 ± 0.2 whereas it is 40.5 ± 2.1 in case of SOC_{5.5} medium (Fig. 1c). In a related study, (Mohammadkazemi et al. 2015) determined the effect of various media on cellulose production and report that the yield % of cellulose in HS medium at the end of 7 days to be ~7%. In our experiments at the end of 7 days the yield in HS medium is ~7% while that in SOC_{5.5} is ~50%. The plot of dry weight versus incubation time is shown in Fig. 1d. The dry weight of bacterial cellulose synthesized using SOC_{5.5} medium is higher than that of bacterial cellulose synthesized using HS medium in accordance to the yield %. The yield of bacterial cellulose is ~1 g/l from HS medium and ~1.8 g/l from SOC_{5.5} medium at the end of 7 days of interaction. SOC_{5.5} medium is more effective in terms of its cellulose production considering its low concentration of carbon source used (3.6 g/l) as compared to HS medium (20 g/l). From SOC_{5.5} the yield of the bacterial cellulose is ~0.5 g/g of glucose after 7 days, while that using HS medium is ~0.05 g/g of glucose. This makes SOC_{5.5} an interesting medium for cultivation of *Gluconobacter xylinus* for the industrial production of bacterial cellulose. Earlier studies have indicated that excess concentration of glucose in the medium led to the formation of gluconic acid extracellularly by the organism thereby interfering with cellulose biosynthesis (Kuo et al. 2016). Considering only the cost of glucose and the corresponding yield of bacterial cellulose, SOC_{5.5} medium is ~30 times cost effective compared to HS medium.

The surface area to volume ratio of growth medium is an important parameter for the production of bacterial cellulose in static cultures (Çakar et al. 2014). Using SOC_{5.5} the yield% of cellulose using

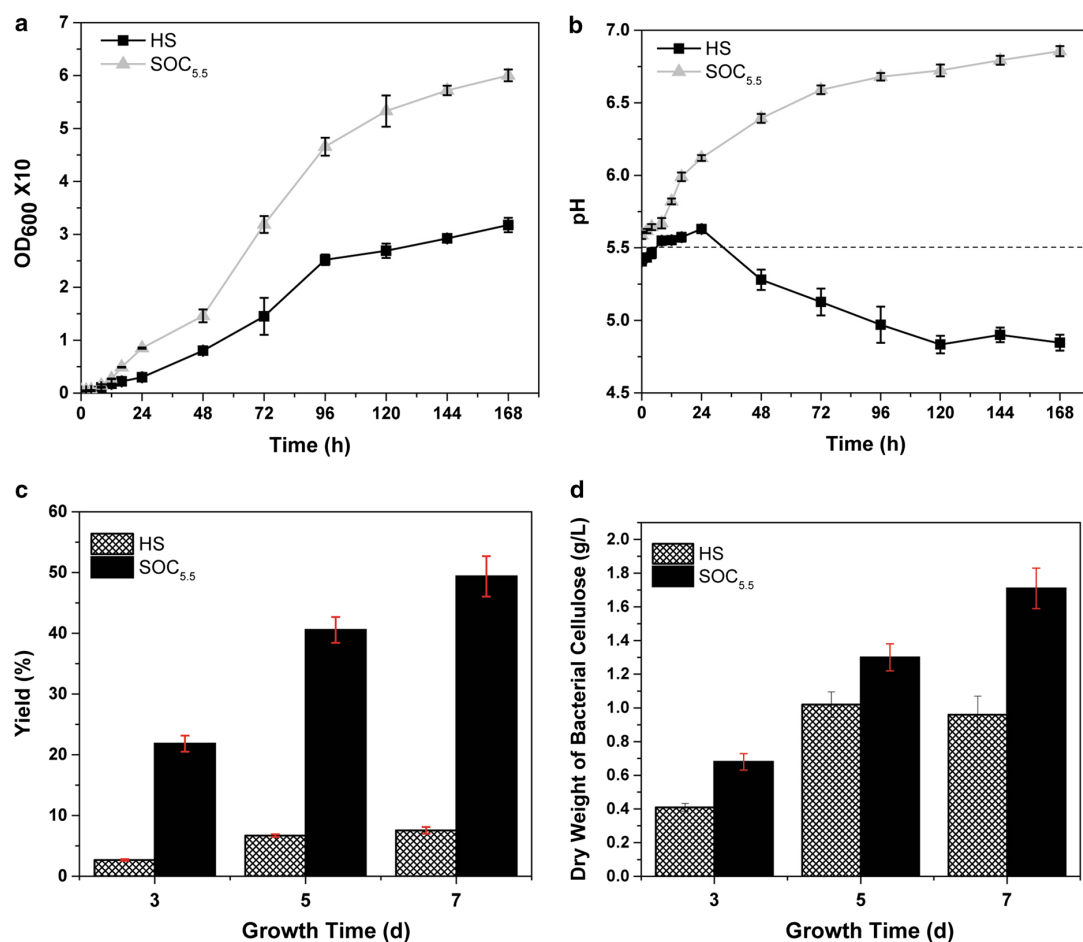


Fig. 1 **a** Growth curve of *Gluconobacter xylinus* in HS and SOC_{5.5} media under static conditions. Overnight cultures of *Gluconobacter xylinus* grown in Luria broth medium is inoculated in HS and SOC_{5.5} media and the OD₆₀₀ is measured time to time in a UV–VIS spectrophotometer. **b** Change of pH of HS and SOC_{5.5} growth media during the interaction with *Gluconobacter xylinus*. **c** Bacterial cellulose yield obtained by

incubation of *Gluconobacter xylinus* HS and SOC_{5.5} media for different time intervals. **d** Dry weight of bacterial cellulose obtained upon incubation in HS and SOC_{5.5}. The incubation time of *Gluconobacter xylinus* in HS and SOC_{5.5} media is varied from 3 to 7 days and the yield and dry weight of bacterial cellulose produced is determined

petri plates with surface area of 1432 cm² is 58 ± 2 while in beakers with surface area of 1068 cm² it is 35 ± 1.0 . In both cases, the volume of the medium is kept constant at 40 ml. An increase in the dry weight of cellulose from 1.3 ± 0.1 to 2.1 ± 0.1 is observed when the surface area of culture vessel to volume of medium ratio increased from 2.7 cm^{-1} (beaker) to 5.3 cm^{-1} (petri plate) respectively. Previous studies have also indicated that increasing the surface area to volume ratio sustained bacterial cellulose production

by enhancing oxygen transport across the bacterial cellulose layer to the microorganisms (Çakar et al. 2014). Sub-culturing of the medium after 2 days of inoculation into the petri dishes, however, did not lead to increase in the yield % of cellulose (50 ± 1) compared to (49 ± 3) in non-sub-cultured media.

Biosynthesis of cellulose is catalyzed by cellulose synthase and takes place in two steps. In the first step, polymerization of glucose units into β -1, 4-glucan units occurs while the next step follows the assembly

and crystallization of the cellulose chain. Optimization of the medium and process parameters is essential for the growth of the microorganism thereby also stimulating the formation of products and changes in the medium composition may affect product formation directly or indirectly (Chawla et al. 2009). Hence, in the next set of experiments, we varied the ionic concentration. The ions varied in this study are Na^+ , Mg^{2+} , PO_4^{3-} , K^+ and SO_4^{2-} . Increasing the ionic concentration of the optimized $\text{SOC}_{5.5}$ medium results in a decrease in the yield% and dry weight of cellulose produced. In a particular instance, the dry weight decreased from 1.47 ± 0.08 to 0.71 ± 0.025 on increasing the ionic concentration from 0.12 to 0.24 M. Metal ions are often required by a cell in trace amounts for biochemical reactions while at higher concentrations they may be toxic (Nies 1999). In a related study, (Son et al. 2001) studied the effect of concentration of PO_4^{3-} on cellulose production and observed that increasing concentration above 0.8% led to a decrease in the cellulose production. Biosynthesis of cellulose is catalyzed by cellulose synthase and takes place in two steps. In the first step, polymerization of glucose units into β -1, 4-glucan units occurs while the next step follows the assembly and crystallization of the cellulose chain. Recent studies have indicated that the cellulose synthase complex (consisting of a number of subunits) preferentially utilizes divalent cations (mostly magnesium or manganese) for the formation of cellulose microfibrils (Basu et al. 2016; Omadjela et al. 2013).

Bacterial cellulose is known for its significant water absorbing and retention capacity as compared to plant cellulose (Wei et al. 2011; Amin et al. 2014; Zhao et al. 2014). The hydration property of the cellulose ultimately affects its usability as a biomaterial in varied applications. Swelling brings about a change in the fiber dimension and results in lowering the crystallinity as well as increases its accessibility (Ehrhardt et al. 2007). In our studies the hydration capacity of cellulose synthesized using HS and $\text{SOC}_{5.5}$ media is determined according to a protocol described in (Mohamad et al. 2014). The maximum hydration capacity is observed in bacterial cellulose from $\text{SOC}_{5.5}$ medium as compared to bacterial cellulose from HS medium respectively. The 0 h reading of the hydration capacity of bacterial cellulose from HS medium is 3.7 ± 0.1 while that from the $\text{SOC}_{5.5}$ medium equivalent is 8.6 ± 1.0 . At the end of 5 h of drying, the

hydration capacity decreased to 3.85 ± 0.63 in bacterial cellulose from $\text{SOC}_{5.5}$ medium while it is 1.08 ± 0.03 in the same from HS medium (Fig. 2a). The results thus indicate that changes in the medium composition lead to differences in the porous structure of the cellulose synthesized. As a control for our experiments we did similar hydration experiments with MCC and the hydration capacity of MCC obtained in our laboratory at the end of 5 h is in accordance with results obtained by Bakre and Jaiyeoba (2009), validating our protocol (unpublished results).

Swelling of a biomaterial is induced by the electrostatic repulsion of the ionic charges in the network (Karada and Saraydin 2002). The swelling % of bacterial cellulose in $\text{SOC}_{5.5}$ medium is $\sim 800\%$ while that from HS medium is $\sim 260\%$ (Fig. 2b). Swelling and water retention are important properties of hydrogels which enable their use in applications such as moist wound healing (Mohamad et al. 2014). Increase in drying periods at room temperature led to decrease in swelling % and moisture content ratio. The moisture content ratio % is $\sim 90\%$ for bacterial cellulose in $\text{SOC}_{5.5}$ medium while it is $\sim 72\%$ for bacterial cellulose in HS medium at 0 h (Fig. 2c). Increased water penetration and retention for bacterial cellulose in $\text{SOC}_{5.5}$ medium as compared to bacterial cellulose from HS medium could possibly be due to its high porosity which led to increased water penetration (Halib et al. 2010). In order to have an idea on the porosity of the bacterial cellulose grown in the two different media we next conducted BET surface area analysis and BJH pore size and volume analysis. The increase in the number and size of the pore surface results in the increase in the total surface area (Gao et al. 2011; Guo and Catchmark 2012), which is observed by the pore size of bacterial cellulose obtained from $\text{SOC}_{5.5}$ and HS medium in the present study. In BET and BJH analysis we observed that the change of growth medium from HS to $\text{SOC}_{5.5}$ changes the average pore size for bacterial cellulose grown in HS medium is 4.5 nm while that in $\text{SOC}_{5.5}$ is 11.9 nm. Similarly, the average pore volume in HS medium and $\text{SOC}_{5.5}$ medium are 0.0129–0.184 cc/g respectively. This results in an increase in the total surface area from $5.66 \text{ m}^2/\text{g}$ in bacterial cellulose from HS media to $8.95 \text{ m}^2/\text{g}$ in bacterial cellulose from $\text{SOC}_{5.5}$ medium. The total pore volume in the bacterial cellulose produced in $\text{SOC}_{5.5}$ medium is 14.2 times higher than

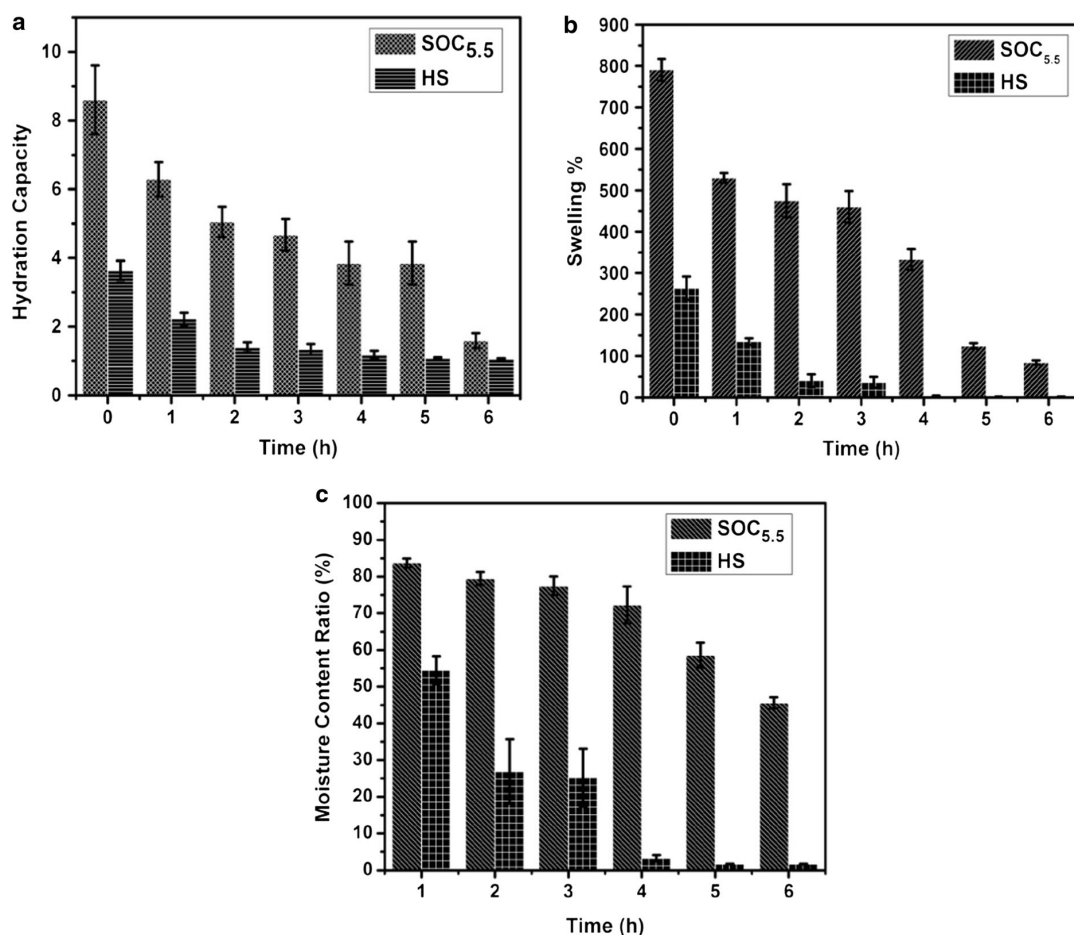


Fig. 2 **a** Hydration capacity and **b** Swelling % of bacterial cellulose. Freeze dried bacterial cellulose is hydrated with water and the hydrated pellet is weighed at different time points to determine the hydration capacity and swelling ratio as per the

equations described in the “Methods” section. **c** Moisture content % of bacterial cellulose. The moisture content % of the hydrated bacterial cellulose is determined using equation described in the “Material” section

that produced in HS media. (Table 1). The adsorption–desorption isotherms of the same are shown in Fig. 3.

Based on these observations the cellulose derived from both SOC_{5.5} and HS medium fall under the category of mesoporous materials (Schlesinger et al. 2015). The packing of the cellulose fibrils determines the surface area and the porosity and the closely arranged fibrils have lower porosity, which also decreases the total surface area (Ul-Islam et al. 2012). The water holding capacity (WHC) of bacterial cellulose samples can be attributed to their respective

Table 1 Surface area and porosity of bacterial cellulose

	HS media	SOC _{5.5} media
Surface area	5.66 m ² /g	8.95 m ² /g
Average pore size	4.57 nm	11.9 nm
Total pore volume	0.0129 cc/g	0.184 cc/g

porosity and surface areas. The water molecules are trapped physically on the surface and inside the bacterial cellulose matrix consisting of reticulated

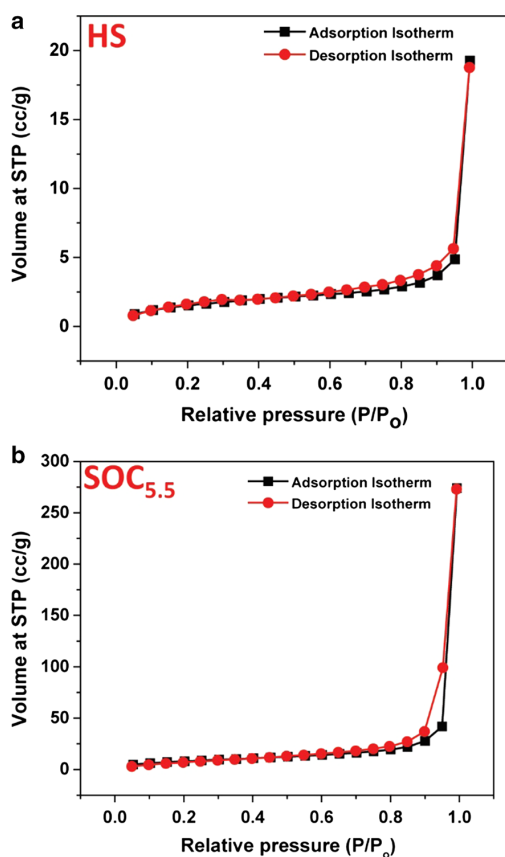


Fig. 3 Adsorption and Desorption isotherms for bacterial cellulose grown in **a** HS and **b** SOC_{5.5} media

fibrils (Watanabe et al. 1998). With more empty spaces among the bacterial cellulose fibrils, more water can penetrate and adsorb onto the material. Thus, the greater the surface area and the larger the pore size, the greater will be the WHC of the bacterial cellulose sample. Bacterial cellulose obtained from SOC_{5.5} medium has 1.6 times higher surface area, 2.7 times higher average pore size and 14.2 times higher pore volume than HS derived bacterial cellulose. This 1.6 times higher surface area and 2.7 times larger pore size leads to higher hydration capacity and swelling ratio while the 14.2 times higher pore volume leads to enhanced water retention as shown (Fig. 2; Table 1). The enhanced total pore volume along with the swelling capacity makes the SOC_{5.5} derived bacterial cellulose a good candidate for moist wound dressing materials.

Next we analyzed the morphology of bacterial cellulose synthesized using both the media using SEM under different processing conditions. Figure 4 shows the SEM micrographs of cellulose synthesized using HS and SOC_{5.5} media respectively with different processing protocols as described in the materials section. The freeze dried samples from HS medium appears more granular (panel A) and discrete while that obtained from the SOC_{5.5} medium offers a porous structure (panel C). One potential factor in the observed differences for freeze-dried samples is the ratio of particles to water before freezing. As the yield from the SOC_{5.5} media is close to 8 times the yield from the HS media the SOC_{5.5} derived samples has a higher particle to water ratio compared to the HS derived samples. This leads to the observed difference in morphology of the two samples (Fig. 4). On the other hand in the air dried samples (0.4 wt%) from both the forms display a swollen morphology. There is a dramatic amount of decrease in the number of pores in the air dried samples of SOC_{5.5} compared to the freeze dried samples suggesting that hydration alters the morphology of the samples to a great extent. The difference in morphology of the final cellulose synthesized using both media may also be due to the difference in the initial carbon content, the interaction of the cellulose with metabolic intermediates during the interaction with the two media and in growth mechanism during bacterial activity (Rambo et al. 2008).

Both the forms of bacterial cellulose reported here show similar physico-chemical properties. The pXRD patterns of bacterial cellulose in HS medium and SOC_{5.5} medium are shown in Fig. 5. The presence of three major peaks at 14°, 16° and 22° in both forms of cellulose reported here which that are indexed to (100), (010) and (110) reflections respectively corresponds to those of cellulose I (French 2014). The three major characteristic peaks indexed to (100), (010) and (110) confirmed the I α structure of bacterial cellulose synthesized using both the media (French 2014). In the HS media the (100) peak is not very prominent. This can be attributed to the preferred orientation of bacterial cellulose causing the (100) peak to be vague in I α form (French 2014). This preferred orientation explains the changes in peak heights in the HS and SOC_{5.5} derived cellulose. Equation 7 is used to calculate the *CrI* of the two forms of cellulose as described in Segal et al. (1959), French and Santiago Cintrón (2013), French (2014). For each analyses, machine blank samples were

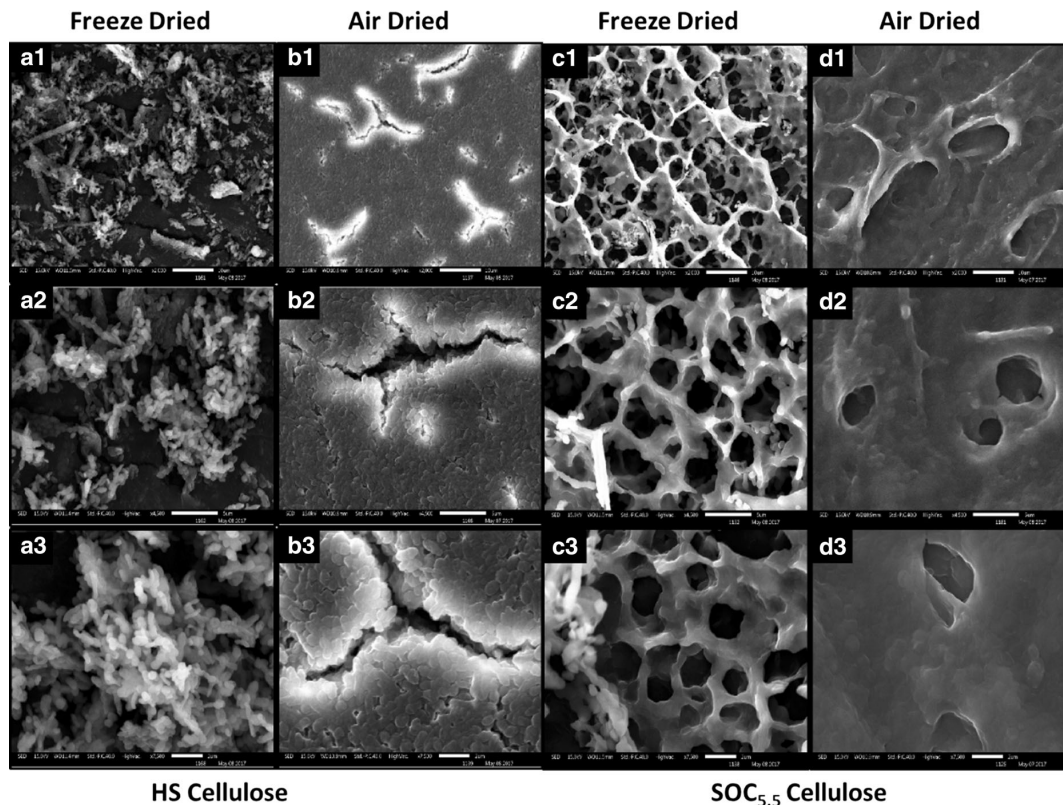


Fig. 4 SEM micrographs of bacterial cellulose synthesized using **a** HS **b** SOC_{5.5} media under different processing conditions (Freeze dried and air dried). Bacterial cellulose

subtracted from raw data. In the present study, the *CrI* of cellulose synthesized using HS and SOC_{5.5} are 79.4 and 77.2% respectively (Fig. 5) which is in accordance to the reported crystallinity of the bacterial cellulose samples obtained from *Gluconobacter* strains using glucose in the growth media (Keshk 2014; Fang and Catchmark 2015). During the initial stages of cellulose formation, bacteria extrude the cellulose fibrils from the enzyme complexes into the culture medium (Römling and Galperin 2015). This nascent cellulose is amorphous and is gradually crystallized upon the production of more cellulose (Norouziyan et al. 2011). The crystallization of bacterial cellulose is affected by several physical and physiological stimuli (Saxena et al. 1994; Hirai et al. 1998). The pXRD spectra of SOC_{5.5} medium also showed the presence of an extra peak at 28° and this could be assigned to (200) plane of KCl (Dai et al. 2014; Samavat et al. 2012). Since $I\alpha$ is a very dense structure

samples were sputter coated with gold before analysis. Magnification A1-D1 at 2000X, A2-D2 at 4500X and A3-D3 at 7500X

with no room for added ions, it is likely that the ions were not incorporated into the cellulose lattice, but present as crystals of foreign substances present.

We also analyzed the chemical structure of both forms of cellulose by comparing the FT-IR spectra of both the forms (Fig. 6). The dominant broad band in the region in between 3400 and 3000 cm^{-1} corresponds to O–H stretch of cellulose while the bands at 2900–2800 cm^{-1} are due to C–H stretching (Tabarsa et al. 2017). The bands in the region 1640–1650 cm^{-1} are due to the bending vibrations of the adsorbed water molecules, while the bands 1450–1250 cm^{-1} are due to different modes of C–H vibrations. The bands in the region 1050–1070 cm^{-1} correspond to C–O–C pyranose ring stretching vibration in cellulose (Shezad et al. 2010). The cellulosic β -glycosidic linkages are observed in the region 870–900 cm^{-1} . The FT-IR spectra of the BC produced by both media were nearly

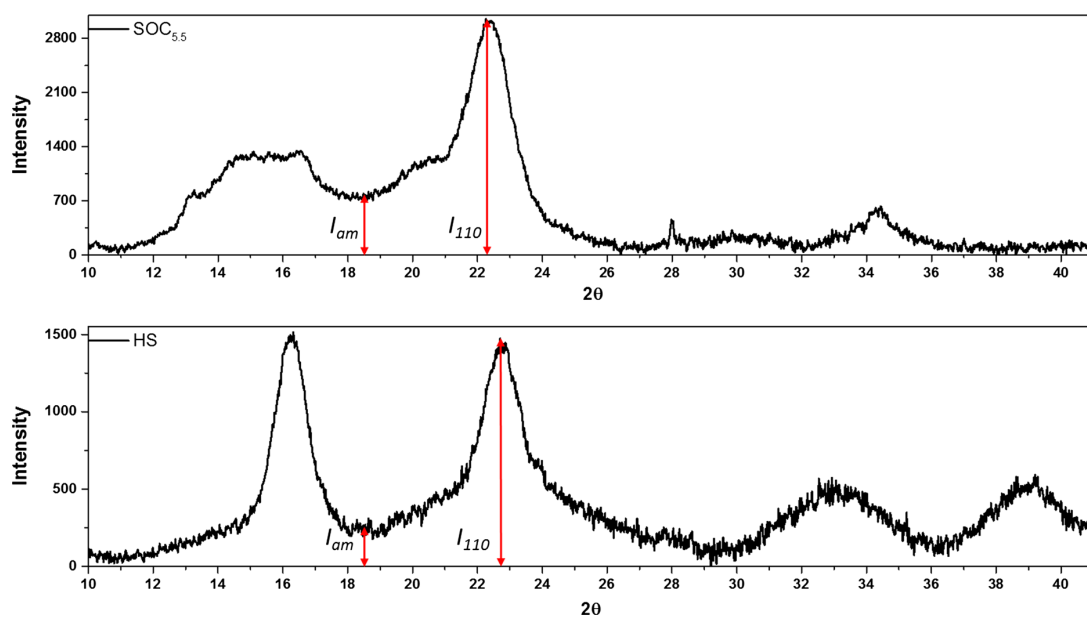


Fig. 5 pXRD of bacterial cellulose. Freeze dried bacterial cellulose is scanned over a range of $2\theta = 10^\circ\text{--}50^\circ$ using Cu K α radiation ($\lambda = 1.54060 \text{ \AA}$)

similar suggesting no major structural alteration due to the altered media.

We further performed gravimetric analyses of both the forms of cellulose. The wt% versus temperature thermo gravimetric curves for the dried bacterial cellulose pellicles in HS and SOC_{5.5} media are shown

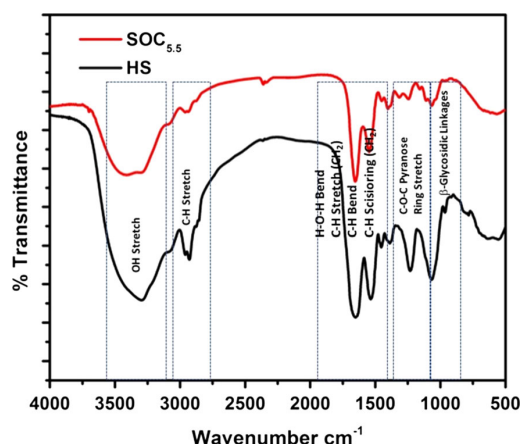


Fig. 6 FT-IR spectra of bacterial cellulose. Freeze dried bacterial cellulose is scanned between a range of $4000\text{--}500 \text{ cm}^{-1}$

in the Fig. 7. Three distinct stages of weight loss associated with HS and SOC_{5.5} cellulose with increase in temperature are observed. A 10–15% weight loss is observed around 100 °C which can be assigned to loss of trapped moisture (Erbaş Kiziltas et al. 2015). The next event is observed between 250 and 350 °C where ~ 55 to 65% weight loss occurred in both media and is characterized by cellulose degradation involving decomposition, and de-polymerization of the glycoside units (Cheng et al. 2009; Vazquez et al. 2013; Vasconcelos et al. 2017). The final 20% weight loss event occurred between 400 and 500 °C which could be attributed to the volatilization and oxidation of char followed by the formation of carbonaceous residue (Cheng et al. 2009; Tyagi and Suresh 2016; Vasconcelos et al. 2017). There were no significant differences between cellulose synthesized using the two media.

The thermal stability of any material is intrinsically dependent of the parameters like crystallinity and fiber orientation (Barud et al. 2007). In the present study, the thermal stability of cellulose synthesized using both media are similar which is supported by the similar crystallinity percentage obtained from pXRD analysis. Similar studies done with HS media

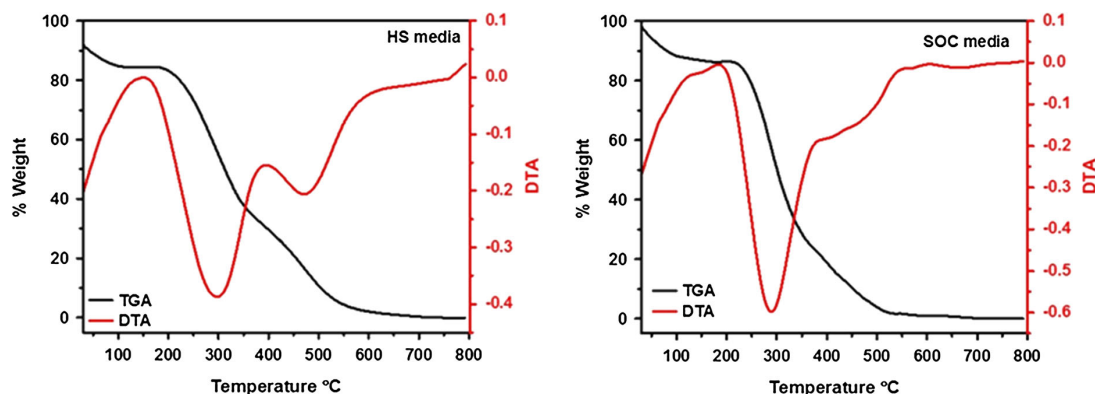


Fig. 7 TGA and DTA curves of bacterial cellulose. Bacterial cellulose samples are scanned over a temperature range of 50–800 °C at a heating rate of 10 °C/min under inert gas atmosphere

supplemented with different carbon sources show that supplementation with mannitol show the highest thermal stability and highest crystallinity (Mohammadkazemi et al. 2015).

We also tested the cyto-compatibility of both forms of BC. MTT assay revealed that the Vero cells showed normal metabolism and growth in the presence of varying concentrations of BC (0.005–50 µg/ml). Increase in the BC concentration from 5 to 50 µg/ml led to a slight decrease in the % cell viability from 115 to 90% at the end of 15 h (Supplementary Fig. S2a). Similarly, membrane permeability assay was performed to understand the cytotoxic activity of BC towards Vero cells at concentrations ranging from 0.005 to 50 µg/ml. Comparing the LDH release at different concentrations of BC, the differences were observed to be insignificant (Supplementary Fig. S2b) which further strengthens the fact the bacterial cellulose is non-toxic as LDH release is directly correlated to rupturing of the cell membranes. The cytotoxicity studies revealed that the produced BC did not affect the cell viability and could be effectively applied in biological implants and applications.

Conclusion

The present study demonstrates that the modified SOC_{5.5} medium enhances the growth rate of *Glucanobacter xylinus* and increases bacterial cellulose yield. The modified medium is more effective than the traditionally used HS medium with a ~8 fold

increase in yield at the end of 7 days of interaction. The purified bacterial cellulose pellicle from SOC_{5.5} demonstrates enhanced hydration properties compared to the pellicle obtained using HS medium. Differences in the pore structural arrangement are observed based on the medium used, although the overall property of the developed material is at par with the properties of the bacterial cellulose reported in the literature. The main essence of this study is the enhanced yield in the cellulose production with much lower use of carbon nutrient. The process developed here allows conversion of 50% of the carbon source used to bacterial cellulose, compared to only 7% conversion in the case of traditional HS medium after 7 days of interaction. This study is the first report to the authors' knowledge on the use of SOC_{5.5} growth medium in enhancing the yield of bacterial cellulose. This formulation will lead to novel avenues for the industrial scale production of bacterial cellulose using low glucose content media.

Acknowledgments The authors thank INST for financial support. PTC thanks INST for postdoctoral fellowship. Dr. Sharmistha acknowledges DST SERB for Women Excellence Award, 2017 (SB/WEA/06/2016) and INST for financial support. The authors thank Dr. Sangita Roy for helpful suggestions and discussions. The authors thank past and present members of Sinha lab for suggestions and discussions.

References

- Amin MCIM, Abadi AG, Katas H (2014) Purification, characterization and comparative studies of spray-dried bacterial cellulose microparticles. *Carbohydr Polym* 99:180–189

- Bae S, Shoda M (2004) Bacterial cellulose production by fed-batch fermentation in molasses medium. *Biotechnol Prog* 20(5):1366–1371
- Bakre LG, Jaiyeoba KT (2009) Effects of drying methods on the physicochemical and compressional characteristics of okra powder and the release properties of its metronidazole tablet formulation. *Arch Pharm Res* 32(2):259–267. doi:10.1007/s12272-009-1231-0
- Barud HS, Ribeiro CA, Crespi M, Martines MAU, Dexpert-Ghys J, Marques RFC, Messaddeq Y, Ribeiro SJL (2007) Thermal characterization of bacterial cellulose–phosphate composite membranes. *J Therm Anal Calorim* 87(3):815–818
- Basu S, Omadjela O, Gaddes D, Tadigadapa S, Zimmer J, Catchmark JM (2016) Cellulose microfibril formation by surface-tethered cellulose synthase enzymes. *ACS Nano* 10(2):1896–1907
- Çakar F, Kati A, Özer I, Demirbağ DD, Şahin F, Aytekin AÖ (2014) Newly developed medium and strategy for bacterial cellulose production. *Biochem Eng J* 92:35–40
- Chawla PR, Bajaj IB, Survase SA, Singhal RS (2009) Microbial cellulose: fermentative production and applications. *Food Technol Biotechnol* 47(2):107–124
- Cheng K-C, Catchmark JM, Demirci A (2009) Enhanced production of bacterial cellulose by using a biofilm reactor and its material property analysis. *J Biol Eng* 3:12
- Dai F, Zai J, Yi R, Gordin ML, Sohn H, Chen S, Wang D (2014) Bottom-up synthesis of high surface area mesoporous crystalline silicon and evaluation of its hydrogen evolution performance. *Nat Commun* 5:3605. doi:10.1038/ncomms4605
- Ehrhardt A, Groner S, Bechtold T (2007) Swelling behaviour of cellulosic fibres. Part I, changes in physical properties. *Fibres Text Eastern Eur* 5–6(64):46–48
- Embuscado ME, Marks JS, BeMiller JN (1994) Bacterial cellulose. I. Factors affecting the production of cellulose by *Acetobacter xylinum*. *Food Hydrocoll* 8(5):407–418
- Erbas Kiziltas E, Kiziltas A, Blumentritt M, Gardner DJ (2015) Biosynthesis of bacterial cellulose in the presence of different nanoparticles to create novel hybrid materials. *Carbohydr Polym* 129:148–155
- Esa F, Tasirin SM, Rahman NA (2014) Overview of bacterial cellulose production and application. *Agric Agric Sci Proc* 2:113–119
- Fang L, Catchmark JM (2015) Characterization of cellulose and other exopolysaccharides produced from *Gluconacetobacter* strains. *Carbohydr Polym* 115:663–669
- Fierro F, Laich F, Garcı RO, Martı JF (2004) High efficiency transformation of *Penicillium nalgiovense* with integrative and autonomously replicating plasmids. *Int J Food Microbiol* 90(2):237–248
- French AD (2014) Idealized powder diffraction patterns for cellulose polymorphs. *Cellulose* 21(2):885–896
- French AD, Santiago Cintrón M (2013) Cellulose polymorphy, crystallite size, and the Segal Crystallinity Index. *Cellulose* 20(1):583–588
- Gao C, Wan Y, Yang C, Dai K, Tang T, Luo H, Wang J (2011) Preparation and characterization of bacterial cellulose sponge with hierarchical pore structure as tissue engineering scaffold. *J Porous Mater* 18(2):139–145
- Gorke B, Stulke J (2008) Carbon catabolite repression in bacteria: many ways to make the most out of nutrients. *Nat Rev Microbiol* 6(8):613–624
- Guo J, Catchmark JM (2012) Surface area and porosity of acid hydrolyzed cellulose nanowhiskers and cellulose produced by *Gluconacetobacter xylinus*. *Carbohydr Polym* 87(2):1026–1037
- Halib N, Amin MCIM, Ahmad I (2010) Unique stimuli responsive characteristics of electron beam synthesized bacterial cellulose/acrylic acid composite. *J Appl Polym Sci* 116(5):2920–2929
- Hanahan D (1983) Studies on transformation of *Escherichia coli* with plasmids. *J Mol Biol* 166(4):557–580
- Hestrin S, Schramm M (1954) Synthesis of cellulose by *Acetobacter xylinum*. 2. Preparation of freeze-dried cells capable of polymerizing glucose to cellulose. *Biochem J* 58(2):345–352
- Hirai A, Tsuji M, Yamamoto H, Horii F (1998) In situ crystallization of bacterial cellulose III. Influences of different polymeric additives on the formation of microfibrils as revealed by transmission electron microscopy. *Cellulose* 5(3):201–213
- Hong F, Qiu K (2008) An alternative carbon source from konjac powder for enhancing production of bacterial cellulose in static cultures by a model strain *Acetobacter aceti* subsp. *xylinus* ATCC 23770. *Carbohydr Polym* 72(3):545–549
- Huang C, Yang XY, Xiong L, Guo HJ, Luo J, Wang B, Zhang HR, Lin XQ, Chen XD (2015a) Evaluating the possibility of using acetone-butanol-ethanol (ABE) fermentation wastewater for bacterial cellulose production by *Gluconacetobacter xylinus*. *Lett Appl Microbiol* 60(5):491–496
- Huang C, Yang XY, Xiong L, Guo HJ, Luo J, Wang B, Zhang HR, Lin XQ, Chen XD (2015b) Utilization of corn cob acid hydrolysate for bacterial cellulose production by *Gluconacetobacter xylinus*. *Appl Biochem Biotechnol* 175(3):1678–1688
- Karada E, Saraydin D (2002) Swelling of superabsorbent acrylamide/sodium acrylate hydrogels prepared using multifunctional crosslinkers. *Turk J Chem* 26(6):863–875
- Keshk SM (2014) Vitamin C enhances bacterial cellulose production in *Gluconacetobacter xylinus*. *Carbohydr Polym* 99:98–100
- Khan T, Khan S, Park J (2008) Simple fed-batch cultivation strategy for the enhanced production of a single-sugar glucuronic acid-based oligosaccharides by a cellulose-producing *Gluconacetobacter hansenii* strain. *Biotechnol Bioprocess Eng* 13(2):240–247
- Klemm D, Schumann D, Kramer F, Heßler N, Hornung M, Schmauder H-P, Marsch S (2006) Nanocelluloses as innovative polymers in research and application. *Polysaccharides II*. D 205:49–96
- Kuo C-H, Chen J-H, Liou B-K, Lee C-K (2016) Utilization of acetate buffer to improve bacterial cellulose production by *Gluconacetobacter xylinus*. *Food Hydrocoll* 53:98–103
- Kurosumi A, Sasaki C, Yamashita Y, Nakamura Y (2009) Utilization of various fruit juices as carbon source for production of bacterial cellulose by *Acetobacter xylinum* NBRC 13693. *Carbohydr Polym* 76(2):333–335
- Lessard JC (2013) Growth media for *E. coli*. *Methods Enzymol* 533:181–189

- Li Z, Wang L, Hua J, Jia S, Zhang J, Liu H (2015) Production of nano bacterial cellulose from waste water of candied jujube-processing industry using *Acetobacter xylinum*. *Carbohydr Polym* 120:115–119
- Lin W-C, Lien C-C, Yeh H-J, Yu C-M, Hsu S-H (2013) Bacterial cellulose and bacterial cellulose–chitosan membranes for wound dressing applications. *Carbohydr Polym* 94(1):603–611
- Lin D, Lopez-Sanchez P, Li R, Li Z (2014) Production of bacterial cellulose by *Gluconacetobacter hansenii* CGMCC 3917 using only waste beer yeast as nutrient source. *Biores Technol* 151:113–119
- Maeda S, Sawamura A, Matsuda A (2004) Transformation of colonial *Escherichia coli* on solid media. *FEMS Microbiol Lett* 236(1):61–64
- Mohamad N, Mohd Amin MCI, Pandey M, Ahmad N, Rajab NF (2014) Bacterial cellulose/acrylic acid hydrogel synthesized via electron beam irradiation: accelerated burn wound healing in an animal model. *Carbohydr Polym* 114:312–320
- Mohammadkazemi F, Azin M, Ashori A (2015) Production of bacterial cellulose using different carbon sources and culture media. *Carbohydr Polym* 117:518–523
- Mohite BV, Patil SV (2014) Physical, structural, mechanical and thermal characterization of bacterial cellulose by *G. hansenii* NCIM 2529. *Carbohydr Polym* 106:132–141
- Nguyen V, Flanagan B, Gidley M, Dykes G (2008) Characterization of cellulose production by a *Gluconacetobacter xylinus* strain from Kombucha. *Curr Microbiol* 57(5):449–453
- Nies DH (1999) Microbial heavy-metal resistance. *Appl Microbiol Biotechnol* 51(6):730–750
- Norouzian D, Farhangi A, Toloeei S, Saffari Z, Mehrabi MR, Chiani M, Ghassemi S, Farahnak M, Akbarzadeh A (2011) Study of nano-fiber cellulose production by *Gluconacetobacter xylinum* ATCC 10245. *Pak J Biol Sci PJSB* 14(15):780–784
- Oliveira Barud HG, Barud Hda S, Cavicchioli M, do Amaral TS, de Oliveira OB Jr, Santos DM, Petersen AL, Celes F, Borges VM, de Oliveira CI, Furtado RA, Tavares DC, Ribeiro SJ (2015) Preparation and characterization of a bacterial cellulose/silk fibroin sponge scaffold for tissue regeneration. *Carbohydr Polym* 128:41–51
- Omadjela O, Narahari A, Strumillo J, Mélida H, Mazur O, Bulone V, Zimmer J (2013) BcsA and BcsB form the catalytically active core of bacterial cellulose synthase sufficient for in vitro cellulose synthesis. *Proc Natl Acad Sci* 110(44):17856–17861
- Park S, Park J, Jo I, Cho SP, Sung D, Ryu S, Park M, Min KA, Kim J, Hong S, Hong BH, Kim BS (2015) In situ hybridization of carbon nanotubes with bacterial cellulose for three-dimensional hybrid bioscaffolds. *Biomaterials* 58:93–102
- Rambo CR, Recouvreur DOS, Carminatti CA, Pitlovanciv AK, Antônio RV, Porto LM (2008) Template assisted synthesis of porous nanofibrous cellulose membranes for tissue engineering. *Mater Sci Eng C* 28(4):549–554
- Römling U, Galperin MY (2015) Bacterial cellulose biosynthesis: diversity of operons, subunits, products, and functions. *Trends Microbiol* 23(9):545–557
- Ruka DR, Simon GP, Dean KM (2012) Altering the growth conditions of *Gluconacetobacter xylinus* to maximize the yield of bacterial cellulose. *Carbohydr Polym* 89(2):613–622
- Samavat F, Ali EH, Solgi S, Ahmad PT (2012) KCl single crystals growth with Mn, Ag and in impurities by Czochralski method and study of impurities influence on their properties. *Open J Phys Chem* 2(3):4
- Saxena IM, Kudlicka K, Okuda K, Brown R (1994) Characterization of genes in the cellulose-synthesizing operon (acs operon) of *Acetobacter xylinum*: implications for cellulose crystallization. *J Bacteriol* 176(18):5735–5752
- Schlesinger M, Hamad WY, MacLachlan MJ (2015) Optically tunable chiral nematic mesoporous cellulose films. *Soft Matter* 11(23):4686–4694
- Segal L, Creely JJ, Martin JAE, Conrad CM (1959) An empirical method for estimating the degree of crystallinity of native cellulose using the X-ray diffractometer. *Text Res J* 29(10):786–794
- Shah J, Malcolm Brown R Jr (2005) Towards electronic paper displays made from microbial cellulose. *Appl Microbiol Biotechnol* 66(4):352–355
- Shezad O, Khan S, Khan T, Park JK (2010) Physicochemical and mechanical characterization of bacterial cellulose produced with an excellent productivity in static conditions using a simple fed-batch cultivation strategy. *Carbohydr Polym* 82(1):173–180
- Son H-J, Heo M-S, Kim Y-G, Lee S-J (2001) Optimization of fermentation conditions for the production of bacterial cellulose by a newly isolated *Acetobacter*. *Biotechnol Appl Biochem* 33(1):1–5
- Sun Q-Y, Ding L-W, He L-L, Sun Y-B, Shao J-L, Luo M, Xu Z-F (2009) Culture of *Escherichia coli* in SOC medium improves the cloning efficiency of toxic protein genes. *Anal Biochem* 394(1):144–146
- Tabarsa T, Sheykhnazari S, Ashori A, Mashkour M, Khazaeian A (2017) Preparation and characterization of reinforced papers using nano bacterial cellulose. *Int J Biol Macromol* 101:334–340
- Tyagi N, Suresh S (2016) Production of cellulose from sugarcane molasses using *Gluconacetobacter intermedius* SNT-1: optimization and characterization. *J Clean Prod* 112:71–80. doi:10.1016/j.jclepro.2015.07.054
- Ul-Islam M, Khan T, Park JK (2012) Water holding and release properties of bacterial cellulose obtained by in situ and ex situ modification. *Carbohydr Polym* 88(2):596–603
- Ul-Islam M, Ha JH, Khan T, Park JK (2013) Effects of glucuronic acid oligomers on the production, structure and properties of bacterial cellulose. *Carbohydr Polym* 92(1):360–366
- Vasconcelos NF, Feitosa JPA, da Gama FMP, Morais JPS, Andrade FK, de Souza MDSM, de Freitas Rosa M (2017) Bacterial cellulose nanocrystals produced under different hydrolysis conditions: properties and morphological features. *Carbohydr Polym* 155:425–431
- Vazquez A, Foresti M, Cerrutti P, Galvagno M (2013) Bacterial cellulose from simple and low cost production media by *Gluconacetobacter xylinus*. *J Polym Environ* 21(2):545–554
- Watanabe K, Tabuchi M, Morinaga Y, Yoshinaga F (1998) Structural features and properties of bacterial cellulose produced in agitated culture. *Cellulose* 5(3):187–200
- Wei B, Yang G, Hong F (2011) Preparation and evaluation of a kind of bacterial cellulose dry films with antibacterial properties. *Carbohydr Polym* 84(1):533–538

- Wu J-M, Liu R-H (2012) Thin stillage supplementation greatly enhances bacterial cellulose production by *Gluconacetobacter xylinus*. *Carbohydr Polym* 90(1):116–121
- Yang XY, Huang C, Guo HJ, Xiong L, Luo J, Wang B, Chen XF, Lin XQ, Chen XD (2014) Beneficial effect of acetic acid on the xylose utilization and bacterial cellulose production by *Gluconacetobacter xylinus*. *Indian J Microbiol* 54(3):268–273
- Yang XY, Huang C, Guo HJ, Xiong L, Luo J, Wang B, Lin XQ, Chen XF, Chen XD (2016) Bacterial cellulose production from the litchi extract by *Gluconacetobacter xylinus*. *Prep Biochem Biotechnol* 46(1):39–43
- Zeng X, Small DP, Wan W (2011) Statistical optimization of culture conditions for bacterial cellulose production by *Acetobacter xylinum* BPR 2001 from maple syrup. *Carbohydr Polym* 85(3):506–513
- Zhao Y, Koizumi S, Yamaguchi D, Kondo T (2014) Hierarchical structure in microbial cellulose: what happens during the drying process. *Eur Phys J E Soft Matter* 37(12):129



Contents lists available at ScienceDirect

Carbohydrate Polymers

journal homepage: www.elsevier.com/locate/carbpol

Cellulose-metallothionein matrix for metal binding

Naimat K. Bari^{a,1}, Shaswat Barua^{a,1}, Ankush Garg^a, Malay K. Sannigrahi^b, Sharmistha Sinha^{a,*}^a Institute of Nano Science and Technology, Phase - 10, Sector - 64, Mohali, Punjab, India^b Indian Institute of Science Education and Research, Knowledge city, Sector 81, Mohali, Punjab, India

ARTICLE INFO

Keywords:

Bacterial cellulose
 Metallothionein
 Epoxidation
 Covalent conjugation
 Metal binding

ABSTRACT

In this report, we have modified bacterial cellulose to a metal binding matrix by covalently conjugating physiological metal chelators known as metallothioneins. The hydroxyl groups of the native bacterial cellulose from *Gluconobacter xylinus* are epoxidized, followed by the covalent conjugation with the amine groups of the proteins. For the first time, a covalent conjugation of protein with bacterial cellulose is achieved using the epoxy-amine conjugation chemistry. Using this protocol, 50% mass by mass of the metallothionein could be attached to bacterial cellulose. The morphological features and porosity of the modified cellulose are different compared to pristine bacterial cellulose. Also, the conjugated material has better thermal stability. A five-fold enhancement in the metal binding capacity of the metallothionein conjugated bacterial cellulose is achieved as compared to pristine bacterial cellulose. Cellular metabolic assay and membrane integrity assay on MCF and HeLa cell lines showed no significant toxicity of the conjugate material. This bacterial cellulose-metallothionein conjugate can be explored for health care applications where management of metal toxicity is crucial. Further, the epoxy-amine chemistry for covalent conjugation of protein can be applied for several other types of proteins to develop specific functional biocompatible and biodegradable cellulose matrices.

1. Introduction

Bacterial cellulose (BC), a linear polymer of glucose (Brown & Montezinos, 1976; Brown, Willison, & Richardson, 1976; Jang, Hwang, Kim, Ryu, & Lee, 2017; Morgan et al., 2016) secreted from certain bacteria as a fibrous matrix is an important healthcare commodity with references to wound management and tissue engineering (Ashjaran, Yazdanshenas, Rashidi, Khajavi, & Rezaee, 2013; Jang et al., 2017; Petersen & Gatenholm, 2011). In this regard, BC has gained a wide scale applications because of its high moisture content (Lopes, Riegel-Vidotti, Grein, Tischer, & de Sousa Faria-Tischer, 2014) high porosity (Yin et al., 2012) biocompatibility and biodegradability (Fernandes et al., 2013; Torres, Commeaux, & Troncoso, 2012) non-immunogenicity, hydrophilicity, high surface area and exceptional mechanical strength (Barud et al., 2015; Czaja, Young, Kawecki, & Brown, 2007; Moniri et al., 2017; Nainggolan, Gea, Bilotti, Peijs, & Hutagalung, 2013; Sai et al., 2015; Yao et al., 2017). BC mimics the fibrous component of the extracellular matrix (e.g. collagen) (Lee et al., 2015; Lopes et al., 2014) and hence can act as a suitable substrate for a tissue regeneration/wound healing matrix (Babu, Doble, & Raichur, 2018; Basmaji, de Olyveira, Manzine Costa, Francozo, & da Costa, 2015; Dhas, Anbarasan, Mukherjee, &

Chandrasekaran, 2015; Habibi, 2014). Current wound dressing materials comprise of the traditional dressings, including gauze, lint, plasters, bandages and cotton wool or the modern dressing which includes semipermeable membrane, hydrogel, hydrocolloid, film and foam dressings (Anjum, Arora, Alam, & Gupta, 2016; Basmaji et al., 2015; Dhivya, Padma, & Santhini, 2015; El-Hoseny et al., 2015). In contrast to the traditional dressings, the modern dressing materials prevent dehydration of the wound and support the healing process. Modern wound dressings can be made of synthetic or natural polymers and interact with the wound for a quick restoration. Most of these materials have the capability of protecting the wound against microbial invasion by acting as a barrier against microbial penetration, however, protection of wounds from inorganic toxins (viz. metals, chemical compounds) has not been addressed in detail.

Metal induced toxicity is observed maximum in gunshot wounds (Centeno et al., 2014; Rentfrow, Vaidya, Elia, & Sethi, 2013; Ryu, Han, Jung, Bae, & Nam, 2007; Skaik et al., 2010). Toxicity due to environmental exposure to metals is also not uncommon and have shown delays in wound healing (Lansdown, Sampson, & Rowe, 2001). Metal toxicity from environmental sources through wounds is serious health concerns and is associated with oxidative stress, carcinogenicity,

Abbreviations: BC, bacterial cellulose; MT, metallothionein; eBC, epoxidized bacterial cellulose; MBP, maltose binding protein; TGA, thermogravimetric analysis

* Corresponding author.

E-mail address: sinhas@inst.ac.in (S. Sinha).

¹ Equal contribution.

<https://doi.org/10.1016/j.carbpol.2018.03.043>

Received 4 January 2018; Received in revised form 26 February 2018; Accepted 15 March 2018

Available online 17 March 2018

0144-8617/ © 2018 Elsevier Ltd. All rights reserved.

hepatotoxicity, neurotoxicity, genotoxicity, nephrotoxicity and mutagenicity. Heavy metals have been reported to impact signalling cascade and associated factors leading to apoptosis and cell death (Bush, 2000; Galanis, Karapetsas, & Sandaltzopoulos, 2009; Gleit et al., 2002; Leonard, Bower, & Shi, 2004; Menon, Chang, & Kim, 2016; Urani et al., 2014). Hence, wound dressing materials that can simultaneously manage wound healing and metal toxicity will be an interesting healthcare merchandise. To achieve this, we proposed to conjugate BC with a biocompatible metal chelator. Metallothioneins (MTs) are a group of metal binding proteins characterized by their small size, high cysteine content, and lack in aromatic amino acids. Owing to high cysteine content and their presence in all organisms, MT is implicated in a number of physiological processes. The most commonly cited processes are metal ion homeostasis, toxic metal detoxification, and protection against oxidative stress (Carpenè, Andreani, & Isani, 2007; Coyle, Philcox, Carey, & Rofe, 2002; Davis & Cousins, 2000; Moffatt & Denizau, 1997; Sutherland & Stillman, 2011).

In terms of surface physico-chemical feature, each of the cellulose monomers bears three hydroxyl groups. The ability of these hydroxyl groups to form hydrogen bonds plays a major role in the formation of fibrillar and semicrystalline packing which governs the important physical properties of these highly cohesive material (Habibi, 2014). These hydroxyl groups can be chemically modified to introduce specific characteristic features to the BC (Fernandes et al., 2013). In this aspect, conjugating MTs to the BC through these hydroxyl functionalities will provide a new paradigm for developing BC-protein conjugate.

Efforts have been made to synthesize cellulose-macromolecule conjugates through non-covalent interactions (Fritz et al., 2015; Holstein et al., 2016; Lee, Rho, & Messersmith, 2009). Orelma et al. studied the physical adsorption of chitosan from aqueous solution irreversibly on cellulose, most likely by virtue of their opposite charges (chitosan) and molecular/structural affinity (chitosan and CMC) (Orelma, Filpponen, Johansson, Laine, & Rojas, 2011; Orelma, Teerinen, Johansson, Holappa, & Laine, 2012). Some other groups report for the introduction of carboxylate groups to cellulose by TEMPO oxidation, which provide a high surface density of negative charges able to drive the adsorption of biomolecules (Orelma, Johansson, Filpponen, Rojas, & Laine, 2012; Weishaupt et al., 2015). The adsorption of biomolecules onto tempo oxidized cellulose is strongly dependent on the isoelectric point (IEP), indicating that interfacial electrostatic forces between the protein surface charges and the carboxylate groups of tempo oxidized cellulose were the main driving force (Weishaupt et al., 2015). TEMPO based oxidation introduces carboxyl group which is further functionalized with EDC-NHS coupling and can be conjugated with amine groups. Kontturi and coworkers carried out the non-covalent surface modification of cellulose nano-papers by physisorption of polymers from aprotic solvents (Kontturi et al., 2017). These conjugates suffer from a severe disadvantage of polymer leaching due to weak non-covalent interactions, which reduces their efficiency and reproducibility.

This problem could be eased by introducing a stronger bond between cellulose and protein. Although there are few reports on covalent conjugation of proteins with biopolymers (Cao, Guan, Li, Tian, & Shen, 2015; Holstein et al., 2016; Orelma, Johansson et al., 2012; Orelma, Teerinen et al., 2012; Weishaupt et al., 2015), yet to the best of our knowledge, there are no available reports on covalent conjugation of cellulose with a protein for metal chelation. The other added advantage of this covalent conjugation protocol is that the amount of modification and conjugation can be quantified which is challenging in cases where the polymer is prone to leaching.

Epoxy-amine chemistry (Miao, Liu, Wang, Su, & Zhang, 2015) has been used for several applications including curing of epoxy resins in paints and adhesives industries (Li, Yang, Zhang, & Tang, 2017; Pradhan, Pandey, Mohanty, & Nayak, 2016). Further bio-based amine hardeners derived from long chain fatty acids and crosslinking epoxy resins with amino carboxylic acids have also been reported (De, Gupta,

Mandal, & Karak, 2013; Mustata, Tudorachi, & Bicu, 2015). On similar lines tryptophan is shown to be a good curing agent for epoxy resins in presence of imidazole catalyst (Li, Xiao, & Wong, 2007). Thus, there triggered the idea of using epoxidized cellulose for covalent conjugation of protein in the present investigation. Most of the reported cellulose-protein conjugates reported are based either on physical adsorption or on non-covalent interactive forces (Diftis & Kiosseoglou, 2003; Fang et al., 2016; Orelma, Teerinen et al., 2012). Kubler-Kielb and Pozsgay developed an elegant approach for covalent conjugation of saccharide and protein by using an aminoxy-thiol hetero bifunctional linker (Kubler-Kielb & Pozsgay, 2005) which requires several reaction steps to yield the precursors. Holestein et al. have reported the epoxide-thiol attachment for the immobilization of proteins which have affinity for thiol groups (Holstein et al., 2016).

In our present study, we have developed a metal binding matrix by conjugating BC with MT through covalent interactions. MTs are chosen for their high metal binding property. The hydroxyl groups of cellulose are epoxidized (Dai et al., 2015) with epichlorohydrin and free amine groups of MTs are covalently linked to the epoxidized cellulose matrix. This conjugate showed a significant binding affinity for di-valent metals. The conjugate material may find an application in management of wounds associated with metal induced toxicity. The proposed material can be tailored as per requirement by regulating the chemistry of the conjugation. This conjugation chemistry can be utilized to develop several cellulose-protein conjugates for different uses.

2. Materials and methods

2.1. Materials

Gluconobacter xylinus (MTCC 7795/ATCC 11142) and TB1 (MTCC 1719) cells are obtained from the Microbial Type Culture Collection, India. pMAL-c2x-MT2 is a gift from David DeRosier & Chris Mercogliano & Cristina Risco Ortiz (Addgene plasmid # 32102) (Mercogliano & DeRosier, 2007). MBP strain (pMAL-c2x, expressed in BL21-DE3) is a gift from Dr. Mahak Sharma, IISER Mohali, India. All chemicals unless specified are procured from Sigma, India.

2.2. Methods

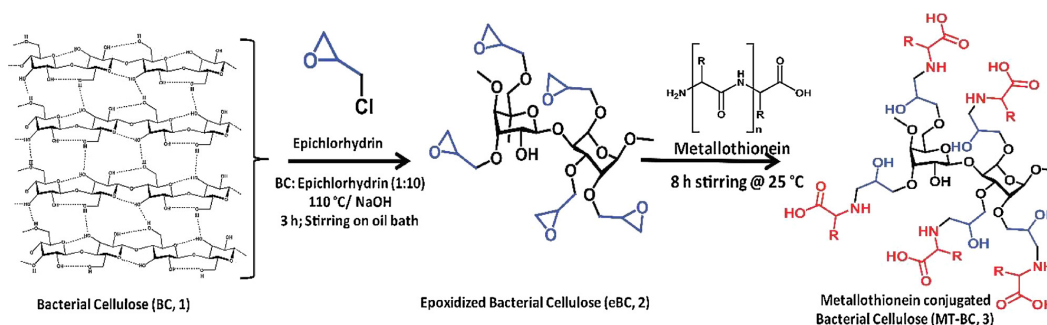
2.2.1. Extraction of bacterial cellulose

Gluconobacter xylinus is cultured and the cellulose produced is purified using a protocol developed by (Chandrasekaran, Bari, & Sinha, 2017). The static cultures are grown at 28 °C for 7 days. After 7 days, the pellicles are harvested at 5000 rpm and processed by repeatedly washing with de-ionized water to get rid of media components. The pellicles are then treated with 0.1% NaOH (w/v) solution and kept at 60 °C for 2 h to get rid of the cellular debris. Subsequently, the pellicles are washed with distilled water until neutral pH is observed. The washed BC is re-suspended in Mili-Q and is freeze dried using a lyophilizer (BenchTop Pro with Omnitronics, VirTis SP Scientific, Pennsylvania).

2.2.2. Expression and purification of metallothionein

Metallothionein protein is expressed and purified as described by Mercogliano and DeRosier (2007). pMAL-c2x-MT2 plasmids are transformed into TB1 *E.coli* cells for overproduction of the metallothionein. The construct has a maltose binding domain tagged for purification. From overnight culture, secondary culture is inoculated in volume of 400 mL with 1% glucose. The cells are grown till an OD₆₀₀ reaches 0.5. The cultures are then induced with 0.2 mM IPTG to initiate protein expression.

After 3 h of induction, cells are pelleted at 6000 rpm and stored at –20 °C till further use. For purification, the cells are re-suspended in 20 mL of wash buffer (20 mM Trizma Base pH 7.5 containing 150 mM sodium chloride and 0.1 mM EDTA). Post lysis the cell suspensions are pelleted at 11000 rpm for 30 min. The resulting supernatants are



Scheme 1. BC is mixed with epichlorohydrin in a ratio of 1:10 and heated at 110 °C with NaOH added dropwise. Reaction carried out for 3 h and washed with brine solution. Lyophilized eBC is mixed with metallothionein and stirred for 8 h, washed, lyophilized and then stored at 4 °C.

diluted in wash buffer and loaded onto a pre-equilibrated amylose column. Post loading, the column is washed with 10 column volumes of wash buffer. Bound protein is eluted in wash buffer supplemented with 10 mM maltose. Protein concentrations of eluted fractions are quantified using Bradford reagent and aliquots are stored at -80°C till further use.

2.2.3. Epoxidation of bacterial cellulose (eBC)

BC is epoxidized using epichlorohydrin in presence of NaOH. In a typical reaction, 0.5 g of BC and 5 g of epichlorohydrin are reacted in 1:10 ratio (w/w) in a 100 mL round bottom flask fitted with a condenser and a pressure equalizing funnel. The reaction temperature is elevated and maintained at 110 °C. A 5 N aqueous solution of NaOH (equivalent to the molar ratio of epichlorohydrin) is added to the reaction mixture through the pressure equalizing funnel very slowly and is allowed to stir for 3 h. The epoxidized bacterial cellulose (eBC) in the organic layer is repeatedly washed with brine solution (Scheme 1). Finally, the product is collected and lyophilized. To determine the extent of epoxidation of BC moieties, epoxy equivalent and hydroxyl values were calculated as per the reported procedures (Barua, Dutta, & Karak, 2013; Evtushenko, Zaitsev, Ivanov, Khalturinskii, & Evtushenko, 2001; He, Wang, Zhao, Ye, & Huang, 2014). Methods for determining the epoxy equivalent and hydroxyl values are detailed in the Supplementary information.

2.2.4. Conjugation of metallothionein with eBC

eBC is cross-linked with the extracted MT by using the basic epoxy-amine chemistry. Required amount of eBC is dispersed in water (1 mg/mL) followed by addition of MT. The mixture is allowed to stir for 8 h at room temperature. Different concentrations of MT are loaded onto eBC. Amount of protein loading and conjugation capacity are validated with the help of UV visible and FTIR spectroscopy. The conjugated system (MT-BC) has been used for further studies.

2.2.5. Properties of the conjugate material

2.2.5.1. Spectroscopic characterization

2.2.5.1.1. Ultraviolet visible spectroscopy. UV spectroscopy is carried out to determine the conjugation of metallothionein to the eBC using a UV-2600, Shimadzu, Japan (Fig. 1). The samples are scanned from 200 to 900 nm with medium scanning speed. Quartz cuvettes with path length of 10 mm is used.

2.2.5.1.2. Fourier transform infra-red (FT-IR) spectroscopy. FT-IR analysis is performed to determine the chemical structure of BC, eBC and MT-BC. The lyophilized samples are mixed with oven dried (70 °C) KBr in a ratio of 1:200 (w/w) to form pellets. The FT-IR spectra are examined in the mid IR range ($400\text{--}4000\text{ cm}^{-1}$) using a FT-IR spectrophotometer (Fig. 1) (Cary 600 series, FTIR Spectrophotometer, Agilent Technologies).

2.2.5.2. Hydration properties. The hydration capacity of BC and its derivatives is determined as described by (Chandrasekaran et al., 2017) Briefly, weighed quantities of dried BC and MT-BC are added with distilled water followed by vortexing. The solution is then allowed to stand for 3–5 min followed by centrifugation at 10000 rpm for 10 min. The supernatant is discarded and the pellet is subjected to drying at 37 °C and weighed at different time points to determine the hydration capacity, as per the equations below (Fig. 1).

$$\text{Hydration Capacity} = (\text{Weight of hydrated sample (g)}) / \text{Dry weight (g)} \quad (1)$$

2.2.5.3. Morphological features. The morphology of freeze dried BC, eBC, and MT-BC are observed using Scanning Electron Microscope (JEOL JSM-IT300, USA) at 15 KV. Freeze dried samples are mounted on carbon tapes followed by gold sputtering for 60 s (Fig. 2). Energy Dispersive X-Ray mapping is carried out to assess the elemental composition.

2.2.5.4. Thermal stability. Thermogravimetric analysis (TGA) is performed to determine the thermal stability of the BC and MT-BC. TGA measurements are carried out using a Simultaneous Thermal Analyzer (STA 8000, Perkin Elmer, USA). Weighed amount of the samples are scanned over a temperature range of 50–800 °C at a heating rate of 10 °C/min under N_2 atmosphere.

2.2.5.5. Metal binding by the conjugate material

2.2.5.5.1. Ultraviolet visible spectroscopy. Binding of various divalent metals to the conjugate materials is studied by UV spectroscopy (UV-2600, Shimadzu, Japan). BC, eBC and MT-BC are aliquoted in and interacted with the divalent metal salts. The mixture is left at room temperature under mild shaking conditions. After 4 h the samples are centrifuged at 10000 rpm for 15 min and supernatant is checked by UV (scanned between 200–900 nm) to determine the unbound metals (Peak position for metals used in study; Iron – 248 nm. Lead and Cadmium- 305 nm, Cobalt- 506 nm and Copper – 850 nm). (Huang et al., 2016) The amount of bound metals per mg of the material is determined for different divalent metals.

2.2.5.5.2. Mapping for metal by SEM. For carrying out the elemental mapping, the MT-BC samples following interaction with metals are drop-casted on silicon wafers. The samples are subjected to higher probe current at 15–30 kV to generate secondary electrons more than 1kcps. The secondary electrons generated are captured and the elemental distribution in the composite matrix is qualitatively observed.

2.2.5.5.3. ICP-MS analysis. BC or MT-BC (1 mg/mL) dispersion in water are interacted with metal salts and incubated on shaker at room temperature. Post incubation the samples are centrifuged at 13000 rpm

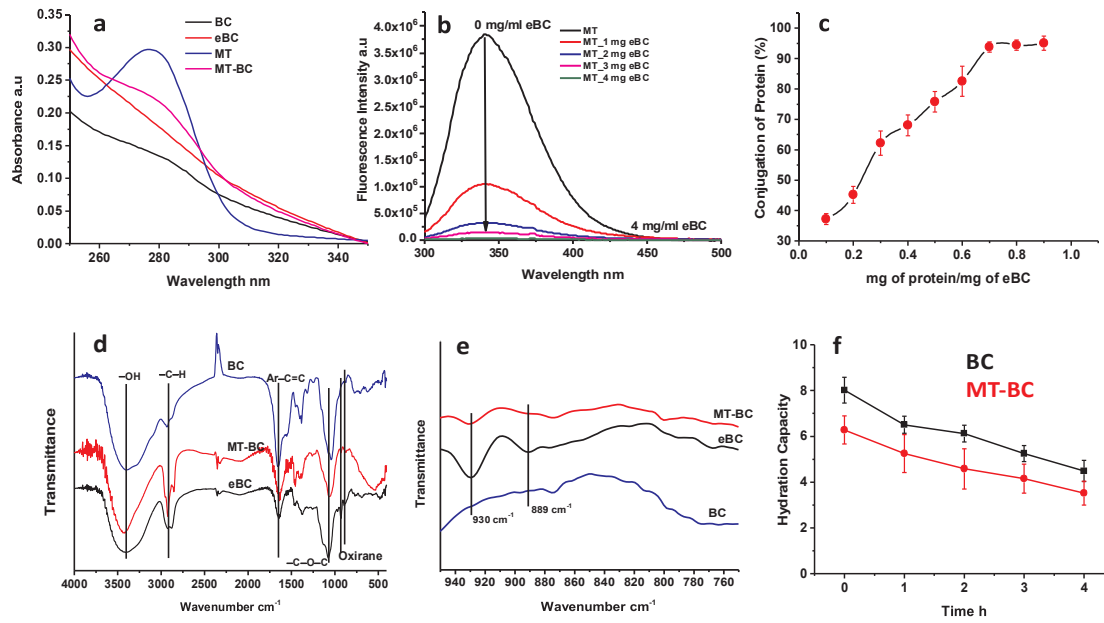


Fig. 1. UV-vis spectra of BC, eBC, MT and MT-BC; Peak broadening in MT-BC showing the interaction of eBC with the protein (a); Tryptophan fluorescence quenching post conjugation with eBC (b); Conjugation of protein on the eBC(c); FTIR spectra of BC, eBC, and MT-BC (d) & (e); Hydration capacity of BC and MT-BC (f).

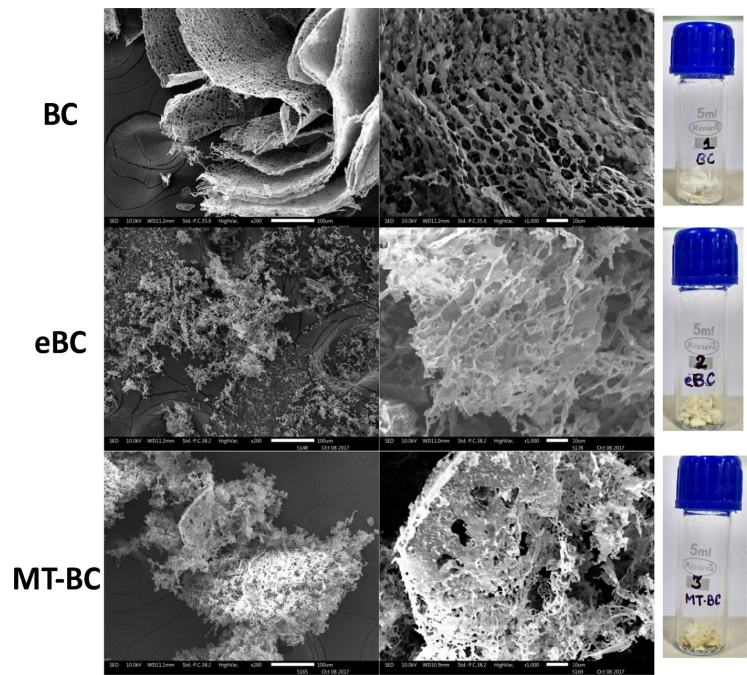


Fig. 2. Scanning electron micrographs for BC, eBC, MT-BC at various magnifications (200 \times and 1000 \times) after freeze-drying.

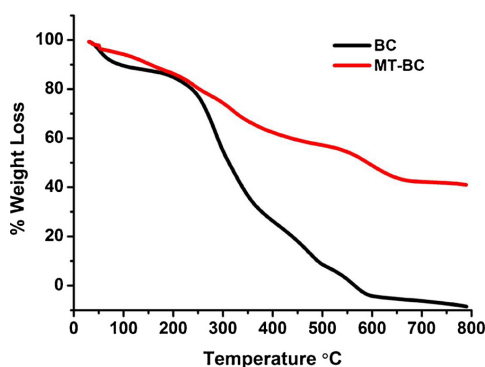


Fig. 3. TGA for BC and MT-BC.

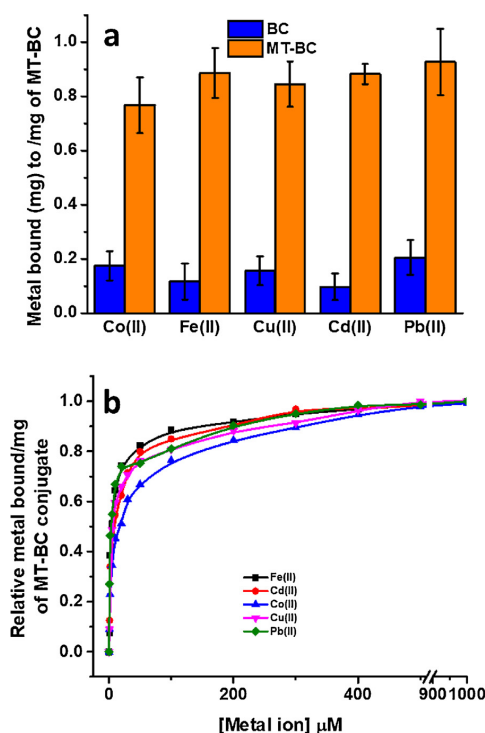


Fig. 4. Metal binding capacity of material, through UV spectroscopy (a); through steady state tryptophan fluorescence (b).

for 15 min and the supernatant is aliquoted and the amount of unbound metals is determined.

2.2.5.6. Toxicity of the conjugate material

2.2.5.6.1. Preparation of BC and MT-BC for cell culture assays. The BC and conjugated material are extensively dialyzed in sterile Milli-Q. Post dialysis the materials are lyophilized in autoclaved microcentrifuge tubes and subjected to UV radiation for 15 min in biological hoods. The materials are dissolved in sterile DMEM media (100 µg/mL) for interaction with the cells.

2.2.5.6.2. MTT assay. Relative cell viability is determined using MTT assay. HeLa and MCF7 cells (10^4 cells/well) are seeded in a 96-well plate. After 12 h incubation, the cells are exposed to varying

concentrations of BC and MT-BC (0.01, 0.1, 1, 10 and 100 mg/mL) for 48 h. Cells treated with medium only served as a negative control group. After 48 h, 10 µL of MTT solution (5 mg/mL in PBS) is added to each well. After incubation for another 4 h, the resultant formazan crystals are dissolved in DMSO (100 µL) and the absorbance intensity is measured by a microplate reader (Bio-RAD 680, USA) at 580 nm with a reference wavelength of 630 nm. All experiments are performed in triplicates, and the relative cell viability (%) is expressed as a percentage relative to the untreated control cells.

2.2.5.6.3. Membrane integrity test using lactate dehydrogenase assay (LDH). Cell lines (HeLa, MCF-7) are seeded at 5000 cells/ml in 6 well plate for 12 h. Then the cells are incubated with fresh media containing DMSO (100 µL/mL), BC and MT-BC (100 ng/µL) for 24 h. After this the medium is refreshed and cells are cultured for an additional 48 h. Culture supernatant is collected for LDH assessment. LDH activity is measured using an LDH cytotoxicity assay (CytoTox 96[®] Non-Radioactive Cytotoxicity Assay, Promega, Cat No-G1780, Madison, WI), per the manufacturers' protocol. Briefly, 50 µL of each supernatant are transferred to a 96-well flat-bottom plate in triplicates and supplemented with 50 µL reconstituted substrate mix. The plate is incubated in the dark at room temperature for 30 min. To stop the reaction a volume of 50 µL of stop solution (provided in the kit) is added to each well and mixed properly. The absorbance is recorded at 490 nm within 20 min after adding stop solution with a microplate reader (Eon Biotek, USA). Lysed cells with cell lysis buffer is used as a positive control for total LDH release and fresh media is used as negative control (NC). LDH release is calculated using the following formula:

$$\text{Total LDH released (\%)} = \frac{(BC_{\text{abs}} - NC_{\text{abs}})}{(PC_{\text{abs}} - NC_{\text{abs}})} \times 100 \quad (2)$$

3. Results and discussion

3.1. Purification of bacterial cellulose, epoxidation and conjugation with MT

Bacterial cellulose forms a thin film on the surface of the culture media post 7 days of interaction with the super optimal broth. The yield of the BC obtained by this way is 0.5 g/g of glucose similar to one reported by (Chandrasekaran et al., 2017). The BC is lyophilized and kept refrigerated till further use. The lyophilized BC is used for epoxidation following which it is conjugated to the MT. MT is purified as per the standard protocol and the concentration of the MT is determined using Bradford reagent (Bradford, 1976). The purified MT is characterized by circular dichroism at different pH for its stability check and they are stable even at high basic pH (pH 11) (Supplementary Fig. S1) at which the BC is soluble. We also checked the thermal stability of MT (Supplementary Fig. S2a and b) and observed that they start denaturing after 50 °C. This is of significance because we are conjugating the protein at room temperature and conjugation temperature will not affect the conformation of protein.

The conjugation of MT to BC is achieved by using an epoxidized cellulose precursor. Epoxidation of cellulose has not been explored to a considerable extent though it confers a vital platform for many biological applications. The epoxidation is carried out as shown in Scheme 1. In cellulose, there are three possible hydroxyl ions that can be epoxidized. In this report we aimed to epoxidize the cellulose partially so that the fibrous structure of the bacterial cellulose held by hydrogen bonding of the hydroxyl groups is not lost completely. The extent of epoxidation has been determined by calculating the epoxy equivalent as per standard procedure (Barua et al., 2013). Epoxy value is found to be 445 ± 27 , which is quite comparable to that of a diglycidyl ether epoxy (De et al., 2013). It is quite obvious that all of OH groups have not taken part in covalent bonding. To address this, we have compared the hydroxyl values of both BC and eBC, which showed that $40.1 \pm 6.8\%$ of the hydroxyl groups have taken part in the epoxidation

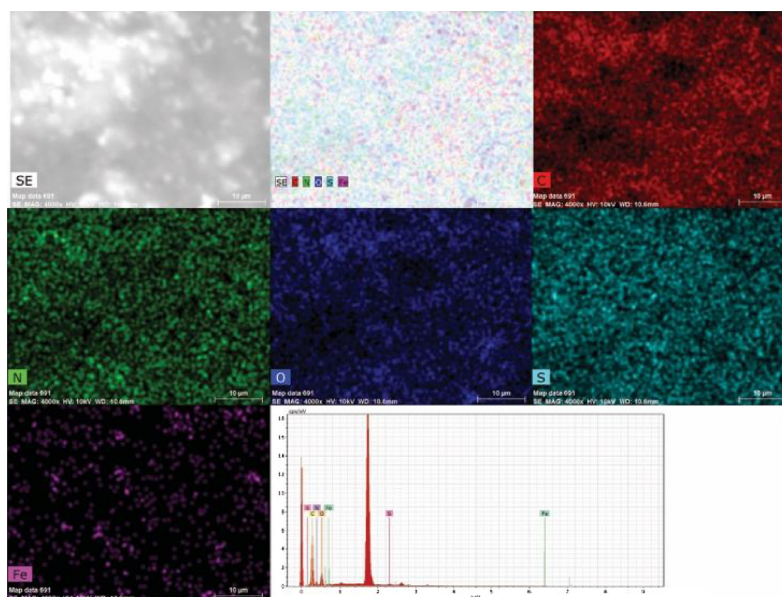


Fig. 5. Elemental mapping for iron in MT-BC.

reaction. The epoxidation% is checked for three different batches to check for the variation and is shown in Supplementary Table T1. The present method in contrast may be regarded as one of the facile and novel approach for the covalent conjugation of cellulose and protein. The highly strained oxirane ring of eBC opens up and instantaneously forms crosslinked network when reacted with MT. Room temperature crosslinking of epoxy by MT is a major achievement of the present investigation. The overall scheme is presented in Scheme 1.

3.2. Characterization of conjugate material

The final conjugated product MT-BC, is confirmed by the presence of the tryptophan-peak at 279 nm (Fig. 1a). Tryptophan is present in the maltose binding protein (MBP) domain of the used protein, thus it is very interesting to note that the band broadens in MT-BC as compared to bare MBP-MT. This also suggests that it is the MBP domain that interacts with the eBC matrix leaving the MT available for the targeted metal binding purpose. UV-vis spectra of BC, and eBC did not exhibit any significant tryptophan absorption peak.

We also checked the fluorescence quenching of MBP-MT with interaction with eBC as shown in Fig. 1b. With increasing eBC concentration for a fixed concentration of MBP-MT we observed a complete quenching in tryptophan fluorescence which suggest and support the conjugation of eBC with MBP-MT and formation of MT-BC. We also studied the conformational change in the MBP-MT post conjugation with eBC with circular dichroism (Supplementary Fig. S3) and FTIR (Supplementary Fig. S4). Conjugation of MBP-MT with eBC doesn't have any effect on the conformation of the MBP-MT, whereas alone eBC doesn't have any conformation of its own.

We did a quantification of the amount of protein that can be loaded onto the eBC matrix. The conjugation of the MT to the eBC matrix is quantified by UV-vis spectroscopy, by plotting against a standard curve of bare protein concentrations. Fig. 1c shows the conjugation of protein onto the eBC matrix. The curve demonstrated saturation in conjugation capacity at a protein loading of 0.9 mg/mg of the MT-BC.

Epoxidation is investigated by FTIR spectroscopy. Appearance of the bands at around 889 and 930 cm^{-1} in EC indicated the successful

epoxidation of BC (Fig. 1d and e). Again, disappearance of the same bands in MT-BC shows the efficient crosslinking between eBC and MBP-MT. The band at around 1047 cm^{-1} confirms the formation of a covalent ether linkage between the cellulose and the *epi*-chlorohydrin moieties (De et al., 2013). The allied bands at around 2934 and 3244 cm^{-1} indicated the presence of C–H and –OH bands of the cellulosic units. It is quite clear from Fig. 1d that the breadth of the –OH band decreases from BC to MT-BC, which indicated the decrease in the bound water content during the epoxidation and protein conjugation reactions. Roman and Winter reported that during the processing of bacterial cellulose, at elevated temperature in presence of acid or alkali, some reactions lead to formation of C=O and C=C bonds, which is reflected by the presence of the bands at around 1660 cm^{-1} . Thus, FTIR study ascertained the successful epoxidation and subsequent conjugation (Roman & Winter, 2004). The bands corresponding to the amide vibrations of the protein are present in the range 1700–1600 cm^{-1} (Supplementary Fig. S4). These bands are, however, of very low intensity due to their involvement in the cross-linking reaction with the oxirane moiety (Barua et al., 2013; Roman & Winter, 2004). SEM elemental mapping of pristine BC and MT-BC is carried out for Carbon(C), Oxygen(O), Nitrogen(N) and Sulphur(S). MT-BC showed higher nitrogen and sulphur content because of covalent conjugation of MT to eBC as shown in Supplementary Fig. S5. Next, we compared the hydration capacity of MT-BC with BC. It has been earlier reported by our group that the hydration capacity of SOC_{5.5} derived cellulose is ~8 (Prathna et al., 2017). In the MT-BC we observe a hydration capacity of ~6. The high hydration capacity of cellulosic materials is due to the presence of hydroxyl groups (Habibi, 2014). In the MT-BC conjugate, the hydroxyl groups are compromised and hence a decrease in the hydration capacity of the conjugate material in comparison to pristine BC as shown in Fig. 1f.

We further studied the alterations in the morphology of BC upon conjugation with MTs. Freeze dried samples of BC, eBC, and MT-BC are analyzed using SEM. Pristine BC shows a porous morphology while the eBC offer a more fibrous morphology. In MT-BC dense fibers compared to the eBC are observed (Fig. 2). We also observed charging of the samples in the case of MT-BC compared to pristine/epoxidized BC. This

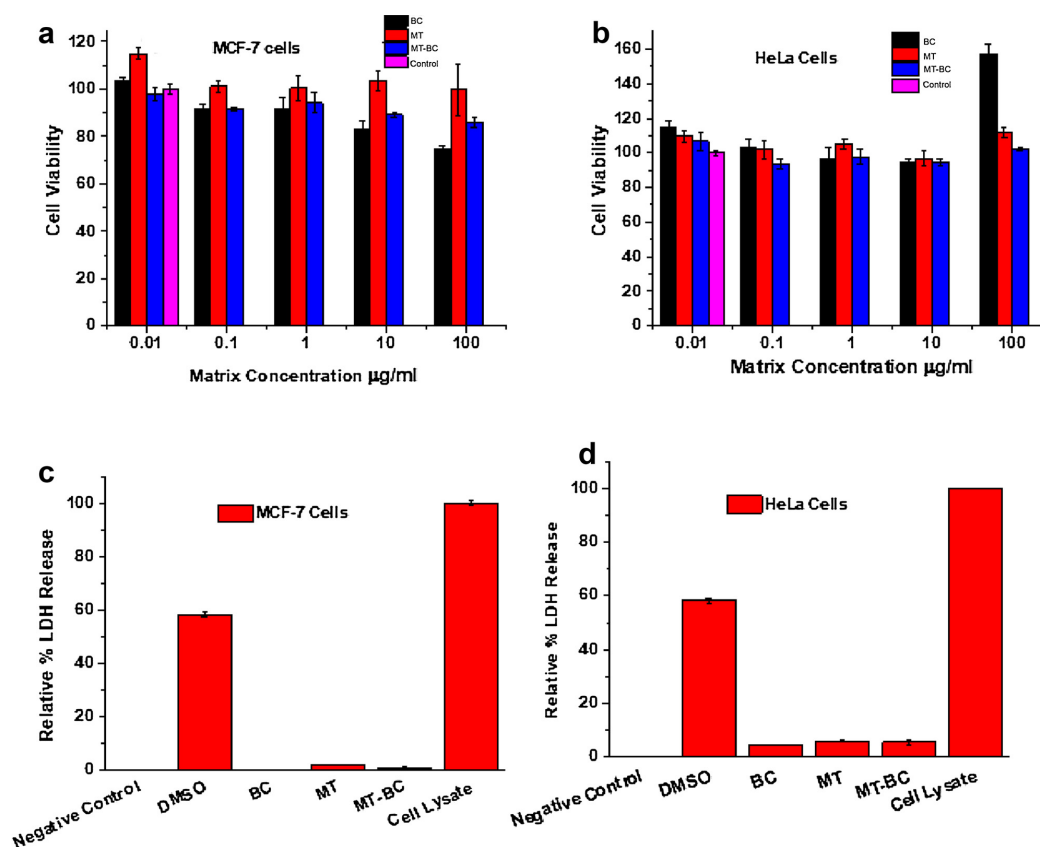


Fig. 6. Cell line toxicity assay for BC, MT and MT-BC on MCF-7 (a) and HeLa (b) cells. Lactate dehydrogenase assay for BC, MT and MT-BC on MCF-7 (c) and HeLa (d) cells.

is often observed for protein samples in SEM. The same samples of BC, eBC and MT-BC are next subjected to complete hydration followed by vacuum drying offered altered morphology. In this case, BC showed swollen morphology with less pores while eBC and MT-BC displayed less swelling and greater number of pores (Supplementary Fig. S6). The less porous hydrated BC is due to the inter sheet connections resulting from the hydrogen bonds between entrapped water molecule and the hydroxyl groups of individual sugar units. Following epoxidation and protein conjugation, the hydrogen bonding network is altered leading to breaking of the sheets as seen in the SEM micrographs of the hydrated eBC and MT-BC. The pore volume of the pristine BC and MT-BC are also analyzed using BET/BJH method (Supplementary Information Table T2). The pore volume in BC is almost 1.55 times that of the MT-BC while the pore surface area of BC is 1.52 times that of MT-BC. The SEM images also show qualitatively that the pore size of BC are larger than that of MT-BC.

In order to compare the thermal stability of MT-BC with BC we performed TGA. MT-BC showed altered thermal properties and changed the profile of the second step of mass loss of the carbohydrate, indicating association of the metallothionein with cellulose (Fig. 3). From the thermograms, it can be seen that for the pure BC there is a specific loss of mass of ~10–15% at around 100 °C followed by a stable no mass loss range up to 250 °C. Above this temperature, the BC start to decompose till 400 °C. This event may also be associated with a degradation of cellulose, including depolymerization, dehydration and decomposition of glucose units, followed by the formation of a carbon

residue (Mohammadkazemi, Azin, & Ashori, 2015; Vazquez, Foresti, Cerrutti, & Galvagno, 2013; Barud et al., 2007). Thermal transition of MT-BC is associated with an initial water loss close to 100 °C followed by gradual mass loss starting at 150 °C and continuing till 400 °C. Initial water loss is less as compared to BC. As discussed in FTIR result that the breadth of the –OH band decreases from BC to MT-BC, which indicated the decrease in the bound water content during the epoxidation and protein conjugation reactions. The gradual mass loss starting from 150 °C can be due to degradation of proteins associated with eBC. Another mass loss event is seen in both pristine BC and MT-BC in the range of 400–600 °C. The final weight loss event could be attributed to the volatilization and oxidation of char followed by the formation of carbonaceous residue. (Cheng, Catchmark, & Demirci, 2009; Tyagi & Suresh, 2016; Vasconcelos et al., 2017). The char residue of MT-BC is much higher than that of pristine BC. This could be due to the enhanced carbon content due to the protein conjugation. The presence of the aliphatic and aromatic side chains of the amino acids lead to a greater residue compared to the cellulose alone.

3.3. Metal binding by conjugate material

Metal binding assays are done with the developed conjugate using four different approaches including UV–vis, fluorescence, SEM elemental mapping and atomic absorption spectroscopy. Salts of divalent metal ions are interacted with BC or MT-BC and incubated for 4 h. Following this the samples are centrifuged and the metal ion

concentration in the supernatant are analyzed using UV–vis spectroscopy or atomic absorption spectroscopy. We observed that upon conjugation with MT, the metal binding capacity of BC is enhanced by almost 5/6 folds (Fig. 4a). We also used the quenching of tryptophan fluorescence to measure the interaction of the metal ions with the covalently conjugated matrix. In this assay we made a saturated solution of the conjugate in water (0.5 mg/mL). The solution is equivalent to 3 μ M of the MT.

This solution was titrated with different divalent metal ions under consideration. All the metal ions showed a quenching and the dissociation constant is in the low μ M range [Co: 28.7 μ M; Fe: 4.7 μ M; Cu: 12.07 μ M; Cd: 7.70 μ M; Pb: 38.3 μ M] (Fig. 4b). SEM provided an estimate of semi-quantitative elemental mapping in MT-BC (Fig. 5 and Supplementary Fig. S7). Elemental mapping of MT-BC showed the presence of metal ions in the matrix along with carbon, oxygen, nitrogen and sulphur. Bacterial cellulose due to its fibrous morphology and presence of huge number of hydroxyl groups can serve to entrap metal. However, the presence of the sulphur rich MT enhances the metal entrapment by close to 5 times for all the divalent metal ions under consideration. We also confirmed the higher metal binding capability of conjugate material as compared to pristine BC with ICP-MS. MT-BC showed 3–5 fold higher binding to metal ions as shown in Supplementary Information Table T3.

3.4. Toxicity of conjugate material

The proliferation potential of MCF7 and HeLa cells are analyzed in presence BC and conjugated material using MTT assay. No effect on cell growth is observed as none of the treated cells showed any significant decrease in cell viability compared to the non-treated ones (Fig. 6a, b). Further, cytotoxic effects of BC and conjugated material is assessed by microscopically analyzing the cell shape and integrity of the cell-membrane using LDH assay (Chan, Moriwaki, & De Rosa, 2013). Neither any significant change in cell shape, nor, any significant LDH release is observed in treated cells suggesting the BC and conjugated material have no cytotoxic effect on the cells (Fig. 6c, d)

4. Conclusion

The work embodied in this article has two important highlights. First, we have developed a protocol for conjugating proteins covalently to cellulosic matrix at ambient conditions. The present method puts forward a facile two-step novel approach for the covalent conjugation of cellulose and protein. This is in contrast to the existing protocols where covalent conjugation involves higher number of steps and use of harsh conditions that may lead to protein denaturation. This conjugation approach opens up interesting possibilities of fabricating cellulose-protein conjugates with diverse functionalities, where enzymes or other structural proteins can be scaffolded on cellulose matrix and can be used for suitable application. The applications may include fabrication of matrices for biocatalysis, bio-storage or biofuel generation. This material may also find its use in the development of 3D cell culture matrices by the impregnation of extracellular matrix proteins onto BC. The essence of this work lies in the fabrication technique that uses no toxic chemicals, high temperature or pressure. This ensures that the protein molecule to be attached to the cellulosic material suffers no loss of property during material development. The other aspect of the work is an application of the above where we have made a cellulose-metallothionein complex (MT-BC) for metal binding. The conjugated matrix has 3–6 times more metal binding capacity compared to pristine BC. The conjugate material doesn't show any significant decrease in cell viability neither have any cytotoxic effect. This kind of matrix will be very important in the management of wounds associated with metal induced insults.

Acknowledgments

The work done here is supported by SERB Women Excellence Award, Dept. of Science and Technology, India (SB/WEA/06/2016). We acknowledge Dr. Sabyasachi Rakshit, Ms. Namrata Singh and Ms Vaishali Chhabra for helpful discussions.

Appendix A. Supplementary data


Supplementary data associated with this article can be found, in the online version, at <https://doi.org/10.1016/j.carbpol.2018.03.043>.

References

- Anjum, S., Arora, A., Alam, M., & Gupta, B. (2016). Development of antimicrobial and scar preventive chitosan hydrogel wound dressings. *International Journal of Pharmaceutics*, 508(1), 92–101.
- Ashjaran, A., Yazdanshenas, M. E., Rashidi, A., Khajavi, R., & Rezaee, A. (2013). Overview of bio nanofabric from bacterial cellulose. *Journal of the Textile Institute*, 104(2), 121–131.
- Babu, P. J., Doble, M., & Raichur, A. M. (2018). Silver oxide nanoparticles embedded silk fibroin spuns: Microwave mediated preparation, characterization and their synergistic wound healing and anti-bacterial activity. *Journal of Colloid and Interface Science*, 513, 62–71.
- Barua, S., Dutta, G., & Karak, N. (2013). Glycerol based tough hyperbranched epoxy: Synthesis, statistical optimization and property evaluation. *Chemical Engineering Science*, 95, 138–147.
- Barud, H., Ribeiro, C., Crespi, M., Martines, M., Dexpert-Ghys, J., Marques, R., ... Ribeiro, S. (2007). Thermal characterization of bacterial cellulose–phosphate composite membranes. *Journal of Thermal Analysis and Calorimetry*, 87(3), 815–818.
- Barud, H. O., Barud, H. d. S., Cavicchioli, M., do Amaral, T. S., de Oliveira Junior, O. B., Santos, D. M., ... de Oliveira, C. I. (2015). Preparation and characterization of a bacterial cellulose/silk fibroin sponge scaffold for tissue regeneration. *Carbohydrate Polymers*, 128, 41–51.
- Basmaji, P., de Olyveira, G., Manzone Costa, L., Francozo, G., & da Costa, O. (2015). Nanoderm extracellular matrix for reconstructive surgery applications. *Peertech Journal of Biomedical Engineering*, 1, 021–024.
- Bradford, M. M. (1976). A rapid and sensitive method for the quantitation of microgram quantities of protein utilizing the principle of protein-dye binding. *Analytical Biochemistry*, 72(1–2), 248–254.
- Brown, R. M., & Montezinos, D. (1976). Cellulose microfibrils: Visualization of biosynthetic and orienting complexes in association with the plasma membrane. *Proceedings of the National Academy of Sciences*, 73(1), 143–147.
- Brown, R. M., Willison, J., & Richardson, C. L. (1976). Cellulose biosynthesis in *Acetobacter xylinum*: Visualization of the site of synthesis and direct measurement of the in vivo process. *Proceedings of the National Academy of Sciences*, 73(12), 4565–4569.
- Bush, A. I. (2000). Metals and neuroscience. *Current Opinion in Chemical Biology*, 4(2), 184–191.
- Cao, R., Guan, L., Li, M., Tian, J., & Shen, W. (2015). A zero-step functionalization on paper-based biosensing platform for covalent biomolecule immobilization. *Sensing and Bio-Sensing Research*, 6, 13–18.
- Carpenè, E., Andreani, G., & Isani, G. (2007). Metallothionein functions and structural characteristics. *Journal of Trace Elements in Medicine and Biology*, 21, 35–39.
- Centeno, J. A., Rogers, D. A., van der Voet, G. B., Fornero, E., Zhang, L., Mullick, F. G., ... Stojadinovic, A. (2014). Embedded fragments from US military personnel—Chemical analysis and potential health implications. *International Journal of Environmental Research and Public Health*, 11(2), 1261–1278.
- Chan, F. K.-M., Moriwaki, K., & De Rosa, M. J. (2013). Detection of necrosis by release of lactate dehydrogenase activity. *Immune Homeostasis: Methods and Protocols*, 65–70.
- Chandrasekaran, P. T., Bari, N. K., & Sinha, S. (2017). Enhanced bacterial cellulose production from *Gluconobacter xylinus* using super optimal broth. *Cellulose*, 24(10), 4367–4381.
- Cheng, K.-C., Catchmark, J. M., & Demirci, A. (2009). Enhanced production of bacterial cellulose by using a biofilm reactor and its material property analysis. *Journal of Biological Engineering*, 3(1), 12.
- Coyle, P., Philcox, J., Carey, L., & Rofe, A. (2002). Metallothionein: The multipurpose protein. *Cellular and Molecular Life Sciences*, 59(4), 627–647.
- Czaja, W. K., Young, D. J., Kaweck, M., & Brown, R. M. (2007). The future prospects of microbial cellulose in biomedical applications. *Biomacromolecules*, 8(1), 1–12.
- Dai, X., Xiong, Z., Ma, S., Li, C., Wang, J., Na, H., & Zhu, J. (2015). Fabricating highly reactive bio-based compatibilizers of epoxidized citric acid to improve the flexural properties of polylactide/microcrystalline cellulose blends. *Industrial & Engineering Chemistry Research*, 54(15), 3806–3812.
- Davis, S. R., & Cousins, R. J. (2000). Metallothionein expression in animals: A physiological perspective on function. *The Journal of Nutrition*, 130(5), 1085–1088.
- De, B., Gupta, K., Mandal, M., & Karak, N. (2013). Biodegradable hyperbranched epoxy from castor oil-based hyperbranched polyester polyol. *ACS Sustainable Chemistry & Engineering*, 2(3), 445–453.
- Dhas, S. P., Anbarasan, S., Mukherjee, A., & Chandrasekaran, N. (2015). Biobased silver nanocolloid coating on silk fibers for prevention of post-surgical wound infections.

- International Journal of Nanomedicine*, 10(1), 159.
- Dhivya, S., Padma, V. V., & Santhini, E. (2015). Wound dressings—A review. *Biomedicine*, 5(4).
- Diftis, N., & Kiosseoglou, V. (2003). Improvement of emulsifying properties of soybean protein isolate by conjugation with carboxymethyl cellulose. *Food Chemistry*, 81(1), 1–6.
- El-Hoseny, S. M., Basmaji, P., de Olyveira, G. M., Costa, L. M. M., Alwahedi, A. M., da Costa Oliveira, J. D., & Francozo, G. B. (2015). Natural ECM-bacterial cellulose wound Healing—Dubai study. *Journal of Biomaterials and Nanobiotechnology*, 6(04), 237.
- Evtushenko, Y. M., Zaitsev, B., Ivanov, V., Khalaturinskii, N., & Evtushenko, G. Y. (2001). Determination of hydroxyl groups in epoxy resins by potentiometric titration using a reaction with maleic anhydride. *Journal of Analytical Chemistry*, 56(11), 1035–1037.
- Fang, W., Arola, S., Malho, J.-M., Kontturi, E., Linder, M. B., & Laaksonen, P. (2016). Noncovalent dispersion and functionalization of cellulose nanocrystals with proteins and polysaccharides. *Biomacromolecules*, 17(4), 1458–1465.
- Fernandes, S. C., Sadocco, P., Alonso-Varona, A., Palomares, T., Eceiza, A., Silvestre, A. J., ... Freire, C. S. (2013). Bioinspired antimicrobial and biocompatible bacterial cellulose membranes obtained by surface functionalization with aminoalkyl groups. *ACS Applied Materials & Interfaces*, 5(8), 3290–3297.
- Fritz, C., Jeuck, B., Salas, C., Gonzalez, R., Jameel, H., & Rojas, O. J. (2015). *Nanocellulose and proteins: Exploiting their interactions for production, immobilization, and synthesis of biocompatible materials. Cellulose chemistry and properties: Fibers, nanocelluloses and advanced materials*. Springer 207–224.
- Galanis, A., Karapetsas, A., & Sandaltzopoulos, R. (2009). Metal-induced carcinogenesis, oxidative stress and hypoxia signalling. *Mutation Research/Genetic Toxicology and Environmental Mutagenesis*, 674(1), 31–35.
- Glei, M., Latunde-Dada, G. O., Klinder, A., Becker, T. W., Hermann, U., Voigt, K., & Pool-Zobel, B. L. (2002). Iron-overload induces oxidative DNA damage in the human colon carcinoma cell line HT29 clone 19A. *Mutation Research/Genetic Toxicology and Environmental Mutagenesis*, 519(1), 151–161.
- Habibi, Y. (2014). Key advances in the chemical modification of nanocelluloses. *Chemical Society Reviews*, 43(5), 1519–1542.
- He, Z., Wang, Y., Zhao, T., Ye, Z., & Huang, H. (2014). Ultrasonication-assisted rapid determination of epoxide values in polymer mixtures containing epoxy resin. *Analytical Methods*, 6(12), 4257–4261.
- Holstein, C. A., Chevalier, A., Bennett, S., Anderson, C. E., Keniston, K., Olsen, C., ... Fu, E. (2016). Immobilizing affinity proteins to nitrocellulose: A toolbox for paper-based assay developers. *Analytical and Bioanalytical Chemistry*, 408(5), 1335–1346.
- Huang, Y., Wu, D., Wang, X., Huang, W., Lawless, D., & Feng, X. (2016). Removal of heavy metals from water using polyvinylamine by polymer-enhanced ultrafiltration and flocculation. *Separation and Purification Technology*, 158, 124–136.
- Jang, W. D., Hwang, J. H., Kim, H. U., Ryu, J. Y., & Lee, S. Y. (2017). Bacterial cellulose as an example product for sustainable production and consumption. *Microbial Biotechnology*, 10(5), 1181–1185.
- Kontturi, K. S., Biegaj, K., Mautner, A., Woodward, R. T., Wilson, B. P., Johansson, L.-S., ... Kontturi, E. (2017). Noncovalent surface modification of cellulose nanopapers by adsorption of polymers from aprotic solvents. *Langmuir*, 33(23), 5707–5712.
- Kubler-Kielb, J., & Pozgay, V. (2005). A new method for conjugation of carbohydrates to proteins using an aminoxy-thiol heterobifunctional linker. *The Journal of Organic Chemistry*, 70(17), 6987–6990.
- Lansdown, A. B., Sampson, B., & Rowe, A. (2001). Experimental observations in the rat on the influence of cadmium on skin wound repair. *International Journal of Experimental Pathology*, 82(1), 35–41.
- Lee, H., Rho, J., & Messersmith, P. B. (2009). Facile conjugation of biomolecules onto surfaces via mussel adhesive protein inspired coatings. *Advanced Materials*, 21(4), 431–434.
- Lee, S.-H., Lim, Y.-M., Jeong, S. I., An, S.-J., Kang, S.-S., Jeong, C.-M., & Huh, J.-B. (2015). The effect of bacterial cellulose membrane compared with collagen membrane on guided bone regeneration. *The Journal of Advanced Prosthodontics*, 7(6), 484–495.
- Leonard, S. S., Bower, J. J., & Shi, X. (2004). Metal-induced toxicity, carcinogenesis, mechanisms and cellular responses. *Molecular and Cellular Biochemistry*, 255(1), 3–10.
- Li, Y., Xiao, F., & Wong, C. (2007). Novel, environmentally friendly crosslinking system of an epoxy using an amino acid: Tryptophan-cured diglycidyl ether of bisphenol A epoxy. *Journal of Polymer Science Part A: Polymer Chemistry*, 45(2), 181–190.
- Li, Y., Yang, L., Zhang, H., & Tang, Z. (2017). Synthesis and curing performance of a novel bio-based epoxy monomer from soybean oil. *European Journal of Lipid Science and Technology*, 119(8) 1600429-n/a.
- Lopes, T. D., Riegel-Vidotti, I. C., Grein, A., Tischer, C. A., & de Sousa Faria-Tischer, P. C. (2014). Bacterial cellulose and hyaluronic acid hybrid membranes: Production and characterization. *International Journal of Biological Macromolecules*, 67, 401–408.
- Menon, A. V., Chang, J., & Kim, J. (2016). Mechanisms of divalent metal toxicity in affective disorders. *Toxicology*, 339, 58–72.
- Mercogliano, C. P., & DeRosier, D. J. (2007). Concatenated metallothionein as a clonable gold label for electron microscopy. *Journal of Structural Biology*, 160(1), 70–82.
- Miao, S., Liu, K., Wang, P., Su, Z., & Zhang, S. (2015). Preparation and characterization of epoxidized soybean oil-based paper composite as potential water-resistant materials. *Journal of Applied Polymer Science*, 132(10).
- Moffatt, P., & Denizeau, F. (1997). Metallothionein in physiological and physiopathological processes. *Drug Metabolism Reviews*, 29(1–2), 261–307.
- Mohammadkazemi, F., Azin, M., & Ashori, A. (2015). Production of bacterial cellulose using different carbon sources and culture media. *Carbohydrate Polymers*, 117, 518–523.
- Moniri, M., Boroumand Moghaddam, A., Azizi, S., Abdul Rahim, R., Bin Ariff, A., Zuhainis Saad, W., ... Mohamad, R. (2017). Production and status of bacterial cellulose in biomedical engineering. *Nanomaterials*, 7(9), 257.
- Morgan, J. L., McNamara, J. T., Fischer, M., Rich, J., Chen, H.-M., Withers, S. G., & Zimmer, J. (2016). Observing cellulose biosynthesis and membrane translocation in crystallo. *Nature*, 531(7594), 329–334.
- Mustata, F., Tudorachi, N., & Bicu, I. (2015). The kinetic study and thermal characterization of epoxy resins crosslinked with amino carboxylic acids. *Journal of Analytical and Applied Pyrolysis*, 112, 180–191.
- Naingolan, H., Gea, S., Bilotti, E., Peijs, T., & Hutagalung, S. D. (2013). Mechanical and thermal properties of bacterial-cellulose-fibre-reinforced Mater-Bi[®] bionanocomposite. *Beilstein Journal of Nanotechnology*, 4, 325.
- Orelma, H., Filpponen, I., Johansson, L.-S., Laine, J., & Rojas, O. J. (2011). Modification of cellulose films by adsorption of CMC and chitosan for controlled attachment of biomolecules. *Biomacromolecules*, 12(12), 4311–4318.
- Orelma, H., Johansson, L.-S., Filpponen, I., Rojas, O. J., & Laine, J. (2012). Generic method for attaching biomolecules via avidin–biotin complexes immobilized on films of regenerated and nanofibrillar cellulose. *Biomacromolecules*, 13(9), 2802–2810.
- Orelma, H., Teerinen, T., Johansson, L.-S., Holappa, S., & Laine, J. (2012). CMC-modified cellulose biointerface for antibody conjugation. *Biomacromolecules*, 13(4), 1051–1058.
- Petersen, N., & Gatenholm, P. (2011). Bacterial cellulose-based materials and medical devices: Current state and perspectives. *Applied Microbiology and Biotechnology*, 91(5), 1277.
- Pradhan, S., Pandey, P., Mohanty, S., & Nayak, S. K. (2016). Insight on the chemistry of epoxy and its curing for coating applications: A detailed investigation and future perspectives. *Polymer-Plastics Technology and Engineering*, 55(8), 862–877.
- Renfrow, B., Vaidya, R., Elia, C., & Sethi, A. (2013). Lead toxicity and management of gunshot wounds in the lumbar spine. *European Spine Journal*, 22(11), 2353–2357.
- Roman, M., & Winter, W. T. (2004). Effect of sulfate groups from sulfuric acid hydrolysis on the thermal degradation behavior of bacterial cellulose. *Biomacromolecules*, 5(5), 1671–1677.
- Ryu, H., Han, J. K., Jung, J. W., Bae, B., & Nam, K. (2007). Human health risk assessment of explosives and heavy metals at a military gunnery range. *Environmental Geochemistry and Health*, 29(4), 259–269.
- Sai, H., Fu, R., Xing, L., Xiang, J., Li, Z., Li, F., & Zhang, T. (2015). Surface modification of bacterial cellulose aerogels' web-like skeleton for oil/water separation. *ACS Applied Materials & Interfaces*, 7(13), 7373–7381.
- Skalk, S., Abu-Shaban, N., Abu-Shaban, N., Barbieri, M., Barbieri, M., Giani, U., & Manduca, P. (2010). Metals detected by ICP/MS in wound tissue of war injuries without fragments in Gaza. *BMC International Health and Human Rights*, 10(1), 17.
- Sutherland, D. E., & Stillman, M. J. (2011). The magic numbers of metallothionein. *Metallomics*, 3(5), 444–463.
- Torres, F. G., Commeaux, S., & Troncoso, O. P. (2012). Biocompatibility of bacterial cellulose based biomaterials. *Journal of Functional Biomaterials*, 3(4), 864–878.
- Tyagi, N., & Suresh, S. (2016). Production of cellulose from sugarcane molasses using *Gluconacetobacter intermedius* SNT-1: Optimization & characterization. *Journal of Cleaner Production*, 112, 71–80.
- Urani, C., Melchiorretto, P., Fabbri, M., Bowe, G., Maserati, E., & Gribaldo, L. (2014). Cadmium impairs p53 activity in HepG2 cells. *ISRN Toxicology*, 9.
- Vasconcelos, N. F., Feitosa, J. P. A., da Gama, F. M. P., Morais, J. P. S., Andrade, F. K., de Souza, M. d. S. M., & de Freitas Rosa, M. (2017). Bacterial cellulose nanocrystals produced under different hydrolysis conditions: Properties and morphological features. *Carbohydrate Polymers*, 155, 425–431.
- Vazquez, A., Foresti, M. L., Cerrutti, P., & Galvagno, M. (2013). Bacterial cellulose from simple and low cost production media by *Gluconacetobacter xylinus*. *Journal of Polymers and the Environment*, 21(2), 545–554.
- Weishaupt, R., Siqueira, G., Schubert, M., Tingaut, P., Maniura-Weber, K., Zimmermann, T., ... Ihsen, J. (2015). TEMPO-oxidized nanofibrillated cellulose as a high density carrier for bioactive molecules. *Biomacromolecules*, 16(11), 3640–3650.
- Yao, J., Chen, S., Chen, Y., Wang, B., Pei, Q., & Wang, H. (2017). Macrofibers with high mechanical performance based on aligned bacterial cellulose nanofibers. *ACS Applied Materials & Interfaces*, 9(24), 20330–20339.
- Yin, N., Chen, S., Li, Z., Ouyang, Y., Hu, W., Tang, L., ... Xu, Q. (2012). Porous bacterial cellulose prepared by a facile surfactant-assisted foaming method in azodicarbonamide-NaOH aqueous solution. *Materials Letters*, 81, 131–134.

Permissions from Journals for reuse of content in Thesis



Nanoparticle Fabrication on Bacterial Microcompartment Surface for the Development of Hybrid Enzyme-Inorganic Catalyst

Author: Naimat Kalim Bari, Gaurav Kumar, Aashish Bhatt, et al

Publication: ACS Catalysis

Publisher: American Chemical Society

Date: Sep 1, 2018

Copyright © 2018, American Chemical Society

PERMISSION/LICENSE IS GRANTED FOR YOUR ORDER AT NO CHARGE

This type of permission/license, instead of the standard Terms & Conditions, is sent to you because no fee is being charged for your order. Please note the following:

- Permission is granted for your request in both print and electronic formats, and translations.
- If figures and/or tables were requested, they may be adapted or used in part.
- Please print this page for your records and send a copy of it to your publisher/graduate school.
- Appropriate credit for the requested material should be given as follows: "Reprinted (adapted) with permission from (COMPLETE REFERENCE CITATION). Copyright (YEAR) American Chemical Society." Insert appropriate information in place of the capitalized words.
- One-time permission is granted only for the use specified in your request. No additional uses are granted (such as derivative works or other editions). For any other uses, please submit a new request.

BACK
CLOSE WINDOW



naimat kalim bari <barinaimat@gmail.com>

Request for use of paper in thesis

2 messages

naimat kalim bari <barinaimat@gmail.com>
To: Contracts-Copyright@rsc.org

Thu, Mar 12, 2020 at 6:06 PM

Dear Sir/Madam
I, Naimat Kalim Bari, Ph.D. student with Dr. Sharmistha Sinha, wish to use my publication, published in JMC-B in my thesis with modifications. The title for my paper is "**Functional protein shells fabricated from the self-assembling protein sheets of prokaryotic organelles**" *J. Mater. Chem. B*, 2020, **8**, 523-533.
<https://doi.org/10.1039/C9TB02224D>.

Please allow me to do the same

With regards
Naimat Kalim Bari
PhD Student

C/o Sharmistha Sinha
Assistant Professor (Scientist E)
Institute of Nano Science and Technology
Habitat Centre, Phase- 10, Sector- 64
Mohali, Punjab - 160062
Phone Numbers: 08527674555
email id- barinaimat@gmail.com; naimatb@inst.ac.in



Sender notified by
Mailtrack

CONTRACTS-COPYRIGHT (shared) <Contracts-Copyright@rsc.org>
To: naimat kalim bari <barinaimat@gmail.com>

Thu, Mar 12, 2020 at 6:13 PM


Many thanks for sending the permissions request below. The Royal Society of Chemistry (RSC) hereby grants permission for the use of your paper(s) specified below in the printed and microfilm version of your thesis. You may also make available the PDF version of your paper(s) that the RSC sent to the corresponding author(s) of your paper(s) upon publication of the paper(s) in the following ways: in your thesis via any website that your university may have for the deposition of theses, via your university's Intranet or via your own personal website. We are however unable to grant you permission to include the PDF version of the paper(s) on its own in your institutional repository. The Royal Society of Chemistry is a signatory to the STM Guidelines on Permissions (available on request).

Please note that if the material specified below or any part of it appears with credit or acknowledgement to a third party then you must also secure permission from that third party before reproducing that material.

Please ensure that the thesis states the following:


Reproduced by permission of The Royal Society of Chemistry

and include a link to the paper on the Royal Society of Chemistry's website.



RightsLink®

[Home](#)
[Help](#)
[Email Support](#)
[Sign in](#)
[Create Account](#)



Cellulose-metallothionein matrix for metal binding

Author: Naimat K. Bari, Shaswat Barua, Ankush Garg, Malay K. Sannigrahi, Sharmistha Sinha

Publication: Carbohydrate Polymers

Publisher: Elsevier

Date: 15 July 2018

© 2018 Elsevier Ltd. All rights reserved.

Please note that, as the author of this Elsevier article, you retain the right to include it in a thesis or dissertation, provided it is not published commercially. Permission is not required, but please ensure that you reference the journal as the original source. For more information on this and on your other retained rights, please visit: <https://www.elsevier.com/about/our-business/policies/copyright#Author-rights>

BACK
CLOSE WINDOW

© 2020 Copyright - All Rights Reserved | [Copyright Clearance Center, Inc.](#) | [Privacy statement](#) | [Terms and Conditions](#)
 Comments? We would like to hear from you. E-mail us at customercare@copyright.com

02/03/2020

RightsLink Printable License

**SPRINGER NATURE LICENSE
TERMS AND CONDITIONS**

Mar 02, 2020

This Agreement between naimat kalim bari ("You") and Springer Nature ("Springer Nature") consists of your license details and the terms and conditions provided by Springer Nature and Copyright Clearance Center.

License Number	4780551236251
License date	Mar 01, 2020
Licensed Content Publisher	Springer Nature
Licensed Content Publication	Cellulose
Licensed Content Title	Enhanced bacterial cellulose production from Gluconobacter xylinus using super optimal broth
Licensed Content Author	Prathna T. Chandrasekaran et al
Licensed Content Date	Jul 22, 2017
Type of Use	Thesis/Dissertation
Requestor type	academic/university or research institute
Format	print and electronic
Portion	full article/chapter
Will you be translating?	no
Circulation/distribution	1 - 29

<https://s100.copyright.com/AppDispatchServlet?PaymentProfileId=0&passThroughTarget=aboutyourwork-select&isMyAccount=false&ref=3d0b9a26-c57d-4...> 1/5

Publications from this thesis

1. **Bari, N. K.**, Kumar, G., and Sinha, S., The Wrappers of the 1, 2-Propanediol Utilization Bacterial Microcompartments; *Biochemical and Biophysical Roles of Cell Surface Molecules*, Springer, Singapore, **2018**, 333-344.
2. **Bari, N. K.**, Hazra, J. P., Kumar, G., Kaur, S., and Sinha, S. Probe into a Multi-Protein Prokaryotic Organelle Using Thermal Scanning Assay Reveals Distinct Properties of the Core and the Shell; (Accepted, BBA-General Subjects, **2020**).
3. **Bari, N. K.**, Hazra, J. P., Kumar, G., Kaur, S., and Sinha, S. (2019). Functional Protein Shells Fabricated from the Self-Assembling Protein Sheets of Prokaryotic Organelles; *J. Mater. Chem. B*, **2020**, 8, 523-533.
4. **Bari, N. K.**, Kumar, G., Bhatt, A., Hazra, J. P., Garg, A., Ali, M. E., and Sinha, S., Nanoparticle Fabrication on Bacterial Microcompartment Surface for the Development of Hybrid Enzyme-Inorganic Catalyst; *ACS Catalysis*, **2018**, 8, 7742-7748.
5. **Bari, N. K.**, Barua, S., Garg, A., Sannigrahi, M. K., and Sinha, S., Cellulose-Metallothionein Matrix for Metal Binding; *Carbohydrate polymers*, **2018**, 192, 126-134.
6. Chandrasekaran, P. T., **Bari, N. K.**, and Sinha, S. Enhanced Bacterial Cellulose Production from *Gluconobacter xylinus* using Super Optimal Broth; *Cellulose*, **2017**, 24, 4367-4381.